Aus dem Lehrstuhl für
Experimentelle Ultrahochfeld Magnetresonanz
der Medizinischen Fakultät Charité – Universitätsmedizin Berlin

DISSERTATION

Untersuchungen experimenteller Theranostikansätze bei Neuroinflammation mittels Ultrahochfeld Magnetresonanz-Methoden

zur Erlangung des akademischen Grades
Doctor rerum medicinalium (Dr. rer. medic.)

vorgelegt der Medizinischen Fakultät
Charité – Universitätsmedizin Berlin

von

Christian Prinz

Datum der Promotion: 03.12.2021

Gewidmet meiner liebevollen Ehefrau Sabrina

Inhalt

Zusammenfassung

Die Überwachung von Therapien wie etwa bei Multipler Sklerose (MS) ist notwendig, um patientenorientierte Behandlungsansätze zu finden. Während Proton (^{1}H) Magnetresonanztomographie (MRT) zur Unterstützung der Diagnose und zur Überwachung des Krankheitszustands verwendet wird, birgt Fluor-19 (^{19}F) MRT das Potential einer nicht-invasiven Methode, um fluorierte Medikamente im Körper zu detektieren und deren Verteilung zu messen. Unter Verwendung von ^{19}F MRT Techniken wurden im Rahmen dieser Arbeit die Substanz spezifischen ^{19}F MR Eigenschaften des MS Medikaments Teriflunomid, sowie anderer fluorierter Substanzen unter verschiedenen Umgebungsbedingungen wie variabler Temperatur, pH und chemischer Umgebung untersucht. In einem Tiermodell der Multiplen Sklerose konnte Teriflunomid schließlich mittels ^{19}F MR Spektroskopie detektiert und die Signalmenge über den Krankheitsverlauf hinweg parallel zu diagnostischer ^{1}H MRT verfolgt werden. Schließlich wurde die Verteilung des Medikaments in Gehirn, Liquor und Blutplasma mittels Massenspektrometrie bestimmt und mit der Signaldetektion aus ^{19}F MR Spektroskopie verglichen. Dass die Signalmenge, die im Sinne entweder kürzerer Messzeiten oder besserer Auflösung mittels Compressed Sensing (CS) erhöht werden kann, konnte ebenfalls gezeigt werden. Die Forschungsarbeiten, die in dieser kumulativen Dissertation beschrieben werden, stellen Schritte hin zu einer Optimierung von ^{19}F MR Methoden dar, die in einer klinischen Anwendung resultieren kann und so eine Bestimmung der Verteilung von Medikamenten und einem therapeutischen Monitoring dienen kann, um MS Therapien auf Patienten zuzuschneiden und die Therapiequalität zu verbessern.

Abstract

Monitoring therapies for treating pathologies such as multiple sclerosis (MS) is necessary to find patient-oriented treatment approaches. While proton (^{1}H) magnetic resonance imaging (MRI) is used to diagnose and monitor disease conditions such as MS, fluorine-19 (^{19}F) MRI holds the potential of a non-invasive method to detect and quantify fluorinated drugs in the body and thereby study their distribution. Using ^{19}F magnetic resonance (MR) techniques, this work investigated the specific ^{19}F MR properties of the MS drug teriflunomide (TF), as well as other fluorinated compounds under varying environmental conditions such as temperature, pH, and chemical environment. Finally, TF was detected in an animal model of MS by ^{19}F MR spectroscopy (MRS) and the amount of signal was followed over the course of the disease in parallel to anatomical ^{1}H MRI. Finally, the distribution of the drug in brain, cerebrospinal fluid (CSF), and blood plasma was determined by mass spectrometry and compared with signal detection by ^{19}F MRS. That the amount of signal that can be increased in terms of either shorter measurement times or better resolution using compressed sensing was also demonstrated. The research described in this cumulative dissertation represents steps towards an optimization of ^{19}F MR methods that may result in a clinical application and thus a determination of drug distribution and therapeutic mounting to tailor MS therapies to patients and improve therapy quality.

1 Einleitung

Multiple Sklerose (MS) ist eine chronisch entzündliche Erkrankung des Zentralnervensystems (ZNS). Der Krankheitsverlauf ist häufig schubförmig und kann schließlich in eine progrediente Phase übergehen. Dementsprechend variabel stellt sich die Symptomatik dar, mit einem breiten Spektrum neurologischer und motorischer Symptome [1].

Proton (^{1}H) Magnetresonanztomographie (MRT) ist eine für die Differential-Diagnose und Überwachung der MS unerlässliche Methode, die in der Klinik standardmäßig durchgeführt wird. Es können chronische von aktiven Läsionen unter Verwendung von Kontrastmittel, um die Integrität der Blut-Hirn-Schranke zu untersuchen, unterschieden werden [2]. Ebenso wird MRT benutzt, um Entscheidungen zur Therapieplanung und Dosisfindung zu unterstützen und im Hinblick auf Disease Modifying Drugs (DMD) eine risikoarme therapeutische Wirkung von Medikamenten zu überwachen [3]. Allerdings können derartige MR gestützte Aussagen zur Medikamentenwirkung bislang und in der Regel nur an sekundären Endpunkten, wie der Anzahl der T_2 Läsionen, oder dem Ausmaß an Gehirnatrophie festgemacht werden [4]. Erst kürzlich wurde eine Veränderung des Ventrikelvolumens über den Krankheitsverlauf als möglicher Biomarker von unserer Arbeitsgruppe beschrieben [5]. Im Hinblick auf die Therapie ermöglichen diese Endpunkte und Messmodalitäten keine Aussagen über die Wirkstoffverteilung im Körper und die Konzentrationen am Zielort und in verschiedenen Kompartimenten.

Das Tiermodell der Experimentellen Autoimmunenzephalomyelitis (EAE) wird als Modell für die MS benutzt. Durch die konzertierte Immunisierung mit Autoantigenen sowie die Stimulation und Verstärkung immunmodulatorischer Prozesse können insbesondere bei SJL/J Mäusen schubförmige Verläufe modelliert, der Krankheitsprozess und die Beeinträchtigungen der Integrität der Blut-Hirn-Schranke mittels MRT abgebildet sowie der Einfluss von Therapien und deren Wirksamkeit untersucht werden [6].

Es steht eine große Anzahl verschiedener Therapien und Medikamente zur Behandlung der MS zur Verfügung [7]. Vorhersagen über den Therapieverlauf, Wirksamkeit und Verträglichkeit sowie die Prognose des Patienten können bislang nur begrenzt getroffen werden [8], mitunter weil die Verteilung und Menge klinisch nur durch die Bestimmung von Serum-, Urin- und selten Liquorkonzentrationen (CSF) erfolgt. Diese Konzentrationen spiegeln allerdings nicht die Konzentrationen von Wirkstoffen an Zielorten wie dem Gehirn bei MS oder lymphatischen Geweben wider.

Während Positronenemissionstomographie (PET) und Einzelphotonen-Emissionscomputertomographie (SPECT) mit dem Einsatz von radioaktiv markierten Medikamenten einhergehen und in klinischen Phase I Studien in einer begrenzten Anzahl an

gesunden Probanden durchgeführt werden, gibt es derzeit keine nicht-invasive, patientenfreundliche und in der Klinik standardmäßig angewandte Technik, um die Verteilung von Wirkstoffen im Körper zu untersuchen.

Fluor-19 (^{19}F) MRT wurde in der Vergangenheit bereits in biomedizinischen Anwendungen benutzt, wie etwa um Immuntherapien bei Krebserkrankungen zu verfolgen [9] oder entzündliche Prozesse mit fluorierten Nanopartikeln in vivo darzustellen [10]. Diese Methodik wurde in unserer Arbeitsgruppe bereits im EAE Mausmodell mit perfluorierten ^{19}F Perfluorocrownether (PFCE) Nanopartikeln (NP) zur Darstellung von neuroinflammatorischen Prozessen und zu verschiedenen Zeitpunkten des Krankheitsverlaufs benutzt.

Ebenso wurden in verschiedenen Studien bereits fluorierte Medikamente im Tierversuch [11] und der Humananwendung untersucht [12, 13]. ^{19}F MR Techniken sind insofern gut geeignet für die Untersuchung biologischer und pharmakologischer Prozesse, als dass der ^{19}F Nukleus eine 100 % Verfügbarkeit für MR Detektion sowie eine hohe gyromagnetische Ratio aufweist und hintergrundfreie Detektion ermöglicht, da ^{19}F im MR detektierbaren Bereich im Körper nicht vorhanden ist [14].

Da mehr als ein Drittel aller aktuell eingesetzten Medikamente in ihrer molekularen Struktur das Element ^{19}F enthalten, kann dieser Nukleus mit ^{19}F MR Techniken detektiert werden [14]. ^{19}F in Wirkstoffmolekülen erhöht deren Lipophilie und verbessert so die Durchlässigkeit an biologischen Membranen, und verlangsamt die Verstoffwechselung, da die Stabilität höher ist, im Vergleich zu Medikamenten ohne ^{19}F [14].

Die Limitierung der Methode liegt vor allem im geringen Vorkommen von ^{19}F, da die verabreichten Wirkstoffdosen geringgehalten werden und somit die totale Anzahl an ^{19}F Atomen, die potenziell detektiert werden können, niedrig ist. Zudem ist die Sensitivität von MR Hardware und Detektionseffizienz von MR Sequenzen limitiert und bietet Potential für Optimierung.

^{19}F MR Techniken stellen somit eine nicht-invasive Methode dar, um parallel zu anatomischer MR Bildgebung die Verteilung von Medikamenten im Körper zu bestimmen und als theranostische Methode zur evidenzbasierten Therapieführung und auf Patienten zugeschnittenen Wirkstoff- und Dosisfindung sowie zur Anpassung bei sich ändernden Krankheitsbedingungen verwendet zu werden.

In bisherigen Studien wurden Wirkstoffe entweder in hoher Dosis [11] verabreicht oder erst kurz vor der Messung gegeben [15], um eine maximal hohe Detektion zu erreichen. Allerdings bildet dies nicht die klinische Situation mit monatelanger Einnahme eines Medikaments ab, kann aber als erster Schritt hin zur klinischen Anwendung gesehen werden. Vorarbeiten

unserer Gruppe bei 7 T zeigten das Potential von ^{19}F MR Techniken, hohe Mengen an ^{19}F haltiger Salbe zu detektieren und mittels ^{19}F MR Bildgebung abzubilden [13].

Mit Teriflunomid (TF) gibt es ein MS Medikament, welches mechanistisch das mitochondriale Enzym Dihydroorotatdehydrogenase (DHODH) hemmt und so zu einer Blockierung der Pyrimidinsynthese führt. Dies entzieht sich schnell teilenden Zellen wie inflammatorischen Zellen die biochemische Grundlage für Proliferation und DNA-Synthese [16]. TF enthält eine Trifluormethylgruppe (CF_3), sodass dieses Medikament potenziell mit ^{19}F MR Techniken während des Krankheitsverlaufs in vivo untersucht werden kann.

Bislang konnte die Verteilung von TF im ZNS im EAE Tiermodell ex vivo bei Ratten durch PET [17] und im Mausmodell mittels MALDI Massenspektrometrie bestimmt werden [18]. Während diese Methoden nur präklinisch beziehungsweise ex vivo verwendet wurden, kann der Einsatz einer nicht-invasiven MR Methode zu einem besseren Verständnis der Verteilung und einer zielgerichteten Therapie beitragen.

Obwohl die Sensitivität und das gyromagnetische Verhältnis von ^{19}F mit denen von ^{1}H vergleichbar sind, ist die Detektion von ^{19}F aufgrund der geringeren Verfügbarkeit von ^{19}F Atomen im Vergleich zu ^{1}H Atomen limitiert. Aus diesem Grund sind die zu erwartenden Signal-zu-Rausch (Signal-to-Noise Ratio, SNR) Werte geringer und die resultierenden Detektionslimits höher. Folglich ist eine genaue Kenntnis der substanzspezifischen ^{19}F MR Eigenschaften und die Auswahl und Optimierung von MR Pulssequenzen nötig, um die Detektion geringer Mengen und Konzentrationen, deren Lokalisierung und potenziell deren Bildgebung zu ermöglichen und so Aussagen zur Wirkstoff-Verteilung und deren therapeutischen Relevanz treffen zu können. Von besonderem Interesse ist hierbei auch die Messung der Verteilung bei sich ändernden Krankheitsbedingungen und zu mehreren Zeitpunkten, was im Hinblick auf eine optimierte Therapie von Patienten und einer verbesserten Sicherheit von Therapien von klinischer Relevanz sein und zu besseren Behandlungserfolgen führen kann.

Diese Herausforderungen wurden in unserer Gruppe bereits durch technologische Entwicklungen sowohl im Bereich von Hardware und Software adressiert. Durch den Einsatz von hochsensitiven kryogengekühlten Spulen [19], Breitbandfrequenzspulen [20], Messungen im Ultrahochfeld bei 21 T [21] , können Detektionslimits herabgesetzt werden und SNRs erhöht werden.

Neben der Innovation im Bereich Hardware, hat die Herausforderung geringer ^{19}F Verfügbarkeit die Entwicklung SNR effizienterer Pulssequenzen motiviert [22, 23], um die Detektion kleiner Features bei geringen ^{19}F Konzentrationen zu ermöglichen. Digitale Signalverarbeitung, insbesondere CS ist eine Möglichkeit und wurde erstmal im

Zusammenhang mit ^{19}F MR Techniken bei Chemical Shift Imaging und ^{19}F MRI gezeigt [24]. Durch Unterabtastung (Undersampling) kann die Messzeit verringert werden. Diese Ersparnis kann folglich in eine höhere Anzahl an Mittlungen der Messung reinvestiert werden, sodass das Detektionslimit herabgesetzt wird, falls durch CS die fehlenden Datenpunkte ergänzt werden können. Dies würde eine Lokalisierung auch kleiner Merkmale geringer Konzentration an ^{19}F erlauben.

Die Zuverlässigkeit von CS insbesondere bei kleinen Features nahe am Detektionslimit ist nicht klar [25]. Vor allem bei quantitativen ^{19}F MR Studien wie etwa bei Zelltherapien oder pharmakologischen Behandlungen ist die Performance von CS und der Erhalt der Datenintegrität unabdingbar und beide müssen auch für kleine SNR Bereiche untersucht werden.

Die nicht-invasive Darstellung pharmakologischer Therapien sowie die Überwachung von Therapieverläufen wie etwa bei Multipler Sklerose stellen bislang nur unzureichend erfüllte Erfordernisse dar, um Arzneimitteltherapien individuell auf Patienten zuzuschneiden und so zu einem verbesserten Behandlungserfolg beizutragen. Der Einsatz von ^{19}F MR Techniken stellt hier eine potenzielle Nutzbarkeit bei klinischen Studien dar sowie eine Übertragung auf klinische Fragestellungen. Um diese Ziele zu erreichen bedarf es einer Optimierung der ^{19}F MR Methode aus unterschiedlichen Perspektiven und unter Einsatz verschiedener Technologien, um die Signaldetektion zu verbessern und auf diese Art ein Level zu erreichen welches es erlaubt, ^{19}F MRT zur Detektion fluorierter Wirkstoffe klinisch zum Einsatz zu bringen.

Das Ziel dieser Arbeit ist der Einsatz von ^{19}F MR Techniken als theranostische Methode zur Detektion des MS Medikaments TF im Krankheitsverlauf der EAE als Modell für die MS.

Hierfür ist zunächst eine Charakterisierung der molekülspezifischen ^{19}F MR Eigenschaften und Umgebungseinflüssen wie Temperatur und pH nötig, um geeignete Pulssequenzen auszuwählen und deren Sequenzparameter mit Hinblick auf eine Maximierung der detektierbaren Signalmenge zu optimieren.

Um die zu erwartenden Hürden geringer Signalmengen und niedriger Detektionslimits zu überwinden, müssen herkömmliche technologische Ansätze zu Gunsten einer höheren Sensitivität, deutlich geringeren Detektionslimits und höheren Auflösungen weiterentwickelt, getestet und mit der Sensitivität bisheriger Hardware verglichen werden.

Die Entwicklung und der Einsatz der ultrasensitiven ^{19}F kryogen gekühlte Oberflächenspule (CRP)[19], die bei dieser Arbeit zum Einsatz kam, legt den Grundpfeiler für eine Detektion auch geringer TF Mengen im Tiermodell als nächsten Schritt im Zuge dieser Arbeit.

Die nicht-invasive ^{19}F MR Detektion von TF zu verschiedenen Zeitpunkten der Therapie und die Untersuchung des Krankheitsverlaufs stellt somit ein wichtiges Hauptziel dieser Arbeit dar, um Rückschlüsse auf Verteilung von TF und den therapeutischen Einfluss zu ermöglichen. Nichtsdestotrotz ist eine Kenntnis der tatsächlich vorhandenen TF Konzentrationen in den untersuchten Geweben durch Massenspektrometrie unabdingbar und stellt einen weiteren wichtigen Schritt in Richtung einer quantitativen nicht-invasiven Messmethode und zur Einschätzung der benötigten Sensitivität sowie zur Bestätigung der ^{19}F MRS Ergebnisse dar.

Über die MR spektroskopische Detektion von TF hinaus und mit dem Ziel einer künftigen Bildgebung von TF soll der Einsatz von CS untersucht werden. Bei erwartungsweise geringer ^{19}F MR Signalmenge in einem EAE Tiermodell kann CS zur weiteren Steigerung der Sensitivität und zur Herabsetzung des Detektionslimits aber gleichzeitig auch gerade bei geringen Signalmengen zur unbedingt notwendigen Verkürzung der Messzeit durch Unterabtastung beitragen. Zuerst soll hierbei die verbesserte und beschleunigte ^{19}F MR Bildgebung von Neuroinflammation bei EAE mit ^{19}F NPs durch CS untersucht werden und in einem nächsten Schritt diese Erkenntnisse potenziell auf die nicht-invasive Bildgebung von TF übertragen werden.

Die Realisierung einer klinisch nutzbaren ^{19}F MR Detektion von TF oder auch anderen fluorierten Medikamenten wird ein Zusammenspiel verschiedener technologischer Entwicklungen sein. Da höhere Magnetfeldstärken generell durch eine höhere Sensitivität charakterisiert sind, soll in einem letzten Schritt dieser Arbeit der Einfluss einer höheren Magnetfeldstärke von 21.1 T auf ^{19}F MR Parameter fluorierter Substanzen, sowie die ^{19}F MR Detektion untersucht werden und so einerseits die ^{19}F MR Detektion in Abhängigkeit multipler Parameter besser verstanden werden sowie das Repertoire an Möglichkeiten, höhere Sensitivität zu erreichen komplettiert werden.

Insgesamt soll mit dieser Arbeit der Einsatz von ^{19}F MR Techniken als nicht-invasive theranostische Methode demonstriert werden. Durch die Optimierung hin zu einer sensitiven und potenziell klinisch sinnvoll nutzbaren Untersuchungsmethode können medikamentöse Therapien während des Krankheitsverlauf überwacht, besser an Patienten angepasst werden und somit zu einem besseren Behandlungserfolg beitragen.

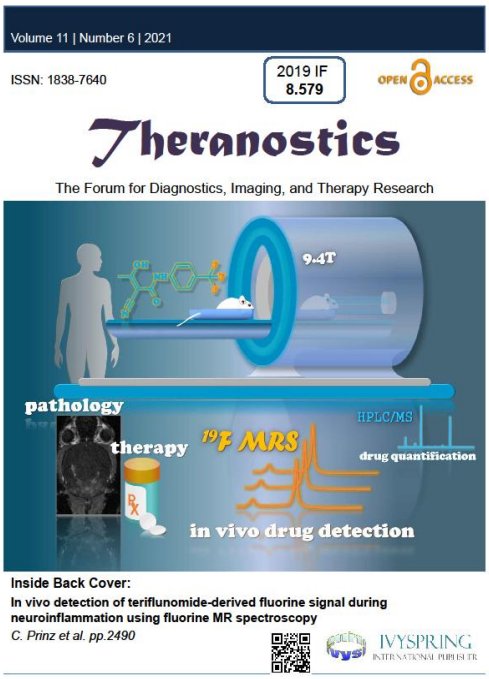

Abbildung 1 Cover Theranostics Volume 11, number 6, 2021, mit schematischer Darstellung des Konzepts und Workflows der in vivo Detektion von Teriflunomid und der anschließenden ex vivo Quantifizierung mit Massenspektrometrie.

2 Methodik

2.1 MR Hardware

Alle MR Studien wurden an einem 9.4 T Kleintierscanner (Bruker, Ettlingen, Deutschland) durchgeführt. Zur Untersuchung des Einflusses der Magnetfeldstärke wurden Experimente an einem 21.1 T Scanner mit vertikaler Bohrung am National High Magnetic Field Laboratory (NHMFL) in Tallahassee, Florida, USA durchgeführt. Eine dual-tunable $^{19}F/^{1}H$ Maus-Kopf-Volumenspule (Durchmesser 16 mm) wurde für die Untersuchung von Phantomen sowie die Untersuchung der Kopfregion in Mäusen eingesetzt [10]. Eine dual-tunable $^{19}F/^{1}H$ Körper-Volumenspule (MRI Tools, Durchmesser 62 mm) wurde für die Untersuchung von Ratten benutzt [26]. Um die Sensitivität zu erhöhen, wurde eine ^{19}F kryogen gekühlte Oberflächenspule benutzt (Cryoprobe, CRP; Bruker, Fällanden, Schweiz, Durchmesser 20 mm) [19]. Bei Einsatz der CRP wurde die Referenzspannung, welche den Flipwinkel determiniert, vor in vivo Messungen mit Phantomen und mit kurzen in vivo Messungen kalibriert, um - abhängig von Beladung und Positionierung der Spule in Relation zum Tier - ein Signalmaximum zu erreichen.

2.2 Konstruktion von Phantomen

Für die Charakterisierung der ^{19}F MR Eigenschaften fluorierter Substanzen wurde Spritzen (2.5 ml und 1 ml) verschiedener Durchmesser verwendet. Die Substanzen wurden in Dimethylsulfoxid (DMSO), Carboxymethlycellulose (CMC), das zur Formulierung einer oral verabreichbaren Suspension benutzt wird und in Humanserum zur Simulation einer in vivo ähnlichen Umgebung gelöst.

2.3 MR Datenakquisition

2.3.1 MR Spektroskopie

Nicht-selektive globale Einzelpuls-Spektroskopie wurde für Frequenzjustierungen, Untersuchung von Chemical Shift und Spektrenform sowie die Bestimmung der T_1 Relaxationszeit (mit variabler Repetitionszeit TR) mit jeweils optimierten Sequenzparametern in Phantomen, in vivo und ex vivo benutzt. Eine Carr-Purcell-Meiboom-Gill-Sequenz (CPMG) wurde zur spektroskopischen Bestimmung der T_2 Relaxationszeit benutzt.

Für die Charakterisierung des Einflusses der Temperatur auf die ^{19}F MR Eigenschaften Chemical Shift, Spektrenform, Relaxationszeiten und SNR bei Perfluoro-15-crown-5-ether (PFCE), Isofluran (Iso), Teriflunomid (TF)(alle in DMSO) und Flupentixol (Flu; in Lipidlösung) wurde die Temperatur mittels einer Messsonde in der Probe gemessen und die Temperatur mittels eines kalibrierten Wasserbades in Schritten von 5 °C variiert (20 °C bis maximal 60 °C).

In CMC wurde neben der Änderung der MR Eigenschaften auch der Einfluss des pH-Wertes sowie in DMSO der Einfluss verschiedener Konzentrationen des Kontrastmittels Gadolinium Dimeglumin (Gd-GTPA, Magnevist) auf die Relaxationszeiten bestimmt. Für die Untersuchung des pH Einflusses wurde in CMC suspendiertem TF HCl oder NaOH zugesetzt. Detektionslimits wurden mit unterschiedlichen TF Konzentrationen in Serum bestimmt.

2.3.2 MR Bildgebung

Für eine bildgebungsbasierte Bestimmung der Relaxationszeiten (T_1 und T_2 Mapping) wurden eine RARE Sequenz mit variabler Repetitionszeit (RAREVTR; T_1-Bestimmung) und eine MSME Sequenz (mit variabler Echo-Zeit TE, T_2-Bestimmung) benutzt. Optimierte RARE, bSSFP, FLASH und UTE Sequenzen wurden für die ^{19}F MR Bildgebung verwendet. FLASH wurde für ^{1}H Referenzbilder und anatomische Bildgebung verwendet, MDEFT zur Charakterisierung der Blut-Hirn-Schranken-Schädigung im EAE-Tiermodell.

2.3.3 Compressed Sensing

Die SNR Effizienz von Compressed Sensing (CS) unter Niedrig-SNR Bedingungen, wie es bei den meisten ^{19}F MRT Anwendungen der Fall ist, wurde in EAE Mäusen untersucht, denen zu Krankheitsbeginn Nanopartikel zur Markierung inflammatorischer Zellen intravenös verabreicht wurden, die aber nicht mit TF behandelt wurden. In vivo MRT Daten wurden zum Höhepunkt der EAE Pathologie zwischen Tag 10 und 14 aufgenommen. Unter anderem wurden Datensätze mit einem 2D-RARE CS Protokoll mit prospektiver Unterabtastung aufgenommen und mit CS rekonstruiert. Diese CS-Daten wurden mit konventionellen Fourier-Rekonstruktion und gefilterten Rekonstruktionen vollständiger Datensätze bei gleicher Scan-Zeit verglichen.

2.4 Behandlung von Tieren

In vivo Experimente wurden mit gesunden Dark Agouti Ratten sowie gesunden und kranken SJL/J und C57BL/6 Mäusen durchgeführt. Alle Mäuse und Ratten wurden auf einem beheizbaren Tierbett, unter Überwachung von Rektaltemperatur und Atemfrequenz und unter Anästhesie, platziert und im MRT untersucht. Alle Tierversuche wurden in Übereinstimmung mit von der Abteilung Tierschutz des Landesamtes für Gesundheit und Soziales in Berlin (LAGeSo) genehmigten Verfahren und unter Berücksichtigung der Richtlinien zur Minimierung der Belastung von Tieren (86/609/EEC) durchgeführt.

Das Tiermodell der MS (Experimentelle Autoimmun Enzephalomyelitis, EAE) wurde durch subkutane Immunisierung von Mäusen mit einer Emulsion generiert. Diese wurde durch die Emulierung von Proteolipid Protein (PLP, SJL/J Mäuse) und Myelin Oligodentrocyte Glykoprotein (MOG, C57BL/6 Mäuse) und M. Tuberculosis in komplettem Freundschen

Adjuvanz hergestellt. Zusätzlich wurde intraperitoneal Pertussis Toxin (Tag 0 und Tag 2) injiziert. Täglich wurde ein Scoring der Tiere durchgeführt, um den Krankheitsverlauf zu verfolgen. MR Untersuchungen an mit TF behandelten Mäusen wurden an den Tagen 8 und 14 durchgeführt, um Krankheitsbeginn und Höhepunkt der EAE Pathologie bei der Untersuchung zu berücksichtigen.

Für die Behandlung von Tieren mit TF wurde TF in CMC formuliert und in Form einer Suspension oral verabreicht. Ratten wurden direkt vor der Messung mittels einer Magensonde im Scanner liegend behandelt, Mäuse jeweils über 14 Tage und ca. 16 bis 24 Stunden vor der MR Messung. Mit TF behandelt wurden sowohl gesunde als auch EAE Mäuse. Ausschließlich mit CMC behandelte EAE Mäuse dienten als Kontrolle für die EAE Pathogenese. Um Blut-Hirn-Schranken Läsionen in SJL/J Mäusen zu charakterisieren, wurde EAE Tieren das Kontrastmittel Gadolinium Dimeglumin intravenös unmittelbar vor der MR Messung verabreicht.

Um den EAE Entzündungsprozess zu verfolgen, wurden ^{19}F PFCE Nanopartikel hergestellt und diese EAE Mäusen zu Krankheitsbeginn intravenös verabreicht, um Entzündungsprozesse durch Labelling von Entzündungszellen darstellen [10].

2.5 Ex vivo Messungen

Nach 14 Tagen TF Gabe wurde gesunden und EAE Tieren nach Verabreichung einer Letaldosis an Anästhetikum und nach Überprüfung ausbleibender Reflexen Blut entnommen. Daraufhin wurden sie durch transkardiale Perfusion mit PBS getötet. Liquor wurde nach der Perfusion mit PBS aus der Zysterna Magna entnommen. Das perfundierte Gehirn wurde ebenfalls entnommen. Gewebe wurden ohne vorherige Fixierung für eine anschließende Untersuchung mittels High performance liquid chromatography mass spectrometry (HPLC/MS) gefroren (-80 °C).

Zur Gewinnung von ex vivo EAE Gewebephantomen mit ^{19}F NP Labelling wurden EAE Mäuse mit PBS und anschließend mit Paraformaldehyd (PFA) perfundiert, präpariert und in 15 ml Falcon-Tubes in PFA konserviert.

Für die Bestimmung der TF Konzentrationen wurde TF aus den homogenisierten Geweben extrahiert und anschließend eine HPLC/MS durchgeführt.

Um eine Korrelation von ^{19}F MR Signalintensitäten und gemessenen Konzentrationen zu ermöglichen, wurden zunächst für eine Kalibrierung Serumproben mit unterschiedlichen TF Konzentrationen versetzt, ^{19}F MR Signalintensitäten bestimmt und schließlich TF HPLC/MS Messungen durchgeführt. Auf dieser Basis wurden Blutproben von gesunden und EAE Tieren, die mit TF behandelt worden waren sowohl mit ^{19}F MRS als auch HPLC/MS vermessen. Die ^{19}F MR Signalintensitäten wurden mittels der vorangegangenen Kalibration in ^{19}F MRS TF

Konzentrationen umgerechnet und mit den gemessenen Konzentrationen aus der HPLC/MS korreliert.

Ex vivo wurde die Änderung von T_1 in Abhängigkeit von der Temperatur nach subkutaner Verabreichung von ^{19}F PFCE Nanopartikeln und mittels subkutaner Temperaturmesssonde in der Nackenregion einer tief anästhesierten C75BL/6 Maus post mortem gemessen.

2.6 MR Daten Auswertung

Bildverarbeitung, Spektralanalyse und Prozessierung wurden in Matlab durchgeführt. Anatomische Bilder von in vivo Untersuchungen wurden in ImageJ analysiert und prozessiert. Die Postprozessierung von MR Spektren beinhaltete Zero-Filling, zur Verbesserung der visuellen Darstellung, und Line-Broadening, zur Erhöhung der Sensitivität. Die Quantifizierung der spektralen Intensität wurde durch Verwendung des y-Achsen-Abschnitts des Free Induction Decay (FID) als Abfall des MR Signals über die Zeit durchgeführt (FID Fit, Zeit-Domäne). Integrale der Spektral-Peaks (Frequenz-Domäne) wurden berechnet und das SNR von MR Spektren und MR Bildern wurde berechnet.

Die Bestimmung der ^{19}F Relaxationszeiten T_1 und T_2 wurde durch Anpassen (Fitten) der Signalintensitätsgleichungen an gemessene und korrigierte Signalintensitäten erreicht. Das SNR wurde aus dem korrigierten Quotienten aus mittlerer Signalintensität über eine Region of interest (ROI) und der Standardabweichung des Hintergrundsignals berechnet.

Um die Bildqualität bei CS zu bestimmen, wurden die mittlere quadratische Abweichung (Root-Mean-Square-Deviation, RMSD),Richtig-Positiv-Raten (True positive rate, TPR), Falsch-Positiv-Raten (false discovery rate, FDR) sowie die relative Signalintensitäts- (SI) Abweichung im Vergleich zu einer Referenz bestimmt.

2.7 Statistische Auswertung

Temperaturunterschiede wurden über die Zeit aufgenommen und der Median und Interquartilsbereich in Matlab bestimmt. Die statistische Analyse von MR-Daten über die Zeit, EAE Scores, Gewichten, Überlebenszeit und Massenspektrometrie-Daten wurde in R durchgeführt. MR und Massenspektrometrie Daten wurden aus allen Experimenten vereinigt. ^{19}F MR Signalintensitäten und gemessene TF Konzentrationen wurden log-transformiert. EAE Scores wurden als Mittelwert und Standardfehler, Maximumscores als Median und Interquartilsbereich angegeben und mit einem Mann-Whitney-U-Test analysiert. Körpergewichte wurden mit einem t-Test untersucht. Zur Analyse des Zeitpunkts des Krankheitsbeginns wurde ein logrank-Test durchgeführt. Die MR Signaldetektion über die Zeit und Massenspektrometrie-Daten wurden mit ANOVA oder 2-Faktor-ANOVA mit Tukey post-hoc Test für multiple Testungen oder mit einem ungepaarten t-Test ausgewertet. Um die Homogenität der Varianz zu testen, wurde ein Levene's Test benutzt. Korrelationsanalysen

wurden mit dem Pearson Korrelationskoeffizienten (R) oder dem nicht-parametrischen Spearman Rangsummen Korrelationskoeffizienten (ρ) durchgeführt. p-Werte < 5 % wurden als statistisch signifikant angenommen (*$p < 0.05$; **$p < 0.01$; ***$p < 0.001$).

3 Ergebnisse

3.1 Beeinflussung der ^{19}F MR Eigenschaften durch Temperatur und chemische Umgebung

Der Einfluss verschiedener Faktoren, wie Temperatur, pH-Wert, chemische Umgebung und Kontrastmittel auf die ^{19}F MR Eigenschaften fluorierter Substanzen, wurde in dieser Studie bestimmt.

Insbesondere der Einfluss der Temperatur auf MR Parameter ist von Bedeutung, da die Messungen von Phantomen meist bei Raumtemperatur erfolgt, die Körpertemperatur bei in vivo Messungen jedoch höher ist und sich bei unter Anästhesie durchgeführten in vivo MR Experimenten ggf. ändern kann. Die ^{19}F MR Eigenschaften von perfluoriertem PFCE und ^{19}F PFCE Nanopartikeln als Labeling-Agens zur Markierung von Entzündungszellen und der Einfluss von Temperatur auf die ^{19}F MR Eigenschaften, insbesondere die Relaxationszeiten, sind bereits in der Literatur beschrieben [27] und sollen in dieser Studie durch die Untersuchung der fluorierten Medikamente Teriflunomid, Isofluran und Flupentixol (**Abbildung 2**) ergänzt werden.

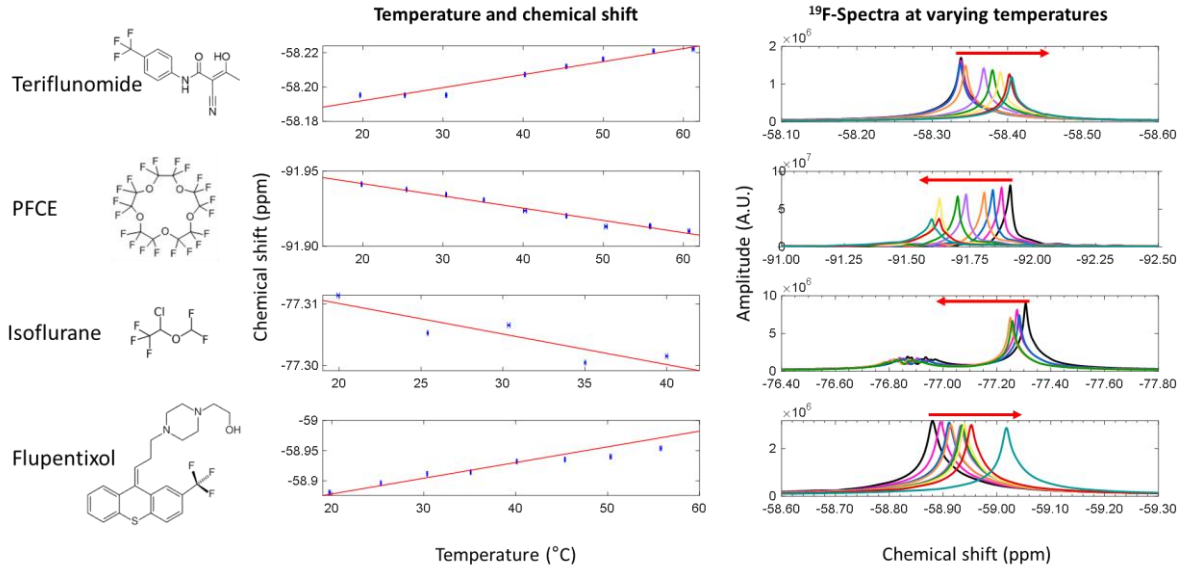

Abbildung 2 Temperaturabhängigkeit von Chemical Shift (Mitte) und Spektrenform (rechts) verschiedener fluorierter Substanzen (links). Nach Prinz, Delgado [28], mit Genehmigung von Springer Nature.

In Prinz, Delgado [28] wurde der Temperatureinfluss im Temperaturbereich von 20 bis 60 °C auf die Veränderung von Chemical Shift und Spektrenform (**Abbildung 2**), Signalintensität sowie SNR gemessen (**Abbildung 4**). Reines PFCE zeigte ein Einzelpeak-Spektrum und eine lineare Abnahme des Chemical Shift in Abhängigkeit von der Temperatur (0.0082 ppm/°C). Das SNR in RARE ^{19}F MR Bildern wurde ebenfalls gemessen und eine temperaturabhängige SNR Erniedrigung (0.97 SNR Einheiten/°C) bestimmt. Das T_1 zeigte in diesem Temperaturbereich eine lineare Steigerung um 16 ms/°C von 905 ms bei 20 °C auf 1536 ms

bei 60 °C. Ebenso zeigte T_2 eine temperaturabhängige Verlängerung um 7 ms/°C von 556 ms auf 887 ms (**Abbildung 4**).

Eine Abnahme des T_1 von PFCE Nanopartikeln konnte post mortem in Gewebe bei abnehmender Temperatur gemessen werden (**Abbildung 3**). Messungen bei 23.6 °C ergaben ein T_1 von 1149 ms, während bei 32.4 °C ein T_1 von 1325 in der Nackenregion einer C57BL/6 Maus gemessen wurde (13 % Reduktion).

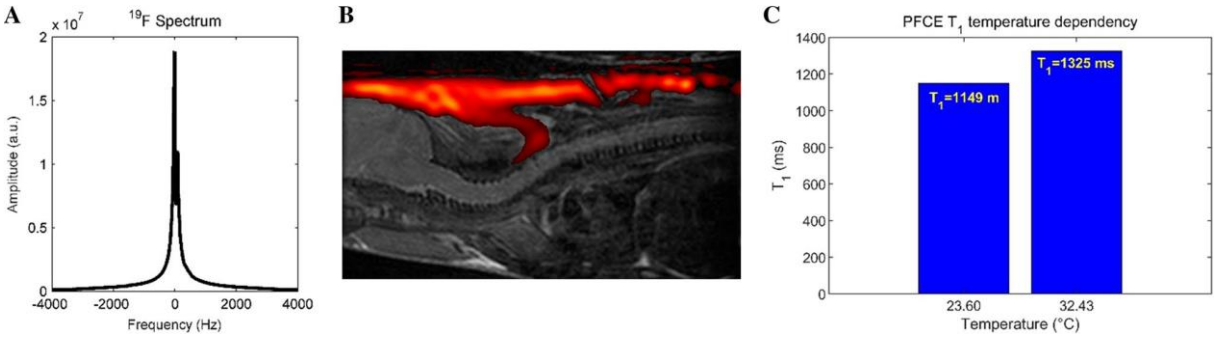

Abbildung 3 Einfluss der Temperatur auf das T_1 von PFCE Nanopartikeln in Gewebe. A. ^{19}F Spektrum, B. Überlagerung eines sagittalen anatomischen Bildes der Nackenregion mit einem ^{19}F MR Bild (3D RARE). C. Messung von T_1 bei zwei verschiedenen Temperaturen. Aus Prinz, Delgado [28], mit Genehmigung von Springer Nature.

Das pentafluorierte Inhalationsanästhetikum Isofluran wurde wegen seines Siedepunktes bis 40 °C untersucht und zeigte, aufgrund von Spin-Spin-Kopplung der Fluor-Atome, ein Spektrum mit multiplen Peaks. Der Hauptpeak zeigte ebenfalls eine Temperaturabhängigkeit des Chemical Shift (0.0025 ppm/°C), Signalintensität (Abnahme um 0.085 SNR Einheiten/°C), des T_1 (um 30 ms/°C von 1851 ms auf 2491 ms) und des T_2 (um 11 ms/°C von 922 ms auf 1154 ms) (**Abbildung 2+4**). Ähnliches Verhalten zeigte das trifluorierte Psychopharmakum Flupentixol.

Der Chemical Shift (-58 ppm) zeigte eine Temperaturabhängigkeit von -0.0026 ppm/°C), eine Abnahme der Signalintensität und des SNR (-0.04 SNR Einheiten/°C), des T_1 (um 1.3 ms/°C von 698 ms auf 762 ms) und des T_2 (um 7.4 ms/°C von 117 ms auf 421 ms) (**Abbildung 2+4**).

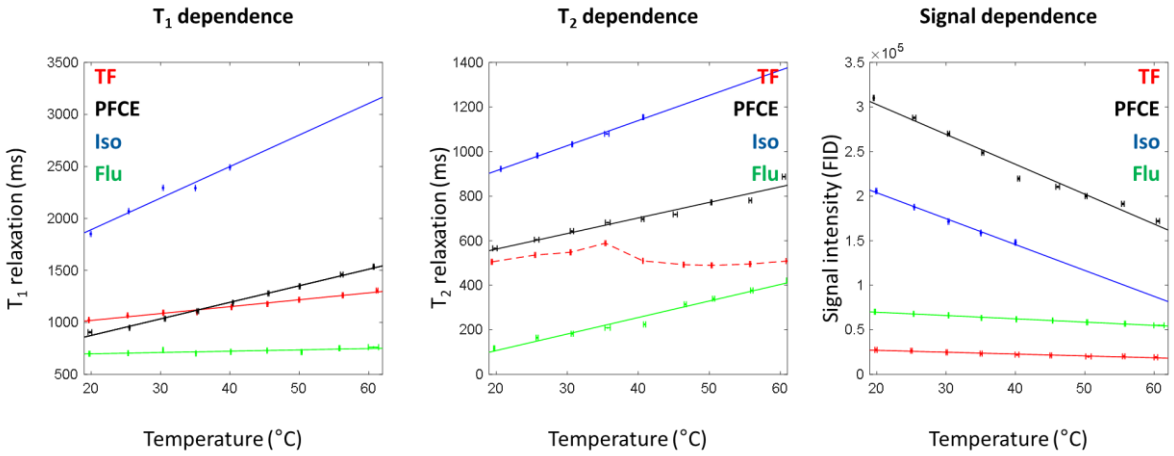

Abbildung 4 Einfluss der Temperatur auf die ^{19}F MR Eigenschaften von TF, PFCE, Isofluran (Iso) und Flupentixol (Flu). Links: T_1, Mitte: T_2, Rechts: Signalintensität

Das trifluorierte MS Medikament Teriflunomid zeigte ein Einzelpeak-Spektrum (-58 ppm) bei Raumtemperatur (20 °C) (**Abbildung 5A**). Der Chemical Shift zeigte eine lineare Abhängigkeit von der Temperatur (-0.0038 ppm/°C), ebenso zeigten Signalintensität und SNR eine temperaturabhängige Abnahme (0.071 SNR Einheiten/°C). T_1 zeigte im Temperaturbereich von 20 bis 60 °C eine Zunahme um 6.6 ms/°C von 1023 ms auf 1307 ms. T_2 zeigte bis 35 °C einen linearen Anstieg um 4.9 ms/°C und schließlich einen Abfall (**Abbildung 2+4**).

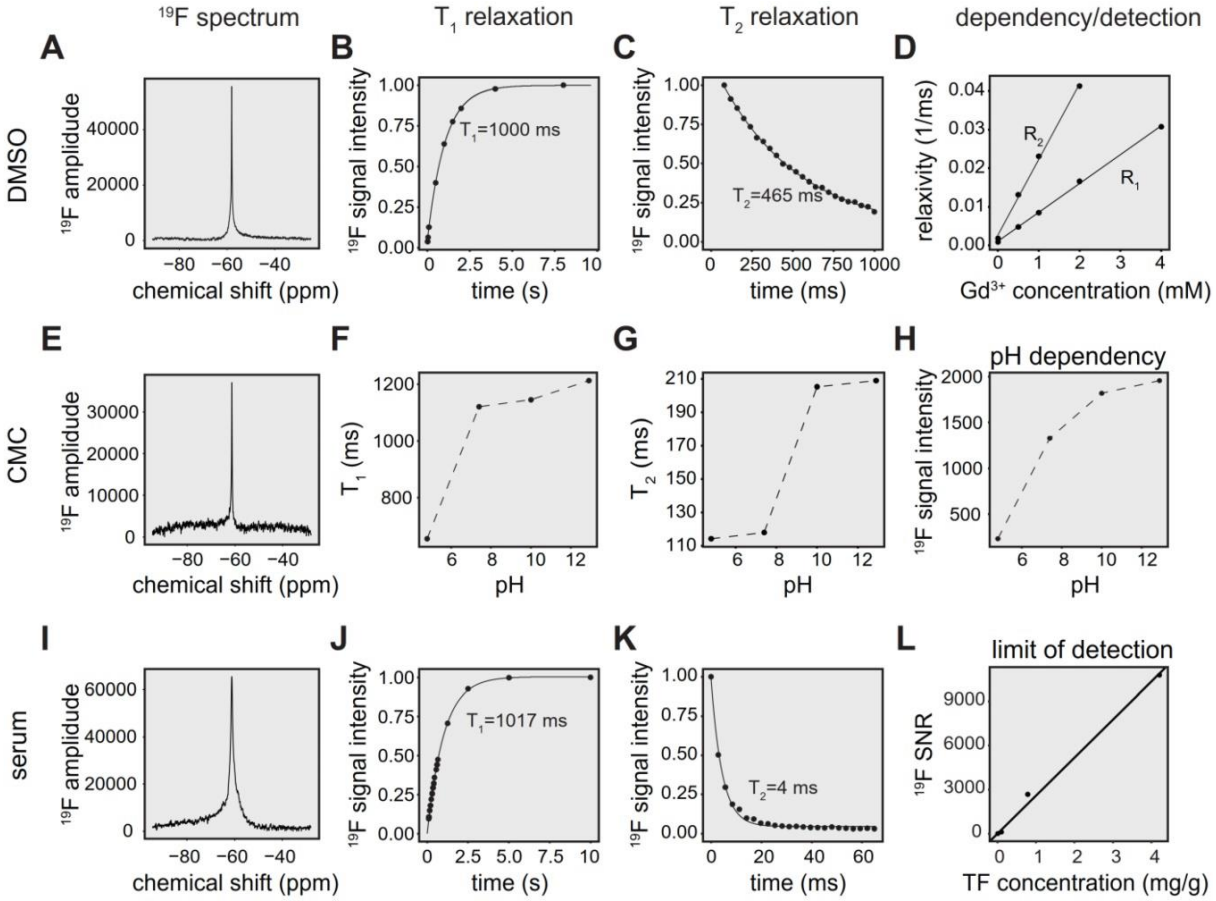

Abbildung 5 ^{19}F MR Charakterisierung von Teriflunomid in unterschiedlichen chemischen Umgebungen. (A) ^{19}F MR Spektrum von TF in einem DMSO-Phantom (Konzentration: 27.02 mg/mL in 1 mL). (B) Spektroskopische Bestimmung von T_1 in DMSO. (C) Spektroskopische Bestimmung von T_2 in DMSO mit CPMG. (D) Korrelation der Relaxationsraten R_1 and R_2 (inverses T_1 und inverses T_2) versetzt mit Gadopentetat Dimeglumin (0.5, 1, 2, 4 mM) in DMSO. (E) ^{19}F MR Spektrum von TF in CMC (Konzentration: 2.70 mg/mL in 1 mL). (F) pH abhängige T_1 Änderung in CMC. (G) pH abhängige T_2 Änderung in CMC. (H) pH abhängige Änderung der ^{19}F Signalintensität in CMC; Konzentration in CMC: 2.70 mg/mL in 1 mL. (I) ^{19}F MR Spektrum von TF in einem Serum-Phantom; Konzentration: 1.3 mM in 1 mL). (J) Spektroskopische Bestimmung von T_1 in Humanserum. (K) Spektroskopische Bestimmung von T_2 in Humanserum. (L) Bestimmung des spektroskopischen Detektionslimits mit verschiedenen TF Konzentrationen. Aus: Prinz, Starke [26].

Bei einer weiteren Charakterisierung von TF in DMSO wurde bei zunehmender Konzentration des Kontrastmittels Gadolinium Dimeglumin eine lineare Korrelation zwischen sowohl inversem T_1 (R_1) und der Gd-DTPA Konzentration, als auch inversem T_2 (R_2) und der Gd-DTPA Konzentration festgestellt (**Abbildung 5D**).

TF in CMC zeigte einen Einzelpeak bei -61 ppm (**Abbildung 5E**). Sowohl T_1 (**Abbildung 5F**) als auch T_2 (**Abbildung 5G**) wurden bei verschiedenen pH-Werten spektroskopisch gemessen und zeigte in beiden Fällen eine Zunahme der Relaxationszeit bei höherem pH. Ebenso war die spektrale Signalintensität bei voller Relaxation höher (**Abbildung 5H**).

In Serum zeigte TF einen breiteren Einzelpeak als in DMSO oder CMC bei -61 ppm (**Abbildung 5I**). Eine Bestimmung von T_1 (**Abbildung 5J**) und T_2 (**Abbildung 5K**) in Serum ergab ein mit T_1 in DMSO vergleichbarem T_1 von 1017 ms und ein stark verkürztes T_2 von 4 ms, was 93-fach erniedrigt ist, im Vergleich zu T_2 in DMSO. Im Hinblick auf in vivo

Experimente bei erwartungsgemäß niedrigen ^{19}F Konzentrationen wurde unter Annahme eines Grenzwertes von SNR=5 ein Detektionslimit mit der sensitiven CRP mittels globaler Spektroskopie von 1.9 µg/g in Serum bestimmt (5.04e+15 ^{19}F Atome in 400 µl) (**Abbildung 5L**).

3.2 Stammabhängiger unterschiedlicher therapeutischer Effekt von Teriflunomid

Das Ansprechen von SJL/J und C57BL/6 EAE Mäusen auf eine Therapie mit TF wurde über einen Zeitraum von 14 Tagen untersucht. In SJL/J Mäusen konnte die TF Behandlung einem Gewichtsverlust im Vergleich zu unbehandelten EAE Kontrolltieren vorbeugen (**Abbildung 6A**). Unbehandelte Tiere zeigten eine signifikante Gewichtsreduktion von Tag 11 an ($p=0.002$). Die Behandlung mit TF resultierte in einer fast vollständigen Abwesenheit klinischer Symptome (nur 8 %) in SJL/J EAE Mäusen, während 100 % der unbehandelten Mäuse den typischen schubförmigen Verlauf der EAE Pathologie zeigten (**Abbildung 6B**). Der über den Beobachtungszeitraum maximal erreichte EAE Score war bei behandelten und unbehandelten EAE Tieren ebenfalls unterschiedlich ($p<0.001$) (**Abbildung 6C**). Es konnte auch gezeigt werden, dass unter TF Behandlung der Zeitpunkt des Krankheitsbeginns (definiert als erstmaliges Auftreten eines Scores von 0.5, also minimaler klinischer EAE Symptome) signifikant später war ($p<0.001$) (**Abbildung 6D**).

Das Ansprechen von C57BL/6 Tieren auf die TF Behandlung war weniger ausgeprägt. TF behandelte EAE Tiere zeigten eine weniger starke Gewichtsreduktion (nicht signifikant) (**Abbildung 6E**) und zeigten klinische Symptome ab Tag 10 (**Abbildung 6F**). Der EAE Score war im Vergleich zu Kontrolltieren nicht signifikant niedriger und auch die erreichten Maximalscores beider Gruppen unterschieden sich nicht signifikant (**Abbildung 6G**). Die Inzidenz war um 65 % reduziert und der Krankheitsbeginn verzögert ($p=0.04$)(**Abbildung 6H**).

In SJL/J EAE Mäusen wurde das Ausmaß der ZNS-Entzündung durch Untersuchung der Blut-Hirn-Schranken-Schädigung mittels Kontrastmittel verstärkendem MRT untersucht (**Abbildung 6I+J**). Kontrastmittelverstärkte Läsionen in TF behandelten SJL/J EAE Mäusen wurden sogar in Tieren beobachtet, die keine klinischen Symptome zeigten. Das Ausmaß der Läsionen variierte unter den Tieren und reichte von mild (**Abbildung 6I**) bis schwer (**Abbildung 6J**). Kontrastmittelverstärkte Läsionen waren im Zerebellum (**Abbildung 6I+J**) und auch in periventrikulären Regionen angesiedelt (**Abbildung 6J**).

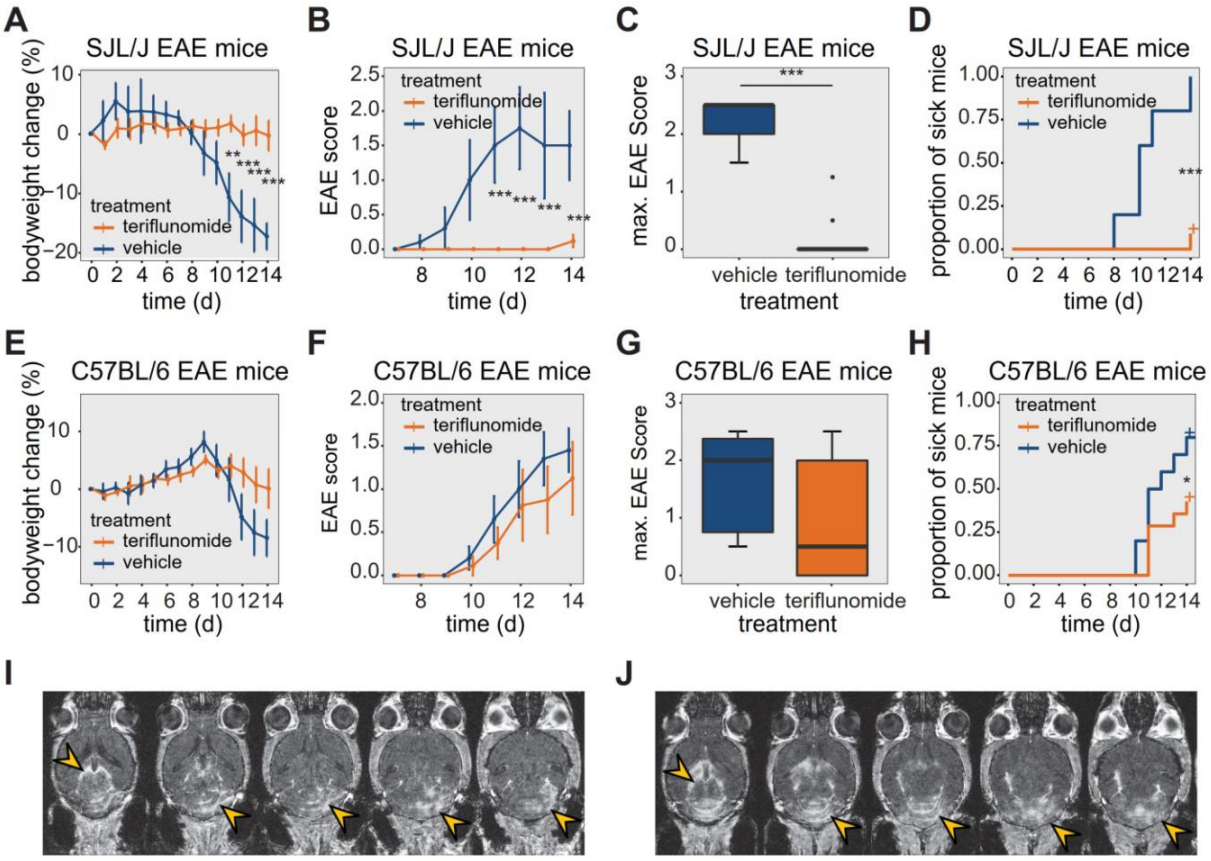

Abbildung 6 Therapeutischer Effekt von Teriflunomid auf den Krankheitsverlauf von EAE in SJL/J und C57BL/6 Mäusen. (A) Änderung des Körpergewichts (prozentual; Mittelwert ± Standardfehler) über die Zeit in unbehandelten (CMC) und TF behandelten SJL/J EAE Mäusen. (B) Mittlere EAE Score ± SE unbehandelter und TF behandelter SJL/J EAE Mäuse. (C) Maximum EAE Score in unbehandelten und TF behandelten SJL/J EAE Mäuse im Krankheitsverlauf. (D) Kaplan-Meier Kurve unbehandelter und TF behandelter SJL/J EAE Mäuse. Die Zeit zum Krankheitsbeginn (Score=0.5) und der Anteil an Mäusen mit klinischen Symptomen sind dargestellt. (E) Änderung des Körpergewichts (prozentual; Mittelwert ± Standardfehler) über die Zeit in unbehandelten (CMC) und TF behandelten C57BL/6 EAE Mäusen. (F) Mittlere EAE Score ± SE unbehandelter und TF behandelter C57BL/6 EAE Mäuse. (G) Maximum EAE Score in unbehandelten und TF behandelten C57BL/6 EAE Mäuse im Krankheitsverlauf. (H) Kaplan-Meier Kurve unbehandelter und TF behandelter C57BL/6 EAE Mäuse. Die Zeit zum Krankheitsbeginn (Score=0.5) und der Anteil an Mäusen mit klinischen Symptomen sind dargestellt. (I-J) MR Bilder mit Darstellung von milder (I) und schwerer (J) Blut-Hirn-Schranken-Schädigung unter Verwendung von Kontrastmittel (i.v.) und MDEFT an Tag 14 in zwei TF behandelten SJL/J EAE Mäusen. Läsionen sind zu finden im Kleinhirn und in periventrikulären Regionen (gelbe Pfeile). Aus: Prinz, Starke [26].

3.3 In vivo Detektion von Teriflunomid in der abdominalen Region gesunder Tiere

In gesunden Dark Agouti Ratten konnte ein ^{19}F MRS Peak bei -61 ppm direkt nach oraler Verabreichung mit der $^{19}F/^{1}H$ Volumen Spule detektiert werden (**Abbildung 7A**). ^{19}F MRS Messungen der Abdomen Region mit intubiertem Magen zeigte einen initialen Anstieg des ^{19}F MRS Signals und eine graduelle Abnahme nach 30 Minuten (**Abbildung 7A**). Ebenfalls konnte 24 Stunden nach letzter TF Gabe TF in der Abdomen Region einer C57BL/6 Maus ein ^{19}F MRS Peak mit der ^{19}F CRP gemessen werden (**Abbildung 7B**).

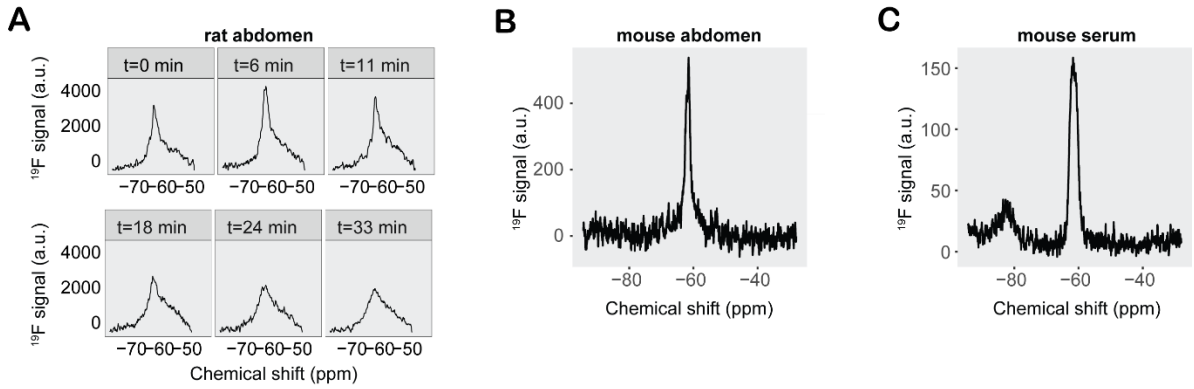

Abbildung 7 ^{19}F MR Detektion von Teriflunomid in vivo und ex vivo. (A) ^{19}F MR TF Signal im Abdomen einer Ratte nach Verabreichung von TF mittels einer Magensonde. Globale Spektroskopie wurde zur Messung des ^{19}F MR Signals an 6 Zeitpunkten über 30 min verwendet. (B) ^{19}F MR TF Signal einer gesunden C57BL/6 Maus im Abdomenbereich nach 14-tägiger TF-Behandlung. (C) ^{19}F MR TF Signal einer ex vivo Serumprobe einer SJL/J Maus. Aus: Prinz, Starke [26].

3.4 In vivo Detektion von Teriflunomid in der Kopf-Region von Mäusen

Analog zu Phantom-Messungen und in vivo Messungen im Abdomenbereich konnte in der Kopfregion ein ^{19}F MRS Peak bei -61 ppm detektiert werden. Untersucht wurde die Veränderung von TF Leveln in TF behandelten gesunden (**Abbildung 8A**) und EAE Mäusen (**Abbildung 8B**) an den Tagen 8 und 14 nach der Immunisierung. Ein zweiter ^{19}F MR-Peak konnte im Bereich von -75 ppm bis -85 ppm in gesunden und kranken Tieren beobachtet werden und war auch im Abdomen von EAE Tieren präsent.

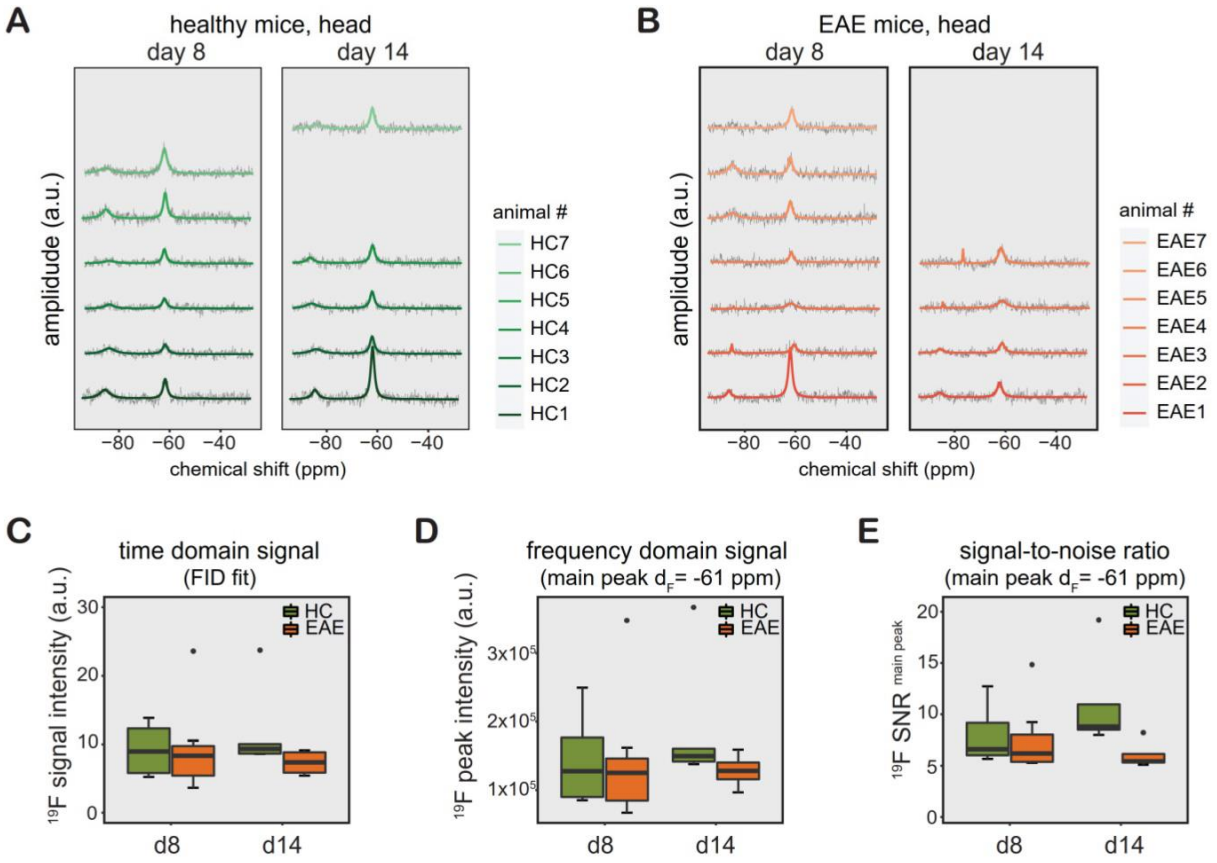

Abbildung 8 ^{19}F MR Detektion von Teriflunomid in vivo. (A-B) ^{19}F MR TF Signal im Kopfbereich von gesunden (A) und EAE (B) Mäusen an Tag 8 und Tag 14 nach Beginn der täglichen TF Behandlung. (C-D) ^{19}F MR Signal berechnet in der Zeitdomäne als Signalintensität (FID fit) (C) und in der Frequenzdomäne als Fläche unter der Kurve (Integral des Hauptpeaks bei δF = -61ppm) unter Verwendung eines Lorentz-Fits (D) und SNR (E) aufgetragen für alle EAE und gesunden SJL/J Mäuse für Tag 8 und Tag 14. Aus: Prinz, Starke [26].

Das ^{19}F MR Signal prozessierter Spektren in gesunden und EAE Mäusen wird sowohl in der Zeit-Domäne als FID Fit (**Abbildung 8C**), in der Frequenz-Domäne als Integral des Hauptpeaks bei -61 ppm (**Abbildung 8D**) und als SNR (**Abbildung 8E**) gezeigt. Es wurden unabhängig von der Art der Auswertung (FID Fit, Integral oder SNR) zwischen Tag 8 und 14 und zwischen EAE und gesunden Tieren oder den paarweisen Vergleichen keine statistisch signifikanten Unterschiede festgestellt ($p>0.1$). Ebenso wurde kein Unterschied in der Varianz der ^{19}F MR Signalintensitäten zwischen den Tiergruppen, Tagen oder den paarweisen Vergleichen festgestellt ($p>0.1$).

3.5 Ex vivo Bestimmung von Teriflunomid-Leveln in gesunden und EAE Mäusen

TF konnte auch ex vivo aber nur im Serum von SJL/J EAE Mäusen mittels ^{19}F MRS gemessen werden (**Abbildung 7C**). Die TF Konzentrationen in Serum, Liquor und perfundiertem Gehirn wurden mittels HPLC/MS sowohl in SJL/J und C57BL/6 Mäusen bei einem Detektionslimit von 4.9 pg/g bestimmt.

In SJL/J Mäusen war ein starker Unterschied in den TF Konzentrationen zwischen den Geweben ($p<0.001$), aber nicht zwischen gesunden und EAE Tieren zu beobachten. Die Serum TF-Konzentrationen waren jeweils eine Größenordnung höher als die in perfundiertem Gehirn oder CSF (alle $p<0.001$) (**Abbildung 9A, links**).

In C57BL/6 Mäusen war ebenfalls ein starker Unterschied in TF Konzentrationen in den verschiedenen Geweben festzustellen ($p<0.001$), mit gegenüber CSF und Gehirn höheren TF Serumkonzentrationen. In sowohl gesunden als auch EAE Tieren zeigte sich ebenfalls eine signifikant höhere TF Konzentration im Liquor, verglichen mit der Konzentration im Gehirn (**Abbildung 9A, rechts**).

Die Quantifizierung mit Massenspektrometrie stellte einen wichtigen Schritt in der Validierung der ^{19}F MR Technologie dar. Eine Kalibrierung von ^{19}F MRS Signalintensitäten (Integral des ^{19}F MRS Peaks) mit Konzentrationswerten, die mittels Massenspektrometrie in Mausserum, welches mit definierten TF Mengen versetzt worden war, diente dem Abschätzen der Konzentration anhand eines gemessenen ^{19}F MRS Signals (**Abbildung 9B**). Verglichen mit HPLC/MS Quantifizierung, waren TF Konzentrationen, die mit ^{19}F MRS bestimmt worden waren mit einer mittleren Abweichung von 83 % erhöht. Nichtsdestotrotz konnte eine klare Korrelation zwischen ^{19}F MRS und HPLC/MS festgestellt werden (**Abbildung 9C**).

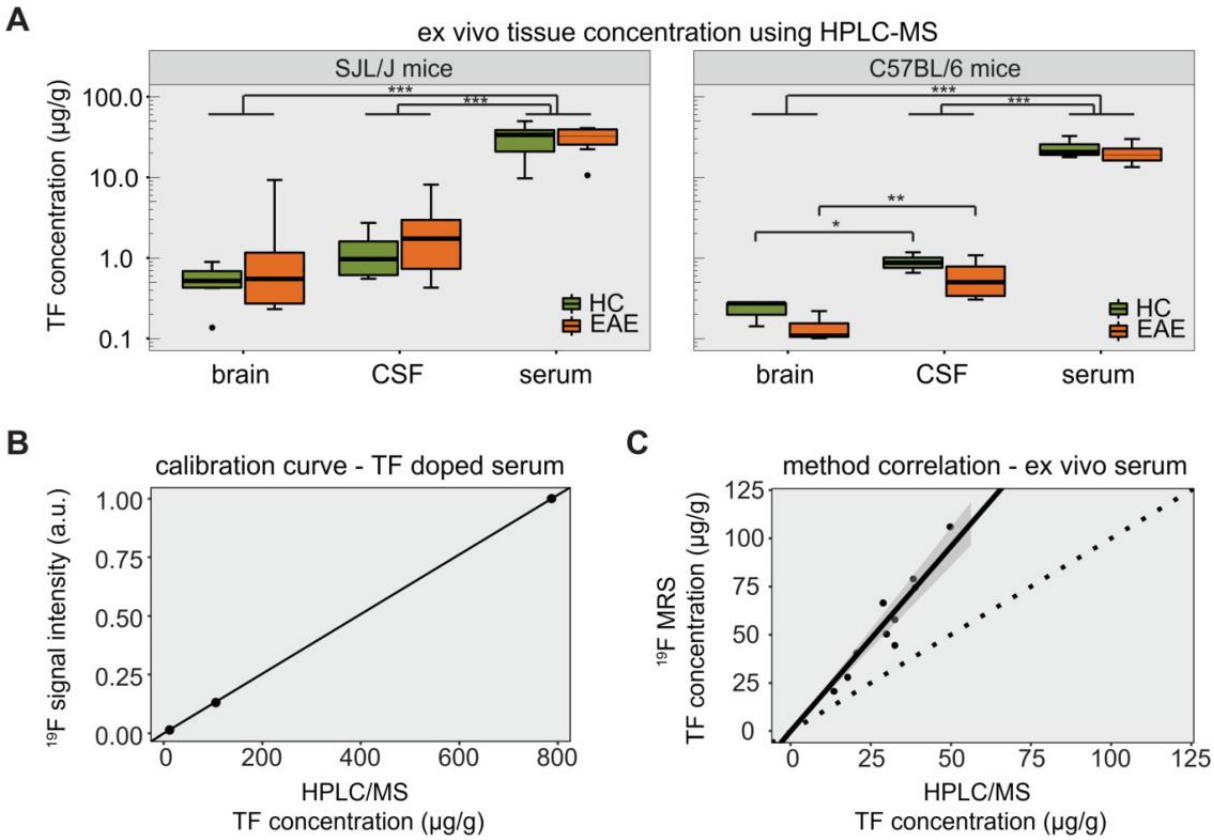

Abbildung 9 Detektion von Teriflunomid durch Massenspektrometrie. (A) Detektion von TF durch Massenspektrometrie in Gehirn, CSF und Serum von EAE und gesunden SJL/J und C57BL/6 Mäusen an Tag 14. (B) Kalibrationskurve für die ^{19}F MRS Quantifizierung mittels HPLC/MS Konzentrationen von TF (gelöst in Serum) und der korrespondierenden ^{19}F MRS Signal Intensitäten. (C) Korrelation der ^{19}F MR Signal Quantifizierung ex vivo mit HPLC/MS bestimmten Konzentrationen in Serum von mit TF behandelten Mäusen. Aus: Prinz, Starke [26].

3.6 Erhöhung der Sensitivität durch technologische Entwicklungen

Die ^{19}F Signalintensität von TF ist durch die vorhandene TF Konzentration in unterschiedlichen Körperbereichen und Organen begrenzt. Mit dem Ziel, die Sensitivität der ^{19}F MRS Methode für die Detektion von TF zu erhöhen und Detektionslimits herabzusetzen, wurde eine kryogen gekühlten Oberflächen-Quadratur-Spule (CRP) eingesetzt.

Die Entwicklung einer ^{19}F CRP und der Vergleich mit einer konventionellen ^{19}F/^{1}H dual tunable Volumenkopfspule [10] zeigte in ^{19}F PFCE NP Phantomen eine Erhöhung der Sensitivität um den Faktor 15. Unter Berücksichtigung einer bei Oberflächenspulen baulich bedingten Signalabschwächung bei zunehmender Entfernung vom Spulenkopf konnten bei EAE ex vivo MRT Messungen hochaufgelöste ^{19}F MRT Bilder aufgenommen werden, die im Vergleich zu ^{19}F MRT Bildern mit konventioneller Volumenspule eine höhere Sensitivität und Auflösung, insbesondere in Regionen nahe des Spulenkopfes ermöglicht (**Abbildung 10A)** [19].

Als weitere Strategie zur Erhöhung der Sensitivität, aber auch, um in vivo Messzeiten potenziell zu beschleunigen, wurde CS bei der MR Untersuchung von EAE Mäusen verwendet. In vivo Experimente mit prospektiver Unterabtastung und anschließender CS Rekonstruktion zeigten, dass die Bildqualität, die mit CS erreicht werden konnte, in vivo höher

war als ohne CS. Die Sensitivität der Detektion erhöhte sich mit Steigerung der Unterabtastrate.

Die Raten an richtig positiv detektierten ^{19}F Features war unter CS Bedingungen bei geringen Signalintensitäten stets anderen Rekonstruktionsmethoden überlegen und konnte durch Erhöhung der Unterabtastrate noch weiter gesteigert werden. FDRs hingegen traten vermehrt bei hoher Unterabtastung auf. Während bei Fourier-rekonstruierten Daten die Signalintensität im Vergleich zu einer Referenz überschätzt wurde, wurde bei CS die Signalintensität unterschätzt (**Abbildung 10B, obere Reihe**). Jeweils gilt, dass für geringere Signalintensitäten die Abweichung zunimmt. Durch Einsatz einer Kalibrierungsmethode konnte diese Über- und Unterschätzung reduziert werden und anhand einer Referenzprobe (**Abbildung 10B, links**) NP-Konzentrationen in EAE Mäusen bestimmt werden (**Abbildung 10B, untere Reihe**) [29].

Über den Einsatz einer ^{19}F CRP und CS hinaus wurde der Einfluss einer höheren Magnetfeldstärke von 21.1 T auf die MR Eigenschaften und Detektion untersucht. In Phantomuntersuchungen von PFCE NPs konnte gezeigt werden, dass die Relaxationszeiten sich in Abhängigkeit von der Feldstärke verkürzen. Für T_1 resultierte dies in einer Verkürzung von T_1=913 ms bei 9.4 T zu T_1=441 ms bei 21.1 T, für T_2 resultierte dies in einer Verkürzung von T_2=503 ms bei 9.4 T zu T_2=195 ms bei 21.1 T. Dieser Effekt wurde auch in einem ex vivo EAE Phantom der Milz, als Ort hoher lymphatischer Zelldichte und somit zu erwartender hoher ^{19}F Signalmenge, beobachtet (**Abbildung 10C**), mit einer Verkürzung von T_1 von T_1=1005 ms bei 9.4 T zu T_1=400 ms.

Eine Abschätzung der SNR Gewinns von Messungen bei 21.1 T gegenüber 9.4 T ergab, unter Berücksichtigung von Rauschen als Einflussfaktor und ohne Berücksichtigung von Einflüssen der Magnetfeldstärke auf Flipwinkel, Relaxationszeiten und die daraus resultierenden Sequenzanpassungen einen SNR Gewinn von 2.68. Bei zusätzlicher Berücksichtigung von Referenzspannungen, die zum Erreichen eines optimalen 90 ° Pulses benötig werden, erhöht sich der SNR Gewinn auf 3.8. In Phantommessungen mit PFCE Nanopartikeln bei 21.1 T und 9.4 T unter Verwendung einer 2D-RARE Methode mit langer Repetitionszeit (TR) aber ohne weitere Optimierungen konnte ein mittlerer SNR Gewinn eines Faktors von 2.1 bestimmt werden.

Zusätzlich wurde unter Verwendung eines PFCE Phantoms die Abhängigkeit des SNR Gewinns vom TR und dem Flipwinkel bei beiden Feldstärken mit einer FLASH Sequenz untersucht. Hierbei hat die Wahl von TR eine direkte Auswirkung auf die Messzeit. Je kürzer TR, desto mehr Mittlungen können innerhalb des gleichen Zeitraums durchgeführt werden. Für einen Vergleich wurde, jeweils bei 9.4 T oder 21.1 T, das SNR, das innerhalb eines festgelegten Zeitraums erreicht werden kann (SNR-Effizienz=SNR/√Zeit) bestimmt. Mit variablem TR und Flipwinkel wurde für beide Feldstärken die bestmögliche SNR-Effizienz

bestimmt. Bei optimalen Bedingungen für 9.4 T war das Verhältnis der SNR-Effizienz zwischen 21.1 T und 9.4 T 6.95, während bei optimalen Bedingungen für 21.1 T das Verhältnis 7.29 betrug.

Da diese erreichten Werte durch die unterschiedlichen T_1 Relaxationszeiten bei beiden unterschiedlichen Feldstärken beeinflusst werden, wurde eine Berücksichtigung dieser Einflüsse auf die SNR-Effizienz bei 21.1 T für das T_1 bei 9.4 T modelliert und ergab ein Verhältnis der SNR-Effizienzen von 5.25, unabhängig vom Einfluss der sich verändernden T_1 Relaxationszeit.

Schlussendlich konnten die Vorteile einer ^{19}F MR Messung bei 21.1 T in einem EAE ex vivo Phantom des ZNS mit Neuroinflammation demonstriert werden (**Abbildung 10D**). Diese ist gekennzeichnet durch das Erreichen einer höheren Auflösung und Sensitivität im Vergleich zu Messungen bei geringeren Feldstärken.

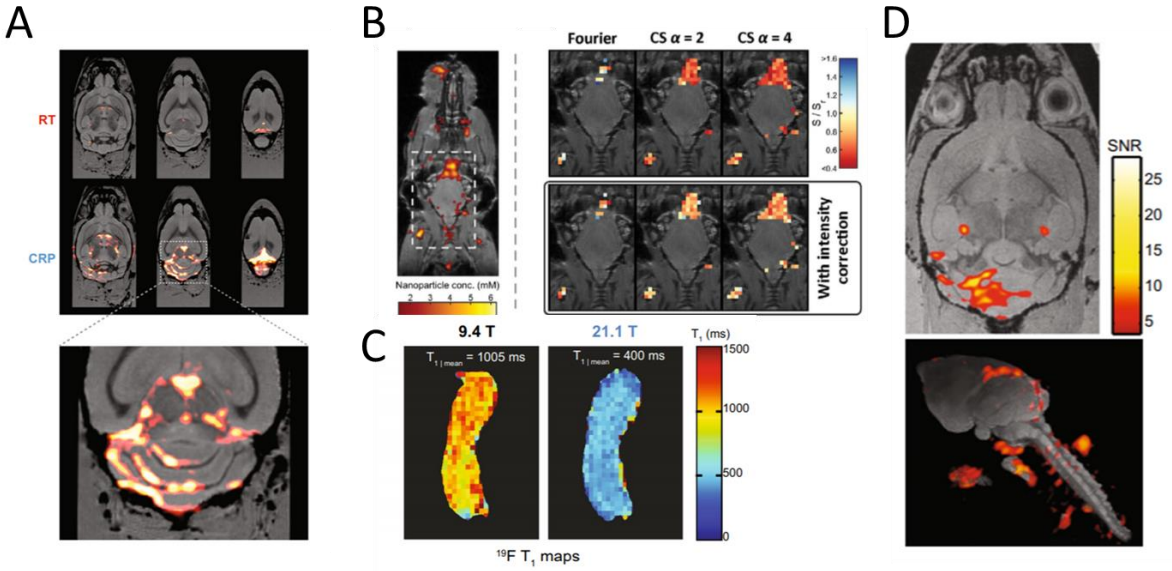

Abbildung 10 Erhöhung der Sensitivität von ^{19}F MRT durch technologische Entwicklungen und Verbesserungen. (A) $^{19}F/^{1}H$ MRT Bilderserie im Horizontalschnitt eines ex vivo Gehirns einer symptomatischen EAE Maus. Überlagerung eines ^{19}F RARE Bildes (rot) mit einem ^{1}H FLASH MRT Bild (grau). Obere Reihe: kombinierte $^{19}F/^{1}H$ Bilder mit Raumtemperatur Volumenspule aufgenommen, untere Reihe: mit ^{19}F CRP aufgenommen; 300 % Vergrößerung unten (B) Prospektives Compressed Sensing in vivo ^{19}F MRT; Links: Referenz-Bild mit Nanopartikelkonzentration, obere Reihe rechts: Vergleich der CS Rekonstruktion mit unterschiedlichen Unterabtastraten und im Vergleich zur Fourier Rekonstruktion ohne Intensitätskorrektur, untere Reihe rechts: Vergleich mit Intensitätskorrektur; blau: Überschätzung, rot: Unterschätzung; (C) ^{19}F Relaxationszeiten von PFCE NPs in der Milz einer EAE Maus ex vivo, bei 9.4 T und 21.1 T; (D) ^{19}F MR Bild einer ex vivo EAE Maus bei 21.1 T (3D-RARE Auflösung=333 µm^3. überlagert mit FLASH ^{1}H anatomischen MR Bildern (grau); Aus Waiczies, Millward [19], Starke, Pohlmann [29] und Waiczies, Rosenberg [21].

4 Diskussion

Diese und andere Arbeiten im Bereich der ^{19}F MR Forschung zeigen das Potenzial einer möglichen Übertragung von ^{19}F MR Techniken auf klinische Anwendungen und ihren Einsatz bei unterschiedlichen biomedizinischen Fragestellungen. Da immer höhere Feldstärken erreicht werden können und 7 T mittlerweile auch klinisch nutzbar ist, MR Antennen mit immer höherer Sensitivität gebaut werden und schnellere und effizientere Pulssequenzen entwickelt und beispielsweise durch Compressed Sensing beschleunigt und im Hinblick auf die individuelle Anwendung in ihren Sequenzparametern optimiert werden können, eröffnen sich gänzlich neue Möglichkeiten, ^{19}F MR in klinischen Studien einzusetzen.

Die Untersuchungen in diesen Studien zeigen, dass ^{19}F MR Eigenschaften von unterschiedlichen äußeren Umwelt- und intrinsischen, molekularen Umgebungseinflüssen abhängen und Sequenzen im Hinblick auf eine optimale Detektion und Maximierung der Signalmenge entsprechend ausgewählt und auch auf eventuelle Änderungen im Verlauf eines Experiments angepasst werden müssen.

Der Einfluss der Temperatur auf die Relaxationszeiten von Perfluorocarbon-Verbindungen wurde bereits demonstriert [27],konnte im Rahmen dieser Arbeit bestätigt und auf pharmakologische Substanzen ausgeweitet werden [36]. Dass sowohl die Temperatur, als auch der pH-Wert einen Einfluss auf MR Eigenschaften haben, konnte bereits für die ^{1}H anatomische Bildgebung gezeigt werden [30] und impliziert die vielfältige thermometrische Anwendung [31]. Die Kenntnis des Verhaltens von ^{19}F MR Eigenschaften bei sich änderndem pH-Wert ist bei der Betrachtung unterschiedlicher Kompartimente im Körper von Bedeutung. pH Änderungen treten etwa bei Entzündungsprozessen oder in der Umgebung von Tumoren auf. In vivo wurden in diesem Kontext pH Änderungen mittels MRT gemessen [32]. Während der Magen als erstes Kompartiment durch einen niedrigen pH und saures Milieu gekennzeichnet ist, liegt im Dünndarm, dem hauptsächlichen Ort der Arzneimittelabsorption ein basisches Milieu, also ein höherer pH-Wert vor, während nach Aufnahme in die Blutbahn ein pH von 7.4 vorliegt. Diese pH Unterschiede müssen bei der MR Detektion ^{19}F haltiger Medikamente berücksichtigt werden, da sie eine Verzerrung der detektierten Menge darstellen können.

Gadolinium-haltige Kontrastmittel werden im klinischen Alltag zur kontrastmittel-verstärkten anatomischen Bildgebung, wie etwa zur Diagnose der Multiplen Sklerose eingesetzt. Durch eine Verkürzung des T_1 kann im Bereich der Anflutung des Kontrastmittels beispielsweise eine Läsion im Gehirn eines MS Patienten, welche durch eine Schädigung der Blut-Hirn-Schranke charakterisiert ist, durch einen Kontrastunterschied dargestellt werden [33]. Für eine Detektion fluorierter Substanzen bedeutet dies, dass Kontrastmittelanflutungen das ^{19}F T_1 verkürzen und so zu einer gesteigerten Detektion beitragen können. Wie die Charakterisierung der ^{19}F MR

Eigenschaften fluorierter Medikamente in unterschiedlicher chemischer Umgebung zeigt, ist eine genaue Kenntnis der Umgebung, wie etwa DMSO, CMC oder Serum, in der eine Signaldetektion entweder angestrebt oder erwartet wird, unabdingbar, um ein maximales SNR erreichen zu können.

Basierend auf den ^{19}F MR Eigenschaften, die in einem bestimmten Setting vorliegen, müssen passende Sequenzen ausgewählt und hinsichtlich der Umwelt- und Umgebungseinflüsse optimiert werden [22, 28], mit dem Ziel einer verbesserte Detektion und gegebenenfalls Verkürzung der benötigten Messzeit, was es erlaubt, ein bestimmtes SNR Level zu erreichen.

Die ^{19}F MR Detektion fluorierter Medikamente wurde sowohl im Tierversuch als auch in der Humananwendung in zahlreichen Studien in der Vergangenheit beschrieben [11-13, 15]. Insbesondere das Vorliegen geringer Mengen und daraus resultierend niedrigen Detektionslimits verhinderten die breite Nutzung von ^{19}F MR Methoden bei klinischen Fragestellungen. Im Zuge dieser Arbeit konnten wesentliche Erkenntnisse hinsichtlich der Steigerung der Sensitivität auf unterschiedlichen Ebenen gewonnen werden, welche für eine potenzielle klinische Nutzbarkeit unabdingbar sind.

In der Entwicklung und Verwendung kryogen gekühlter Spulen liegt großes Potential für die Steigerung der Sensitivität [34], sowohl bei anatomischer ^{1}H Bildgebung, als auch gesteigerter Detektion von ^{19}F, aber auch bei anderen Nuclei, wie ^{23}Na oder ^{39}K für metabolische oder funktionelle Bildgebung [35, 36]. Für alle diese möglichen Anwendungsbereiche besteht ein Bedarf höherer Sensitivität. Durch die Entwicklung einer ^{19}F CRP konnte erstmalig eine stark verbesserte Darstellung von Neuroinflammation im Tiermodell der EAE erreicht werden. Einerseits wird durch kryogene Kühlung, andererseits durch ein Quadraturdesign der ^{19}F CRP eine Steigerung der Sensitivität insgesamt um den Faktor 15 im Oberflächenbereich der Spule erzielt [19].

Dies erlaubt durch eine höhere Auflösung eine verbesserte Detailgenauigkeit und gleichzeitig eine Detektion von Merkmalen, die mit herkömmlicher Technologie unter dem Detektionslimit gelegen hätten. Die Entwicklung der ^{19}F CRP stellt somit einen wichtigen Meilenstein für die Detektion fluorierter Medikamente im Mausmodell der EAE dar und wird durch die Entwicklung von Techniken zur Korrektur der durch die Bauweise von Oberflächenspulen bedingten Abnahme der Signalintensität mit zunehmender Entfernung von der Spulenoberfläche komplettiert [37].

Durch den Einsatz von CS bei ^{19}F MRT Messungen konnten einerseits die Anzahl der detektierbaren Merkmale und die räumliche Auflösung durch eine Steigerung der Sensitivität erhöht werden, andererseits die Messzeit verkürzt werden. Hierbei konnte gezeigt werden, dass eine hohe Verlässlichkeit hinsichtlich einer immer noch geringen Falsch-Positiv-Rate

auch bei hohen Unterabtastraten gegeben ist. Aus diesem Grund wird sich CS insbesondere bei kleinen ^{19}F Mengen und niedrigen Detektionsgrenzen, wie es bei pharmakologischen Studien der Fall ist, als hilfreich erweisen.

Bislang werden im klinischen Alltag MRT Untersuchungen vor allem bei 1.5 und 3 T durchgeführt. Die klinische Zulassung der höheren Feldstärke von 7 T und die Forcierung höherer Feldstärken eröffnen Wege der genaueren anatomischen Darstellung und der präziseren Diagnose von Krankheiten, aber auch der funktionellen und metabolischen Bildgebung [38].

^{19}F MR Detektion profitierte immens von einer höheren Feldstärke von 21.1 T [21]. Im Entzündungsmodell der EAE resultierte dies in einer höheren Detailgenauigkeit und einem niedrigeren Detektionslimit im Vergleich zu Messungen bei 9.4 T und kann bei der Untersuchung fluorierter Medikamente in vivo eine bessere Detektion und potenziell Bildgebung ermöglichen.

Eine Steigerung der Sensitivität, entweder durch kryogene Kühlung, CS oder höhere Magnetfeldstärken kann somit in höhere Detailgenauigkeit oder verkürzte Messzeiten investiert werden. Dadurch können einerseits Regionen oder Verteilungsmuster präziser bestimmt und unterschieden werden, gleichzeitig aber auch Studien im Sinne einer geringeren Belastung von Patienten vereinfacht werden. Durch die Herabsetzung von Detektionslimits kann eine Detektion unter Umständen überhaupt erst möglich gemacht werden.

Eine weitere Steigerung der SNR, insbesondere im Fall von TF, kann durch eine synthesechemische Weiterentwicklung von TF durch Substitution der Trifluormethylgruppe (CF_3) mit einer Pentafluorosulfanylgruppe (SF_5) erreicht werden [39]. Diese Modifizierung erlaubt nicht nur eine potentiell verbesserte Bildgebung in vivo sondern auch eine gesteigerte Wirksamkeit in der Reduktion enzymatischer DHODH Aktivität und Proliferationshemmung in Zellkultur. Diese technischen Entwicklungen können es erlauben, Moleküle wie TF oder Weiterentwicklungen wie SF_5-TF [39] zunächst im Tiermodell auf Wirksamkeit und Bildgebung zu untersuchen.

Um ^{19}F MR Techniken auch zur Detektion kleiner Mengen, wie etwa zum Monitoring pharmakologischer Therapien und das in klinisch vertretbaren und sinnvollen Messzeiten zum Einsatz zu bringen, ist es erforderlich, dass technologische Ansätze ausgereizt, optimiert und weiterentwickelt werden, um bei kombinierter Anwendung verschiedener technologischer Maßnahmen und deren Optimierung hinsichtlich der ^{19}F MR Eigenschaften und Berücksichtigung der Umgebungseinflüsse eine hohe Sensitivität und eine hohe SNR-Effizienz zu erreichen.

So können Detektionslimits überwunden werden und eine ungenaue Lokalisierung in Folge mangelnder räumlicher Auflösung beispielsweise mittels lokalisierter Spektroskopietechniken oder Bildgebung erfolgreich adressiert werden.

Präklinische Anwendungen von ^{19}F MR zur Detektion, Lokalisierung, Bildgebung und schließlich Quantifizierung von fluorierten Medikamenten in vivo unter physiologischen und pathologischen Bedingungen können die Vorlage sein für die Anwendung in klinischen Phase I Studien mit dem Ziel, die Verteilung und Bioverfügbarkeit fluorierter Medikamente zu bestimmen und mit konventionellen Methoden wie PET oder SPECT, zusammen mit der Bestimmung der Konzentrationen in biologischen Proben zu vergleichen und korrelieren.

TF wurde ex vivo bereits in einem EAE Rattenmodell mittels Ganzkörperautoradiographie und in gesunden Ratten gemessen und die Anwesenheit im ZNS bestätigt, ohne dass ein Unterschied zwischen gesunden und kranken Ratten festgestellt wurde [17]. Die gefundenen TF Konzentrationen in Gehirn, Rückenmark und Blut waren vergleichbar mit den Konzentrationen, die im Rahmen dieser Arbeit in Prinz, et al., 2021 [26] in Gehirn, Liquor und Plasma gefunden wurden. Im Gegensatz hierzu konnte eine Studie von Rzagalinski, et al., 2019 [18] TF im ZNS mittels MALDI Massenspektrometrie Imaging nicht nachweisen.

Diese Befunde zeigen, ein Vergleich der verschiedenen Methoden erfolgen sollte und so Informationen zur Verteilung sich potenziell ergänzen können. Im Gegensatz zu PET oder SPECT erlauben ^{19}F MR Techniken hierbei die Unterscheidung von Metaboliten durch unterschiedliche Chemical Shifts und eine nicht-invasive, da nicht mit Radioaktivität verbundene Methode. Mit einem Einsatz bei Bioverfügbarkeitsstudien in Phase I klinischen Studien mit geringer Patientenzahl kann sich ^{19}F MR Technologie im klinischen Alltag etablieren und zu einem wertvollen Tool der Therapieführung werden. Parallel zur Diagnosestellung und zum regelmäßigen MR gestützten Monitoring des Krankheitsverlaufs wie etwa bei MS kann die Konzentration fluorierter Wirkstoffe wie des TF an verschiedenen Zielorganen ergänzend zur Bestimmung von Plasmaspiegeln gemessen werden. So kann eine Dosisanpassung, Überwachung potentieller unerwünschter Arzneimittelwirkungen und Beurteilung und Prognose eines Therapieverlaufs unterstützt werden und die Therapie von MS Patienten auf die individuellen Bedürfnisse angepasst werden.

Hauptlimitation der ^{19}F MR Methodik ist die geringe SNR, die auf der geringen Anzahl für die Signalentstehung verfügbaren ^{19}F Nuclei gründet. Da die Dosis durch die angestrebte Zielkonzentration und Wirksamkeit festgelegt und daher begrenzt ist, kann eine gesteigerte Detektion nur durch eine Erhöhung der Sensitivität erreicht werden. Die Feldstärke klinisch eingesetzter MRT Scanner ist in der Regel geringer, als die Feldstärke präklinischer Geräte, sodass tierexperimentelle Befunde und Methodik nicht unmittelbar auf Patientenstudien übertragen werden können. Eine weitere Limitierung ist die Erwärmung von Gewebe durch

energetisch anspruchsvolle MR Pulssequenzen, welche in Humanstudien durch SAR Obergrenzen geregelt ist. Zudem kann der Effekt kryogener Kühlung bei Antennen für Humananwendungen nicht oder nur begrenzt ausgenutzt werden. Einer potenziell längeren Messzeit und somit hohen Anzahl notwendiger Mittlungen des Signals kann mittels Unterabtastungstechniken wie Compressed Sensing entgegengewirkt werden. Nichtsdestotrotz sind weitere technologische Entwicklungen wie auch SNR effizienterer Pulssequenzen und deren Optimierung notwendig, um für klinische Szenarien vollumfänglich verfügbar sein zu können.

Die hier beschriebenen Forschungsarbeiten bilden den Ausgangspunkt für weitergehende Fragestellungen, die mit der Nutzung bereits etablierter MR Methoden und deren Fortentwicklung bearbeitet werden können. Durch die Optimierung der Sensitivität mit kombinierten Methoden auf den Ebenen von Hardware, Sequenz und Rekonstruktion kann die ^{19}F MR Detektion von TF und auch anderen fluorierten Substanzen in die Unterscheidung und Quantifizierung von Metaboliten eines Wirkstoffs aber auch verschiedener Wirkstoffe bei Kombinationstherapie münden. Eine Optimierung kann eine genaue Lokalisierung und Bildgebung erlauben. Die Korrelation verschiedener Messmethoden wie PET, SPECT, Massenspektrometrie und ^{19}F MRT sowie deren synergistische Kombination stellen einen potenziell umfangreichen, aber auch mächtigen Ansatz dar, um Bioverfügbarkeit und Verteilung zu bestimmen.

Eine weitere Dimension wird der klinischen Bildgebung durch ^{19}F MRT Technologie hinzugefügt, wenn die immunologischen Prozesse wie etwa bei der MS Pathologie neben kontrastmittelverstärkter Untersuchung von Läsionen mittels fluorhaltiger Nanopartikel studiert und verfolgt wird. Der Ansatz des Cell-Trackings bei immuntherapeutischen Prozessen wurde bereits klinisch in Krebspatienten demonstriert [40]. Somit ist eine Übertragung auf das Therapiemonitoring mit höherer Anforderung an die Sensitivität greifbar geworden. Denkbar ist auch eine Ausweitung und Ergänzung des nicht-invasiven experimentellen MRT Workflows. So kann Massenspektrometrie zur exakten Bestimmung von Wirkstoffkonzentrationen verwendet werden und bei präklinischen Fragestellungen ergänzend Immunhistochemie zur Befundung der Pathologie auf Proteinebene und Verteilung immunhistochemisch darstellbarer Nanopartikel auf zellulärer Ebene durchgeführt werden. Für eine zusätzliche Lokalisierung von Wirkstoffmolekülen und Metaboliten könnte ebenfalls präklinisch 3D MALDI MS zum Einsatz kommen. Auf diese Art kann ein umfassendes Bild sowohl von Pathogenese als auch des Therapieverlaufs gewonnen werden und Informationen integriert werden.

Die Weiterentwicklung bestehender Wirkstoffe und die Entwicklung neuer fluorierter Substanzen mit einer höheren Anzahl an ^{19}F Nuclei pro Molekül, wie etwa der SF_5-Seitengruppe birgt ebenfalls hohes Potential für künftige Fragestellungen [39].

Durch die Einführung von ^{19}F MR Techniken in der präklinischen Wirkstoffentwicklung, in klinischen Studien und in der klinischen Anwendung, um Bioverfügbarkeit, Verteilung aber auch Metabolismus von Medikamenten abzubilden, stellt in jedem Fall eine vielversprechende Technologie dar, deren Einsatz es erlaubt, zu einem besseren Verständnis und einer besseren Überwachung von Therapien bei MS beizutragen und evidenzbasierte und patientenorientiere Lösungen anzubieten um Arzneimitteltherapien effizienter, sicherer und vor allem erfolgreicher zu machen.

5 Literaturverzeichnis

1. Reich DS, Lucchinetti CF, Calabresi PA. Multiple Sclerosis. New England Journal of Medicine. 2018; 378: 169-80.
2. Sinnecker T, Kuchling J, Dusek P, Dörr J, Niendorf T, Paul F, Wuerfel J. Ultrahigh field MRI in clinical neuroimmunology: a potential contribution to improved diagnostics and personalised disease management. The EPMA journal. 2015; 6: 16.
3. Bermel RA, Naismith RT. Using MRI to make informed clinical decisions in multiple sclerosis care. Curr Opin Neurol. 2015; 28: 244-9.
4. Tintore M, Rovira A, Rio J, Otero-Romero S, Arrambide G, Tur C, Comabella M, Nos C, Arevalo MJ, Negrotto L, Galan I, Vidal-Jordana A, Castillo J, Palavra F, Simon E, Mitjana R, Auger C, Sastre-Garriga J, Montalban X. Defining high, medium and low impact prognostic factors for developing multiple sclerosis. Brain. 2015; 138: 1863-74.
5. Millward JM, Ramos Delgado P, Smorodchenko A, Boehmert L, Periquito J, Reimann HM, Prinz C, Els A, Scheel M, Bellmann-Strobl J, Waiczies H, Wuerfel J, Infante-Duarte C, Chien C, Kuchling J, Pohlmann A, Zipp F, Paul F, Niendorf T, Waiczies S. Transient enlargement of brain ventricles during relapsing-remitting multiple sclerosis and experimental autoimmune encephalomyelitis. JCI Insight. 2020; 5.
6. Lepore S, Waiczies H, Hentschel J, Ji Y, Skodowski J, Pohlmann A, Millward JM, Paul F, Wuerfel J, Niendorf T, Waiczies S. Enlargement of cerebral ventricles as an early indicator of encephalomyelitis. PloS one. 2013; 8: e72841.
7. Tintore M, Vidal-Jordana A, Sastre-Garriga J. Treatment of multiple sclerosis - success from bench to bedside. Nature reviews Neurology. 2019; 15: 53-8.
8. Grossman I, Knappertz V, Laifenfeld D, Ross C, Zeskind B, Kolitz S, Ladkani D, Hayardeny L, Loupe P, Laufer R, Hayden M. Pharmacogenomics strategies to optimize treatments for multiple sclerosis: Insights from clinical research. Progress in neurobiology. 2017; 152: 114-30.
9. Ahrens ET, Flores R, Xu H, Morel PA. In vivo imaging platform for tracking immunotherapeutic cells. Nature biotechnology. 2005; 23: 983-7.
10. Waiczies H, Lepore S, Drechsler S, Qadri F, Purfürst B, Sydow K, Dathe M, Kühne A, Lindel T, Hoffmann W, Pohlmann A, Niendorf T, Waiczies S. Visualizing brain inflammation with a shingled-leg radio-frequency head probe for 19F/1H MRI. Scientific reports. 2013; 3: 1280.
11. Doi Y, Shimmura T, Kuribayashi H, Tanaka Y, Kanazawa Y. Quantitative (19)F imaging of nmol-level F-nucleotides/-sides from 5-FU with T(2) mapping in mice at 9.4T. Magnetic resonance in medicine. 2009; 62: 1129-39.
12. Bolo NR, Hode Y, Nedelec JF, Laine E, Wagner G, Macher JP. Brain pharmacokinetics and tissue distribution in vivo of fluvoxamine and fluoxetine by fluorine magnetic resonance spectroscopy. Neuropsychopharmacology : official publication of the American College of Neuropsychopharmacology. 2000; 23: 428-38.
13. Ji Y, Waiczies H, Winter L, Neumanova P, Hofmann D, Rieger J, Mekle R, Waiczies S, Niendorf T. Eight-channel transceiver RF coil array tailored for (1)H/(1)(9)F MR of the human knee and fluorinated drugs at 7.0 T. NMR in biomedicine. 2015; 28: 726-37.
14. Niendorf T, Ji Y, Waiczies S. Fluorinated Natural Compounds and Synthetic Drugs. In: Ahrens ET, Flögel U., editor. Fluorine Magnetic Resonance Imaging. 1 ed: Pan Stanford Publishing; 2016. p. 311-44.
15. Morikawa S, Inubushi T, Morita M, Murakami K, Masuda C, Maki J, Tooyama I. Fluorine-19 fast recovery fast spin echo imaging for mapping 5-fluorouracil. Magn Reson Med Sci. 2007; 6: 235-40.
16. Derfuss T, Mehling M, Papadopoulou A, Bar-Or A, Cohen JA, Kappos L. Advances in oral immunomodulating therapies in relapsing multiple sclerosis. The Lancet Neurology. 2020.
17. Kaplan J, Cavalier S, Turpault S. Biodistribution of Teriflunomide in Naïve Rats vs Rats With Experimental Autoimmune Encephalomyelitis. Poster presented at: 31st Congress of the European Committee for Treatment and Research in Multiple Sclerosis (ECTRIMS), October 7–10, 2015, Barcelona, Spain. 2015.

18. Rzagalinski I, Hainz N, Meier C, Tschernig T, Volmer DA. Spatial and molecular changes of mouse brain metabolism in response to immunomodulatory treatment with teriflunomide as visualized by MALDI-MSI. Analytical and bioanalytical chemistry. 2019; 411: 353-65.
19. Waiczies S, Millward JM, Starke L, Delgado PR, Huelnhagen T, Prinz C, Marek D, Wecker D, Wissmann R, Koch SP, Boehm-Sturm P, Waiczies H, Niendorf T, Pohlmann A. Enhanced Fluorine-19 MRI Sensitivity using a Cryogenic Radiofrequency Probe: Technical Developments and Ex Vivo Demonstration in a Mouse Model of Neuroinflammation. Scientific reports. 2017; 7: 9808.
20. Eigentler TW, Winter L, Han H, Oberacker E, Kuehne A, Waiczies H, Schmitter S, Boehmert L, Prinz C, Trefna HD, Niendorf T. Wideband Self-Grounded Bow-Tie Antenna for Thermal MR. NMR in biomedicine. 2020; 33: e4274.
21. Waiczies S, Rosenberg JT, Kuehne A, Starke L, Delgado PR, Millward JM, Prinz C, Dos Santos Periquito J, Pohlmann A, Waiczies H, Niendorf T. Fluorine-19 MRI at 21.1 T: enhanced spin-lattice relaxation of perfluoro-15-crown-5-ether and sensitivity as demonstrated in ex vivo murine neuroinflammation. Magma (New York, NY). 2019; 32: 37-49.
22. Faber C, Schmid F. Pulse Sequence Considerations and Schemes. In: Ahrens ET, Flögel U., editor. Fluorine Magnetic Resonance Imaging: Pan Stanford Publishing; 2016. p. 3-27.
23. Mastropietro A, De Bernardi E, Breschi GL, Zucca I, Cametti M, Soffientini CD, de Curtis M, Terraneo G, Metrangolo P, Spreafico R, Resnati G, Baselli G. Optimization of rapid acquisition with relaxation enhancement (RARE) pulse sequence parameters for (1)(9)F-MRI studies. J Magn Reson Imaging. 2014; 40: 162-70.
24. Kampf T, Fischer A, Basse-Lüsebrink TC, Ladewig G, Breuer F, Stoll G, Jakob PM, Bauer WR. Application of compressed sensing to in vivo 3D ^{19}F CSI. J Magn Reson. 2010; 207: 262-73.
25. Zhong J, Mills PH, Hitchens TK, Ahrens ET. Accelerated fluorine-19 MRI cell tracking using compressed sensing. Magnetic resonance in medicine. 2013; 69: 1683-90.
26. Prinz C, Starke L, Millward JM, Fillmer A, Delgado PR, Waiczies H, Pohlmann A, Rothe M, Nazare M, Paul F, Niendorf T, Waiczies S. In vivo detection of teriflunomide-derived fluorine signal during neuroinflammation using fluorine MR spectroscopy. Theranostics. 2021; 11: 2490-504.
27. Kadayakkara DK, Damodaran K, Hitchens TK, Bulte JW, Ahrens ET. (19)F spin-lattice relaxation of perfluoropolyethers: Dependence on temperature and magnetic field strength (7.0-14.1T). J Magn Reson. 2014; 242: 18-22.
28. Prinz C, Delgado PR, Eigentler TW, Starke L, Niendorf T, Waiczies S. Toward (19)F magnetic resonance thermometry: spin-lattice and spin-spin-relaxation times and temperature dependence of fluorinated drugs at 9.4 T. Magma (New York, NY). 2019; 32: 51-61.
29. Starke L, Pohlmann A, Prinz C, Niendorf T, Waiczies S. Performance of compressed sensing for fluorine-19 magnetic resonance imaging at low signal-to-noise ratio conditions. Magnetic resonance in medicine. 2020; 84: 592-608.
30. Moser E, Winklmayr E, Holzmüller P, Krssak M. Temperature- and pH-dependence of proton relaxation rates in rat liver tissue. Magnetic resonance imaging. 1995; 13: 429-40.
31. Ji Y, Winter L, Navarro L, Ku MC, Periquito JS, Pham M, Hoffmann W, Theune LE, Calderón M, Niendorf T. Controlled Release of Therapeutics from Thermoresponsive Nanogels: A Thermal Magnetic Resonance Feasibility Study. Cancers (Basel). 2020; 12.
32. Anemone A, Consolino L, Arena F, Capozza M, Longo DL. Imaging tumor acidosis: a survey of the available techniques for mapping in vivo tumor pH. Cancer and Metastasis Reviews. 2019; 38: 25-49.
33. Absinta M, Sati P, Reich DS. Advanced MRI and staging of multiple sclerosis lesions. Nature reviews Neurology. 2016; 12: 358-68.
34. Niendorf T, Pohlmann A, Reimann HM, Waiczies H, Peper E, Huelnhagen T, Seeliger E, Schreiber A, Kettritz R, Strobel K, Ku M-C, Waiczies S. Advancing Cardiovascular, Neurovascular, and Renal Magnetic Resonance Imaging in Small Rodents Using Cryogenic Radiofrequency Coil Technology. Front Pharmacol. 2015; 6: 255-.

35. Boehmert L, Waiczies H, Kuehne A, Oezerdem C, Waiczies S, Starke L, Ku MC, Pohlmann A, Seeliger E, Niendorf T. Cardiorenal sodium MRI in small rodents using a quadrature birdcage volume resonator at 9.4 T. Magma (New York, NY). 2020; 33: 121-30.
36. Wenz D, Nagel AM, Lott J, Kuehne A, Niesporek SC, Niendorf T. In vivo potassium MRI of the human heart. Magnetic resonance in medicine. 2020; 83: 203-13.
37. Delgado PR, Kuehne A, Periquito JS, Millward JM, Pohlmann A, Waiczies S, Niendorf T. B1 inhomogeneity correction of RARE MRI with transceive surface radiofrequency probes. Magnetic resonance in medicine. 2020; 84: 2684-701.
38. Niendorf T, Barth M, Kober F, Trattnig S. From ultrahigh to extreme field magnetic resonance: where physics, biology and medicine meet. Magma (New York, NY). 2016; 29: 309-11.
39. Prinz C, Martos-Riano V, Ramspoth T, Starke L, Neuenschwander M, von Kries JP, Pohlmann A, Nazaré M, Niendorf T, Waiczies S. Enhancing Fluorine-19 Magnetic Resonance Drug Imaging: Chemical Variations in the Fluorine Side-Groups of the Immunomodulatory Drug Teriflunomide. Proc Intl Soc Mag Reson Med; 2019.
40. Ahrens ET, Helfer BM, O'Hanlon CF, Schirda C. Clinical cell therapy imaging using a perfluorocarbon tracer and fluorine-19 MRI. Magnetic resonance in medicine. 2014; 72: 1696-701.

6 Eidesstattliche Versicherung

„Ich, Christian Prinz, versichere an Eides statt durch meine eigenhändige Unterschrift, dass ich die vorgelegte Dissertation mit dem Thema: „Untersuchungen experimenteller Theranostikansätze bei Neuroinflammation mittels Ultrahochfeld Magnetresonanz-Methoden“/„Investigation of experimental theranostic approaches in neuroinflammation using ultrahigh field magnetic resonance techniques“ selbstständig und ohne nicht offengelegte Hilfe Dritter verfasst und keine anderen als die angegebenen Quellen und Hilfsmittel genutzt habe.

Alle Stellen, die wörtlich oder dem Sinne nach auf Publikationen oder Vorträgen anderer Autoren/innen beruhen, sind als solche in korrekter Zitierung kenntlich gemacht. Die Abschnitte zu Methodik (insbesondere praktische Arbeiten, Laborbestimmungen, statistische Aufarbeitung) und Resultaten (insbesondere Abbildungen, Graphiken und Tabellen) werden von mir verantwortet.

Ich versichere ferner, dass ich die in Zusammenarbeit mit anderen Personen generierten Daten, Datenauswertungen und Schlussfolgerungen korrekt gekennzeichnet und meinen eigenen Beitrag sowie die Beiträge anderer Personen korrekt kenntlich gemacht habe (siehe Anteilserklärung). Texte oder Textteile, die gemeinsam mit anderen erstellt oder verwendet wurden, habe ich korrekt kenntlich gemacht.

Meine Anteile an etwaigen Publikationen zu dieser Dissertation entsprechen denen, die in der untenstehenden gemeinsamen Erklärung mit dem/der Erstbetreuer/in, angegeben sind. Für sämtliche im Rahmen der Dissertation entstandenen Publikationen wurden die Richtlinien des ICMJE (International Committee of Medical Journal Editors; www.icmje.og) zur Autorenschaft eingehalten. Ich erkläre ferner, dass ich mich zur Einhaltung der Satzung der Charité – Universitätsmedizin Berlin zur Sicherung Guter Wissenschaftlicher Praxis verpflichte.

Weiterhin versichere ich, dass ich diese Dissertation weder in gleicher noch in ähnlicher Form bereits an einer anderen Fakultät eingereicht habe.

Die Bedeutung dieser eidesstattlichen Versicherung und die strafrechtlichen Folgen einer unwahren eidesstattlichen Versicherung (§§156, 161 des Strafgesetzbuches) sind mir bekannt und bewusst.“

Datum Unterschrift

Anteilserklärung an den erfolgten Publikationen

Christian Prinz hatte folgenden Anteil an den folgenden Publikationen:

Publikation 1: **Prinz, C.**, Delgado, P. R., Eigentler, T. W., Starke, L., Niendorf, T., & Waiczies, S., Toward ^{19}F magnetic resonance thermometry: spin-lattice and spin-spin-relaxation times and temperature dependence of fluorinated drugs at 9.4 T. *Magma (New York, N.Y.)*, *2019*

Beitrag im Einzelnen (bitte ausführlich ausführen):

- Literaturrecherche
- Planung, Vorbereitung und Durchführung aller MR-Experimente
- Auswertung der MR-Daten (außer Abbildungen 1B, 2B, 3B, 4B, durchgeführt von PRD)
- Auswertung der Veränderung der MR Eigenschaften in Abhängigkeit von der Temperatur (außer statistische Auswertung der Temperaturmessdaten, durchgeführt von TWE)
- Interpretation experimenteller Daten und Ergebnisse
- Verfassen des ersten Entwurfs des Manuskripts und aller Abbildungen (außer Abbildungen 1B, 2B, 3B, 4B) sowie Überarbeitungen bei der Revision

Publikation 2: **Prinz, C.**, Starke, L., Millward, J. M., Fillmer, A., Delgado, P. R., Waiczies, H., Pohlmann, A., Rothe, M., Nazaré, M., Paul, F., Niendorf, T., & Waiczies, S., *In vivo* detection of teriflunomide-derived fluorine signal during neuroinflammation using fluorine MR spectroscopy. *Theranostics*, *2021*

Beitrag im Einzelnen (bitte ausführlich ausführen):

- Literaturrecherche
- Planung und Durchführung aller MR-Experimente außer Kontrastmittelverabreichung
- gesamte statistische Auswertung der Krankheitsverläufe (außer Homogenität der Varianz und Massenspektrometrie-Daten) und MR Daten (außer Postprozessierung und MR Datenauswertung)
- Interpretation experimenteller Daten und Ergebnisse
- Verfassen des ersten Entwurfs des Manuskripts und der Abbildungen sowie Überarbeitungen bei der Revision

Experimente und statistische Auswertungen spiegeln sich wider in folgenden Beiträgen zu Abbildungen:

- Abbildungen 1A-J (Unterstützung Statistik JM, Unterstützung Kontrastmittelapplikation JM)
- Abbildungen 2A-K (2L Analyse von LS)
- Abbildungen 3A-E (MR Auswertung und Postprozessierung von Spektren mit Unterstützung von LS)
- Abbildungen 4A (4B-C mit Unterstützung bei der MR Auswertung von LS)

Publikation 3: Starke, L., Pohlmann, A., **Prinz, C.**, Niendorf, T., & Waiczies, S., Performance of compressed sensing for fluorine-19 magnetic resonance imaging at low signal-to-noise ratio conditions. *Magnetic resonance in medicine*, *2020*

Beitrag im Einzelnen (bitte ausführlich ausführen):

- Planung und Durchführung von vivo Experimenten und Unterstützung bei MR Methoden
- Beitrag zum Verfassen von Einleitung und Methodenanteil bezüglich des EAE Tiermodells
- Überarbeitung und kritische Korrektur des ersten Entwurfs des Manuskripts
- Experimenteller Beitrag resultierte in Abbildungen 1B, 6E, 7A, 9A-B

Publikation 4: Waiczies, S., Millward, J. M., Starke, L., Delgado, P. R., Huelnhagen, T., **Prinz, C.**, Marek, D., Wecker, D., Wissmann, R., Koch, S. P., Boehm-Sturm, P., Waiczies, H., Niendorf, T., & Pohlmann, A. (2017). Enhanced Fluorine-19 MRI Sensitivity using a Cryogenic Radiofrequency Probe: Technical Developments and Ex Vivo Demonstration in a Mouse Model of Neuroinflammation. *Scientific reports, 2017*

Beitrag im Einzelnen (bitte ausführlich ausführen):

- Planung und Durchführung von Phantom und ex vivo Experimenten und Unterstützung bei MR Methoden und Phantom-Konstruktion
- Interpretation experimenteller Daten und Ergebnisse
- Überarbeitung und kritische Korrektur des ersten Entwurfs des Manuskripts und der Revision
- Experimente und statistische Auswertungen spiegeln sich wider in folgenden Beiträgen zu Abbildungen: 4A+B (Phantom-Konstruktion und MR Datenakquisition)

Publikation 5: Waiczies, S., Rosenberg, J. T., Kuehne, A., Starke, L., Delgado, P. R., Millward, J. M., **Prinz, C.**, Dos Santos Periquito, J., Pohlmann, A., Waiczies, H., & Niendorf, T. (2019). Fluorine-19 MRI at 21.1 T: enhanced spin-lattice relaxation of perfluoro-15-crown-5-ether and sensitivity as demonstrated in ex vivo murine neuroinflammation. *Magma (New York, N.Y.), 2019*

Beitrag im Einzelnen (bitte ausführlich ausführen):

- Konstruktion von Phantomen, ex vivo Phantomen
- Planung und Durchführung von Phantom und in vivo und ex vivo Experimenten
- Unterstützung bei MR Methoden
- Unterstützung bei der Datenanalyse (Änderung der Relaxationszeiten im Phantom und ex vivo bei 9.4 T und 21 T)
- Interpretation experimenteller Daten und Ergebnisse
- Überarbeitung und kritische Korrektur des ersten Entwurfs des Manuskripts und der Revision
- Experimente und statistische Auswertungen spiegeln sich wider in folgenden Beiträgen zu Abbildungen: 1A (Phantomkonstruktion und Unterstützung bei MR Experimenten), 5A+B (Analyse der Relaxationszeiten), Tabelle 2+3, Abbildung 6 (Analyse der Relaxationszeiten)

_____

Unterschrift, Datum und Stempel des/der erstbetreuenden Hochschullehrers/in

_____

Unterschrift des Doktoranden/der Doktorandin

7 Publikation 1: Toward ^{19}F magnetic resonance thermometry

Magnetic Resonance Materials in Physics, Biology and Medicine
https://doi.org/10.1007/s10334-018-0722-8

RESEARCH ARTICLE

Toward ^{19}F magnetic resonance thermometry: spin–lattice and spin–spin-relaxation times and temperature dependence of fluorinated drugs at 9.4 T

Christian Prinz[1] · Paula Ramos Delgado[1] · Thomas Wilhelm Eigentler[1] · Ludger Starke[1] · Thoralf Niendorf[1,2] · Sonia Waiczies[1]

Received: 1 July 2018 / Revised: 11 October 2018 / Accepted: 21 November 2018

Abstract

Objective This study examines the influence of the environmental factor temperature on the ^{19}F NMR characteristics of fluorinated compounds in phantom studies and in tissue.

Materials and methods ^{19}F MR mapping and MR spectroscopy techniques were used to characterize the ^{19}F NMR characteristics of perfluoro-crown ether (PFCE), isoflurane, teriflunomide, and flupentixol. T_1 and T_2 mapping were performed, while temperature in the samples was changed (T = 20–60 °C) and monitored using fiber optic measurements. In tissue, T_1 of PFCE nanoparticles was determined at physiological temperatures and compared with the T_1 measured at room temperature.

Results Studies on PFCE, isoflurane, teriflunomide, and flupentixol showed a relationship between temperature and their physicochemical characteristics, namely, chemical shift, T_1 and T_2. T_1 of PFCE nanoparticles was higher at physiological body temperatures compared to room temperature.

Discussion The impact of temperature on the ^{19}F NMR parameters of fluorinated compounds demonstrated in this study not only opens a trajectory toward ^{19}F MR-based thermometry, but also indicates the need for adapting MR sequence parameters according to environmental changes such as temperature. This will be an absolute requirement for detecting fluorinated compounds by ^{19}F MR techniques in vivo.

Keywords Magnetic resonance · Fluorine MR · 19F MR · Thermometry · Spin–lattice relaxation

Introduction

Fluorine-19 (^{19}F) magnetic resonance imaging (MRI) and spectroscopy (MRS) techniques are proving to be fundamental to a multitude of biomedical applications [1]. These applications include tracking of cells labelled with fluorinated nanoparticles to study inflammatory processes [2–4] and for studying the distribution of fluorinated drugs in humans [5–9] and animals [10–13]. Studying ^{19}F is favorable due to its 100% natural abundance and high gyromagnetic ratio which is comparable to that of proton (^{1}H) and provides background free signal due to its nearly complete intrinsic absence in the human body [14]. The ^{19}F signal for each individual compound is dependent on its ^{19}F NMR properties, which are in turn influenced by factors such as concentration, pH, and temperature [15]. An influence of temperature on the relaxivity ($R_1 = 1/T_1$) of perfluoro-15-crown-5 ether (PFCE) and perfluoropolyether (PFPE) was previously demonstrated [16, 17].

Studying the physicochemical characteristics of ^{19}F compounds is crucial for optimizing detection and increasing their signal-to noise ratio (SNR) in vivo. ^{19}F compounds used for labeling cells such as PFCE contain a large number of ^{19}F atoms per molecule, thereby providing a sufficient signal when studied by ^{19}F MR techniques. In contrast, currently available ^{19}F pharmacological agents contain low

✉ Sonia Waiczies
sonia.waiczies@mdc-berlin.de

1 Berlin Ultrahigh Field Facility (B.U.F.F.), Max Delbrueck Center for Molecular Medicine in the Helmholtz Association, Robert Roessle Straße 10, 13125 Berlin, Germany

2 Experimental and Clinical Research Center, A Joint Cooperation Between the Charité Medical Faculty and the Max Delbrueck Center for Molecular Medicine in the Helmholtz Association, Robert Roessle Straße 10, 13125 Berlin, Germany

Published online: 04 December 2018

numbers of ^{19}F atoms per molecule and are usually present at low therapeutic concentrations in vivo, making detection of these ^{19}F drugs even more challenging. The number of ^{19}F atoms per drug molecule ranges from the typical monofluorination (e.g., dexamethasone, midazolam) and trifluorination (teriflunomide) to the less common pentafluorination (isoflurane).

Spectral line splitting and the chemical shift range of chemical substances are a consequence of J-coupling, affecting the relative intensities, separation, and distances of peaks as a result of different J-coupling constants. ^{19}F J-coupling constants depend on the number and configuration of atoms in a molecular structure (single ^{19}F, CF_2, and CF_3) as well as the chemical environment of these ^{19}F atoms. Homonuclear ^{19}F coupling constants are usually very large compared with ^{1}H-coupling constants. In addition, heteronuclear coupling constants between ^{1}H and ^{19}F are relatively large [18]. Changes in environmental conditions might, therefore, have an effect on the different configurations of ^{19}F atoms in fluorinated compounds resulting in chemical shift changes, variations in signal intensities, or peak amplitudes as a function of the varying parameters during the measurements.

The influence of temperature on the ^{19}F NMR characteristics of pharmacological compounds containing a low number of ^{19}F atoms has not been reported so far. Here, we studied the influence of the temperature on the ^{19}F NMR characteristics of different fluorinated compounds. We analyzed the influence of temperature on the chemical shift, spectrum, signal intensity, SNR, longitudinal (spin–lattice) relaxation time (T_1) and transversal (spin–spin) relaxation time (T_2) of PFCE, the anesthetic isoflurane (Iso), the anti-inflammatory drug teriflunomide (TF), and the antipsychotic flupentixol (Flu) in phantom studies. We also studied the temperature influence on T_1 of PFCE nanoparticles in animal tissue.

Materials and methods

Temperature measurements in phantoms

Phantoms were prepared in separate 2 ml syringes using pure perfluoro-15-crown-5-ether (1.72 M; Fluorochem Ltd, Hadfield, UK), 10% (0.54 M) isoflurane (Baxter, Unterschleißheim, Germany) in dimethylsulphoxide (DMSO, Roth, Karlsruhe Germany), 100 mM teriflunomide (Sigma-Aldrich, Steinheim, Germany) in DMSO, and the flupentixoldecanoat ready to inject solution (0.169 M; in medium chain triglycerides) for the flupentixol (Fluanxol Depot 10%, Lundbeck, Copenhagen, Denmark) phantom. The number of ^{19}F atoms per voxel was calculated for each compound: PFCE = 1.9421×10^{18}, isoflurane = 3.0601×10^{17}, teriflunomide = 1.1291×10^{17}, and flupentixol = 1.34×10^{20}.

For absolute temperature measurements, a fiber optic probe (Omniflex, Neoptix, Québec, Canada) was placed in the radial center of the phantom syringes through a hole in the plunger. A water bath was used to heat the sample to the desired temperature (T = 20–60 °C in increments of 5 °C). The magnetic field interferes with the correct temperature measurements by the fiber optic probe. The temperature measured at the isocenter of the magnet (B_0 = 9.4 T) was systematically determined to be 4.7 °C lower than the actual temperature (measured outside of the magnet bore) and decreases as a function of the magnetic field strength. We measured the temperature throughout each experiment involving a temperature change. Each new experiment included a battery of MR measurements (see below) including pilot proton scans, spectroscopy, and mapping experiments with an approximate duration of 15 min. During this time, we acquired temperature measurements. Median and interquartile temperatures were calculated from these measurements using MATLAB R2016b (The MathWorks Inc., Natick, Massachusetts, USA). We used these temperature values in the plots depicting the MR variable (e.g., T_1) versus temperature. Additional to the temperature computation, the fiber optic probe information was used to assess the establishment of a stable temperature before the subsequent measurement.

Temperature measurements in tissue

Animal experiments were carried out in accordance with guidelines provided and approved by the Animal Welfare Department of the State Office of Health and Social Affairs Berlin (LAGeSo). For measuring the T_1 temperature dependency of PFCE nanoparticles in tissue, a female C57BL/6 mouse (13 g) was intraperitoneally administered with a lethal dose of ketamine and medetomidine in 0.9% NaCl in a volume of 130 µl. Upon the absence of reflexes, a fiber optic temperature probe was inserted under the skin in the neck region to measure temperature, next to the injection site of PFCE. In addition, the rectal temperature of the animal was monitored. The animal was placed on a warm animal MR bed supplied with oxygen and air, and the respiration monitored using a respiration pad. 400 µl of 1.2 M Pluronic–PFCE nanoparticles were prepared and characterized as previously described [19] and administered subcutaneously in the neck region of the mouse. T_1 was measured at 32.4 °C (temperature of the mouse after lethal anesthesia during the terminal stage) and at 23.6 °C (temperature of the mouse post mortem) using an axial slice in the neck region of the animal. The animal died during the course of the experiment through the lethal dose of the anesthetic.

MR experiments

All MR experiments were performed on a 9.4 T MR scanner (Bruker Biospec, Ettlingen, Germany) using the Paravision 6.0.1 software and a dual-tunable ^{19}F/^{1}H mouse head RF coil [3]. Reference pilot scans and anatomical images were acquired using 2D FLASH. A global single pulse spectroscopy (TR = 1000 ms, TA = 8 s) was used to detect the ^{19}F signal and to make frequency adjustments. Anatomical scans were performed using a 3D-RARE sequence (TR = 1300 ms, TE = 5.4 ms, ETL = 16, FOV = 28 mm × 16 mm × 16 mm, matrix size = 448 × 256 × 256, spatial resolution 0.06 mm isotropic, TA = 8 min 20 s, and slice thickness = 16 mm). ^{19}F imaging was performed using a 3D-RARE sequence (TR = 800 ms, TE = 3.1 ms, ETL = 26, FOV = 28 mm × 16 mm × 16 mm, matrix size = 137 × 78 × 78, spatial resolution 0.2 mm isotropic, TA = 11 min 5 s, and slice thickness = 16 mm).

T_1 mapping in phantom and in tissue experiments was performed using RARE [TE = 4.6 ms, ETL = 4, FOV = 16 mm × 16 mm, matrix size = 64 × 64, with nine variable repetitions times (TR = 25–8000 ms)]. The slice thickness and number of averages were altered according to the fluorine signal. PFCE: 1 mm, 4 m 34 s, isoflurane: 1 mm, 4 m 34 s, teriflunomide: 10 mm, 9 m 9 s, flupentixol: 6 mm, 9 m 9 s, and PFCE in tissue: 15 mm, 4 m 34 s.

T_2 mapping was also performed in phantoms using a multi-slice multi-echo sequence (MSME: TR = 2000 ms FOV = 16 mm × 16 mm, matrix size = 64 × 64) with 25 different TEs (TE = 40–1000 ms in steps of 40 ms, for flupentixol TE = 8–200 in steps of 8 ms). The slice thickness and number of averages were altered according to the fluorine signal. PFCE: 1 mm, 2 m 8 s, isoflurane: 10 mm, 4 m 16 s, teriflunomide: 7.5 mm, 17 m 4 s, and flupentixol: 7 mm, 5 m 20 s.

After each temperature change, tuning and matching of the coil as well as scanner adjustments for basic frequency, shim, and reference power were performed.

Data analysis

Image processing as well as spectral analysis and processing were performed in MATLAB R2018a (The MathWorks Inc., Natick, USA). Images from animal experiments were also analyzed and processed using ImageJ [20]. Temperature changes were recorded over time, and the calculation of median and interquartile temperatures was also performed in MATLAB.

Quantification of the spectral signal intensity was achieved by calculating the *Y*-axis intercept of the free-induction decay (FID) fit in MATLAB. Post-processing of the magnitude spectra included zero-filling of the original FID data and a line broadening of 70 Hz. Chemical shifts in ppm were calculated using the mathematical expression:

$$\delta = \frac{f_{\text{compound}} - f_{\text{reference}}}{f_{\text{reference}}} 10^6 [\text{ppm}], \tag{1}$$

where f_{compound} and $f_{\text{reference}}$ are the frequencies of the compound being investigated and the reference derived by the scanner by multiplying the ^{1}H (0 ppm) frequency with the gyromagnetic ratio of ^{19}F, respectively. Ultimately, chemical shifts of the magnitude spectra were plotted using MATLAB. The chemical shift dependency on the temperature was fitted with a linear function using MATLAB basic fitting tool.

For estimating the spin–lattice relaxation (T_1) time constant, the measured intensities were first averaged over the signal region and corrected for the non-Gaussian noise distribution in MR magnitude images [21]. Repetition times where the averaged signal (S) was below the noise standard deviation were excluded from further analysis. T_1 was determined by fitting the relation [22]:

$$S(T_{\text{R}}) \propto \left(1 - \exp\left(-\frac{T_{\text{R}}}{T_1}\right)\right), \tag{2}$$

to the obtained data points using least-squares optimization.

For T_2 mapping, the MSME data were prepared similarly as above. The data point corresponding to the shortest echo time was excluded from further analysis [23], and T_2 was determined by fitting the relation [22]:

$$S(T_{\text{E}}) \propto \exp\left(-\frac{T_{\text{E}}}{T_2}\right), \tag{3}$$

to the remaining data points using least-squares optimization.

SNRs were measured in images from the RARE sequence for T_1 mapping (TR = 4000 ms). Here, as well, the measured signal was averaged over the signal region and the obtained value was corrected for the non-Gaussian noise distribution in MR magnitude images [21]. The image noise σ was estimated by measuring the noise standard deviation in a known background region σ_{B} (Fig. 1e) and dividing by the correction factor 0.6551 appropriate for single-channel RF coil [24]. SNR was thus calculated as

$$\text{SNR} = \frac{S}{\sigma} = 0.6551 \frac{S}{\sigma_{\text{B}}}, \tag{4}$$

where S denotes the corrected signal amplitude.

All MR parameters (δ, S, SNR, T_1, and T_2) were plotted versus the measured median temperature. The coefficient of determination (r^2) was calculated for every fit and reflects the error of all MR parameters. Apart from the error for temperature measurements, we calculated the possible error for T_1 and

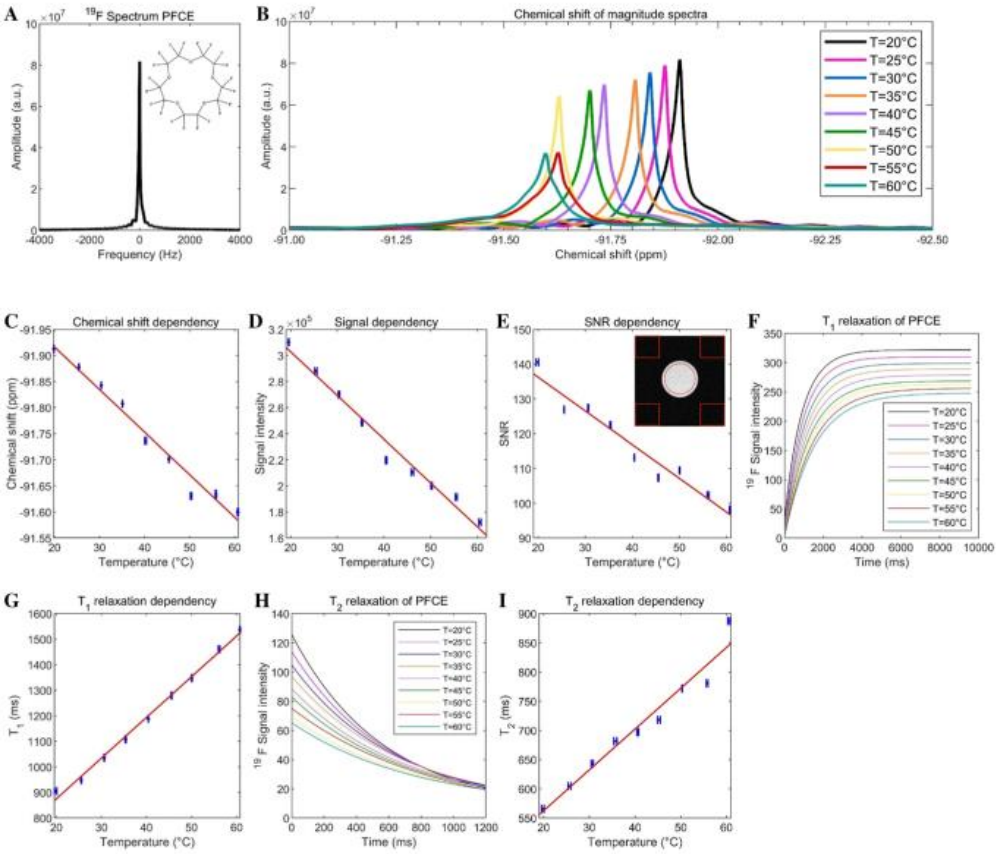

Fig. 1 Influence of the temperature on the ^{19}F NMR characteristics of PFCE; **a** ^{19}F magnitude spectrum of PFCE, **b** chemical shift dependency from the temperature (20–60 °C), **c** chemical shift dependency from the temperature and linear fitting ($r^2 = 0.98$), **d** dependency of the signal intensity from the temperature and linear fitting ($r^2 = 0.98$, graphical explanation of SNR measurement with the signal ROI in the center and four background regions at the edges of the image, **e** dependency of the SNR from the temperature and linear fitting ($r^2 = 0.97$), **f** T_1 relaxation curves of PFCE at different temperatures and mono-exponential fitting, **g** dependency of T_1 from the temperature and linear fitting ($r^2 = 0.99$), **h** T_2 relaxation curves of PFCE at different temperatures and fitting, and **i** dependency of T_2 from the temperature and linear fitting ($r^2 = 0.95$)

signal intensity. We studied isoflurane at 20 °C and measured T_1 and signal intensity ($n = 8$). The level of error (SD) for T_1 (1811 ms) was 8 ms, and the level of error for signal intensity (241,892) was 28. The level of error for temperature was relatively small (mean interquartile range = 0.17 °C, mean range = 1.02 °C).

Results

Temperature influences the ^{19}F NMR properties of PFCE, isoflurane, teriflunomide and flupentixol

We studied the temperature dependency of ^{19}F MR characteristics, namely, chemical shift, spin–lattice- and spin–spin relaxation time, signal intensity, and SNR of pure PFCE at temperatures ranging from 20 to 60 °C using

steps of 5 °C. The basic frequency was readjusted, after each temperature change. PFCE demonstrates a spectrum with a single peak (−91.9128 ppm) at room temperature (Fig. 1a). Upon varying temperature, it became evident that the chemical shift decreased with increasing temperature (Fig. 1b). The chemical shift was quantified and plotted against temperature (Fig. 1c). From the slope in the equation of the linear fit, we calculated the change in chemical shift to be +0.0082 ppm/°C with a coefficient of determination $r^2 = 0.98$. We observed a negative correlation of the signal intensity ($r^2 = 0.98$) with increasing temperatures (Fig. 1d).

Moreover, we estimated the SNR in RARE images (Fig. 1e) and observed a temperature-dependent decline of the SNR with increasing temperatures (Fig. 1e). The signal drop was determined to be 0.97 SNR units/°C ($r^2 = 0.95$).

T_1 at 20 °C was 905 ms and 1536 ms at a temperature of 60 °C. Upon varying the temperature as for the above measurements, we observed a linear dependency ($r^2 = 0.99$) of T_1 values (Fig. 1f). T_1 values at different temperature conditions were quantified and plotted against temperature (Fig. 1g). We calculated the variation in T_1 as a function of temperature to be +16 ms/°C.

We also studied T_2 of PFCE and the dependency on the temperature (Fig. 1h), ranging from 556 to 887 ms. We observed a linear increase of T_2 with increasing temperatures (7 ms/°C; $r^2 = 0.95$) (Fig. 1i).

Isoflurane was investigated at temperatures ranging from 20 °C to its boiling point of 40 °C. The pentafluorination on the isoflurane molecule results in several spin–spin couplings as shown by the multiple spectral peaks, one major peak and several minor ones (Fig. 2a). Isoflurane also demonstrated a chemical shift dependency by temperature variations, although to a lesser extent as for PFCE (Fig. 2b). The different chemical shifts were quantified and plotted against temperature (Fig. 2c). We calculated the change in the chemical shift to be +0.0025 ppm/°C ($r^2 = 0.80$). We performed an additional experiment (not shown here) to investigate the influence of the temperature on the chemical shift with shorter intervals between the measurements and found a chemical shift of +0.0031 ppm/°C with a $r^2 = 0.61$ which at least shows a trend of the chemical shift.

In the case of isoflurane, we observed a decrease in signal intensity with increasing temperatures (Fig. 2d; $r^2 = 0.99$). We observed a decrease in SNR with increasing temperature (Fig. 2e) with an SNR drop of 0.085 SNR units/°C ($r^2 = 0.54$).

T_1 was found to be 1851 ms at 20 °C, and this increased to 2491 ms at temperature of 40 °C (Fig. 2f). From the linear dependency of T_1 on temperature ($r^2 = 0.95$), we calculated T_1 change of +30 ms/°C (Fig. 2g).

T_2 mapping of isoflurane at varying temperatures (Fig. 2h) revealed a linear increase of T_2 (11 ms/°C; $r^2 = 0.98$) (Fig. 2i) from 922 ms at 20 °C to 1154 ms at 40 °C.

Teriflunomide is an anti-inflammatory compound that has a trifluoromethyl moiety; this side group is commonly included during drug design to improve the pharmacological properties [25] of the parent drug. Trifluoromethyl moieties provide a single non-coupled signal [18]. Indeed, teriflunomide demonstrates a spectrum with a single peak (−58.0764 ppm) at room temperature (Fig. 3a). The ^{19}FMR properties of this drug were also studied at temperatures ranging from 20 to 60 °C. The chemical shifts (Fig. 3b) were quantified and plotted against temperature showing a linear correlation ($r^2 = 0.96$) with a change in chemical shift of −0.0038 ppm/°C (Fig. 3c). In addition, we observed a negative correlation ($r^2 = 0.99$) of signal intensity and temperatures (Fig. 3d) as well as a negative correlation ($r^2 = 0.96$) with an SNR drop of 0.071 SNR units/°C (Fig. 3e).

T_1 at 20 °C was found to be 1023 ms, ranging to 1307 ms at 60 °C, demonstrating a linear correlation ($r^2 = 0.99$) at varying temperatures (Fig. 3e) and a calculated change in T_1 of +6.6 ms/°C (Fig. 3f). T_2 was studied in the range of 20–60 °C (Fig. 3h) and revealed a linear increase of T_2 of 4.9 ms/°C ($r^2 = 0.96$) until a temperature of 35 °C and drops again (Fig. 3i).

A second drug with a trifluoromethyl moiety, the antipsychotic flupentixol was also investigated. Similar to teriflunomide, it showed a single-peak spectrum (−58.8807 ppm) at room temperature (Fig. 4a). Similar to teriflunomide, we observe a negative chemical shift at varying temperatures (Fig. 4b) of −0.0026 ppm/°C and a coefficient of determination of $r^2 = 0.85$ (Fig. 4c). Furthermore, we observed a linear dependency of the signal intensity (FID) from temperature changes ($r^2 = 0.99$; Fig. 4d). The SNR also showed a linear dependency from temperature (−0.04 SNR units/°C; $r^2 = 0.94$) (Fig. 4e).

We measured T_1 of 698 ms at 20 °C increasing to 762 ms at 60 °C (Fig. 4f). There is a linear correlation ($r^2 = 0.62$) with a T_1 increase of 1.3 ms/°C (Fig. 4g). We also studied T_2 in this temperature range with T_2 values from 117 to 421 ms at 60 °C. We found a positive linear correlation of T_2 and temperature with a T_2 increase of 7.4 ms/°C ($r^2 = 0.97$) (Fig. 4i).

Overall, isoflurane showed the strongest dependency of T_1 from temperature changes ($\Delta T_1 = +30$ ms/°C) and also the strongest dependency of T_2 from temperature changes ($\Delta T_2 = +11$ ms/°C). Teriflunomide and flupentixol both showed similar chemical shift behavior. All compounds studied showed an increase of T_1 and T_2 with increasing temperature, except teriflunomide, which shows first an increase, followed by a decrease in T_2.

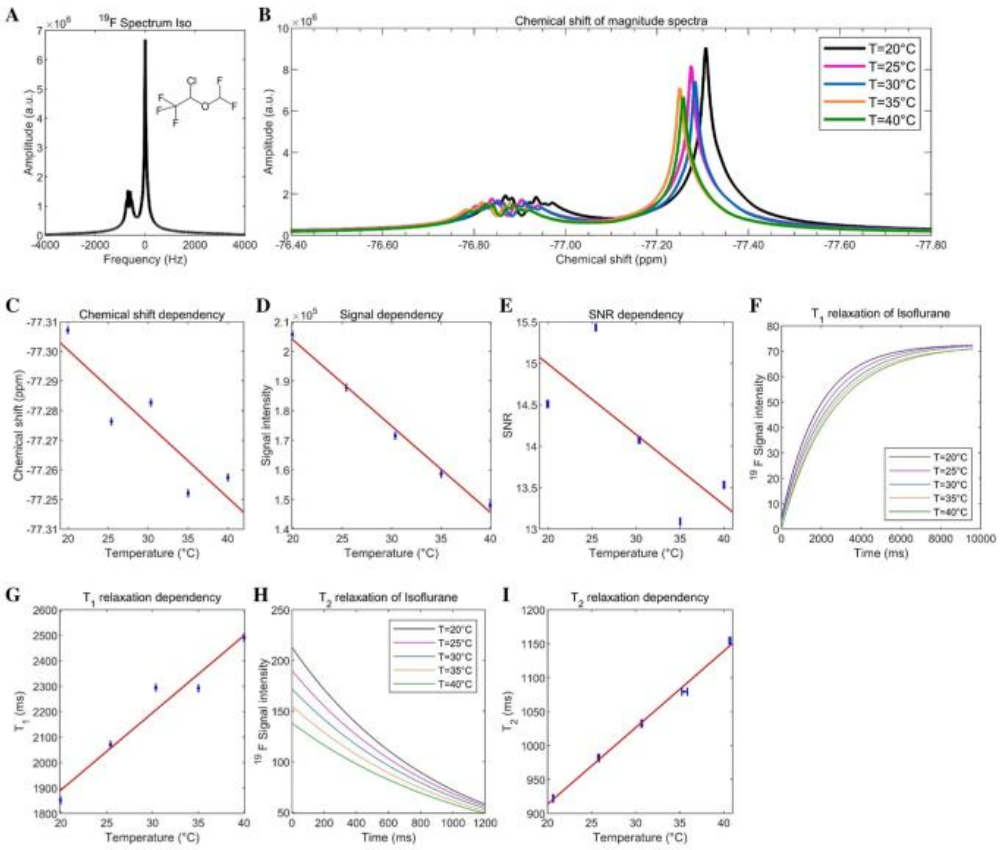

Fig. 2 Influence of the temperature on the ^{19}F NMR characteristics of isoflurane; **a** ^{19}F magnitude spectrum of isoflurane, **b** chemical shift dependency from the temperature (20–40 °C), **c** chemical shift dependency from the temperature and linear fitting ($r^2 = 0.80$), **d** dependency of the signal intensity from the temperature and linear fitting ($r^2 = 0.99$), **e** dependency of the SNR from the temperature and linear fitting ($r^2 = 0.54$), **f** T_1 relaxation curves of isoflurane at different temperatures and mono-exponential fitting, **g** dependency of T_1 from the temperature and linear fitting ($r^2 = 0.95$), **h** T_2 relaxation curves of isoflurane at different temperatures and fitting, and **i** dependency of T_2 from the temperature and linear fitting ($r^2 = 0.98$)

Changes in ^{19}F spin–lattice relaxation of PFCE nanoparticles in tissue

PFCE was also studied in tissue by measuring T_1 at body temperature (after lethal anesthesia during the terminal stage) as well as at room temperature (post mortem) (Fig. 4). For this, a female C57BL/6 mouse was given a lethal dose of anesthetic, after which PFCE nanoparticles were injected subcutaneously in the neck region at the scanner and a 3D RARE MR measurement was performed to validate the correct positioning and successful injection and distribution of PFCE nanoparticles (Fig. 4b). The rectal temperature and temperature in the neck region were controlled over time. T_1 mapping was performed at a temperature of 32.4 °C in the neck region. This revealed T_1 of 1325 ms. The T_1 observed at room temperature (23.6 °C) was 1149 ms, representing a reduction of 13% in T_1 at 23.6 °C compared to 32.4 °C (Fig. 4c).

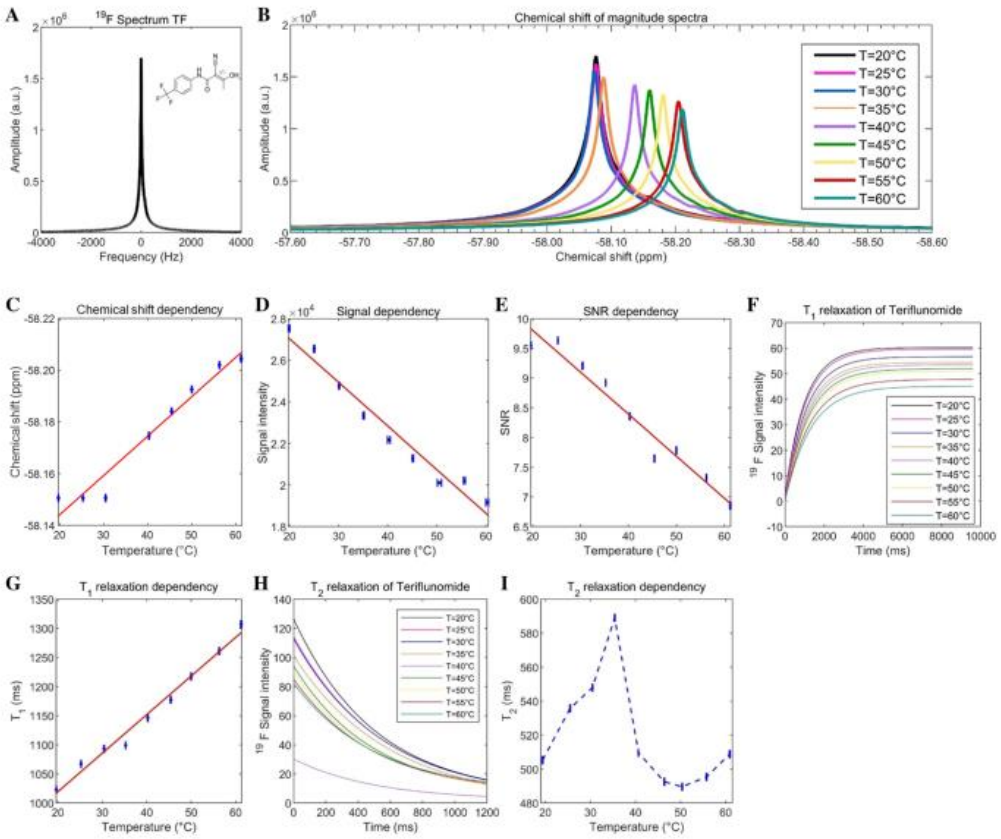

Fig. 3 Influence of the temperature on the ^{19}F NMR characteristics of teriflunomide; **a** ^{19}F magnitude spectrum of teriflunomide, **b** chemical shift dependency from the temperature (20–60 °C), **c** chemical shift dependency from the temperature and linear fitting ($r^2 = 0.96$), **d** dependency of the signal intensity from the temperature and linear fitting ($r^2 = 0.99$), **e** dependency of the SNR from the temperature and linear fitting ($r^2 = 0.96$), **f** T_1 relaxation curves of teriflunomide at different temperatures and mono-exponential fitting, **g** dependency of T_1 from the temperature and linear fitting ($r^2 = 0.99$), **h** T_2 relaxation curves of teriflunomide at different temperatures and fitting, and **i** dependency of T_2 from the temperature

Discussion

En route to ^{19}F MR-based thermometry, we investigated the influence of temperature on both the spin–lattice and spin–spin relaxation times, chemical shift, signal intensity and SNR of PFCE, isoflurane, teriflunomide, and flupentixol. We also examined changes in T_1 relaxation of PFCE nanoparticles under postmortem conditions.

The spin–lattice relaxation time of PFCE and of the fluorinated drugs isoflurane, teriflunomide, and flupentixol increased as a function of temperature. The same was true for the spin–spin relaxation times of PFCE, isoflurane and flupentixol. Higher temperatures resulted in longer T_1 and T_2 values. One exception was found at T_2 of teriflunomide which decreased from a temperature of 35 °C on. The degree of influence varied between each substance, as can be seen by the degree of T_1 and T_2 change per unit temperature. Isoflurane showed the largest degree of T_1 change (30 ms/°C) and flupentixol the smallest (1.3 ms/°C). Isoflurane also showed the largest degree of T_2 change (11 ms/°C). This is to be expected due to the different chemical properties of the investigated compounds, their concentration as well as the number of ^{19}F atoms on their molecular structure. Chemical modifications of substances

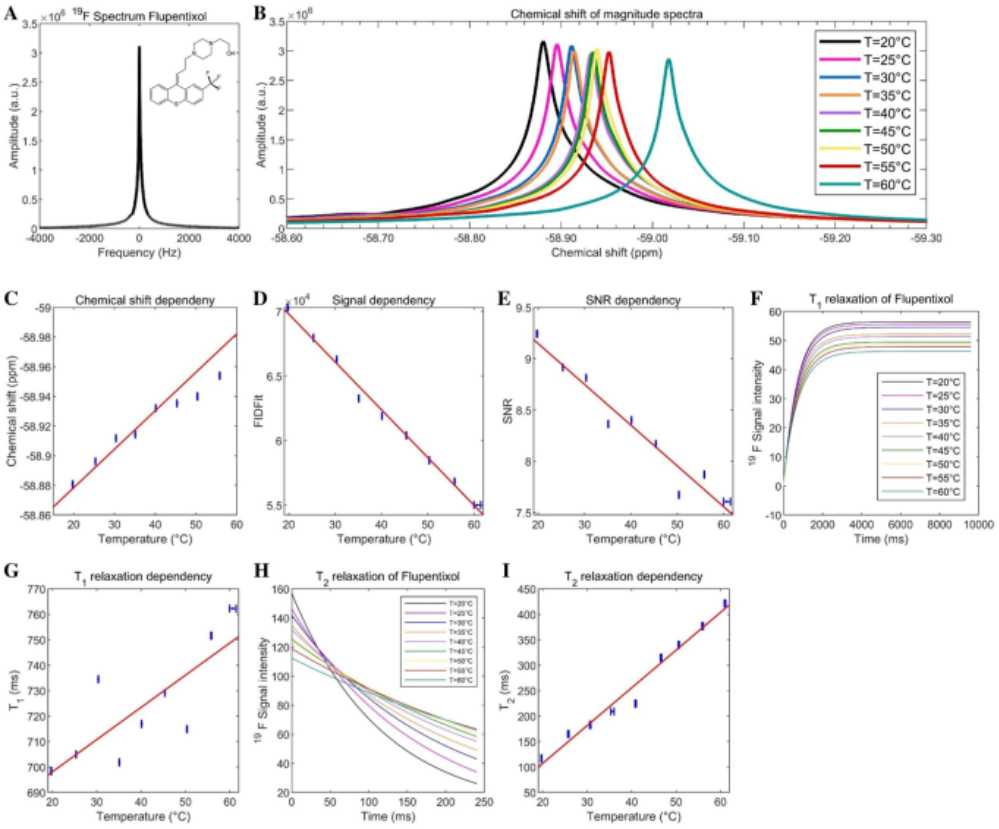

Fig. 4 Influence of the temperature on the ^{19}F NMR characteristics of flupentixol; **a** ^{19}F magnitude spectrum of flupentixol, **b** chemical shift dependency from the temperature (20–60 °C), **c** chemical shift dependency from the temperature and linear fitting (r^2=0.85), **d** dependency of the signal intensity from the temperature and linear fitting (r^2=0.99), **e** dependency of the SNR from the temperature and linear fitting (r^2=0.94), **f** T_1 relaxation curves of flupentixol at different temperatures and mono-exponential fitting, **g** dependency of T_1 from the temperature and linear fitting (r^2=0.62), **h** T_2 relaxation curves of flupentixol at different temperatures and fitting, and **i** dependency of T_2 from the temperature and linear fitting (r^2=0.97)

might change their relaxation time, but also their susceptibility to environmental influences [17].

The linear correlation between T_1 values and temperature demonstrated here for PFCE is in line with a previous study by Kadayakkara et al. [17], and the correlation for a different perfluorocarbon (PFPE) was described as a third degree polynomial function. Here, we found a linear correlation for all four compounds investigated.

Since we observe a marginal error from the temperature measurements (see "Methods"), we believe that the deviation of T_1 values from the fitting curve is due to the T_1 mapping itself. The coefficient of determination was calculated for every fit and reflects the T_1 error.

An influence of the temperature on the relaxation times has been assumed in the past [4], and there is evidence for this; however, to our knowledge, a systematic study of pharmacological substances other than PFCE has never been published.

The influence of temperature on the chemical shift varied between the four investigated fluorine compounds. While teriflunomide and flupentixol both showed an increased chemical shift, both the shift in ppm for PFCE and isoflurane decreased with increasing temperature. The fluorine compounds were also distinguishable by the extent of their susceptibility toward the temperature-induced chemical shift, with PFCE displaying the largest shift range. One reason for

this variation in chemical shift is due to J-coupling effects, which will differ between compounds due to differences in the number of ^{19}F atoms as well as the position of the ^{19}F atoms on the molecule.

Differences in the configuration of fluorine containing groups and different chemical environments will result in different possible inter- and intramolecular interaction. This could explain the observed differences in chemical shifts and in the shapes of the spectra upon changing the temperature of the environment. The orientation of the ^{19}F groups relative to other molecules or chemical groups on the molecular structure will have an impact on these inter- and intramolecular interactions. Due to differences in these configurations and electron distributions, different shielding effects will lead to different MR behaviors [26]. Varying temperatures lead to an increase in the molecular tumbling rate of a molecule in a certain environment which defines the time of relaxation [27]. Dipole–dipole interactions mostly determine spin–lattice relaxation. With varying temperatures, internuclear distances and dynamics of molecular motions, and the reorientation of structures change, this results in a change in T_1. Spin–spin relaxation depends on the anisotropy of the fluorine chemical shift (CSA). The electron configuration of a molecule determines the movement of electrons and the behavior in different molecular orientations. When placed into a magnetic field, this configuration decides the orientation of movement, which is not equal for all direction, thus anisotropic. Motions cause oscillations of the local magnetic field, and these time-varying fields lead to relaxation [26].

The different behaviors in the chemical shift might also be explained by the presence of the trifluoromethyl moiety in teriflunomide and flupentixol. Both show a covalent link to a benzene moiety which results in a delocalization of electrons (Figs. 3a, 4a). In spectroscopy, both drugs are characterized by only one peak in ^{19}F MRS. The trifluoromethyl moiety is not present in either PFCE or isoflurane, and this chemical configuration could be one explanation for the differences in chemical shifts ^{19}F MR characteristics.

The overall chemical shift range of isoflurane appeared to be the smallest of all compounds studied. We observed an alternation of the data points from the linear fit. The reason for these fluctuations in the chemical shift might be the several resonances of the compound in difference to compounds demonstrating a single peak.

In addition, the shape of the PFCE spectrum changed with increasing temperatures, as can be seen in a broadening of the ^{19}F peak (Fig. 1b). This was not the case for teriflunomide and flupentixol when measuring the peak width at half maximum. In cases where a line broadening occurs for pharmacological compounds at body temperature, a better understanding of such changes in the ^{19}F MR properties will be necessary to identify and distinguish the drug from its metabolites; the latter might have different susceptibilities to temperature. In such cases, further phantom experiments will be required for the drug metabolites to be able to separate their peaks from those of the main compound in tissue.

Changes in temperature caused changes in signal intensity. The reason for a decrease in the signal intensity in PFCE, isoflurane, teriflunomide, and flupentixol with increasing temperature could be explained by the longer T_1 values occurring at higher temperatures. Signal intensity is also influenced by the spin–spin relaxation time T_2. For all compounds studied, we observed a drop in SNR with increasing temperatures which can be explained by the longer T_1, while using the same scan parameters for each temperature step results in a prolonged time to complete relaxation and loss in SNR.

In this study, we observed the same trend in T_1 changes with varying temperature for all investigated ^{19}F compounds. This might not hold true for trends in T_2 values. Colotti et al. [15] showed that both T_1 and T_2 values of PFCE increase with temperature; however, in this study, only two temperatures (24 °C and 37 °C) were investigated. In this study, we could show that an increasing temperature does not necessarily result in a linear increase in T_2. In the case of teriflunomide, this holds true for the range of 20–35 °C with a maximum T_2 at the physiologic temperature in animal studies. In future studies, it would be valuable to look closer at specific temperature ranges such as those found in vivo. In this study, we used temperature increments of 5 °C; smaller temperature steps might offer more detailed information into the actual relationship between temperature and the MR parameter investigated. Furthermore, it might be valuable to investigate changes in the T_1/T_2 ratio as a function of temperature to draw conclusions on the overall influence of relaxation times on the MR signal. In an ideal experiment, a short T_1 and a long T_2 are desirable to achieve a maximum SNR.

Moving to animal studies, one notices that findings from phantom studies are not always reflected in vivo. Due to movement artifacts, limitations in shimming procedures and also different chemical environments (e.g., intracellular or extracellular locations, proximity to different types of tissue or body fluid with different chemical consistency and pH, as well as small temperature gradients in the anatomical regions) deviations from phantom data are to be expected. This can be reflected by the two narrow peaks in the ^{19}F MRS for PFCE during experiments in tissue (Fig. 5a), in contrast to the expected single peak from the phantom studies (Fig. 1a). Therefore, even though bandwidths are chosen large enough, a detailed knowledge about low fluorinated drug molecules at low concentrations in the body is essential.

In conclusion, our results show that lower temperatures are favorable to achieve the highest ^{19}F MR signal intensity

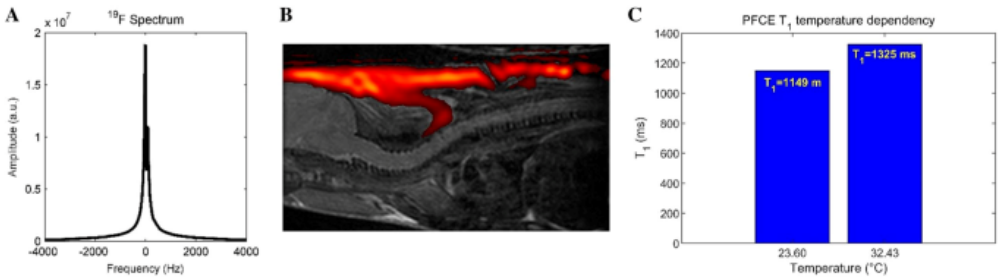

Fig. 5 Influence of the temperature on T_1 of PFCE nanoparticles in animal tissue; **a** ^{19}F Spectrum of PFCE in tissue, **b** overlay of a sagittal anatomical ^{1}H image (3D-RARE) showing the neck region of a mouse and a ^{19}F image (3D-RARE) indicating the injected PFCE nanoparticle emulsion; the fluorine data was thresholded at SNR = 3.5 and we removed all groups of less than three connected signal voxels, and **c** measurement of T_1 of PFCE nanoparticles in tissue

and detect PFCE, isoflurane, teriflunomide, and flupentixol. The signal intensity of these compounds decreased with increasing temperature. Therefore, it will be more challenging to detect these compounds at physiological temperatures. While this could hinder the detection of pharmacological compounds present at low concentrations in vivo, it indicates the necessity of more ex vivo studies to study these compounds more thoroughly.

We chose a broad range of compounds with different clinical indication and application. We studied the widely used cell-labeling contrast agent PFCE, the standard anesthetic for animal experiment isoflurane commonly used in ^{19}F studies, as well as two therapeutic agents with a trifluoromethyl moiety. Particularly, for compounds such as teriflunomide and flupentixol that suffer from a low ^{19}F content and a potentially low availability following administration, understanding their ^{19}F MR characteristics will be crucial to image them in vivo. From the ^{19}F MR characteristics, one can deduce the best sequence/s that can be used and adjust them with the optimal scan parameters. This will improve the SNR efficiency substantially and thereby allow detection of lower amount of these ^{19}F compounds.

Especially, for pharmacological substances, it will be particularly crucial to understand how temperature might influence the MR measurement. These influences should be taken into consideration when optimizing the ^{19}F MR signal per unit time. Since increasing temperatures lengthen T_1 of ^{19}F compounds, it might also be useful to implement strategies that shorten T_1 to compensate for the increase in T_1 in vivo, e.g., by introducing T_1-shortening contrast agents. By decreasing T_1, the number of averages achievable during the same measurement time can be increased to boost the expected ^{19}F MR signal. Other strategies to increase the sensitivity of ^{19}F MR are to promote higher SNR using ultrahigh and extreme magnetic field technology [28–30], cryogenically cooled probes [31], improved MR methods [32], and accelerated acquisition techniques such as compressed sensing [33]. These entire efforts combined will make ^{19}F MR a powerful technique for studying biological processes and monitoring drug therapies. Especially valuable for targeted therapy, the adapted fluorine-19 MR methods will be central for visualizing and quantifying MR sensitive probes after release from thermo-sensitive nanocarriers via targeted radio-frequency-induced heating. In these studies, adapted fluorine-^{19} MR methods will be crucial to study and quantify the spatiotemporal release characteristics of the pay load. The benefits of these studies are in positive alignment with the needs for explorations into the potential of ^{19}F MR for the in vivo assessment of the efficacy of thermal interventions.

Acknowledgements CP would like to thank Yiyi Ji for helpful discussions on thermometry. TN wishes to acknowledge the support provided by the European Research Council (ERC advanced Grant, ThermalMR, EU project 743077). SW wishes to acknowledge the support provided by the Germany Research Council (DFG WA2804).

Author contributions Study conception and design: CP, PR, TE, TN, and SW. Acquisition of data: CP, TE, LS, and SW. Drafting of manuscript: CP, PR, TE, LS, TN, and SW. Critical revision: CP, PR, TE, LS, TN, and SW.

Funding This study was funded (in part) by the Deutsche Forschungsgemeinschaft to SW (DFG WA2804). TN received funding from the European Research Council (ERC advanced Grant, ThermalMR, EU project 743077).

Compliance with ethical standards

Conflict of interest Thoralf Niendorf is founder and CEO of MRI. TOOLS GmbH, Berlin, Germany.

Statement of human/animal rights All animal experiments were conducted in accordance with procedures approved by the Animal Welfare

Department of the State Office of Health and Social Affairs Berlin (LAGeSo), and conformed to national and international guidelines to minimize discomfort to animals (86/609/EEC).

References

1. Schmieder AH, Caruthers SD, Keupp J, Wickline SA, Lanza GM (2015) Recent advances in 19Fluorine magnetic resonance imaging with perfluorocarbon emulsions. Engineering (Beijing, China) 1(4):475–489
2. Ahrens ET, Flores R, Xu H, Morel PA (2005) In vivo imaging platform for tracking immunotherapeutic cells. Nat Biotechnol 23(8):983–987
3. Waiczies H, Lepore S, Drechsler S, Qadri F, Purfürst B, Sydow K, Dathe M, Kühne A, Lindel T, Hoffmann W, Pohlmann A, Niendorf T, Waiczies S (2013) Visualizing brain inflammation with a shingled-leg radio-frequency head probe for 19F/1H MRI. Sci Rep 3:1280
4. Ruiz-Cabello J, Barnett BP, Bottomley PA, Bulte JW (2011) Fluorine (19F) MRS and MRI in biomedicine. NMR Biomed 24(2):114–129
5. Karson CN, Newton JE, Livingston R, Jolly JB, Cooper TB, Sprigg J, Komoroski RA (1993) Human brain fluoxetine concentrations. J Neuropsychiatry Clin Neurosci 5(3):322–329
6. Karson CN, Newton JE, Mohanakrishnan P, Sprigg J, Komoroski RA (1992) Fluoxetine and trifluoperazine in human brain: a 19F-nuclear magnetic resonance spectroscopy study. Psychiatry Res 45(2):95–104
7. Komoroski RA, Newton JE, Cardwell D, Sprigg J, Pearce J, Karson CN (1994) In vivo 19F spin relaxation and localized spectroscopy of fluoxetine in human brain. Magn Reson Med 31(2):204–211
8. Bolo NR, Hode Y, Nedelec JF, Laine E, Wagner G, Macher JP (2000) Brain pharmacokinetics and tissue distribution in vivo of fluvoxamine and fluoxetine by fluorine magnetic resonance spectroscopy. Neuropsychopharmacology 23(4):428–438
9. Ji Y, Waiczies H, Winter L, Neumanova P, Hofmann D, Rieger J, Mekle R, Waiczies S, Niendorf T (2015) Eight-channel transceiver RF coil array tailored for (1)H/(1)(9)F MR of the human knee and fluorinated drugs at 7.0 T. NMR Biomed 28(6):726–737
10. Desmoulin F, Gilard V, Malet-Martino M, Martino R (2002) Metabolism of capecitabine, an oral fluorouracil prodrug: (19) F NMR studies in animal models and human urine. Drug Metab Dispos 30(11):1221–1229
11. Doi Y, Shimmura T, Kuribayashi H, Tanaka Y, Kanazawa Y (2009) Quantitative (19)F imaging of nmol-level F-nucleotides/-sides from 5-FU with T(2) mapping in mice at 9.4T. Magn Reson Med 62(5):1129–1139
12. Cron GO, Beghein N, Ansiaux R, Martinive P, Feron O, Gallez B (2008) 19F NMR in vivo spectroscopy reflects the effectiveness of perfusion-enhancing vascular modifiers for improving gemcitabine chemotherapy. Magn Reson Med 59(1):19–27
13. Morikawa S, Inubushi T, Morita M, Murakami K, Masuda C, Maki J, Tooyama I (2007) Fluorine-19 fast recovery fast spin echo imaging for mapping 5-fluorouracil. Magn Reson Med Sci 6(4):235–240
14. Reid DG, Murphy PS (2008) Fluorine magnetic resonance in vivo: a powerful tool in the study of drug distribution and metabolism. Drug Discov Today 13(11–12):473–480
15. Colotti R, Bastiaansen JAM, Wilson A, Flögel U, Gonzales C, Schwitter J, Stuber M, van Heeswijk RB (2017) Characterization of perfluorocarbon relaxation times and their influence on the optimization of fluorine-19 MRI at 3 tesla. Magn Reson Med 77(6):2263–2271
16. Berkowitz BA, Handa JT, Wilson CA (1992) Perfluorocarbon temperature measurements using 19F NMR. NMR Biomed 5(2):65–68
17. Kadayakkara DK, Damodaran K, Hitchens TK, Bulte JW, Ahrens ET (2014) (19)F spin-lattice relaxation of perfluoropolyethers: dependence on temperature and magnetic field strength (7.0–14.1T). J Magn Reson 242:18–22
18. Dolbier WR (2016) Guide to fluorine NMR for organic chemists. Wiley, New York
19. Waiczies S, Lepore S, Sydow K, Drechsler S, Ku MC, Martin C, Lorenz D, Schutz I, Reimann HM, Purfurst B, Dieringer MA, Waiczies H, Dathe M, Pohlmann A, Niendorf T (2015) Anchoring dipalmitoyl phosphoethanolamine to nanoparticles boosts cellular uptake and fluorine-19 magnetic resonance signal. Sci Rep 5:8427
20. Schindelin J, Arganda-Carreras I, Frise E, Kaynig V, Longair M, Pietzsch T, Preibisch S, Rueden C, Saalfeld S, Schmid B, Tinevez JY, White DJ, Hartenstein V, Eliceiri K, Tomancak P, Cardona A (2012) Fiji: an open-source platform for biological-image analysis. Nat Methods 9(7):676–682
21. Henkelman RM (1985) Measurement of signal intensities in the presence of noise in MR images. Med Phys 12(2):232–233
22. Haacke E (1999) Magnetic resonance imaging: physical principles and sequence design. Wiley-Liss, New York
23. Ben-Eliezer N, Sodickson DK, Block KT (2015) Rapid and accurate T_2 mapping from multi-spin-echo data using Bloch-simulation-based reconstruction. Magn Reson Med 73(2):809–817
24. National Electrical Manufacturers A (2001) Determination of signal-to-noise ratio (SNR) in diagnostic magnetic resonance imaging. NEMA Standards Publication MS 1-2001
25. Niendorf T, Ji Y, Waiczies S (2016) Fluorinated natural compounds and synthetic drugs. In: Ahrens ET, Flögel U (eds) Fluorine magnetic resonance imaging. Pan Stanford Publishing, Singapore, pp 311–344
26. Gerig J (2001) Fluorine NMR
27. Bushberg JT (2002) The essential physics of medical imaging. lippincott. Williams & Wilkins, Philadelphia
28. Sinnecker T, Kuchling J, Dusek P, Dörr J, Niendorf T, Paul F, Wuerfel J (2015) Ultrahigh field MRI in clinical neuroimmunology: a potential contribution to improved diagnostics and personalised disease management. EPMA J 6(1):16
29. Niendorf T, Schulz-Menger J, Paul K, Huelnhagen T, Ferrari VA, Hodge R (2017) High field cardiac magnetic resonance imaging: a case for ultrahigh field cardiac magnetic resonance. Circ Cardiovasc Imaging 10:(6)
30. Niendorf T, Barth M, Kober F, Trattnig S (2016) From ultrahigh to extreme field magnetic resonance: where physics, biology and medicine meet. Magma (New York, NY) 29(3):309–311
31. Waiczies S, Millward JM, Starke L, Delgado PR, Huelnhagen T, Prinz C, Marek D, Wecker D, Wissmann R, Koch SP, Boehm-Sturm P, Waiczies H, Niendorf T, Pohlmann A (2017) Enhanced fluorine-19 MRI sensitivity using a cryogenic radiofrequency probe: technical developments and ex vivo demonstration in a mouse model of neuroinflammation. Sci Rep 7(1):9808
32. Faber C, Schmid F (2016) Pulse sequence considerations and schemes. In: Ahrens ET, Flögel U (eds) Fluorine magnetic resonance imaging. Pan Stanford Publishing, Singapore, pp 3–27
33. Zhong J, Mills PH, Hitchens TK, Ahrens ET (2013) Accelerated fluorine-19 MRI cell tracking using compressed sensing. Magn Reson Med 69(6):1683–1690

8 Publikation 2: In vivo detection of teriflunomide-derived fluorine signal using fluorine MR spectroscopy

Theranostics 2021, Vol. 11, Issue 6 2490

IVYSPRING INTERNATIONAL PUBLISHER

Theranostics

2021; 11(6): 2490-2504. doi: 10.7150/thno.47130

Research Paper

In vivo detection of teriflunomide-derived fluorine signal during neuroinflammation using fluorine MR spectroscopy

Christian Prinz[1,2], Ludger Starke[1], Jason M. Millward[1,2], Ariane Fillmer[3], Paula Ramos Delgado[1,2], Helmar Waiczies[4], Andreas Pohlmann[1], Michael Rothe[5], Marc Nazaré[6], Friedemann Paul[2,7], Thoralf Niendorf[1,2] and Sonia Waiczies [1,2]✉

1. Berlin Ultrahigh Field Facility (B.U.F.F.), Max Delbrück Center for Molecular Medicine, Berlin, Germany.
2. Experimental and Clinical Research Center, a joint cooperation between the Charité - Universitätsmedizin Berlin and the Max Delbrück Center for Molecular Medicine in the Helmholtz Association, Berlin, Germany.
3. Physikalisch-Technische Bundesanstalt (PTB), Berlin, Germany.
4. MRI TOOLS GmbH, Berlin, Germany.
5. Lipidomix GmbH, Berlin, Germany.
6. Medicinal Chemistry, Leibniz-Institut für Molekulare Pharmakologie (FMP), Berlin, Germany.
7. Charité – Universitätsmedizin Berlin, corporate member of Freie Universität Berlin, Humboldt-Universität zu Berlin, and Berlin Institute of Health (BIH), Berlin, Germany.

✉ Corresponding author: Dr. Sonia Waiczies, Berlin Ultrahigh Field Facility (B.U.F.F.), Max Delbrück Center for Molecular Medicine (MDC) in the Helmholtz Association, Robert-Rössle-Str. 10 | D-13125 Berlin-Buch; E-mail: sonia.waiczies@mdc-berlin.de.

Received: 2020.04.17; Accepted: 2020.11.17; Published: 2021.01.01

Abstract

Background: Magnetic resonance imaging (MRI) is indispensable for diagnosing neurological conditions such as multiple sclerosis (MS). MRI also supports decisions regarding the choice of disease-modifying drugs (DMDs). Determining *in vivo* tissue concentrations of DMDs has the potential to become an essential clinical tool for therapeutic drug monitoring (TDM). The aim here was to examine the feasibility of fluorine-19 (^{19}F) MR methods to detect the fluorinated DMD teriflunomide (TF) during normal and pathological conditions.

Methods: We used ^{19}F MR spectroscopy to detect TF in the experimental autoimmune encephalomyelitis (EAE) mouse model of multiple sclerosis (MS) *in vivo*. Prior to the *in vivo* investigations we characterized the MR properties of TF *in vitro*. We studied the impact of pH and protein binding as well as MR contrast agents.

Results: We could detect TF *in vivo* and could follow the ^{19}F MR signal over different time points of disease. We quantified TF concentrations in different tissues using HPLC/MS and showed a significant correlation between *ex vivo* TF levels in serum and the *ex vivo* ^{19}F MR signal.

Conclusion: This study demonstrates the feasibility of ^{19}F MR methods to detect TF during neuro-inflammation *in vivo*. It also highlights the need for further technological developments in this field. The ultimate goal is to add ^{19}F MR protocols to conventional ^{1}H MRI protocols in clinical practice to guide therapy decisions.

Key words: MRI, MRS, Fluorine, Teriflunomide, Magnetic Resonance Spectroscopy, experimental autoimmune encephalomyelitis, Multiple Sclerosis

Introduction

Multiple sclerosis (MS) is a chronic inflammatory disease of the central nervous system (CNS) [1, 2]. The disease course is highly variable, involving a wide spectrum of neurological and motoric symptoms [3]. Most patients show a relapsing and remitting (RRMS) disease course, which ultimately transitions to a progressive phase [2, 4].

^{1}H Magnetic resonance imaging (^{1}H MRI) has been indispensable for diagnosing MS [5-7]. ^{1}H MRI can distinguish chronic from active lesions when using contrast agents to reveal blood brain barrier (BBB) disruptions [8-11]. Furthermore, MRI has been

vital for making safe informed decisions with respect to disease modifying drugs (DMDs) [12, 13] to ensure a better dampening of disease activity [14]. Typically, T_2 lesion load [15, 16] and brain atrophy [16] are used as outcome measures, especially during clinical studies. These MRI endpoints are commonly used as primary and secondary measures in phase II DMD trials involving large amounts of patients [17]. Despite the substantial armamentarium of DMDs available for MS [18-20], predicting treatment outcomes and tailoring DMD dosages to treatment objectives for individual patients poses a major unmet clinical need [21-23]. DMDs may need to traverse the BBB, to modify inflammatory responses within the CNS or to reduce neurodegeneration [24].

Currently there are no standard clinical methods to non-invasively monitor the distribution of drugs in patients. However, the possibility to quantify the concentration of drugs in the brain would greatly improve the assessment of individual treatment responses [22]. Drug levels are typically measured in blood, urine, saliva, and infrequently cerebrospinal fluid (CSF). However, drug levels in these fluids do not reliably reflect concentrations within the CNS. Imaging techniques such as positron emission tomography (PET) and single-photon emission computed tomography (SPECT) are used to detect drugs labeled with a radioisotope; these imaging methods are highly sensitive and are particularly useful in phase I clinical studies for small cohorts of human subjects [25-29]. However, they are not used for standard drug monitoring in patients; disadvantages include high costs, the necessity to inject radioactive compounds, restricted observation window due to short radiotracer half-life (^{18}F $t_{1/2}$ = 110 min), and a lack of distinction between drugs and their metabolites.

One third of all approved drugs are fluorinated, and are potentially detectable by fluorine-19 (^{19}F) MRI *in vivo* [30-32]. The amount of ^{19}F atoms endogenously present in the human body that can be detected with MR methods is negligible. The absence of background signal makes the ^{19}F nucleus a unique and highly attractive biomarker for detecting administered fluorinated DMDs *in vivo* using ^{19}F-MR methods. ^{19}F MR methods have been applied to detect fluorinated drugs in animal [33-38] and human studies [39-45] in the past. They have also been applied in combination with drugs encapsulated in fluorine rich nanoparticles to monitor the efficacy of these therapies in animal models [46]. ^{19}F-MR methods have also been employed in diagnostic imaging [47], for guiding tumor ablation therapies [48], and for imaging intracellular therapeutic targeting [49]. However, they remain under-utilized for the majority of drugs, especially in MS.

Teriflunomide (TF) is an anti-inflammatory DMD approved for use in MS that contains a trifluoromethyl group [50]. TF is administered orally once-daily and has a rapid, complete absorption with a long half-life (> 2 weeks) due to extensive enterohepatic recycling [51]. In RRMS patients, it reduces the annual relapse rate, slows disability progression, reduces the lesion volume [51, 52] and brain volume loss [53]. TF has a high tolerability and low discontinuation rate [50, 54]. TF was investigated in preclinical studies using the animal model of MS, experimental autoimmune encephalomyelitis (EAE) [55-57]. In rats, TF administration at EAE onset reduced disease severity and delayed progression [55, 57]. TF treatment delayed EAE onset in SJL/J mice, and suppressed disease entirely in C57BL/6 mice.

In this study we used ^{19}F MR spectroscopy to study the possibility of detecting TF during EAE *in vivo*. We characterized the MR properties of TF *in vitro*, studying the impact of pH, protein binding, and MR contrast agents. We demonstrated the feasibility of ^{19}F MR methods to detect TF non-invasively during neuroinflammation, with the ultimate goal for further development into future clinical applications.

Methods

Teriflunomide

Teriflunomide (TF) (Sanofi-Genzyme, Bridgewater, US) was formulated in 0.6% carboxymethylcellulose, sodium salt (CMC, Sigma, Schnelldorf, Germany) in the form of a suspension for *in vivo* use. CMC is an inactive ingredient used as thickening excipient, stabilizer and suspending agent. TF (20 mg) was mixed with 5 mL CMC/Tween-80 (0.6% CMC, 0.5% Tween-80 in water) using medium speed magnetic stirring (circa 24 h at RT) until a uniform milky suspension was obtained. The suspension was transferred to a clean glass vial and the original vial rinsed with a further 5 mL of CMC/Tween-80. The TF suspension (2 mg/mL) was adjusted to a pH of 7 using HCl and NaOH. For phantom experiments, TF was prepared in CMC, DMSO and human serum to study the effects of protein binding.

Animals

Dark Agouti rats (n = 2, Janvier Labs, Le Genest-Saint-Isle, France), C57BL/6N mice (n = 27, Charles River, Sulzfeld, Germany) and SJL/J (n = 33, Janvier Labs, Le Genest-Saint-Isle, France) mice (all female, age 2-4 months) were used to study the TF signal following oral application *in vivo*. The numbers of animals within each group are specified in the relevant experiments below.

Animal experiments were conducted in accordance with procedures approved by the Animal Welfare Department of the State Office of Health and Social Affairs Berlin (LAGeSo) and conformed to guidelines to minimize discomfort to animals (86/609/EEC).

EAE induction

EAE was induced by subcutaneous immunization of SJL/J mice with proteolipid protein peptide ($PLP_{139-151}$) and C57BL/6 mice with myelin oligodendrocyte glycoprotein peptide (MOG_{35-55}); for both peptides 250 µg peptide (Pepceuticals, Leicester, UK) per animal were emulsified with M. Tuberculosis H37RA (List Biological Laboratories, Campbell, US, 800 µg/animal) in 100 µL Complete Freund's Adjuvant (BD Difco, Heidelberg, Germany). Pertussis Toxin (Biotrend, Cologne, Germany, 1.25 ng/µL in SJL/J and 2 ng/µL in C57BL/6) was administered intraperitoneally in 200 µL PBS on days 0 and 2 [58].

EAE scoring was performed daily: righting reflex weakness = 0.5, tail paresis = 0.5, tail paralysis = 1, unilateral hindlimb paresis = 0.5, bilateral hindlimb paralysis = 1, unilateral forelimb paresis = 0.75, bilateral forelimb paralysis = 1.5.

Teriflunomide treatment and preparation for *in vivo* MR measurements

Rats (n = 2) were treated orally with 10 mg/kg TF and MR measurements were performed directly following administration. Animals were anesthetized by intraperitoneal (ip) injection using ketamine (40 mg/kg, WDT, Garbsen, Germany) and medetomidine (0.5 to 0.75 mg/kg, Henry Schein, Berlin, Germany) maintained by an ip catheter line. TF was administered via a catheter line to the stomach while the animal was in the scanner.

Mice were treated daily for 14 days with 30 mg/kg TF [55-57, 59] or vehicle control (CMC) administered by oral gavage. The increased dose used in mice takes into consideration guidelines on dose conversions in animals and is mostly due to differences in metabolism [56, 60]. EAE mice were treated with TF (C57BL/6 n = 12, SJL/J n = 12) or CMC (C57BL/6 n = 6, SJL/J n = 6). Healthy non-immunized C57BL/6 (n = 9) or SJL/J (n = 15) mice served as therapy controls. MR measurements in mice were performed on days 8 and 14 following EAE start, 16-24 h after the last drug administration. For *in vivo* MR measurements, mice were anesthetized by intraperitoneal injection using a mixture of xylazine (5 mg/kg, CP Pharma, Burgdorf, Germany) and ketamine (50 mg/kg, WDT, Garbsen, Germany) maintained by an ip catheter line.

Animals were transferred to a temperature-regulated bed (receiving circulated warm water from a water bath) and supplied with pressurized air (30 %) and O_2 (70 %). Pulse, respiration and body temperature (Neoptix, OmniLink version 1.15, Omniflex, Neoptix, Québec, Canada) were continuously monitored. The body temperature was kept at 37 °C throughout the experiments.

For studying the BBB disruption in SJL/J EAE mice, gadopentetate dimeglumine (0.2 mmol/kg Gd-DTPA Magnevist, Bayer Pharma, Berlin, Germany) was administered intravenously via the tail vein using an infusion pump (Harvard PHD 2000, Harvard Apparatus, Cambridge, US).

Phantom construction

For characterizing the ^{19}F MR properties (chemical shift, spectral shape and relaxation times) of TF, phantoms were prepared in 2.5 mL syringes (inner diameter, id: 9.7 mm, total length: 7.6 cm, B.Braun, Melsungen, Germany) equipped with stopper closing-cones (B.Braun, Melsungen, Germany) using dimethylsulfoxide (DMSO, Roth, Karlsruhe, Germany, 27.02 mg/mL), human serum (4.84 mg/mL) or CMC (2.70 mg/mL) as solvents/suspending agent. Given the different pH of various compartments *in vivo*, we studied the influence of pH on the relaxation times T_1 and T_2 as well as the ^{19}F signal intensity in CMC in 1 mL syringes (id: 4.7 mm, total length: 9.6 cm, B.Braun, Melsungen, Germany). The pH for the 2.70 mg/mL TF concentration was adjusted to pH values of 5, 7.4, 10 and 13 with HCl or NaOH.

For studying the influence of contrast agent on ^{19}F MR properties, 4 phantoms containing 16.67 mg/mL TF and different concentrations of Gd-DTPA (0.5 mM, 1 mM, 2 mM, and 4 mM) in DMSO were prepared in NMR tubes (id: 4.2 mm).

For assessing the limit of detection (LOD) for ^{19}F MRS and performing calibrations, four TF concentrations were prepared in serum (400 µL) and the exact concentration for each sample was determined by mass spectrometry (11.8, 105.7, 787.4, 4208.2 µg/g). The serum samples (350 to 500 µL) were prepared in 1 mL syringes (as above).

MR methods

Hardware

MR experiments were performed on a Bruker Biospec 9.4 T MR scanner (Bruker Biospin, Ettlingen, Germany) with a horizontal bore. A room temperature (RT) dual-tunable $^{19}F/^{1}H$ head RF transceive coil (16 mm inner diameter) [61] was used to characterize TF in DMSO/serum/CMC in phantom experiments.

A RT dual-tunable $^{19}F/^{1}H$ rat body RF transceive

coil (MRI.TOOLS GmbH, Berlin, Germany, 62 mm inner diameter) was used to study *in vivo* ^{19}F MR spectroscopy (MRS) signals in the abdomen of the rat.

A cryogenically-cooled transceive ^{19}F quadrature RF surface probe (20 mm inner diameter, Cryogenic Radiofrequency Probe, CRP, Bruker, Fällanden, Switzerland) [62] was used for *in vivo* ^{19}F MRS measurements of the mouse head and abdomen as well as serum samples. With this coil we had previously shown that ^{19}F MR sensitivity is enhanced by a factor of 15 compared to RT head coils [62]. The bed of the ^{19}F CRP was adjusted with respect to the surface of the coil in order to acquire ^{19}F MRS in different regions of the mouse body. The measurement volume above the bed was adjusted with respect to the surface of the coil-head by using a position gauge. This device reproduces the geometry of the coil-head and supporting components and can be used to adjust the position of the mouse on the bed outside of the MR scanner. Anatomical ^{1}H scans ensured correct positioning and complete coverage of the regions of interest.

Phantom MR measurements

A non-selective single-pulse ^{19}F MRS FID-acquire sequence (TR = 1000 ms, nominal flip angle = 90°, blockpulse, 4096 sampling points, acquisition delay = 0.05 ms, excitation pulse bandwidth = 10000 Hz, spectral read bandwidth = 25000 Hz, averages for serum/CMC/DMSO phantoms: avg_{serum} = 8, avg_{CMC} = 16, avg_{DMSO} = 16) was used for detecting TF in phantoms and studying chemical shift and spectral shape (full-width half maximum, FWHM). This sequence (later referred to as default) was slightly modified e.g. using increased averages or bandwidth to increase signal-to-noise ratio (SNR) in *in vivo* and *ex vivo* experiments (see below).

^{19}F T_1 and T_2 relaxation times were measured using MR spectroscopy. For T_1, the default FID-acquire sequence was used but with 16 TRs ranging from 100 to 10000 ms, avg_{serum} = 40, avg_{DMSO} = 30, avg_{CMC} = 30. For T_2, a CPMG pulse sequence was used: 25 echoes, echo spacing for serum/CMC/DMSO phantoms: es_{serum} = 2.8 ms, es_{DMSO} = 40 ms, $es_{DMSO+Gd\text{-}DTPA}$ = 10.6 ms, es_{CMC} = 10.6 ms, excitation pulse = 5000 Hz, spectral read bandwidth = 25000 Hz; TR_{serum} = 2000 ms, TR_{DMSO} = 5000 ms, TR_{CMC} = 5000 ms, avg = 50 (for all phantoms).

For studying the influence of pH on the ^{19}F MR signal detection, the default FID-acquire sequence was used, but a long TR of 8000 ms was chosen to allow full relaxation.

The LOD for the ^{19}F CRP to perform ^{19}F MRS *in vivo* was assessed using the above four concentrations of TF in serum and the default ^{19}F MRS FID-acquire sequence but using avg = 1024, acquisition time = 17 min. The SNR of these spectra was measured and the LOD was determined as the concentration/number of ^{19}F atoms that corresponded to an SNR of 5 (SNR_1 estimation below) using a linear fit with y-axis intercept = 0. The SNR value of 5 was chosen as a conservative threshold for determining LOD.

In vivo ^{1}H MRI using ^{19}F/^{1}H coils

Anatomical ^{1}H MRI was performed using FLASH (Fast Low-Angle Shot) [63] and T_2 weighted TurboRARE (Rapid Acquisition with Relaxation Enhancement) [64] pulse sequences. In EAE mice, BBB disruptions were assessed using an MDEFT (Modified Driven-Equilibrium FT) [65] sequence with inversion (TR/TE/TI 2600/3.9/950 ms, FOV (30.2×12.8×9) mm^3, matrix size = 256×170×18, avg = 2, acquisition time = 3 m 7 s).

In vivo ^{19}F MRS using ^{19}F CRP

TF-derived ^{19}F MR signal was studied in healthy and EAE mice immediately following acquisition of the anatomical scans. To account for the B_1 inhomogeneity of the CRP surface coil during *in vivo* measurements, we calibrated the flip angle. Before *in vivo* measurements, a phantom reference sample of 1 mL TF in DMSO (27.02 mg/mL) was used to manually calibrate the flip angle and reference power. This sample was in a 2.5 mL syringe and was positioned at the coil surface. We acquired 10 spectra with the default ^{19}F MRS FID-acquire sequence using different reference powers (0.0001 - 0.01 W). The best reference power from these manual measurements was verified by the automatically adjusted power settings for this sample by the MR system. Prior to each *in vivo* measurement, we adjusted the reference power manually (automatic ^{19}F adjustments were not possible due to low SNR): spectra (avg = 128, 2 min 8 s each) with different reference powers (0.001, 0.002, 0.004, 0.008 W) were acquired from the head region of mice *in vivo* using the default FID-acquire method. The optimal reference power yielding the highest signal intensity was then chosen for the ^{19}F MRS data acquisitions. For these acquisitions, the default FID-acquire sequence was used with avg = 1024, acquisition time = 17 min.

In vivo ^{19}F MRS using ^{19}F/^{1}H rat body coil

To study ^{19}F MRS signal of TF in the abdominal region of rats at different time points, the default FID-acquire sequence was used with alterations in: TR = 1500 ms, avg = 256, acquisition time = 6 min.

Ex vivo measurements

Tissue processing

Animals were sacrificed after 14 days of *in vivo* experiments. Under deep anesthesia, blood was withdrawn and animals were transcardially perfused with 30 mL (> 10× the estimated total mouse blood volume) phosphate-buffered saline (PBS) solution. CSF was collected from the cisterna magna and the perfused brain was isolated. The perfused brain samples are mostly depleted of blood and CSF. Samples were frozen (-80 °C) for subsequent mass spectrometry studies.

Perfused brain tissue (50 mg), serum (50 µL) or CSF (1-3 mg) was weighed/measured and homogenized in 450 µL phosphate buffer (100 mmol/L, pH = 6.0). 1 mL ethylacetate was added. The mixture was shaken vigorously for 5 min and centrifuged at 11000 rpm for 10 min. The upper layer was transferred to a 2 mL glass vial. The extraction was repeated twice. The organic extract was evaporated to dryness with a gentle N_2 stream at 40 °C, after which the residue was dissolved in 1 mL ethanol.

High performance liquid chromatography mass spectrometry (HPLC/MS)

For assessing the LOD for HPLC/MS, 5 TF concentrations (1 ng/mL to 1000 ng/mL) were prepared in DMSO. LOD was calculated at an SNR = 9 using peak-to-peak algorithm from lowest calibrator 1 ng/mL.

HPLC-measurements were performed using an Agilent 1290 HPLC system with binary pump, autosampler and column thermostat equipped with a Phenomenex Kinetex-C18 column 2.6 µm, 2.1×150 mm column (Phenomenex, Aschaffenburg, Germany). Ammonium acetate (5 mM) and acetonitrile was used as solvent system. All solvents and buffers in HPLC-MS-grade were obtained from VWR Germany. The solvent gradient started at 5 % acetonitrile and was increased to 95 % within 5 min until 8 min with a flow rate of 0.4 mL/min and 1 µL injection volume. The HPLC was coupled with an Agilent 6470 triplequad mass spectrometer with electrospray ionization source using established parameters (gas temp = 250 °C, gas flow = 9 L/min, nebulizer pressure = 20 psi, sheath gas temp = 390 °C, sheath gas flow = 12 L/min, capillary voltage = 2700 V, nozzel voltage = 300 V) operated in negative multiple reaction monitoring mode (269.2 –160 capillary electrophoresis (CE) 28 V, – 82 CE 21, fragmentor voltage = 120 V, mass resolution wide/wide).

Ex vivo ^{19}F MRS

For correlating the TF-derived ^{19}F MR signal with HPLC/MS TF quantification, calibrations were first performed with mouse sera spiked with TF (using 3 concentrations closer to biologically expected values) in 1 mL syringes. These concentrations were measured with HPLC/MS (11.8, 105.7, 787.4 µg/g) and the default ^{19}F MRS FID-acquire method (but excitation pulse = 70000 Hz, spectral read bandwidth = 70000 Hz, avg = 4096, acquisition time = 1 h 8 min). Next we measured the *ex vivo* serum samples from EAE mice (n = 10) in 1 mL syringes using the default FID-acquire method and HPLC/MS.

For both the calibration experiment (spiked serum) as well as the between-method correlation (*ex vivo* serum) we computed a linear fit with y-axis intercept = 0 to determine the relation of signal to concentration and then used this ratio to estimate TF concentrations in *ex vivo* serum samples from the ^{19}F MRS signal intensity after accounting for slight volume differences.

MR data analysis

For *in vivo* proton image processing and analysis, the freely available software Fiji (Image J v1.47p, Open source software, NIH, MD, USA) [66] was used.

All spectral analyses and processing were performed in MATLAB (The MathWorks Inc., Natick, USA). Chemical shifts are referenced to trichloro-fluoro-methane, $CFCl_3$ (δ_F=0 ppm). Post-processing of the real spectra included zero-filling to 2^{14} points of all original FID data and a line-broadening of 70 Hz. The signal from both receive channels was averaged after zeroth and first order phase-correction.

We used two conventions to measure SNR of the main spectral peaks: SNR_1 was measured by calculating the ratio of the peak amplitude (maximal peak height minus mean background signal) and one standard deviation of the background noise (σ_1), as suggested in a recent expert's consensus paper on *in vivo* MR spectroscopy [67]. SNR_2 was measured by calculating the ratio of the peak amplitude and the noise height (peak-to-peak) divided by 2.5 (σ_2) [68]. Both SNR estimations are shown for all *in vivo* ^{19}F MR measurements in healthy and EAE mice (**Table S1**). SNR_1 was used for all data analysis. SNR_2 is only reported in Table S1.

The time domain (TD) signal intensity was measured by calculating the y-axis intercept of the magnitude free-induction decay using a 4–th degree polynomial fit (FID fit) in MATLAB. The frequency domain (FD) signal intensity was determined by computing the integral of the MRS peak at -61 ppm (peak area). For this, we used a Lorentzian fit of the real spectrum [69] including a baseline offset and a

secondary peak if the amplitude of the secondary peak exceeded $SNR_1 = 2$. Only the area of the main peak was attributed to TF.

T_1 and T_2 were determined by mono exponential fitting of data points obtained from ^{19}F MRS (T_1) and CPMG (T_2, three parameter fit).

Statistical analysis

MR-data and mass spectrometry data were pooled from all experiments. ^{19}F signal intensities from ^{19}F MR and TF concentrations in serum, perfused brain tissue and CSF samples from HPLC/MS experiments were log transformed, and the log-normal distribution confirmed using the Shapiro-Wilk normality test. EAE disease scores were presented as mean and standard error of the mean, maximum scores as median and interquartile range and were analyzed with the Mann-Whitney U test. Bodyweight was analyzed using the t-test; the logrank test was used to analyze the time-to-onset of clinical signs. ^{19}F MR signal detection over time and mass spectrometry data was analyzed using ANOVA or 2-factor ANOVA, with the Tukey post-hoc test for multiple comparisons, or with an unpaired t-test. Levene's test was used for testing for homogeneity of variance. Correlation was assessed using the Pearson correlation (R) or the non-parametric Spearman rank-order correlation (ρ), as appropriate. *p*-values < 5 % were considered significant (depicted as $*p < 0.05$; $**p < 0.01$; $***p < 0.001$). Statistical analysis was performed using the statistical computing environment R (version 3.6.1, R Foundation; https://R-project.org).

Results

Strain differences in response to teriflunomide treatment in EAE mice

We studied TF treatment response in both SJL/J (**Figure 1A-D**) and C57BL/6 (**Figure 1E-H**) EAE mice. In SJL/J mice, TF treatment prevented weight loss during the EAE disease course (**Figure 1A**, n = 12,

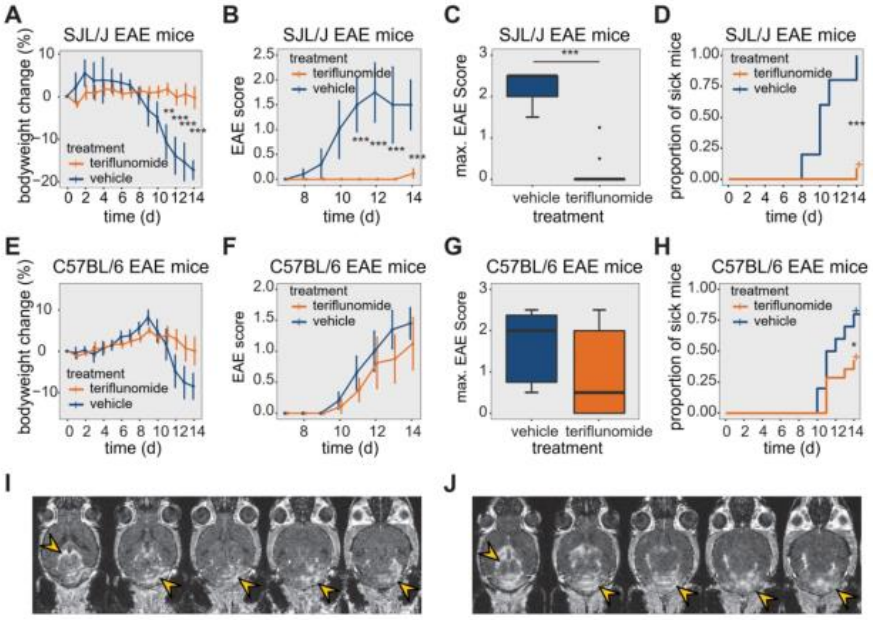

Figure 1. *Effect of teriflunomide treatment on the disease course of EAE in SJL/J and C57BL/6 mice.* **(A)** Change in bodyweight (Mean ± SE) over time in untreated (carboxymethylcellulose vehicle, n = 5) and TF treated (n = 12) SJL/J EAE mice. Changes in percent compared to the initial bodyweight are shown. **(B)** Mean EAE score ± SE of untreated (n = 5) and TF treated (n = 12) SJL/J EAE animals. The time axis is restricted to days with non-zero EAE score. **(C)** Maximum EAE score reached during the EAE disease course in untreated (n = 5) and TF treated (n = 12) SJL/J EAE animals. **(D)** Kaplan-Meier plot of untreated (n = 5) and TF treated (n = 12) SJL/J EAE animals depicting the time to disease onset (score=0.5) and the proportion of animals with clinical symptoms. **(E)** Change in bodyweight (Mean ± SE) over time in untreated (carboxymethylcellulose, n = 6) and TF treated (n = 9) C57BL/6 EAE mice. Changes in percent of the initial bodyweight is shown. **(F)** Mean EAE score ± SE of untreated (n = 6) and TF treated (n = 9) C57BL/6 EAE animals. The time axis is restricted to days with non-zero EAE score. **(G)** Maximum EAE score reached during the EAE disease course in untreated (n = 6) and treated (n = 9) C57BL/6 EAE animals. **(H)** Kaplan-Meier plot of untreated (n = 6) and treated (n = 9) C57BL/6 EAE animals depicting the time to onset (score = 0.5) of the EAE disease and the proportion of animals with clinical symptoms. **(I-J)** MR images showing mild (I) and severe (J) blood brain barrier disruption using contrast agent (i.v.) and MDEFT on day 14 in two TF treated EAE mice. Lesions are indicated (yellow arrows) in the cerebellum and also in periventricular regions. Differences in body weight were analysed using Student's t-test; EAE scores and max scores were analysed using the Mann-Whitney U test; time to disease onset was analysed using the logrank test.

pooled from 4 EAE experiments). Control EAE mice (n = 5, pooled from 4 EAE experiments) treated with vehicle showed a substantial weight loss from day 11 post-immunization (p.i.) onward ($p = 0.002$) (**Figure 1A**). TF treatment resulted in an almost complete absence of clinical signs in SJL/J mice. TF-treated EAE mice had lower clinical scores compared to vehicle-treated EAE mice, which showed a typical disease course for SJL/J mice, reaching peak clinical score at day 12 p.i. (**Figure 1B**). In the TF-treated group, only 8% of animals showed clinical signs by day 14 p.i. compared to untreated mice (100% incidence). The maximum disease score was also different between treated (0 ± 0, median ± interquartile range, IQR) and untreated (2.5 ± 0.5, median ± IQR) EAE mice ($p < 0.001$) (**Figure 1C**). TF delayed disease onset ($p < 0.001$), which is defined as time to reach a minimum clinical score of 0.5 (**Figure 1D**).

The response of C57BL/6 EAE mice (n = 9, pooled from 3 EAE experiments) to TF treatment was less pronounced. TF-treated C57BL/6 EAE mice showed a less marked reduction in weight over time, but there was no significant difference in weight loss compared to vehicle-treated C57BL/6 EAE controls (n = 6, pooled from 3 EAE experiments) ($p > 0.1$) (**Figure 1E**). TF-treated C57BL/6 mice began to show clinical signs by day 10 p.i., and while EAE scores were generally lower than those of vehicle treated controls, there were no differences in EAE scores between the two groups ($p > 0.5$) (**Figure 1F**). Also, there was no significant decrease in maximum EAE score in TF-treated C57BL/6 EAE mice (0.5 ± 2, median ± IQR) compared to vehicle-treated (2 ± 1.625, median ± IQR) C57BL/6 EAE mice ($p > 0.05$) (**Figure 1G**). TF treatment reduced disease incidence by 65% and also delayed onset, compared to untreated mice ($p = 0.04$) (**Figure 1H**).

The extent of CNS inflammation was examined on day 14 by measuring BBB disruption using contrast-enhanced MRI (**Figure 1I-J**). We observed contrast-enhancing lesions in SJL/J EAE mice treated with TF, even in the absence of clinical signs. The extent of these lesions varied among animals, with some showing comparatively mild (**Figure 1I**) and others comparatively severe (**Figure 1J**) disruption. Contrast-enhancing lesions were particularly prominent in the cerebellum (**Figure 1I-J**) and were also present in periventricular regions (**Figure 1J**).

Environmental factors alter the magnetic resonance properties of teriflunomide

The physicochemical properties of TF in DMSO, including chemical shift, ^{19}F T_1 and ^{19}F T_2 relaxation times are shown in **Figure 2A-C**. Changes in T_1 and T_2 occur with different concentrations of gadopentetate dimeglumine (**Figure 2D**). We observed a linear correlation between the inverse T_1 (R_1) (T_1-relaxation times 1099 ms, 209 ms, 117 ms, 60 ms, 33 ms; Pearson R = 0.999, $p < 0.001$) and inverse of T_2 (R_2; T_2-relaxation times 547 ms, 76 ms, 43 ms, 24 ms; Pearson R = 0.999, $p = 0.001$) with increasing Gd-DTPA concentrations (**Figure 2D**).

TF in CMC exhibits a single narrow peak spectrum (FWHM = 116 Hz) at -61 ppm (**Figure 2E**), in comparison to a peak at -58 ppm for experiments performed in DMSO (FWHM = 117 Hz) [70].

Both T_1 (**Figure 2F**) and T_2 (**Figure 2G**) were increased with increasing pH. We also observed increased signal intensity at higher pH using global single pulse spectroscopy with full relaxation (**Figure 2H**).

Compared to spectra in DMSO (FWHM = 117 Hz) [70], we observed a broader peak for TF in serum (FWHM = 528 Hz) at -61 ppm (**Figure 2I**). In addition, we characterized T_1 (**Figure 2J**) and T_2 (**Figure 2K**) in human serum in order to optimize pulse sequences for subsequent *in vivo* measurements. T_1 of TF in serum was 1017 ms (**Figure 2J,** $R^2 = 0.999$), which was comparable to the T_1 of 1000 ms in DMSO (**Figure 2B**). Conversely, T_2 was markedly shortened to 4 ms (**Figure 2K,** $R^2 = 0.963$) in the presence of serum, which is 93-fold lower than the T_2 of 465 ms in DMSO [70].

We obtained a detection limit for the ^{19}F CRP using ^{19}F MRS, validating the concentrations with mass spectrometry. At an SNR threshold of 5, the LOD was 1.9 µg/g, which is equal to 5.04e + 15 ^{19}F atoms in a volume of 400 µL (**Figure 2L**).

In vivo detection of teriflunomide in the abdominal region of healthy animals

Similar to TF spectra in CMC phantoms, we observed a TF peak at -61 ppm in healthy Dark Agouti rats (n=2) using ^{19}F MRS (**Figure S1A**). Qualitatively, we discerned an initial increase in ^{19}F MR signal followed by gradual decrease during the observation period of 30 minutes. We also detected TF in the abdominal region of healthy C57BL/6 mice (**Figure S1B**) 24 hours after the last drug administration, using the ^{19}F CRP.

In vivo detection of teriflunomide in the head region

Similar to CMC phantoms and *in vivo* measurements in the rat abdomen, we observed a TF peak at -61 ppm in the mouse head region. We studied changes in TF levels in TF-treated healthy mice (**Figure 3A**, n = 6 on day8, n = 5 on day14, from 1 EAE experiment), and TF-treated EAE mice (**Figure 3B**, n = 7 on day8, n = 4 on day14, from 1 EAE

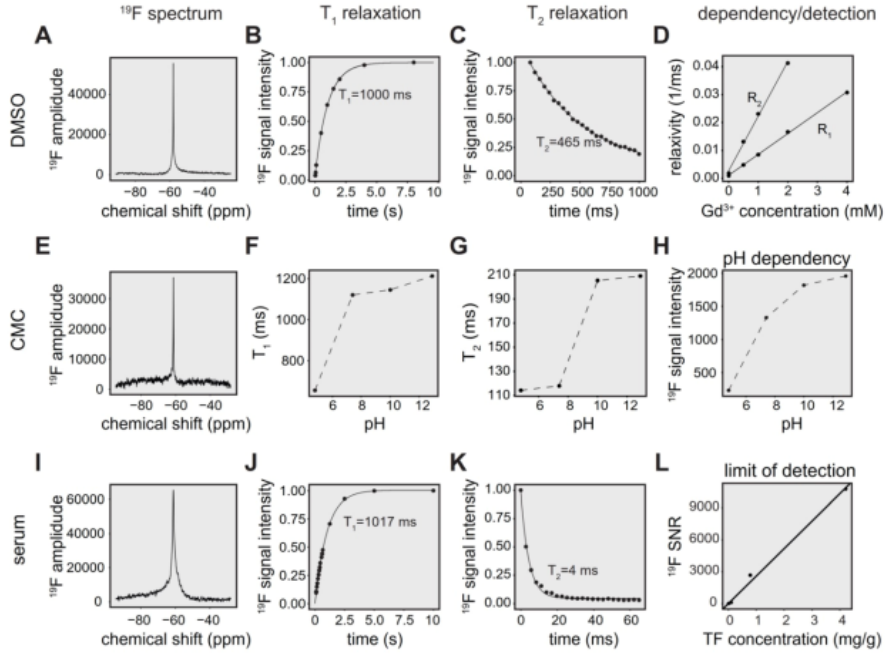

Figure 2. *19F MR characterization of teriflunomide in different chemical environments.* **(A)** 19F MR spectrum of TF in a DMSO phantom (global single pulse, TR=1000 ms, acquisition time = 16 s, concentration: 27.02 mg/mL in 1 mL). **(B)** Spectroscopic determination of T_1 of teriflunomide in DMSO (T_1 = 1000 ms). **(C)** Spectroscopic determination of T_2 of teriflunomide in DMSO (T_2 = 465 ms) using a CPMG sequence. **(D)** Correlation of the relaxation rates R_1 and R_2 (inverse T_1 and inverse T_2) with the concentration of the contrast agent gadopentetate dimeglumine (0.5, 1, 2, 4 mM) in DMSO (R_1 = 0.998, p = 9.17e-6 for R_1 and R_2 = 0.999, p = 0.001 for R_2). TF concentration = 27.02 mg/mL. **(E)** 19F MR spectrum of TF in a carboxymethylcellulose (CMC) phantom (global single pulse, TR=1000 ms, acquisition time = 16 s, concentration: 2.70 mg/mL in 1 mL). **(F)** Change of the 19F T_1 with pH in CMC. **(G)** Change of the 19F T_2 with pH in CMC. **(H)** Change of the 19F signal intensity with pH in CMC; concentration in CMC: 2.70 mg/mL in 1 mL, pH was controlled by adding HCl and NaOH. **(I)** 19F MR spectrum of teriflunomide in a serum phantom (acquisition time = 8 s, concentration: 1.3 mM in 1 mL). **(J)** Spectroscopic determination of T_1 of teriflunomide in human serum (T_1 = 1017 ms). **(K)** Spectroscopic determination of T_2 of teriflunomide in human serum (T_2 = 4 ms) using a CPMG sequence. **(L)** Assessment of the spectroscopic limit of detection (SNR_1) using different TF concentrations in serum (19F MRS measured with a 19F CRP, global single pulse, TR = 1000 ms, acquisition time = 17 min).

experiment). Differences in animal numbers between the time points were either due to technical problems (4 cases) or due to animal welfare (mice needed to be euthanized due to disease severity, 2 cases). We observed a distinct second 19F peak in healthy and EAE animals (-75 to -85 ppm). The -75 ppm peak was seen at a later stage of EAE and was also observed in the abdomen of EAE mice (data not shown).

The 19F MR signal from the processed spectra of EAE and healthy mice is represented in both TD as FID fit (**Figure 3C**) and FD as peak area (integral of the main peak) at -61 ppm (**Figure 3D**) and SNR_1 of this peak (**Figure 3E**). Data from these mice are shown separately in **Table S1** (the raw data is also available as supplemental material). We did not observe any significant differences between the groups between day 8 and day 14, between EAE and healthy control mice (all $p > 0.1$) or in the pairwise comparisons (all $p > 0.1$) for all data, irrelevant whether FID fit, integral or SNR of main peak. In addition, we did not observe differences in variance of the 19F signal intensities (FID fit, integral or SNR) among the animals groups on any day or any of the pairwise comparisons (all $p > 0.1$).

Ex vivo determination of teriflunomide levels in healthy and EAE animals

The TF-derived signal was also measured in the serum of SJL/J EAE mice by 19F MRS (**Figure S1C**). TF concentrations in serum, CSF and perfused brain tissue were quantified by HPLC/MS for both SJL/J and C57BL/6 mice (**Table 1**). We calculated the LOD of the HPLC method to be 4.9 pg/g. In SJL/J mice there was a strong difference between biological samples (main effect $p < 0.001$), but no significant difference between healthy and EAE animals. TF concentrations in serum were an order of magnitude higher than those in perfused brain tissue or CSF, for both healthy and EAE animals (all p values < 0.001) (**Figure 4A, left panel**). In C57BL/6 mice, there was again a strong difference between biological samples

(main effect $p < 0.001$), with TF concentrations in serum greater than those in perfused brain tissue or CSF ($p < 0.001$). Upon post-hoc comparisons, we observed that TF concentrations in the CSF were greater than in the perfused brain tissue, both for C57BL/6 EAE mice ($p = 0.0025$) and for C57BL/6 healthy control mice ($p = 0.032$) (**Figure 4A, right panel**).

Table 1. Concentrations of teriflunomide in µg/g detected via HPLC/MS from *ex vivo* samples from EAE and healthy SJL/J and C57BL/6 mice (median ± interquartile range)

	SJL/J		C57BL/6	
	EAE (n = 7)	Healthy (n = 6)	EAE (n = 4)	Healthy (n = 3)
Serum	32.5 ± 13.8	33.8 ± 17.9	19.0 ± 6.8	20.6 ± 7.4
CSF	1.7 ± 2.2	1.0 ± 1.0	0.5 ± 0.5	0.9 ± 0.3
Brain	0.6 ± 0.9	0.5 ± 0.3	0.1 ± 0.0	0.3 ± 0.1

We observed significant differences in the variance of TF concentrations. In SJL/J mice, these differences were seen among perfused brain, CSF and serum samples ($p < 0.001$) but not between EAE and healthy control groups when considering all *ex vivo* samples ($p = 0.945$). When comparing EAE vs. healthy controls for each tissue separately (pairwise comparisons), the variance in TF concentration was significantly greater in the EAE group in the case of brain tissue ($p = 0.048$), but not CSF and serum samples (**Figure 4A, left panel**). In C57BL/6 mice, differences in variance were also seen among perfused brain, CSF and serum samples ($p < 0.001$). There was again no difference in TF variance between EAE and healthy controls ($p = 0.406$), even when performing the pairwise comparisons for each tissue (**Figure 4A, right panel**).

The HPLC/MS quantification of TF concentrations was important to establish the ground truth for validating *in vivo* ^{19}F MRS data. A calibration of FD ^{19}F MRS signal intensities with HPLC/MS concentration values in mouse serum (spiked with different TF dilution) is shown in **Figure 4B**. The resulting linear fit (Spearman $\rho = 1.000$, $p = 0.333$), was used to estimate the concentration from the FD ^{19}F MR signal intensity. Compared to the HPLC/MS quantification, TF concentrations estimated from ^{19}F MRS were elevated with a maximum relative deviation of 130% and a mean relative deviation of 83% (**Figure 4C**). However, TF concentrations determined by ^{19}F MRS showed a clear correlation with concentrations determined by HPLC/MS (Spearman $\rho = 0.903$, $p = 0.001$).

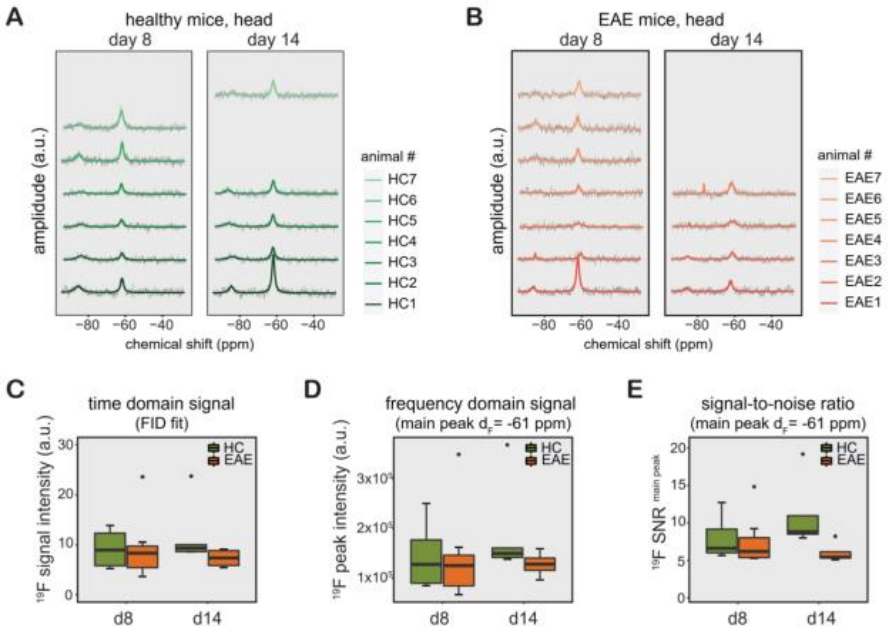

Figure 3. *^{19}F MR detection of teriflunomide (TF) in vivo.* **(A-B)** ^{19}F MR teriflunomide signal from the heads of healthy (A) and EAE (B) mice on day 8 and day 14 following the start of daily teriflunomide treatments. Measurements were performed 16-24 h after the last gavage (acquisition time = 17 min). **(C-D)** ^{19}F MR signal calculated in the time domain as signal intensity from the FID fit (C) and frequency domain as peak area, integral of the main peak (δ_F = -61ppm) using the Lorentzian fit (D) and SNR (signal per one SD of the noise) of the same peak (E) plotted as arbitrary units for all EAE and healthy SJL/J animals for days 8 and 14.

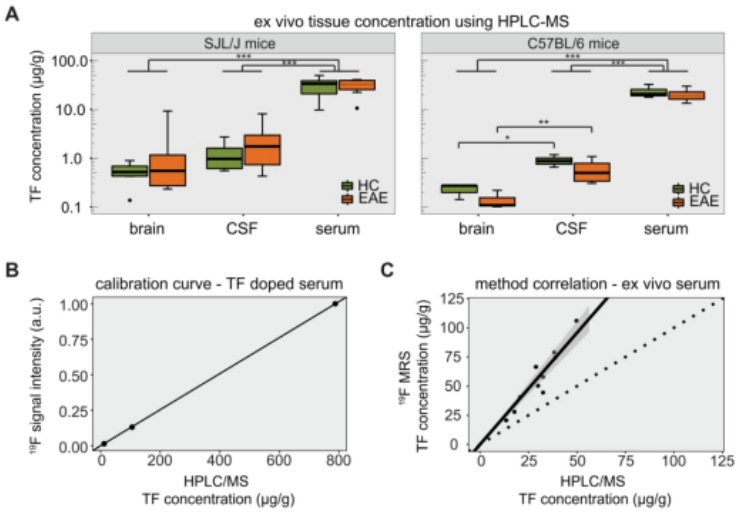

Figure 4. *Detection of teriflunomide by mass spectrometry.* **(A)** Plot showing the detection of teriflunomide by mass spectrometry in the brain, CSF and serum of EAE and healthy animals of both strains SJL/J and C57BL/6 on day 14 (EAE SJL/J n = 7, healthy SJL/J n = 6, EAE C57BL/6 n = 4, healthy C57BL/6 n = 3). **(B)** Calibration curve for ^{19}F MRS quantification using HPLC/MS concentrations of TF dissolved in serum and the corresponding ^{19}F MRS signal intensities (SNR_1; ^{19}F MRS measured with a ^{19}F CRP, global single pulse, TR = 1000 ms, acquisition time = 17 min, linear fit with Spearman ρ = 1.000, p = 0.333). **(C)** Correlation of ^{19}F MR signal quantification *ex vivo* in the serum of TF treated mice with concentrations measured by mass spectrometry in serum (^{19}F MRS measured with a ^{19}F CRP, global single pulse, TR = 1000 ms, acquisition time=1 min, Spearman ρ = 0.903, p = 0.001, dotted line with slope = 1).

Discussion

In this study, we show that non-invasive ^{19}F MR methods can be used to detect TF *in vivo*. *Ex vivo* HPLC/MS analyses confirmed the availability of TF in the CNS at pharmacologically relevant concentrations [56]. The therapeutic effect was strain-dependent, being less pronounced in C57BL/6 mice. This could be attributed to the diverging pathology that both strains present during the course of an EAE: in SJL/J mice the pathology is mainly localized to the brain, in C57BL/6 mice lesions are mostly prevalent in the spinal cord [71]. EAE in SJL/J mice presents as a relapsing-remitting disease (similar to RRMS patients). EAE in C57BL/6 mice follows a chronic disease progression without remissions and relapses (similar to progressive/secondary progressive MS). These strain differences were behind the rationale for studying different mechanism of action of DMDs for the treatment of RRMS and P/SPMS [56]. Different responses to TF treatment among species and strains could be also attributed to differences in target binding potencies [72] or immune cell susceptibilities [56].

Despite increasing concerns regarding the risks of long-term deposition in the brain, contrast-enhanced MRI remains a key tool for diagnosis and differential diagnosis [73-75]. In this study we observed contrast-enhanced brain lesions at the expected time of peak disease, even in asymptomatic TF-treated EAE mice. This underscores the critical role of MRI for early detection of pathology in MS and EAE, even prior to the occurrence of clinical signs and that clinical scoring alone is not sufficient to fully assess the disease status [58].

In addition to peripheral effects and mechanisms of action, many DMDs for MS are expected to work within the CNS. Thus a non-invasive method that studies drug distribution in the CNS would be a useful tool in MS drug development and in treatment monitoring. Hence, we are addressing an area of major interest in MS that could benefit from new studies investigating therapies and their distribution *in vivo*. Nevertheless, the *in vivo* detection of ^{19}F compounds with ^{19}F MR methods remains challenging. This is primarily due to the low drug concentrations available in the human body [70]. Additionally, technological challenges in terms of hardware sensitivity and measurement precision and accuracy limit swift transitions to clinical applications.

^{19}F MR spectroscopy techniques have been used for several years to detect fluorinated drugs in small animals [33-38] and humans [39-45]. The chemotherapeutic agent 5-Fluorouracil (5-FU) has been studied by ^{19}F MRS in tumor-bearing rats [34] and patients with head and neck tumors [45] and more recently it was detected by ^{19}F MRI in tumor bearing mice using high drug doses and fast spin echo

sequences [38]. ^{19}F MRS imaging (MRSI) of fluvoxamine and fluoxetine was performed in patients with major depressive disorder who were on long term treatment with these drugs [42]. Alternatively, therapeutic compounds containing cytosine (e.g. the neuroprotective drug citicoline or the anticancer drug gemcitabine) can be detected via chemical exchange saturation transfer (CEST) MRI; these molecules contain exchangeable protons that can be selectively saturated and then detected indirectly through the water signal. Recently, the potential of CEST MRI to detect these therapeutic compounds *in vivo* has been shown [76, 77].

Compared to studies investigating fluorinated drugs at high doses [38, 44], in our present study we administered therapeutic doses of the fluorinated drug, which previously had shown an influence on the disease course in SJL/J EAE mice [56]. Additionally, we did not only acquire ^{19}F MR signals right after administration of the drug as has previously been done [36, 78, 79], but we also detected accumulated TF levels over time, and during pathology.

Furthermore, in this study we characterized the MR properties of TF in serum, DMSO and CMC and at varying pH, to assess alterations in the physicochemical and MR properties, which are important to consider during interpretation of data. The pH in different compartments has a known impact on the solubility, binding kinetics and hence bioavailability of drug molecules [80]. pH variations result in different protonation of molecules, changing their MR properties, such as chemical shift [81] and relaxation times [82-86]. pH changes can also effect drug solubility, e.g. at low pH only a fraction of TF is dissolved and thus detected by ^{19}F MR, the precipitated portion will not contribute to the MR signal. Furthermore, pH could also affect the properties of the CMC support matrix. The stomach environment could alter its protonation state and therefore its solubility, thereby affecting the ^{19}F MR properties of TF [87, 88].

While the T_1 of TF in serum was comparable to that in DMSO, the T_2 was substantially shortened in serum, which is also indicated by a broader TF peak [89] in serum, when compared to DMSO. Similar to micelles and nanoparticles [90], CMC could perhaps bind to serum proteins, although one would assume that the drug will be mostly bound to serum proteins in the blood stream. In any case, a shortening of T_2 if caused by drug serum binding (or CMC serum binding) makes signal detection more challenging when using standard pulse sequences.

Here, we used a three-parameter exponential fit, taking an offset of the signal decay into account until reaching the level of noise. Potentially, another fraction of TF exhibiting a different relaxation behavior might contribute to the acquired signal, which however, cannot be distinguished in the experiments performed here. Conversely, an increase in TF MR signal can be expected in short TR measurements in the presence of gadolinium-based contrast agents due to a reduction in T_1 saturation effects. This has implications for neuroinflammation since TF is likely to localize at sites of inflammatory activity in the brain or the spinal cord, and thus its proximity to gadolinium-enhanced lesions in the CNS might increase its detection.

We previously showed that temperature can influence the MR parameters of TF [70]. Here, ^{19}F MR signals increased with increasing pH. Differences in spectral widths between TF in DMSO, CMC and serum can be explained by environmental effects such as different solubility of the drug in the medium and protein-binding effects (99% of TF is plasma protein bound) [91].

As a first step towards studying drug distribution *in vivo*, we measured the ^{19}F MR signal in the abdominal region of healthy rats. The ^{19}F MR signal was acquired directly after TF administration into the stomach; we assume that most of this signal originates from the stomach during the first few minutes. Changes in ^{19}F signal in rats following oral administration can be attributed to pH and temperature changes in the stomach that may alter the solubility or binding of TF to CMC. We hypothesize that pH might play an ambivalent role in different environments e.g. in the stomach, in CMC or in DMSO with respect to solubility and consequently TF detection. The decreasing trend in ^{19}F signal after the six-minute measurement could suggest a gradual influence of the acidic pH in the stomach on signal intensity but also a gradual distribution to the intestinal compartment and absorption into the blood circulation. We expect that the ^{19}F MR signal from the abdominal region in EAE mice, measured 24 h after the last drug administration originates primarily from the liver (highest concentration of TF after blood) [92].

When studying the *in vivo* ^{19}F MR signal of TF in the head region, we observed no changes between day 8 and day 14 p.i. In patients, TF has a half-life of approximately 15 days [51, 93] administered at a dose of 14 mg per day (circa 250 µg/kg). This corresponds to a mouse dose of circa 3 mg/kg [60]. In the current study and previous ones [55, 56] mice received 3-10 times this dose, which is needed to have an effect on the disease course [56]. Leflunomide, the prodrug of TF, reaches steady state in 7 weeks when administered orally at a daily dose of 20 mg (circa 350 µg/kg). If linear pharmacokinetics are assumed

[94], the steady state of TF dose used in mice is expected to be reached earlier than day 8.

Interestingly, we observed a second peak in the range of -75 to -85 ppm alongside the main TF peak at -61 ppm in healthy and EAE mice, and in their *ex vivo* sera, but not in *in vivo* experiments carried out soon after drug administration in the rat. We assume that this peak is a TF metabolite. While we are not aware of any specific TF metabolites that resonate at this range, we are certain that this is not a contamination since it was not reproduced in our phantom experiments and our animals had not been exposed to any other ^{19}F compounds. We believe this second peak surely warrants further investigation and might be valuable to further pharmacological research.

The major metabolite of TF in human plasma is 4-trifluoro-methylaniline oxanilic acid (4-TMOA) [51, 95]. This metabolite has a chemical shift of -59.7 ppm and would overlap with the TF parent compound [96]. Other metabolites such as mono-oxidated TF sulfate, 4-trifluoromethylaniline 2-hydroxy-maionanlc malonamic acid and its sulfate were identified in urine, and mono-oxidated TF sulfate and mono-oxidated TF in feces [95].

The chemical shifts of most CF3 groups lie within the range of -60 to -80 ppm. A more negative chemical shift would indicate increased shielding of the CF3 group, which can occur as a result of branching near the CF3 group or close proximity to hydrogen bond donors [97]. In human subjects the total amount of these metabolites in plasma is lower than 1 % of the parent compound (in contrast to urine and feces) and probably not detectable *in vivo* [95, 98]. However, this might also be different in mice. Different metabolic rates and processes can be an explanation of this finding. Even the EAE pathology might have an impact due to changes in metabolic processes during inflammation [99] and warrants further investigation in future studies.

In a rat EAE model, TF distribution to the brain was shown by whole-body autoradiography [92], whereas no TF could be detected in the brains of EAE mice when using MALDI-MS [100]. The *in vivo* ^{19}F MR signal that we acquired in the head region of healthy and EAE mice with ^{19}F MRS could reflect TF signals in the blood, CSF, brain parenchyma, or perhaps even infiltrating immune cells that are causing the pathology. Since we did not observe any significant differences in TF signal between the healthy controls and EAE mice *in vivo*, there is no evidence of pathology-related alterations in the drug distribution into the head region.

The results from mass spectrometry measurements also did not show significant differences in TF concentrations in perfused brain tissue, CSF and serum between EAE mice and healthy controls. Nevertheless, TF was detectable in CSF and perfused brain tissue in both SJL/J and C57BL/6 mice, though these were significantly lower than serum concentrations. This distribution pattern could reflect the route of the drug from the systemic circulation to the brain via the CSF or the vasculature.

The observed interindividual differences in TF levels are consistent with a TF study performed in patients where steady state plasma concentrations were in the range 7.6-14.8 mg/L and 11-16.9 mg/L following at least 8 weeks daily intake [93].

One caveat of the study was that we could not perform automatic power adjustments during the *in vivo* measurements in the mouse head, due to low SNR; instead we performed short measurements with different reference power settings on the living animal to determine the optimal reference power to reach the 90 ° flip angle. Nonetheless the uncertainty in the flip angle due to potential differences in the positioning of the animal or coil filling factors could be a potential source of variability in the ^{19}F detection. We did not use a reference tube during the *in vivo* measurements for several technical (overlapping signals, potential signal losses), physical (complex *in vivo* setup and limited space) and animal welfare related (breathing obstruction) reasons.

A comparison between the ^{19}F MRS method and the HPLC/MS method in *ex vivo* serum samples showed a linear correlation. However, there were deviations between HPLC/MS and ^{19}F MRS concentration estimations; one could attribute these either to an overestimation by the ^{19}F MRS method or an underestimation by the HPLC/MS method. The proportion of metabolite to parent compound might be higher in mice than in human subjects. Therefore, one could speculate, that the ^{19}F MRS peak at -61 ppm overlaps with a significant amount of its metabolite. Potentially, metabolites detected by ^{19}F MRS are not quantified by the HPLC/MS method and thereby could explain the deviation in the concentration estimation in both methods. Alternatively, differences in the properties of TF between spiked and *ex vivo* serum samples (e.g. differences in protein composition, conductive properties) might be a source for this deviation. Still, both methods were shown to correlate with each other and indicate that TF concentrations could be measured with ^{19}F MRS in future studies, possibly even as non-invasive tool *in vivo*.

While there are still limitations in terms of technological development — in particular with regard to exact calibration of reference power due to low ^{19}F amounts — we highlight here the usefulness

and general feasibility of this approach for studying the biodistribution of fluorinated drugs. In this study, we needed to address several challenges for detecting TF *in vivo*. The quadrature, cryogenically cooled surface coil that we used in this study confers a theoretical increase in sensitivity of 40% [101] compared to a linear coil, but prohibits a dual-tunable feature that accommodates ^{1}H imaging.

To distinguish the distribution of TF in different brain regions ^{19}F MR imaging or localized ^{19}F MR spectroscopy would be highly valuable. This is possible when studying neuroinflammation with ^{19}F MRI and perfluoro-15-crown-5-ether nanoparticles; the ^{19}F MR signal in the CNS and associated lymphatic system is sufficient for single-voxel spectroscopy e.g. PRESS (Point RESolved Spectroscopy) [61] and ^{19}F MR imaging, even when using a RT coil [61]. This is not the case for small molecules such as TF that are available in much smaller quantities in the CNS. Understanding the specific ^{19}F MR properties of the drug of interest will allow the choice and tailoring of appropriate MR pulse sequences. While determining the specific origin of signals detected with non-localized MR spectroscopy is not possible, hypotheses on the origin of signals could be verified by using single voxel spectroscopy. Nevertheless, due to a low T_2 of TF in serum as well as the low TF concentrations expected *in vivo* at a therapeutic level, localized single-voxel MR spectroscopy or MRSI are not trivial techniques to be applied.

In this study we characterized the MS drug teriflunomide in phantom experiments and *in vivo* in the animal model of MS. The ^{19}F CRP significantly boosts SNR compared to other available RF coil technologies and enabled the *in vivo* detection of TF-derived ^{19}F MR signals in EAE mice within a short time [62]. However, more technological developments are needed to further boost ^{19}F MR signal sensitivity to ultimately achieve drug quantification within specific tissue compartments [102]. The combination of multiple approaches such as using cryogenically cooled RF coils [62], higher magnetic fields [103] and methods to accelerate data acquisition such as compressed sensing [104] will be key to achieve this goal and allow monitoring drugs *in vivo* with ^{19}F MRI.

Abbreviations

BBB: blood brain barrier; CFA: complete Freund's adjuvants; CMC: carboxymethylcellulose; CNS: central nervous system; CRP: cryoprobe; CSF: cerebrospinal fluid; DMD: disease modifying drug; EAE: experimental autoimmune encephalomyelitis; FWHM: full-width half maximum; HPLC/MS: high performance liquid chromatography mass spectrometry; LOD: limit of detection; MOG: myelin oligodendrocyte glycoprotein peptide; MR: magnetic resonance; MRI: magnetic resonance imaging; MRS: magnetic resonance spectroscopy; MS: Multiple Sclerosis; PLP: proteolipid protein peptide; PRESS: Point RESolved Spectroscopy; RRMS: relapse-remitting Multiple Sclerosis; SNR: signal-to-noise ratio; TF: teriflunomide.

Acknowledgments

This study was supported by Sanofi-Aventis, the European Research Council (ERC) to TN (743077, ThermalMR) and the *Deutsche Forschungsgemeinschaft* to SW (DFG WA2804). The authors would like to thank Stefanie Münchberg, Victoria Prochnov and Mariya Aravina for technical assistance.

Author Contributions

CP acquired, analyzed, interpreted the data and wrote the first draft of the manuscript; LS and JMM assisted with data acquisition, analysis and interpretation; MR acquired and analyzed the HPLC/MS data; AF, PRD, HW and AP assisted with analysis of MR data, AF, MN, FP and TN revised the manuscript critically for important intellectual content, SW conceived the experiments, analyzed and interpreted the data and wrote the manuscript with CP.

Supplementary Material

Supplementary figures and tables.
http://www.thno.org/v11p2490s1.pdf

Competing Interests

C.P. received presentation fees from Sanofi-Aventis. J.M.M. received presentation fees from Novartis. M.R. is founder and CEO of Lipidomix GmbH. T.N. is founder and CEO of MRI.TOOLS GmbH and received travel funds from Siemens Healthcare. S.W. received research grants from Novartis and Genzyme and presentation fees from Novartis.

References

1. Dendrou CA, Fugger L, Friese MA. Immunopathology of multiple sclerosis. Nat Rev Immunol. 2015; 15: 545-58.
2. Baecher-Allan C, Kaskow BJ, Weiner HL. Multiple Sclerosis: Mechanisms and Immunotherapy. Neuron. 2018; 97: 742-68.
3. Reich DS, Lucchinetti CF, Calabresi PA. Multiple Sclerosis. N Engl J Med. 2018; 378: 169-80.
4. Krieger SC, Cook K, De Nino S, Fletcher M. The topographical model of multiple sclerosis: A dynamic visualization of disease course. Neurol Neuroimmunol Neuroinflamm. 2016; 3: e279.
5. Sinnecker T, Kuchling J, Dusek P, Dörr J, Niendorf T, Paul F, et al. Ultrahigh field MRI in clinical neuroimmunology: a potential contribution to improved diagnostics and personalised disease management. EPMA J. 2015; 6: 16.
6. Wuerfel J, Sinnecker T, Ringelstein EB, Jarius S, Schwindt W, Niendorf T, et al. Lesion morphology at 7 Tesla MRI differentiates Susac syndrome from multiple sclerosis. Mult Scler. 2012; 18: 1592-9.

7. Sinnecker T, Dorr J, Pfueller CF, Harms L, Ruprecht K, Jarius S, et al. Distinct lesion morphology at 7-T MRI differentiates neuromyelitis optica from multiple sclerosis. Neurology. 2012; 79: 708-14.
8. Absinta M, Sati P, Reich DS. Advanced MRI and staging of multiple sclerosis lesions. Nat Rev Neurol. 2016; 12: 358-68.
9. Filippi M, Preziosa P, Banwell BL, Barkhof F, Ciccarelli O, De Stefano N, et al. Assessment of lesions on magnetic resonance imaging in multiple sclerosis: practical guidelines. Brain. 2019; 142: 1858-75.
10. Geraldes R, Ciccarelli O, Barkhof F, De Stefano N, Enzinger C, Filippi M, et al. The current role of MRI in differentiating multiple sclerosis from its imaging mimics. Nat Rev Neurol. 2018; 14: 199.
11. Thompson AJ, Banwell BL, Barkhof F, Carroll WM, Coetzee T, Comi G, et al. Diagnosis of multiple sclerosis: 2017 revisions of the McDonald criteria. Lancet Neurol. 2018; 17: 162-73.
12. Cohan S, Chen C, Baraban E, Stuchiner T, Grote L. MRI utility in the detection of disease activity in clinically stable patients with multiple sclerosis: a retrospective analysis of a community based cohort. BMC Neurol. 2016; 16: 184.
13. Bermel RA, Naismith RT. Using MRI to make informed clinical decisions in multiple sclerosis care. Curr Opin Neurol. 2015; 28: 244-9.
14. Naismith RT. Multiple sclerosis should be treated using a step-down strategy rather than a step-up strategy-NO. Mult Scler. 2016; 22: 1400-2.
15. Erbayat Altay E, Fisher E, Jones SE, Hara-Cleaver C, Lee J-C, Rudick RA. Reliability of classifying multiple sclerosis disease activity using magnetic resonance imaging in a multiple sclerosis clinic. JAMA Neurol. 2013; 70: 338-44.
16. Tintore M, Rovira A, Rio J, Otero-Romero S, Arrambide G, Tur C, et al. Defining high, medium and low impact prognostic factors for developing multiple sclerosis. Brain. 2015; 138: 1863-74.
17. O'Connor PW, Li D, Freedman MS, Bar-Or A, Rice GP, Confavreux C, et al. A Phase II study of the safety and efficacy of teriflunomide in multiple sclerosis with relapses. Neurology. 2006; 66: 894-900.
18. Tintore M, Vidal-Jordana A, Sastre-Garriga J. Treatment of multiple sclerosis - success from bench to bedside. Nat Rev Neurol. 2019; 15: 53-8.
19. Rommer PS, Milo R, Han MH, Satyanarayan S, Sellner J, Hauer L, et al. Immunological Aspects of Approved MS Therapeutics. Front Immunol. 2019; 10: 1564.
20. Gehr S, Kaiser T, Kreutz R, Ludwig WD, Paul F. Suggestions for improving the design of clinical trials in multiple sclerosis-results of a systematic analysis of completed phase III trials. EPMA J. 2019; 10: 425-36.
21. Tsareva E, Kulakova O, Boyko A, Favorova O. Pharmacogenetics of multiple sclerosis: personalized therapy with immunomodulatory drugs. Pharmacogenet Genomics. 2016; 26: 103-15.
22. Grossman I, Knappertz V, Laifenfeld D, Ross C, Zeskind B, Kolitz S, et al. Pharmacogenomics strategies to optimize treatments for multiple sclerosis: Insights from clinical research. Prog Neurobiol. 2017; 152: 114-30.
23. Pistono C, Osera C, Boiocchi C, Mallucci G, Cuccia M, Bergamaschi R, et al. What's new about oral treatments in Multiple Sclerosis? Immunogenetics still under question. Pharmacol Res. 2017; 120: 279-93.
24. Lassmann H. Targets of therapy in progressive MS. Mult Scler J. 2017; 23: 1593-9.
25. Gomes CM, Abrunhosa AJ, Ramos P, Pauwels EK. Molecular imaging with SPECT as a tool for drug development. Adv Drug Deliv Rev. 2011; 63: 547-54.
26. Perkins AC, Frier M. Radionuclide imaging in drug development. Curr Pharm Des. 2004; 10: 2907-21.
27. Matthews PM, Rabiner EA, Passchier J, Gunn RN. Positron emission tomography molecular imaging for drug development. Br J Clin Pharmacol. 2012; 73: 175-86.
28. Lindner JR, Link J. Molecular Imaging in Drug Discovery and Development. Circ Cardiovasc Imaging. 2018; 11: e005355.
29. Waaijer SJH, Kok IC, Eisses B, Schröder CP, Jalving M, Brouwers AH, et al. Molecular Imaging in Cancer Drug Development. J Nucl Med. 2018; 59: 726-32.
30. Niendorf T, Ji Y, Waiczies S. Fluorinated Natural Compounds and Synthetic Drugs. In: Ahrens ET, Flögel U., editor. Fluorine Magnetic Resonance Imaging. 1 ed: Pan Stanford Publishing, 2016; p: 311-44.
31. Reid DG, Murphy PS. Fluorine magnetic resonance *in vivo*: a powerful tool in the study of drug distribution and metabolism. Drug Discov Today. 2008; 13: 473-80.
32. Wolf W, Presant CA, Waluch V. 19F-MRS studies of fluorinated drugs in humans. Adv Drug Deliv Rev. 2000; 41: 55-74.
33. Stevens AN, Morris PG, Iles RA, Sheldon PW, Griffiths JR. 5-Flourouracil metabolism monitored *in vivo* by 19F NMR. Br J Cancer. 1984; 50: 113-7.
34. McSheehy P, Prior M, Griffiths J. Prediction of 5-fluorouracil cytotoxicity towards the Walker carcinosarcoma using peak integrals of fluoronucleotides measured by MRS *in vivo*. Br J Cancer. 1989; 60: 303-9.
35. Desmoulin F, Gilard V, Malet-Martino M, Martino R. Metabolism of capecitabine, an oral fluorouracil prodrug: (19)F NMR studies in animal models and human urine. Drug Metab Dispos. 2002; 30: 1221-9.
36. Morikawa S, Inubushi T, Morita M, Murakami K, Masuda C, Maki J, et al. Fluorine-19 fast recovery fast spin echo imaging for mapping 5-fluorouracil. Magn Reson Med Sci. 2007; 6: 235-40.
37. Cron GO, Beghein N, Ansiaux R, Martinive P, Feron O, Gallez B. 19F NMR *in vivo* spectroscopy reflects the effectiveness of perfusion-enhancing vascular modifiers for improving gemcitabine chemotherapy. Magn Reson Med. 2008; 59: 19-27.
38. Doi Y, Shimmura T, Kuribayashi H, Tanaka Y, Kanazawa Y. Quantitative (19)F imaging of nmol-level F-nucleotides/-sides from 5-FU with T(2) mapping in mice at 9.4T. Magn Reson Med. 2009; 62: 1129-39.
39. Karson CN, Newton JE, Livingston R, Jolly JB, Cooper TB, Sprigg J, et al. Human brain fluoxetine concentrations. J Neuropsychiatry Clin Neurosci. 1993; 5: 322-9.
40. Karson CN, Newton JE, Mohanakrishnan P, Sprigg J, Komoroski RA. Fluoxetine and trifluoperazine in human brain: a 19F-nuclear magnetic resonance spectroscopy study. Psychiatry Res. 1992; 45: 95-104.
41. Komoroski RA, Newton JE, Cardwell D, Sprigg J, Pearce J, Karson CN. *In vivo* 19F spin relaxation and localized spectroscopy of fluoxetine in human brain. Magn Reson Med. 1994; 31: 204-11.
42. Bolo NR, Hode Y, Nedelec JF, Laine E, Wagner G, Macher JP. Brain pharmacokinetics and tissue distribution *in vivo* of fluvoxamine and fluoxetine by fluorine magnetic resonance spectroscopy. Neuropsychopharmacology. 2000; 23: 428-38.
43. Ji Y, Waiczies H, Winter L, Neumanova P, Hofmann D, Rieger J, et al. Eight-channel transceiver RF coil array tailored for (1)H/(1)(9)F MR of the human knee and fluorinated drugs at 7.0 T. NMR Biomed. 2015; 28: 726-37.
44. Durst P, Schuff N, Crocq M-A, Mokrani M-C, Macher J-P. Noninvasive *in vivo* detection of a fluorinated neuroleptic in the human brain by 19F nuclear magnetic resonance spectroscopy. Psychiatry Res Neuroimaging. 1990; 35: 107-14.
45. Schlemmer H-P, Becker M, Bachert P, Dietz A, Rudat V, Vanselow B, et al. Alterations of intratumoral pharmacokinetics of 5-fluorouracil in head and neck carcinoma during simultaneous radiochemotherapy. Cancer Res. 1999; 59: 2363-9.
46. Lanza GM, Jenkins J, Schmieder AH, Moldobaeva A, Cui G, Zhang H, et al. Anti-angiogenic Nanotherapy Inhibits Airway Remodeling and Hyper-responsiveness of Dust Mite Triggered Asthma in the Brown Norway Rat. Theranostics. 2017; 7: 377-89.
47. Wu L, Wen X, Wang X, Wang C, Sun X, Wang K, et al. Local Intratracheal Delivery of Perfluorocarbon Nanoparticles to Lung Cancer Demonstrated with Magnetic Resonance Multimodal Imaging. Theranostics. 2018; 8: 563-74.
48. Shin SH, Park EJ, Min C, Choi SI, Jeon S, Kim YH, et al. Tracking Perfluorocarbon Nanoemulsion Delivery by 19F MRI for Precise High Intensity Focused Ultrasound Tumor Ablation. Theranostics. 2017; 7: 562-72.
49. Metelev V, Zhang S, Zheng S, Kumar ATN, Bogdanov A, Jr. Fluorocarbons Enhance Intracellular Delivery of Short STAT3-sensors and Enable Specific Imaging. Theranostics. 2017; 7: 3354-68.
50. Derfuss T, Mehling M, Papadopoulou A, Bar-Or A, Cohen JA, Kappos L. Advances in oral immunomodulating therapies in relapsing multiple sclerosis. Lancet Neurol. 2020; p: 336-47.
51. Wiese MD, Rowland A, Polasek TM, Sorich MJ, O'Doherty C. Pharmacokinetic evaluation of teriflunomide for the treatment of multiple sclerosis. Expert Opin Drug Metab Toxicol. 2013; 9: 1025-35.
52. Xu M, Lu X, Fang J, Zhu X, Wang J. The efficacy and safety of teriflunomide based therapy in patients with relapsing multiple sclerosis: A meta-analysis of randomized controlled trials. J Clin Neurosci. 2016; 33: 28-31.
53. Radue EW, Sprenger T, Gaetano L, Mueller-Lenke N, Cavalier S, Thangavelu K, et al. Teriflunomide slows BVL in relapsing MS: A reanalysis of the TEMSO MRI data set using SIENA. Neurol Neuroimmunol Neuroinflamm. 2017; 4: e390.
54. Bar-Or A. Teriflunomide (Aubagio®) for the treatment of multiple sclerosis. Exp Neurol. 2014; 262, Part A: 57-65.
55. Merrill J, Hanak S, Pu S-F, Liang J, Dang C, Iglesias-Bregna D, et al. Teriflunomide reduces behavioral, electrophysiological, and histopathological deficits in the Dark Agouti rat model of experimental autoimmune encephalomyelitis. J Neurol. 2009; 256: 89-103.
56. Merrill JE. *In vitro* and *in vivo* pharmacological models to assess demyelination and remyelination. Neuropsychopharmacology. 2009; 34: 55-73.
57. Ringheim GE, Lee L, Laws-Ricker L, Delohery T, Liu L, Zhang D, et al. Teriflunomide attenuates immunopathological changes in the dark agouti rat model of experimental autoimmune encephalomyelitis. Front Neurol. 2013; 4: 169.
58. Lepore S, Waiczies H, Hentschel J, Ji Y, Skodowski J, Pohlmann A, et al. Enlargement of cerebral ventricles as an early indicator of encephalomyelitis. PloS one. 2013; 8: e72841.
59. Iglesias-Bregna D, Hanak S, Ji Z, Petty M, Liu L, Zhang D, et al. Effects of Prophylactic and Therapeutic Teriflunomide in Transcranial Magnetic Stimulation-Induced Motor-Evoked Potentials in the Dark Agouti Rat Model of Experimental Autoimmune Encephalomyelitis. J Pharmacol Exp Ther. 2013; 347: 203-11.
60. Nair AB, Jacob S. A simple practice guide for dose conversion between animals and human. J Basic Clin Pharm. 2016; 7: 27-31.
61. Waiczies H, Lepore S, Drechsler S, Qadri F, Purfürst B, Sydow K, et al. Visualizing brain inflammation with a shingled-leg radio-frequency head probe for 19F/1H MRI. Sci Rep. 2013; 3: 1280.
62. Waiczies S, Millward JM, Starke L, Delgado PR, Huelnhagen T, Prinz C, et al. Enhanced Fluorine-19 MRI Sensitivity using a Cryogenic Radiofrequency Probe: Technical Developments and *Ex vivo* Demonstration in a Mouse Model of Neuroinflammation. Sci Rep. 2017; 7: 9808.

63. Haase A, Frahm J, Matthaei D, Hanicke W, Merboldt KD. FLASH imaging. Rapid NMR imaging using low flip-angle pulses. J Magn Reson. 1986; 67: 258-66.
64. Hennig J, Nauerth A, Friedburg H. RARE imaging: a fast imaging method for clinical MR. Magn Reson Med. 1986; 3: 823-33.
65. Uğurbil K, Garwood M, Ellermann J, Hendrich K, Hinke R, Hu X, et al. Imaging at high magnetic fields: initial experiences at 4 T. Magn Reson Q. 1993; 9: 259-77.
66. Schindelin J, Arganda-Carreras I, Frise E, Kaynig V, Longair M, Pietzsch T, et al. Fiji: an open-source platform for biological-image analysis. Nat Methods. 2012; 9: 676-82.
67. Kreis R, Boer V, Choi IY, Cudalbu C, de Graaf RA, Gasparovic C, et al. Terminology and concepts for the characterization of *in vivo* MR spectroscopy methods and MR spectra: Background and experts' consensus recommendations. NMR Biomed. 2020; p: e4347.
68. Günther H. NMR spectroscopy: basic principles, concepts, and applications in chemistry. 3 ed. Weinheim: Wiley-VCH. 2013.
69. Near J, Harris AD, Juchem C, Kreis R, Marjańska M, Öz G, et al. Preprocessing, analysis and quantification in single-voxel magnetic resonance spectroscopy: experts' consensus recommendations. NMR Biomed. 2020; p: e4257.
70. Prinz C, Delgado PR, Eigentler TW, Starke L, Niendorf T, Waiczies S. Toward (19)F magnetic resonance thermometry: spin-lattice and spin-spin-relaxation times and temperature dependence of fluorinated drugs at 9.4 T. Magn Reson Mater Phy. 2018; 10.1007/s10334-018-0722-8.
71. Pierson E, Simmons SB, Castelli L, Goverman JM. Mechanisms regulating regional localization of inflammation during CNS autoimmunity. Immunol Rev. 2012; 248: 205-15.
72. Fox RI, Herrmann ML, Frangou CG, Wahl GM, Morris RE, Strand V, et al. Mechanism of action for leflunomide in rheumatoid arthritis. Clin Immunol. 1999; 93: 198-208.
73. El-Khatib AH, Radbruch H, Trog S, Neumann B, Paul F, Koch A, et al. Gadolinium in human brain sections and colocalization with other elements. Neurol Neuroimmunol Neuroinflamm. 2019; 6: e515.
74. Schlemm L, Chien C, Bellmann-Strobl J, Dörr J, Wuerfel J, Brandt AU, et al. Gadopentetate but not gadobutrol accumulates in the dentate nucleus of multiple sclerosis patients. Mult Scler. 2017; 23: 963-72.
75. Boyken J, Niendorf T, Flemming B, Seeliger E. Gadolinium Deposition in the Brain after Contrast-enhanced MRI: Are the Data Valid? Radiology. 2018; 288: 630-2.
76. Li Y, Chen H, Xu J, Yadav NN, Chan KW, Luo L, et al. CEST theranostics: label-free MR imaging of anticancer drugs. Oncotarget. 2016; 7: 6369-78.
77. Liu H, Jablonska A, Li Y, Cao S, Liu D, Chen H, et al. Label-free CEST MRI Detection of Citicoline-Liposome Drug Delivery in Ischemic Stroke. Theranostics. 2016; 6: 1588-600.
78. Wolf W, Presant CA, Servis KL, el-Tahtawy A, Albright MJ, Barker PB, et al. Tumor trapping of 5-fluorouracil: *in vivo* 19F NMR spectroscopic pharmacokinetics in tumor-bearing humans and rabbits. Proc Natl Acad Sci USA. 1990; 87: 492-6.
79. Nakada T, Kwee IL, Griffey BV, Griffey RH. 19F 2-FDG NMR imaging of the brain in rat. Magn Reson Imaging. 1988; 6: 633-5.
80. Florence AT, Attwood D. Solubility of Drugs in Liquids. In: Florence AT, Attwood D, editors. Physicochemical Principles of Pharmacy. London: Macmillan Education UK. 1981; p:125-72.
81. Farrell D, Miranda E, Webb H, Georgi N, Crowley P, McIntosh L, et al. Titration_DB: Storage and analysis of NMR-monitored protein pH titration curves. Proteins. 2010; 78: 843-57.
82. Moser E, Winklmayr E, Holzmüller P, Krssak M. Temperature- and pH-dependence of proton relaxation rates in rat liver tissue. Magn Reson Imaging. 1995; 13: 429-40.
83. Meiboom S, Luz Z, Gill D. Proton Relaxation in Water. J Chem Phys. 1957; 27: 1411.
84. Schilling AM, Blankenburg FB, Bernarding J, Heidenreich JO, Wolf KJ. Intracerebral pH affects the T2 relaxation time of brain tissue. Neuroradiology. 2002; 44: 968-72.
85. Gerken JB. Measurement of pH by NMR Spectroscopy in Concentrated Aqueous Fluoride Buffers. J Fluor Chem. 2011; 132: 68-70.
86. Grant R, Condon B, Moyns S, Patterson J, Hadley D, Teasdale G. Temporal physiochemical changes during *in vitro* relaxation time measurements: the cerebrospinal fluid. Magn Reson Med. 1988; 6: 397-402.
87. Barbucci R, Magnani A, Consumi M. Swelling Behavior of Carboxymethylcellulose Hydrogels in Relation to Cross-Linking, pH, and Charge Density. Macromolecules. 2000; 33: 7475-80.
88. Koshkina O, White PB, Staal AHJ, Schweins R, Swider E, Tirotta I, et al. Nanoparticles for "two color" 19F magnetic resonance imaging: Towards combined imaging of biodistribution and degradation. J Colloid Interface Sci. 2020; 565: 278-87.
89. Jansen JF, Backes WH, Nicolay K, Kooi ME. 1H MR spectroscopy of the brain: absolute quantification of metabolites. Radiology. 2006; 240: 318-32.
90. Corbo C, Molinaro R, Tabatabaei M, Farokhzad OC, Mahmoudi M. Personalized protein corona on nanoparticles and its clinical implications. Biomater Sci. 2017; 5: 378-87.
91. Warnke C, Stuve O, Kieseier BC. Teriflunomide for the treatment of multiple sclerosis. Clin Neurol Neurosurg. 2013; 115 Suppl 1: S90-4.
92. Kaplan J, Cavalier S, Turpault S. Biodistribution of teriflunomide in naive rats vs rats with experimental autoimmune encephalomyelitis. Mult Scler J. 2015; 21: 141-.
93. Rakhila H, Rozek T, Hopkins A, Proudman S, Cleland L, James M, et al. Quantitation of total and free teriflunomide (A77 1726) in human plasma by LC-MS/MS. J Pharm Biomed Anal. 2011; 55: 325-31.
94. Haraoui B. 57 - Leflunomide. In: Hochberg MC, Silman AJ, Smolen JS, Weinblatt ME, Weisman MH, editors. Rheumatology (Sixth Edition). Philadelphia. 2015; p:451-8.
95. Yao X, Liu Y, Song L, Jiang J, Xiao F, Liu D, et al. Development of a simple HPLC-MS/MS method to simultaneously determine teriflunomide and its metabolite in human plasma and urine: Application to clinical pharmacokinetic study of teriflunomide sodium and leflunomide. Biomed Chromatogr. 2019; 33: e4420.
96. Wade KE, Troke J, Macdonald CM, Wilson ID, Nicholson JK. 19F NMR Studies of the Metabolism of Trifluoromethylaniline. In: Reid E, Robinson JD, Wilson ID, editors. Bioanalysis of Drugs and Metabolites, Especially Anti-Inflammatory and Cardiovascular. 1 ed. Boston, MA: Springer US. 1988; p:383-8.
97. Dalvit C, Vulpetti A. Intermolecular and Intramolecular Hydrogen Bonds Involving Fluorine Atoms: Implications for Recognition, Selectivity, and Chemical Properties. ChemMedChem. 2012; 7: 262-72.
98. Brunetti L, Wagner ML, Maroney M, Ryan M. Teriflunomide for the treatment of relapsing multiple sclerosis: a review of clinical data. Ann Pharmacother. 2013; 47: 1153-60.
99. Morgan ET. Impact of infectious and inflammatory disease on cytochrome P450-mediated drug metabolism and pharmacokinetics. Clin Pharmacol Ther. 2009; 85: 434-8.
100. Rzagalinski I, Hainz N, Meier C, Tschernig T, Volmer DA. Spatial and molecular changes of mouse brain metabolism in response to immunomodulatory treatment with teriflunomide as visualized by MALDI-MSI. Anal Bioanal Chem. 2018; p:353-65.
101. Glover GH, Hayes CE, Pelc NJ, Edelstein WA, Mueller OM, Hart HR, et al. Comparison of linear and circular polarization for magnetic resonance imaging. J Magn Reson. 1985; 64: 255-70.
102. Waiczies S, Srinivas M, Flögel U, Boehm-Sturm P, Niendorf T. Special issue on fluorine-19 magnetic resonance: technical solutions, research promises and frontier applications. Magn Reson Mater Phy. 2019; 32: 1-3.
103. Waiczies S, Rosenberg JT, Kuehne A, Starke L, Delgado PR, Millward JM, et al. Fluorine-19 MRI at 21.1 T: enhanced spin-lattice relaxation of perfluoro-15-crown-5-ether and sensitivity as demonstrated in *ex vivo* murine neuroinflammation. Magn Reson Mater Phy. 2018.
104. Starke L, Pohlmann A, Prinz C, Niendorf T, Waiczies S. Performance of compressed sensing for fluorine-19 magnetic resonance imaging at low signal-to-noise ratio conditions. Magn Reson Med. 2019; p:1-17.

9 Publikation 3 Performance of compressed sensing for fluorine-19 magnetic resonance imaging at low signal-to-noise ration conditions

Received: 23 August 2019 | Revised: 19 November 2019 | Accepted: 27 November 2019

DOI: 10.1002/mrm.28135

FULL PAPER

Magnetic Resonance in Medicine

Performance of compressed sensing for fluorine-19 magnetic resonance imaging at low signal-to-noise ratio conditions

Ludger Starke[1] | Andreas Pohlmann[1] | Christian Prinz[1] | Thoralf Niendorf[1,2] | Sonia Waiczies[1]

[1]Berlin Ultrahigh Field Facility (B.U.F.F.), Max Delbrück Center for Molecular Medicine in the Helmholtz Association, Berlin, Germany

[2]Experimental and Clinical Research Center, a joint cooperation between the Charité Medical Faculty and the Max Delbrück Center for Molecular Medicine in the Helmholtz Association, Berlin, Germany

Correspondence
Ludger Starke, Berlin Ultrahigh Field Facility (B.U.F.F.), Max Delbrück Center for Molecular Medicine in the Helmholtz Association, Robert-Rössle-Strasse 10, 13125 Berlin, Germany.
Email: Ludger.Starke@mdc-berlin.de

Funding information
Deutsche Forschungsgemeinschaft, Grants/Award Numbers: DFG WA2804, DFG PO1869, SFB 1365; H2020 European Research Council, Grants/Award Numbers: 743077 (ThermalMR)

Purpose: To examine the performance of compressed sensing (CS) in reconstructing low signal-to-noise ratio (SNR) ^{19}F MR signals that are close to the detection threshold and originate from small signal sources with no a priori known location.

Methods: Regularization strength was adjusted automatically based on noise level. As performance metrics, root-mean-square deviations, true positive rates (TPRs), and false discovery rates were computed. CS and conventional reconstructions were compared at equal measurement time and evaluated in relation to high-SNR reference data. ^{19}F MR data were generated from a purpose-built phantom and benchmarked against simulations, as well as from the experimental autoimmune encephalomyelitis mouse model. We quantified the signal intensity bias and introduced an intensity calibration for in vivo data using high-SNR ex vivo data.

Results: Low-SNR ^{19}F MR data could be reliably reconstructed. Detection sensitivity was consistently improved and data fidelity was preserved for undersampling and averaging factors of $\alpha = 2$ or $= 3$. Higher α led to signal blurring in the mouse model. The improved TPRs at $\alpha = 3$ were comparable to a 2.5-fold increase in measurement time. Whereas CS resulted in a downward bias of the ^{19}F MR signal, Fourier reconstructions resulted in an unexpected upward bias of similar magnitude. The calibration corrected signal-intensity deviations for all reconstructions.

Conclusion: CS is advantageous whenever image features are close to the detection threshold. It is a powerful tool, even for low-SNR data with sparsely distributed ^{19}F signals, to improve spatial and temporal resolution in ^{19}F MR applications.

KEYWORDS

compressed sensing, experimental autoimmune encephalomyelitis, fluorine-19, magnetic resonance, neuroinflammation, signal bias

1 | INTRODUCTION

Fluorine (^{19}F) MRI has been commonly used in cell tracking and molecular imaging.[1-4] Its widespread applicability, along with the challenge that ^{19}F is only sparsely available in vivo, has motivated the development of strategies that enhance signal-to-noise ratio (SNR) efficiency, for example, more sensitive hardware[5-7] and more time-efficient pulse sequences.[8-10] Digital signal processing, particularly compressed sensing (CS),[11-13] is a new avenue to boost detection performance.

The first application of CS to ^{19}F MR methods was in chemical shift imaging.[14-16] When applied to ^{19}F MRI, the potential of CS to improve acquisition time efficiency was demonstrated.[17,18] Under optimal conditions, CS improved SNR efficiency by a factor of ~8.5.[17,18] At SNR = 58, even small features consisting of fewer than 5 voxels were correctly recovered from 32-fold undersampled phantom experiment data.[17] However, lower SNRs (8 and 14) resulted in a loss of these features in all CS reconstructions.[17] In a phantom experiment, reinvesting the time saved by undersampling into increased averaging lowered the detection threshold, when compared to fully sampled data at equal acquisition time.[18] Application of CS to in vivo ^{19}F MR was previously shown in situations where the location of ^{19}F signals in vivo was known: localized wound inflammation and transplantation of labeled pancreatic islets.[17,18] In the latter, 4-fold undersampling lowered the detection threshold, but also introduced false positives.[18] Regarding reconstruction of the correct signal intensity (SI), CS was found to introduce a downward bias of more than 50% in phantom experiments.[17]

From this rich body of literature, it is not clear how well CS performs under more challenging conditions (i.e., when studying small features close to detection thresholds). It is these conditions which necessitate sensitivity improvements most to boost detection and make high resolutions viable. SNR efficiency does not convey information regarding edge preservation,[19,20] and image defects are generally not captured by known noise distributions.[17] Given that CS is a nonlinear algorithm,[11-13] results cannot be extrapolated from experiments studying higher SNRs, and reconstruction methods must be compared at equal acquisition time.[21] This is particularly relevant for quantitative ^{19}F MR studies and raises a fundamental question under which conditions CS improves detection performance without compromising data fidelity. To draw valid conclusions about performance at low SNRs, a large number of reconstructions, signal distributions, and sampling patterns must be investigated to exclude random effects.

Unknown signal locations introduce additional challenges. The measured information and sparsity constraints need to be balanced in CS. For low-SNR data, case-by-case optimization based on visual inspection is not feasible. Given that the optimal choice depends on data scaling, noise level, undersampling factor, and image sparsity,[22] adopting a value optimized for a reference data set is problematic. To address this issue, we propose automatic regularization strength selection following Morozov's discrepancy principle.[23,24]

Studying the distribution of ^{19}F-labeled inflammatory cells in the central nervous system (CNS) during the disease course of experimental autoimmune encephalomyelitis (EAE) is 1 of many biomedical applications that could benefit greatly from improved time efficiency,[1,5,25-28] where addressing the aforementioned issues is necessary to conclude whether CS will be beneficial. EAE is a model of multiple sclerosis characterized by inflammatory lesions in the CNS,[29] which appear in arbitrary locations especially in the cerebrum, but can also follow fine anatomical structures, such as white matter tracts, in the cerebellum.[6] ^{19}F nanoparticles (NPs) are applied intravenously in animal models to study the distribution of inflammatory cell lesions in vivo.[17-21]

To study the performance of CS for ^{19}F MRI applications that include low-SNR conditions, we compared undersampled and CS reconstructed data with conventional Fourier and denoised reconstructions of fully sampled data. Reliability of automatic regularization strength selection and dependence of CS performance on undersampling factor and noise level was investigated in digital and MR phantom experiments. Fully sampled ^{19}F MR data of inflammation in EAE were acquired from ex vivo tissue phantoms and in vivo animals to allow preparation of 2000 k-spaces with different undersampling patterns and noise realizations by retrospective undersampling. The 2 setups corresponded to different EAE cohorts. In a third cohort, prospectively undersampled in vivo data were acquired with a genuine CS sequence. For performance assessment, we examined the root-mean-square deviation (RMSD) from the reference as a universal metric of image quality, the number of recovered features or true positive rates (TPRs) to assess detection performance, false discovery rates (FDRs) to quantify data fidelity, and the relative SI deviation from the reference to investigate bias effects. Finally, we propose a scheme for signal-level–specific intensity calibration using the ex vivo tissue collection as calibration data and assess the method's performance for in vivo measurements.

2 | METHODS

Simulations, data preparation, image reconstruction, and analysis were performed in MATLAB (R2018a; The MathWorks, Inc., Natick, MA), using pvmatlab for data import (Buker Biospin MRI, Ettlingen, Germany).

2.1 | Compressed sensing, denoising, and automatic regularization strength selection

CS reconstructions were computed identically for all setups, and denoised images were computed by applying the same

algorithm to fully sampled data. ^{19}F MR images are generally sparse, with the main component being background. It has been shown that ^{19}F chemical shift Imaging reconstructions enforcing strict data consistency and using only regularization with the ℓ^1-norm of the image, $\|r\|_1 = \sum_i |r_i|$, necessitate additional postprocessing attributable to spike artifacts.[14,15] Similar to previous work,[17] we therefore opted for relaxed data consistency, the common choice for noisy data,[30] and also added a total variation constraint to ensure robustness at low SNRs and effective noise reduction. The CS reconstruction $\hat{r}$ was computed as (Equation 1):

$$\hat{r} = \text{argmin}_r \left\| F_u r - y \right\|_2^2 + \lambda \left(\|r\|_1 + \text{TV}_{\text{iso}}(r) \right), \quad (1)$$

where F_u denotes the undersampled Fourier transform, y the measured k-space data, $\text{TV}_{\text{iso}}(r)$ the isotropic total variation,[31] and λ the regularization strength controlling the balance between the regularization terms and the data and thereby the data consistency $\varepsilon = \left\| F_u \hat{r} - y \right\|_2^2$. The used regularization terms have the advantage of being easily interpretable compared to wavelet constraints commonly utilized in anatomical MRI.[32] Equation 1 was solved using an implementation of the accelerated alternating direction method of multipliers[33] with fast Fourier transform–based exact inversion exploiting the circulant matrix structure that arises from periodic boundary conditions for the total variation.[33,34]

To determine the desired data consistency, we applied Morozov's discrepancy principle.[23,24] The data consistency of the reconstruction is matched with the accuracy of the data itself. Given noise standard deviation σ and n sampled complex data points, the expected deviation of the data from true, but unknown, image r_t is $\varepsilon' \left\langle \left\| F_u r_t - y \right\|_2^2 \right\rangle = 2n\sigma^2$. Multiple reconstructions are performed until a value of λ is found for which $\varepsilon \approx \eta\varepsilon'$ with η specifying the desired ratio of ε and ε'.[24,35] To this end, we used the Illinois algorithm.[36]

We performed simulations based on a digital phantom to determine a suitable value of η. The [128 × 128] pixel phantom consisted of 8 circular features (each with a diameter of 4.9 pixels), with SI (1/8, 2/8, …, 8/8) forming a larger circle. Partial volume effects were emulated by creating the digital phantom image 20 times more resolved, before downsampling. k-Space data were generated by adding complex Gaussian noise to the digital phantom before applying the Fourier transform and, if appropriate, an undersampling mask in 1 dimension (see "Data Preparation" section). We examined 5 different noise levels ($\sigma = 0.01$ to $\sigma = 0.2$ with 4-fold undersampling ($f_{us} = 1/4$) and 5 different undersampling factors ($f_{us} = 1$ to $f_{us} = 1/8$) with $\sigma = 0.04$. For each condition and 20 values of η between 0.9 and 1.05, we performed 40 reconstructions of data with individual noise realizations and undersampling masks. As a metric of image quality, we computed the mean and standard deviation of the RMSD from the reference.

2.2 | MR measurements and experimental setups

We used 3 MR measurement setups to examine CS performance. All MR experiments were carried out on a 9.4T MR system (BioSpec 94/20, G_{max} = 440 mT/m, slew rate = 3440 mT/m/ms, B-GA12, PV6.1 software, Bruker BioSpin MRI; Bruker Corporation, Billerica, MA), using an ^{19}F/^{1}H mouse head volume radiofrequency (RF) coil.[5] Animal experiments were conducted in accord with procedures approved by the Animal Welfare Department of the State Office of Health and Social Affairs Berlin (LAGeSo, Ref0127-16) and conformed to guidelines to minimize discomfort to animals (86/609/EEC).

2.2.1 | Setup 1: capillary tube phantom

Eight concentrically-arranged capillary tubes (inner diameter, 1.15 mm) submerged in water (placed horizontally in the magnet bore) were filled with (1/8, 2/8, … 8/8) × 33% trifluoroethanol diluted in water and 1 mmol/L of gadolinium (Magnevist; Bayer Vital, Leverkusen, Germany). Axial 2D images were acquired using rapid acquisition with relaxation enhancement (RARE; flip-back module, echo train length [ETL] = 8, TR = 600 ms, TE = 12 ms, [30 × 30] mm2 field of view [FOV], 128 × 128 matrix). To construct data with different noise levels, 6 slice thicknesses were used (0.1, 0.25, 0.5, 1, 2.5, and 5 mm) and 64 repetitions/slice acquired. The digital phantom described in the preceding section was designed to conform to this phantom such that the MR experiment could be replicated by simulations.

2.2.2 | Setup 2: ex vivo EAE tissue

EAE was actively induced in female 3-month-old SJL/J mice (n = 5), by subcutaneously immunizing with the CNS antigen proteolipid protein ($PLP_{139–151}$, 250 µg/animal) emulsified with Mycobacterium Tuberculosis H37RA (800 µg/animal in 100 µL of complete Freund's adjuvant).[37] Pertussis toxin (1.25 ng/µL in 200 µL of phosphate-buffered saline [PBS]) was administered intraperitoneally on days 0 and 2. Animals were weighed daily, and a neurological scoring was performed daily to assess the EAE symptoms. Adding up scoring points (righting reflex weakness 0.5, tail paresis 0.5, tail paralysis 1, unilateral hindlimb paresis 0.5, bilateral hindlimb paralysis 1, unilateral forelimb paresis 0.75, and bilateral forelimb paralysis 1.5) results in the final EAE score.

High-fluorine-content Pluronic-PFCE NPs consisting of perfluoro-15-crown-5-ether (PFCE; Fluorochem Ltd, Hadfield, UK), emulsified in Pluronic F-68 (Sigma-Aldrich,

Steinheim, Germany), were prepared (1.2 M) and characterized as previously described.[26,38] NPs containing 5 µmol of PFCE were administered daily from day 5 after immunization until the end of the experiment.[6] Animals were sacrificed on day 10 using a lethal dose of anesthetic and transcardially perfused (20 mL of PBS and 20 mL of 4% paraformaldehyde [PFA] fixative). Tissue was prepared for ex vivo MRI as described previously[6] and secured within 15-mL tubes filled with 4% PFA, keeping the CNS as well as draining lymph nodes in situ. A cylindrical cap (diameter 3 mm, height 1 mm) containing NPs (2 mM of PFCE in 2% agarose) was fixed outside of the tube as an external standard. ^{19}F MRI was conducted using 3D-RARE (flip-back module, ETL = 40, TR = 800 ms, TE = 4.1 ms, [40 × 16 × 16] mm^3 FOV, 100 × 40 × 40 matrix, 25 repetitions, each repetition = 6 averages). For ^{1}H MR, 3D-RARE (flip-back module, ETL = 8, TR = 1000 ms, TE = 5.6 ms, [40 × 16 × 16] mm^3 FOV, 241 × 96 × 96 matrix, 1 average) was used.

2.2.3 | Setup 3: in vivo EAE model, measurements with retrospective undersampling

In a second cohort of EAE mice (n = 5), 11 fully sampled data sets were acquired between days 10 and 14 after induction. EAE was induced as described for setup 2. Mice were anesthetized using a mixture of isoflurane (0.5–1.5%) in pressurized air and oxygen as inhalation narcosis. The animal was placed on a warm animal MR bed and supplied with oxygen and air. Respiration was monitored using a respiration pad and temperature by a rectal probe. To distinguish NP ^{19}F signals from isoflurane, excitation/refocusing RF pulses were restricted to a bandwidth of 3000 Hz. 3D MRI was performed as in setup 2, keeping parameters including resolution the same, but reducing FOV and matrix size in the frequency-encoding direction to [45 × 16 × 16] mm^3 and 112 × 40 × 40 or 270 × 96 × 96 for ^{19}F or ^{1}H imaging, respectively. In vivo, only 25 repetitions could be acquired. The PFCE NP cap used in setup 2 was positioned on the tooth bar.

2.2.4 | Setup 4: in vivo EAE model, measurements with prospective undersampling

In a third cohort of EAE mice (n = 4), 4 data sets with prospective undersampling were acquired on days 12 to 14 after EAE induction (as described for setups 2 and 3). We developed a 2D-RARE CS protocol for ^{19}F MRI (flip-back module, ETL = 40, TR = 1020 ms, TE = 5.1 ms, [20 × 20] mm^2 FOV, 128 × 128 matrix, 3.2-mm slice thickness, 0.4-mm slice gap, 6 slices). Two hundred ninety-six, 592, and 1184 averages were acquired with no, 2-fold, and 4-fold undersampling, respectively (acquisition time = 20 minutes). The fully sampled measurement was repeated 4 times as a reference (80 minutes), and a pure noise scan was acquired to determine the noise level.[39] For ^{1}H MR, 2D-RARE (no flip-back module, ETL = 4, TR = 1000 ms, TE = 5.5 ms, [20 × 20] mm^2 FOV, 256 × 256 matrix, 0.8 mm slice thickness, 0.4 mm slice gap, 18 slices, 8 averages) was used.

2.3 | Undersampling and data preparation

Undersampling patterns were generated based on polynomial variable-density distributions adapted from Zijstra et al.[40] For setups 1 to 3, undersampled data were created by retrospectively undersampling k-space data in the phase-encoding direction(s). For setup 4, undersampling was implemented prospectively in the data acquisition. Ten percent of the sampled k-space lines were assigned deterministically to the k-space center. The remaining lines were drawn randomly. For the 2D acquisitions (setups 1 and 4), undersampling masks were sampled from the 1D distribution (Equation 2):

$$p\left(k_x\right) \propto \left(1-\left|k_x\right|\right)^{\frac{3}{2}}, \tag{2}$$

where $k_x \in [-1, 1]$ denotes the x-position of the k-space line. Similarly, a 2D distribution was used to undersample the 3D data of setups 2 and 3 (Equation 3):

$$p\left(k_x, k_y\right) \propto \max\left(1-\sqrt{k_x^2+k_y^2}, 0\right)^{\frac{3}{2}}, \tag{3}$$

where k_x, $k_y \in [-1, 1]$ denote x and y positions of the sampled lines. Both distributions are weighted toward lower spatial frequencies by choosing an exponent >1.

We compared Fourier and denoised reconstructions of fully sampled data with CS reconstructions of undersampled data at equal scan time. For setups 1 to 3, multiple repetitions were averaged to offset the accelerated data acquisition (Figure 1A). Averaging was performed on the k-space data before image reconstruction. The factor α denotes undersampling and averaging: $\alpha = 1$ signifies fully sampled data ($f_{us} = 1$); $\alpha = 3$ signifies 3-fold undersampling ($f_{us} = 1/3$) with 3-fold averaging. Table 1 summarizes the data preparation for all setups.

2.3.1 | Setup 1

For each slice thickness, the SI of the tube with the highest ^{19}F signal was determined. Because of slice profile imperfections, the SI values are not simply proportional to the slice thickness. The data were scaled relative to each other by assigning the same SI to the tube with the highest ^{19}F signal. Twelve noise-level conditions were examined (Table 1).

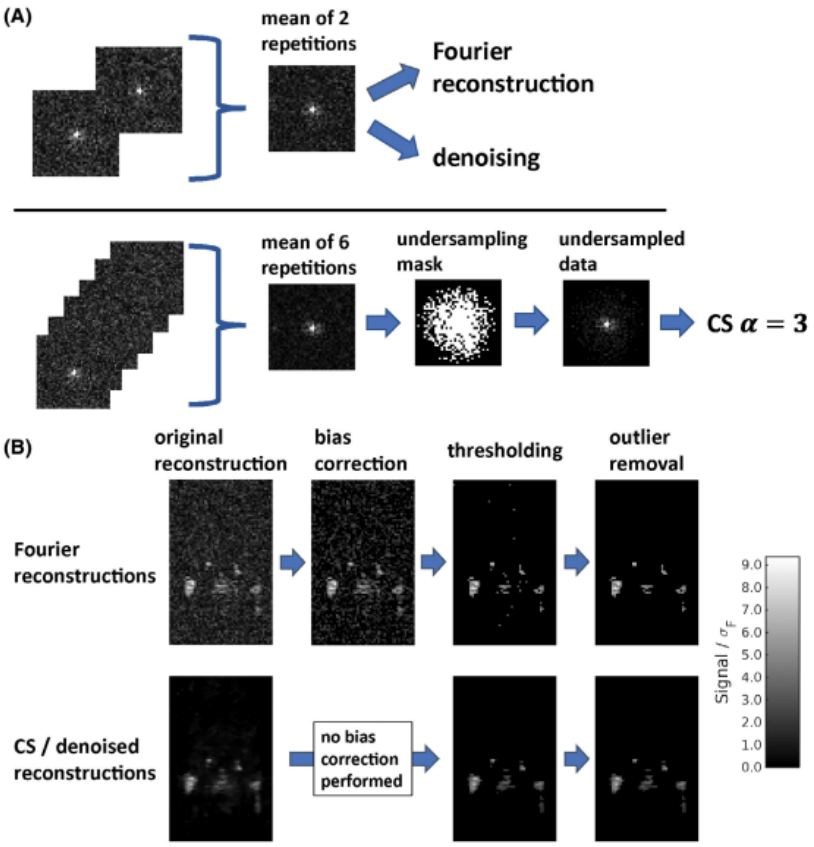

FIGURE 1 Data preparation and background subtraction. (A) In the MR experiments of setups 1 to 3, multiple repetitions of fully sampled data were acquired, which were then averaged to generate data with different noise levels. For the EAE experiments (setups 2 and 3), the acquisition of a single repetition took 3 minutes 12 seconds. Thus, for example, fully sampled data corresponding to a measurement time of 6 minutes 24 seconds was generated by averaging 2 randomly selected repetitions. These data were then either reconstructed using a simple Fourier transform or they were denoised. To generate 3-fold undersampled data for the same measurement time ($\alpha = 3$), 6 randomly selected repetitions were averaged before application of an undersampling mask focusing on the k-space center. Multiple noise realizations were obtained by selecting different repetitions. (B) Before further analysis, image voxels were classified as either signal or background. Here, the used multistep procedure is demonstrated in a slice of an exemplary Fourier reconstruction and CS reconstruction of in vivo data (setup 3). The slice is cropped in read direction to focus the illustration on the fluorine signal. For the Fourier reconstructions only, first the Rician noise bias was corrected. Second, the data were thresholded at 3.5σ (Fourier reconstructions) or 2σ (denoised and CS reconstructions), where σ denotes the noise standard deviation of the underlying k-space data. Last, remaining groups of <3 connected signal voxels were interpreted as outliers and removed from the data. Denoised reconstructions were treated identical to CS reconstructions. σ_F in the label of the color scale denotes the noise standard deviation of the Fourier reconstruction

These conditions signify different measurement times and are distinguished by peak SNR ($pSNR_F$, the SNR of the highest SI tube in the Fourier reconstruction). For each noise condition and each undersampling and averaging factor ($\alpha = 1$ to 8), 60 k-space data sets with individual undersampling masks and combinations of averaged repetitions were generated. Artificial data were generated based on the digital phantom with the same noise conditions, undersampling and averaging factors, and number of data sets. Thus, for both the capillary tube phantom and digital phantom, 5760 different k-spaces were reconstructed.

2.3.2 | Setups 2 and 3

In the EAE model, 5 measurement times (192–960 seconds) were investigated. Four CS undersampling and averaging factors were used ($\alpha = [2, 3, 4, 5]$). For each

TABLE 1 Summary of acquired data, data preparation, and computed reconstructions

	Setup 1		Setup 2	Setup 3	Setup 4
	Capillary tube phantom	Digital phantom	EAE ex vivo	EAE in vivo	EAE in vivo
Dimension	2D	2D	3D	3D	2D
No. of individual datasets	1	1	5	11	4
Data in each dataset	6 slice thicknesses (0.1–5.0 mm) with 64 repetitions each	-	40 repetitions	25 repetitions	Fourier: 4 repetitions $\alpha = 2$: 1 rep. $\alpha = 4$: 1 rep.
Ground truth	Average of 64 repetitions, slice thickness 5 mm ($pSNR_F = 481.5$)	Digital phantom	Average of 40 repetitions (meas. time 128 min)	Average of 25 repetitions (meas. time 80 min)	Average of 4 repetitions (meas. time 80 min)
No. of investigated measurement times	12	12	5	5	1
Corresponding fully-sampled data	0.1 mm slice thickness, 1 average ($pSNR_F = 1.0$) to 2.5 mm slice thickness, 2 averages ($pSNR_F = 41.1$)	$pSNR_F = 1.0$ to $pSNR_F = 41.1$	1 repetition (192 sec) to 5 averaged repetitions (960 sec)	1 repetition (192 sec) to 5 averaged repetitions (960 sec)	1 repetition
Investigated acquisition and reconstruction methods	Fourier, denoised, CS $\alpha = 2$ to CS $\alpha = 8$	Fourier, denoised, CS $\alpha = 2$ to CS $\alpha = 8$	Fourier, denoised, CS $\alpha = 2$ to CS $\alpha = 5$	Fourier, denoised, CS $\alpha = 2$ to CS $\alpha = 5$	Fourier, denoised, CS $\alpha = 2$, CS $\alpha = 4$
No. of reconstructions for each measurement time and method	60	60	5	5	1
Overall no. of recon.	6480	6480	750	1650	16

$pSNR_F$ denotes the peak SNR of the Fourier reconstruction at equal measurement time and α the factor of undersampling and averaging.

measurement time and each acquisition and reconstruction method, 5 k-space datasets were built. For the 5 ex vivo and 11 in vivo data sets, this led to overall 625 and 1375 different k-spaces.

2.3.3 | Setup 4

No further data preparation was required because of prospective undersampling.

2.4 | Data analysis

Performance was assessed by comparing reconstructions with fully sampled high-SNR reference data. The average of 64 repetitions of the thickest slice (pSNR = 481.5) and the digital phantom itself were used in setup 1. In setup 2, a measurement time of 128 minutes and in setups 3 and 4 measurement times of 80 minutes were used (Table 1).

Each data set of setup 3 was considered to be independent because the distribution of the ^{19}F MR signal changed over time. Before further analysis, the ^{19}F MR signal from the reference cap and investigated sample was segregated and only the latter part included in the evaluation of performance (setups 2 and 3).

2.4.1 | Rician noise bias correction

Conventional Fourier-reconstructed MR magnitude images are biased because of noise effects.[41] The measured signal follows a Rician distribution.[42] For true but unknown signal, S_t, the expected measured signal is[43] (Equation 4):

$$<S>_{p(S|S_t)} = \sigma\sqrt{\frac{\pi}{2}}L_{1/2}\left(-\frac{S_t^2}{2\sigma^2}\right), \quad (4)$$

where σ denotes the standard deviation of the Gaussian noise in the real and imaginary image and $L_{1/2}$ a Laguerre polynomial.

This function cannot be analytically inverted to yield a function $S_t(\langle S \rangle)$. Thus, we inverted it by means of a lookup table to implement the noise correction.[41] Noise bias correction was applied only to Fourier reconstructions (Figure 1B).

2.4.2 | Background subtraction

All reconstructions were thresholded to distinguish signal and background voxels based on the noise standard deviation of the underlying k-space data σ (Figure 1B). The threshold was set to 3.5σ for Fourier reconstructions and to 2σ for CS and denoised reconstructions (reflecting reduced background noise level). Groups of <3 connected signal voxels were removed as outliers (Figure 1B).

2.4.3 | Performance metrics

As a general metric of image quality, we used the RMSD from the reference. To visualize image quality gains between methods, we computed the relative RMSD (RMSD divided by the average RMSD of the Fourier reconstructions at equal measurement time). For setups 2 and 3, also the standard deviation of the relative RMSD over all reconstructions with a given measurement time and reconstruction method was calculated.

In setup 1, the number of detected tubes was counted as a measure of detection performance. Tubes were counted as detected if more than half of the corresponding voxels were classified as signal. For setups 2, 3, and 4, we used TPRs as a statistical measure of sensitivity and FDRs as a measure of reliability (Equations 5 and 6):

$$\mathrm{TPR} = n_{\mathrm{TP}} / \left(n_{\mathrm{TP}} + n_{\mathrm{FN}}\right) \tag{5}$$

$$\mathrm{FDR} = n_{\mathrm{FP}} / \left(n_{\mathrm{TP}} + n_{\mathrm{FP}}\right), \tag{6}$$

where n_{TP}, n_{FN}, and n_{FP} denote the number of true positives, false negatives, and false positives, respectively. We used a sliding window approach to compute signal-level–specific TPRs (Figure 2) and FDRs: All reconstructions were scaled to σ_{F} (noise standard deviation of the Fourier reconstruction at equal scan time) to make results at different measurement times comparable. The TPR was computed for different levels of the reference signal, S_r, whereas the FDR was computed for different levels of the measured signal, S. Four hundred windows with a width of 0.5 σ_{F} and equally spaced centers between 0 and 8 σ_{F} were considered. To combine the results for different reconstructions, the weighted mean and standard deviation were computed with weights given by the number of true signal voxels for the TPR and the number of observed signal voxels for the FDR (Figure 2). For setup 4, only the weighted mean was computed because of the smaller sample size.

For setup 1, we determined the signal deviation (measured signal divided by reference signal, S/S_t) averaged over all true positive voxels. For setups 2 and 3, the signal deviation of true positive voxels in each reconstruction was computed for windows of the measured signal, S (Figure 2), whereas mean and standard deviation were computed as weighted by the number of true positives in the subinterval. ^{19}F concentration was determined in the reference measurements by comparing signal intensities in tissue with those in the NP cap.

2.4.4 | Signal intensity calibration

Signal deviations measured in setup 2 (ex vivo) were used to compute a signal-level and method-specific correction factor, which was then applied to calibrate the reconstructions of setup 3 (in vivo), as illustrated in Figure 3. A fifth-degree polynomial was fitted to the signal deviation observed in the reference setup, yielding a function $f_\beta\left(\frac{S}{\sigma_{\mathrm{F}}}\right)$ for every reconstruction method β smoothly approximating the deviation at S/σ_{F}. The corrected signal $S_i^{(c)}$ for voxel i of the in vivo data was then computed as (Equation 7):

$$S_i^{(c)} = \left(f_\beta\left(\frac{S_i}{\sigma_{\mathrm{F}}}\right)\right)^{-1} S_i. \tag{7}$$

3 | RESULTS

3.1 | Automatic regularization strength selection

Choice of parameter η strongly influenced the suppression of background noise and the rendering of low-SNR features, following qualitative assessment (Figure 4A). Dependence of image quality on η was quantified by computing the RMSD from the reference (Figure 4B,C). For 4-fold undersampling, image quality was barely affected at $0.93 < \eta < 0.98$ for various noise levels (Figure 4B). In this range, RMSD differences remained below random data variability. The same held true for $f_{\mathrm{us}} = 1/6$ and $f_{\mathrm{us}} = 1/8$ (Figure 4C). Pure denoising and $f_{\mathrm{us}} = 1/2$ results, however, depended more critically on η (Figure 4C), with optimal performance at $\eta = 0.979$ and $\eta = 0.963$, respectively. Thus, $\eta = 0.97$ was chosen for all further reconstructions.

3.2 | Performance of CS in phantom experiments

Compared to Fourier reconstructions at the same measurement time, CS improved image quality and increased the number of detected features in phantom experiments (Figure 5A). No false positives occurred. At $\mathrm{pSNR_F} = 1.0$, the RMSD was

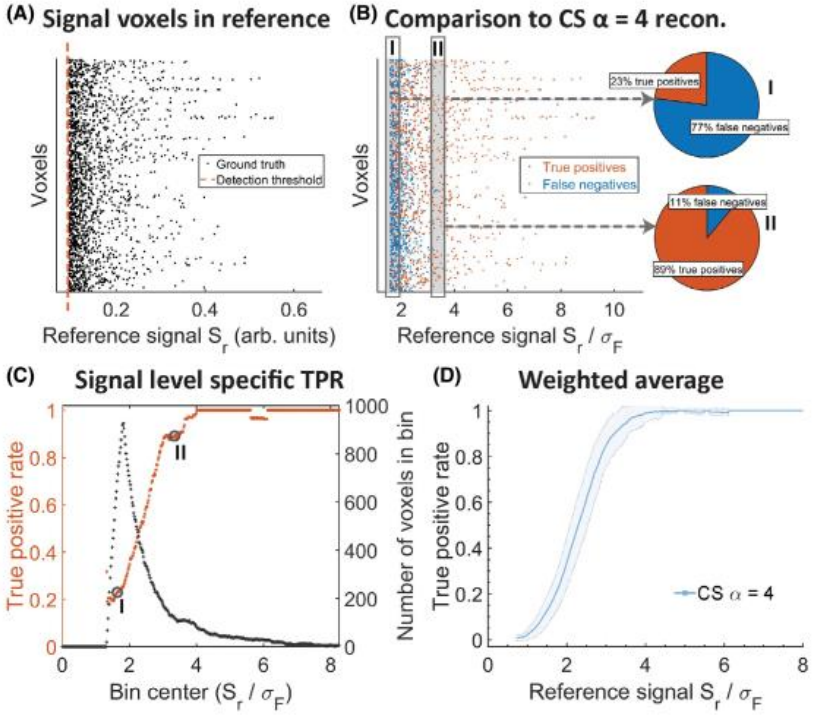

FIGURE 2 Computation of signal-level–specific TPRs. Based on data with a long scan time, a reference was computed for each data set. This reference typically contained a few hundred voxels above the detection threshold (A). The voxels are shown in an arbitrary order. A given reconstruction correctly detected a subset of these signal voxels (true positives), while other voxels are classified as background (false negatives; B). It is expected that the detection performance mainly depends on the SNR. Thus, the signal level is normalized by the noise standard deviation of the Fourier reconstruction at equal scan time σ_F to allow comparisons between different reconstruction methods and data sets. Considering only a subinterval of the signal range, a signal-level–specific TPR can be computed (I and II). Computing TPRs for a moving window yields a TPR curve summarizing the detection performance in a single reconstruction (C). The number of reference signal voxels in the window determines the reliability of the obtained results. Thus, it is used as a weight when averaging results for, for example, CS $\alpha = 4$ reconstructions from all data sets and investigated measurement times (d). The weighted standard deviation serves as a measure of variability. FDRs and SI deviations were computed analogously. arb. units = arbitrary units

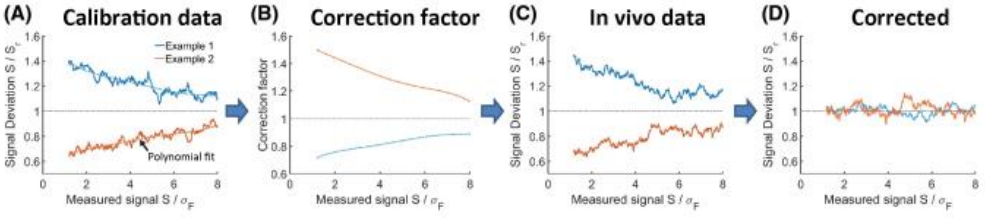

FIGURE 3 Signal intensity calibration. The figure shows artificial example data for 2 hypothetical reconstruction methods. (A) The intensity deviation is computed at different signal levels for a given reconstruction method based on a high-SNR reference. These reference calibration data should have a signal distribution similar to the in vivo data that need correction. The calibration data could be ex vivo data from a different animal cohort as shown in this article. For retrospective studies, this could also be ex vivo data acquired from the same animals postmortem. Even phantom or simulated data could be used. A smooth approximation of the observed deviation is achieved by fitting a fifth-degree polynomial function. (B) The inverse of this polynomial fit yields a method- and signal-level–specific correction factor. (C) Signal deviation observed in in vivo data reconstructed with the 2 methods. (D) Multiplication with the correction factor yields on average unbiased estimates

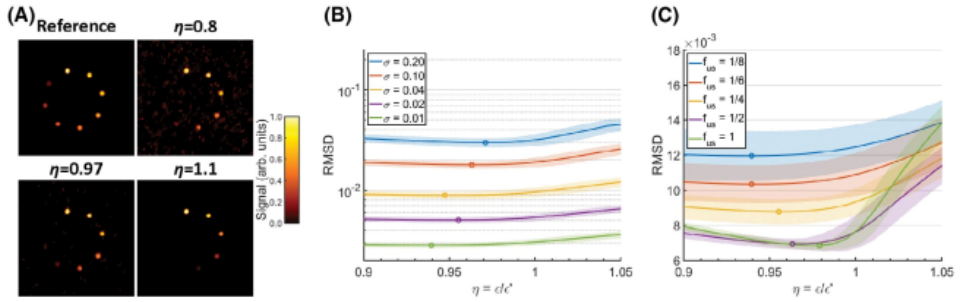

FIGURE 4 Automatic regularization strength selection. The discrepancy principle selects a value for the regularization strength by matching the data consistency of the reconstruction ε with the deviation of the data from the true, but unknown, image ε'. Their desired relation is specified by parameter $\eta = \varepsilon/\varepsilon'$. (a) Digital phantom reference with example reconstructions ($f_{us} = 1/4$, $\sigma = 0.1$). For $\eta = 0.8$, the image is only partially denoised and retains aliasing artifacts, making it difficult to distinguish between true features and noise. With $\eta = 0.97$, most features are well delineated and distinguishable from the background. With $\eta = 1.1$, the reconstruction is oversmoothed. Signal intensities are depressed and low-intensity features are missing. (b) RMSD from the reference for different values of η at 4-fold undersampling ($f_{us} = 1/4$) and 5 different noise standard deviations σ. The shaded area is given by the standard deviation of the metric over 40 reconstructions. The circle labels the minimal mean RMSD. (c) Analogous results for 5 different undersampling factors at $\sigma = 0.04$

equally high for all methods given that only few signal voxels were detected (Figure 5B). CS reconstructions were advantageous in the range of $pSNR_F = 1.5$ to 29.1. Between $pSNR_F = 2.1$ and $pSNR_F = 16.1$, CS reduced the RMSD by more than 20%. Whereas the largest reduction was achieved with $\alpha = 8$ (46%), most of the improvement was already achieved with $\alpha = 4$ (up to 45%; Figure 5B). At $pSNR_F = 1.5$, only $\alpha > 4$ offered an improvement >2%. At $pSNR_F = 29.1$, only $\alpha < 6$ was beneficial. Fourier reconstructions were only superior to CS at $pSNR_F = 41.1$, but here the absolute error in CS reconstructions was still small.

CS reconstructions consistently detected more image features (Figure 5C). Performance improved with increasing α though the difference between $\alpha = 6$, 7, or 8 was small (Figure 5C). The strongest improvement was achieved in conditions where few or no features were observed using conventional methods: at $pSNR_F = 3.0$ on average 5.1 tubes were detected with CS $\alpha = 8$, 4.3 with $\alpha = 4$, 2.8 with $\alpha = 2$, and only 0.1 in the Fourier reconstructions. At $pSNR_F = 6.2$, the difference between $\alpha = 8$ and $\alpha = 2$ was reduced to an average of 6.9 and 6.0 detected features. At $pSNR_F = 41.1$, all tubes were detected regardless of the method.

The signal was underestimated by up to 39% ($S/S_t = 0.61$) averaged over all true positive pixels in CS and denoised reconstructions (Figure 5D). The largest deviations were observed in noisy conditions ($pSNR_F = 2.1$–4.3) and with higher α factors. However, the trend was reversed at the lowest SNRs, and in some cases an overestimation occurred (CS $\alpha = 5$ at $pSNR_F = 1.0$ and denoised reconstructions at $pSNR_F = 2.1$). The average deviation dropped to <20% at $pSNR_F \geq 11.4$ for all α values. Fourier reconstructions also displayed an SI bias despite Rician noise bias correction. In contrast to CS, the signal was overestimated by up to 41% close to the detection threshold ($pSNR_F = 3.0$). For $pSNR_F \geq 8.8$, the average signal overestimation was below 5%.

3.3 | Performance of CS in simulations of a digital phantom

The results obtained from the experimental phantom setup could be accurately replicated in simulations (Figure 5E–H). It was only at high SNRs, especially at $pSNR_F = 41.1$, that CS performed better in simulations compared to measured MR data: This was the case for relative RMSD (Figure 5F) and signal deviation (Figure 5H), but not signal detection (Figure 5G).

3.4 | Performance of CS in animal experiments

We next studied CS performance using retrospective undersampling in the EAE animal model. In this animal model, some of the ^{19}F signals are close to the detection threshold as shown from representative reconstructions of both ex vivo (Figure 6A) and in vivo (Figure 6E) data. Additional reconstructions can be found under: central.xnat.org/data/projects/CSperf_19F-MRI. Compared to Fourier and denoised reconstructions, more true-signal voxels were detected with CS; already, CS $\alpha = 2$ identified features that would have remained undetected using conventional approaches. Although more true positive ^{19}F signals were uncovered with increasing α, more false positives also emerged; these generally had

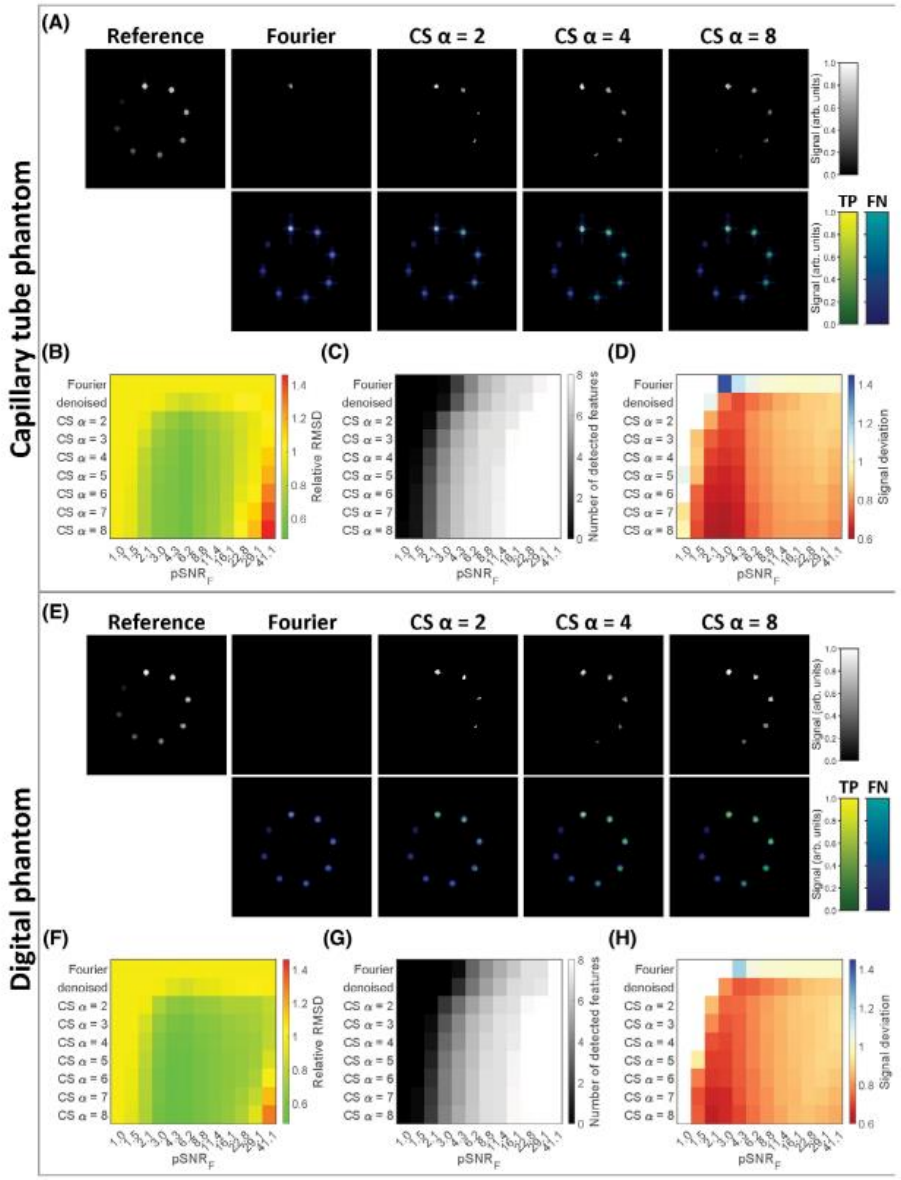

FIGURE 5 Phantom experiments (setup 1). (A) to (D) show results for the capillary tube phantom MR data and (F) to (H) for the digital phantom simulations. (A,E) Example reconstructions. The second line depicts the same reconstructions as the first with true positives (TPs) in green/yellow and false negatives (FNs) in blue/turquoise. No false positives occurred in these examples. (B,F) RMSD from the reference relative to the RMSD of the Fourier reconstruction at equal scan time. $pSNR_F$ denotes the peak SNR in the Fourier reconstruction at equal scan time. (C,G) Average number of detected features. A tube was counted as detected if half of its voxels were classified as signal. (D,H) Signal deviation averaged over all true positive voxels. The deviation was calculated as measured signal divided by reference signal

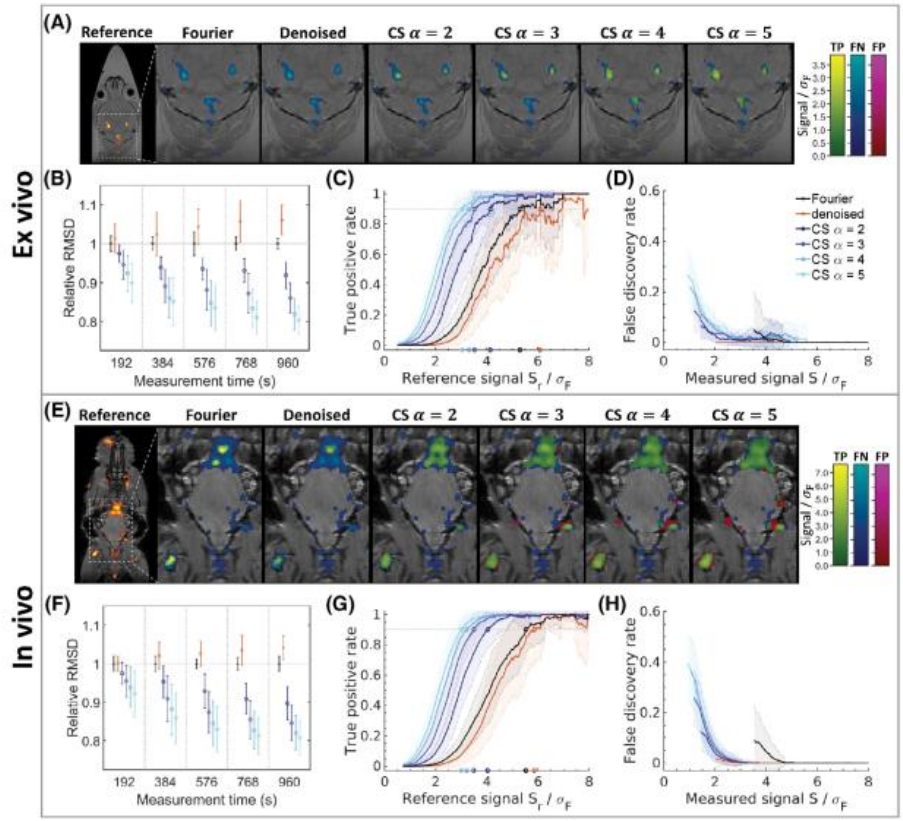

FIGURE 6 Detection performance for imaging inflammation in the EAE mouse model (setups 2 and 3). (A) to (D) show results for the ex vivo condition (setup 2) and (E) to (H) for the in vivo condition (setup 3). A legend is displayed in (D). (A,E) Comparisons of the different acquisition and reconstruction methods for exemplary slices. The reconstructions in both subfigures correspond to a measurement time of 16 minutes (960 seconds). A whole view of the slice with ^{19}F MR signal is shown in the reference image (far left) in the standard red hot color scale. True positives (TP) shown in green/yellow, false negatives (FN) in blue/turquoise, and false positives (FP) in red/violet were calculated in accord with the reference. (B,F) RMSD from the reference relative to the RMSD of the Fourier reconstruction at equal measurement time. Bars show the standard deviation of the measured improvement. (C,G) True positive rates (TPRs). Circles indicate the signal level where a TPR of 90% is reached. σ_F is the noise standard deviation of the Fourier reconstruction at equal measurement time and S_r the signal level in the reference. The shaded area marks the weighted standard deviation (see Figure 2). (D,H) FDRs. S denotes the measured signal level. Panels (B) to (D) and (F) to (H) summarize results from 750 and 1650 reconstructions, respectively

intensities close to the detection threshold and were localized at the edges of true ^{19}F features. This blurring was more pronounced in the in vivo data (Figure 6E).

Image quality was clearly improved in CS reconstructions compared to Fourier reconstructions, as shown by a consistently reduced relative RMSD (Figure 6B,F). This improvement increased with growing α. Denoising impaired image quality. For all measurement times except 192 seconds, image-quality improvements exceeded the variability (i.e., the standard deviation of the relative RMSDs). At measurement times longer than 384 seconds (ex vivo) and 768 seconds (in vivo), a differentiation in image-quality improvement appeared between $\alpha = 2$ and $\alpha = 5$.

Detection sensitivity, estimated from signal-level–specific TPRs, improved with increasing α (Figure 6C,G). Whereas TPRs for all reconstructions converged to 1 at high signal levels (reference signal $S_r \geq 6\sigma_F$), TPRs for CS reconstructions were consistently superior to other reconstructions at lower signal levels. For voxels with $S_r < 4\sigma_F$ (ex vivo) or $S_r < 4.5\sigma_F$ (in vivo), improvements exceeded

the variability. CS TPRs increased with increasing α, yet the differences were smaller than those compared to Fourier or denoised reconstructions. Lower TPRs were observed for denoised than Fourier reconstructions. Supporting Information Table S1 shows the reference signal levels at which a TPR of 90% was reached. In vivo, this level was at $5.5\sigma_F$ (Fourier), $4.0\sigma_F$ (CS $\alpha = 2$), and $3.0\sigma_F$ (CS $\alpha = 5$). The achieved improvement in detection performance with CS would translate to a 1.9- and 3.4-fold reduced measurement time compared to a Fourier reconstruction for $\alpha = 2$ and $\alpha = 5$, respectively.

FDRs were generally lower in ex vivo (Figure 6D) compared to in vivo data (Figure 6H). In all cases, the highest levels were reached just above the background detection threshold, and FDRs increased with increasing α: In vivo FDRs reached a maximum of 9%, 12%, and 40% for Fourier, CS $\alpha = 2$, and CS $\alpha = 5$ reconstructions, respectively. Values for all reconstruction methods are shown in Supporting Information Table S1. FDRs dropped with increasing signal level. In vivo CS and denoised reconstructions FDRs converged to 0 at signal levels greater than $3\sigma_F$ and for Fourier reconstructions FDRs approached 0 at $S \geq 4.7\sigma_F$ (Figure 6H). An overlap of the measured FDR variation was observed between all CS reconstructions.

3.5 | Performance of CS with prospective undersampling

In vivo experiments with prospective undersampling confirmed the above results. Compared to conventional Fourier reconstructions, the number of detected ^{19}F signal voxels was greatly enhanced with CS $\alpha = 2$ (Figure 7A). Slight blurring was only present at the edges of true positive features. The number of

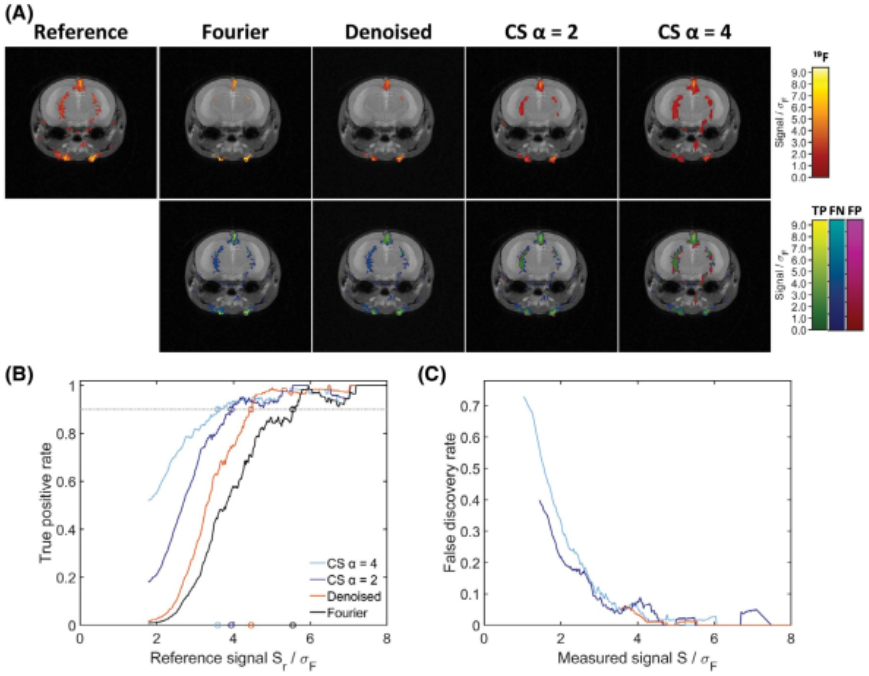

FIGURE 7 Detection performance for ^{19}F MRI in the EAE mouse brain using prospective undersampling. (A) Representative slice comparing conventional Fourier and CS reconstructions (20 minutes' measurement time) with the reference (Fourier reconstruction, 80 minutes' measurement time). The first row shows an overlay of the ^{19}F signal (red hot), normalized by the noise standard deviation of the Fourier reconstruction σ_F, on an anatomical image. The second row shows true positives (TP) in green/yellow, false negatives (FN) in blue/turquoise, and false positives (FP) in red/violet. Panels (B) and (C) show quantitative results for all 4 data sets acquired with prospective undersampling. (B) TPRs computed for different levels of the reference signal S_r using a sliding window approach. Circles indicate the signal level where a TPR of 90% is reached, and σ_F is the noise standard deviation of the Fourier reconstruction at equal measurement time. (C) FDRs computed for different levels of the measured signal S

true positives was further increased with $\alpha = 4$, but so was the blurring effect. CS showed improved TPRs at all signal levels (Figure 7B). A TPR of 90% was reached at $5.5\sigma_F$ (Fourier), $4.5\sigma_F$ (denoised), $3.9\sigma_F$ (CS $\alpha = 2$), and $3.6\sigma_F$ (CS $\alpha = 4$). FDRs in CS reconstructions, on the other hand, were elevated at low signal levels, especially for $\alpha = 4$ (Figure 7C). All reconstructions of prospectively undersampled data can be found under: central.xnat.org/data/projects/CSperf_19F-MRI.

3.6 | Signal intensity bias in animal experiments

Deviation of measured signal from reference signal was computed over an SI range for the EAE data (Figure 8). The SI bias ex vivo and in vivo (Figure 8) showed patterns similar to the observations in phantoms (Figure 5D). Fourier reconstructions overestimated SI by 10% ($S = 8\sigma_F$) to 35% ($S = 3.5\sigma_F$; Figure 8A); denoised (Figure 8B), and CS (Figure 8C–F) reconstructions underestimated the ^{19}F signal. CS reconstructions underestimated the signal by ~30% and denoised reconstructions by ~40% (Figure 8B–F). For all reconstructions, deviations increased with decreasing SI. The largest downward deviations were observed in CS $\alpha = 4$ and $\alpha = 5$. In vivo and ex vivo results showed a similar bias, except for CS reconstructions at lower SI. All CS reconstructions showed a similar bias at signal levels $S < 3\sigma_F$. At $S < 4\sigma_F$, the signal bias in CS reconstructions was up to 10% smaller in ex vivo than in in vivo data.

Using the calibration method for correcting in vivo images (Figure 3), bias was reduced for both conventional (Figure 8A,B) and CS (Figure 8C–F) reconstructions. Average signal deviation did not exceed 10% in the corrected reconstructions. Variability remained unchanged, and the best accuracy was achieved in cases where ex vivo and uncorrected in vivo data showed similar biases. In corrected Fourier (Figure 8A), denoised (Figure 8B), and CS $\alpha = 2$ (Figure 8C) in vivo data, deviations did not exceed the result variability at any signal level. For CS $\alpha = 3$, 4, and 5 (Figure 8D–F), correction reduced bias in the in vivo data to <5% for measured signals $S > 5.5\sigma_F$. For lower signal levels, the larger discrepancies between ex vivo and in vivo data resulted in signal deviations of ~10% in the in vivo data following correction.

Nearly all voxels in Fourier reconstructions show an overestimated ^{19}F signal, whereas most voxels in CS reconstructions show an underestimated signal before correction (Figure 9B, upper panel). Correction resulted in a more balanced distribution of the observed SI around the correct value (Figure 9B, lower panel). When studying NP concentrations measured in the reference data (Figure 9A), we observed that for both in vivo and ex vivo conditions, the occurrence

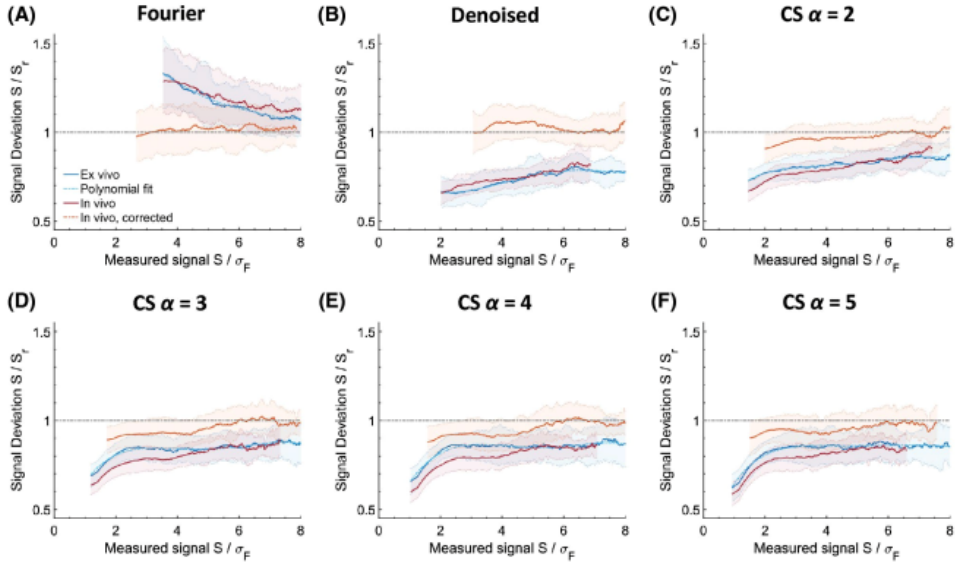

FIGURE 8 Signal intensity bias for imaging inflammation in the EAE mouse model (setups 2 and 3). (A–F) Average signal deviations for Fourier, denoised, and CS reconstruction. α denotes the factor of undersampling and averaging. Each subfigure gathers results for 1 acquisition and reconstruction method and contains the signal deviation measured in the ex vivo condition (setup 2), a polynomial fit of this measurement, the signal deviation measured in vivo (setup 2), and results for the corrected in vivo data (see also Figure 3 for an illustration of the calibration method). A legend is shown in (A), and the shaded areas mark the variability of the results

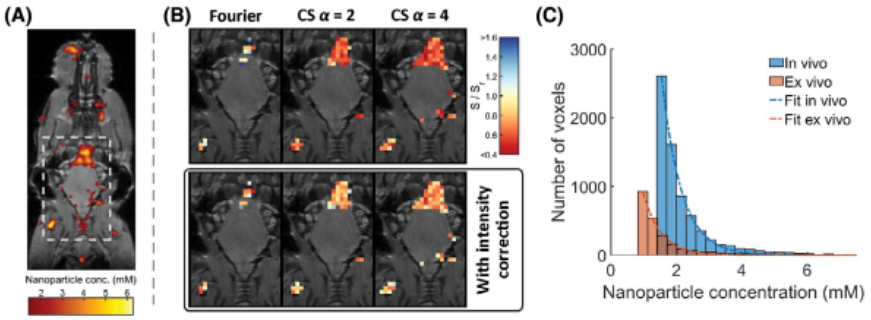

FIGURE 9 Signal intensity calibration example and NP concentration rate of occurrence. (A) Nanoparticle concentration measured in the reference (in vivo). (B) Deviation of the reconstructed SI from the reference before correction (upper panel) and following correction (lower panel). Only true positive voxels are shown, and the cutout is marked in (A). Blue color indicates overestimation, and red color indicates underestimation. (C) Histogram of NP concentrations measured in the references of ex vivo and in vivo data sets (setups 2 and 3). The dashed lines show fits of the negative exponential distribution with rate parameters $\varphi = 1.89\text{mM}^{-1}$ and 1.68mM^{-1} for ex vivo and in vivo data, respectively

rates closely followed a negative exponential distribution that decayed with increasing signal level (Figure 9C).

4 | DISCUSSION AND CONCLUSION

Our study shows that CS can be successfully applied to reconstruct small, low-SNR ^{19}F MR features without an a priori known location. The automatic regularization strength selection we propose reconstructed high-quality images without the need of any manual input. We demonstrated that CS improves detection performance and provides reliable information, not only for high-SNR signals, but even for small image features close to the detection threshold. Although previous work had shown that CS has potential for ^{19}F MRI, our results constitute the first thorough validation of CS for a challenging ^{19}F MRI application. In order to maintain reliability, the undersampling factor and background subtraction threshold need to be chosen with care. Negative SI bias is inherent to CS[35,44] and poses a challenge for quantitative ^{19}F MRI.[17,45] However, and quite unexpectedly, Fourier reconstructions also showed an SI bias with a similar magnitude. The intensity calibration we propose provides a strategy to obtain close to unbiased results, yet it necessitates additional MR reference measurements and postprocessing.

We observed that CS achieved a favorable trade-off between undersampling losses and averaging gains whenever image features were close to the detection threshold. The undersampling patterns that we used focus on the low spatial frequencies, which contain the bulk of contrast information. Allocating a larger share of acquisition time to these data points and thus measuring them with higher SNR lifts features above the noise background. Missing high-spatial-frequency information did not introduce false positives in phantom experiments, even with 8-fold undersampling. This is probably attributable to the extreme sparsity of the images. In the animal model data, reduced sparsity and more complex-shaped features led to slight blurring at the feature edges for $\alpha > 2$. The blurring increased with the degree of undersampling. Higher FDRs in the in vivo compared to ex vivo experiments can be attributed to movement artifacts and shorter reference data measurement times. Given that the detection performance consistently increased with higher α, operators must decide on a balance between sensitivity and data fidelity. For in vivo studies similar to the present one, we recommend 2- to 3-fold undersampling. It should be noted that FDRs dropped to 0 or close to 0 rapidly with increasing SI, so that higher background subtraction thresholds can always be chosen post hoc to obtain more conservative results. At SNRs that were high enough for all features to be detected regardless of the method, only minor differences in image quality were observed between Fourier and CS reconstructions. These SNRs are practically not reached in challenging in vivo ^{19}F MR applications.

The large number of reconstructions (>2000) of ex vivo and in vivo measurements leading to these conclusions guarantees that the observed improvment is not attributable to randomness. Our in vivo experiments with prospective undersampling showed good agreement with results from retrospectively undersampled data and demonstrate the applicability of CS for preclinical imaging studies. The automatic regularization strength selection we used provides a method to optimize CS reconstructions based on objective criteria that yields high-quality images. Because of the small matrix typical of ^{19}F MR images, the increased reconstruction time does not pose practical problems. Required knowledge of the noise level can easily be made available by performing a pure noise scan,[39] which should also be executed to facilitate data analysis. It is a recognized problem of CS-MRI that regularization parameter

values are not reported or the choice is not sufficiently substantiated.[32] Automatic selection provides independence from manual adjustments, making CS more accessible to nonexpert users and improving the reproducibility and comparability of results.

Contrary to our expectation,[17] we observed a positive SI bias in Fourier reconstructions despite Rician noise bias correction. This bias is explained by the exponentially decaying rate of occurrence of NP concentrations (Figure 9C): Assuming a negative exponential prior distribution over the true SI (S_t) with rate parameter φ and a simplified Gaussian forward model, the expected true SI for measured SI S is $<S_t>_{p(S_t|S)}=S-\frac{\varphi\sigma^2}{2}$, which is smaller than S itself (see the Appendix for details). In CS and denoised reconstructions, this effect reduced the signal underestimation. Our proposed intensity calibration corrected the systematic deviations. Therefore, high-quality ex vivo scans of comparable signal distributions are recommended for in vivo applications utilizing CS and ^{19}F MR for quantitative analyses. Taking not only the SI, but also feature size into account could further improve performance and applicability of the method. This method could potentially also be used in human in vivo studies, but would require long ex vivo reference MR measurements of similar tissue (e.g., from biopsy or autopsy material). Given that similar bias effects would pose a major challenge for future ^{19}F MR studies, further detailed investigations are required to seek and correct discrepancies as early as possible.

Another avenue for future CS research is to offset motion artifacts and long-term drift effects.[46] Although the increased averaging reduces the magnitude of motion artifacts, especially in cardiac and abdominal applications, shortened scan times would reduce the influence of signal drift. However, investigating these highly circumstantial effects would necessitate proper controls, which is challenging, given that parallel acquisitions of reference measurements, even motion correction data, introduce a technical hurdle.

We expect the demonstrated improvement of signal detection without impaired data fidelity or necessarily compromised quantification to hold for other ^{19}F MRI preclinical applications with similar signal distributions. Besides lowering the detection threshold, increased ^{19}F sensitivity can be translated into shorter measurement times or improved spatial resolution. CS will be particularly useful in studies that involve small amounts of ^{19}F, as is the case in pharmacokinetic studies[47] as well as studies involving ^{19}F-target–specific theranostic nanoparticles,[48] ^{19}F/^{1}H MR smart probes,[49,50] or ^{19}F-labeled cells administered as therapies for tumor disease.[2,51]

ACKNOWLEDGMENTS

This study was funded, in part, by the Deutsche Forschungsgemeinschaft to S.W. and A.P. (DFG WA2804, DFG PO1869). This work was funded in part (Thoralf Niendorf, Sonia Waiczies, Andreas Pohlmann) by the German Research Foundation (Gefoerdert durch die Deutsche Forschungsgemeinschaft (DFG), Projektnummer 394046635, SFB 1365, *RENOPROTECTION*. Funded by the Deutsche Forschungsgemeinschaft (DFG, German Research Foundation), Project number 394046635, SFB 1365, *RENOPROTECTION*). This project has received funding in part (Thoralf Niendorf) from the European Research Council (ERC) under the European Union's Horizon 2020 research and innovation program under grant agreement No 743077 (ThermalMR).

The funders had no role in study design, data collection and analysis, decision to publish, or preparation of the manuscript. We thank Stefanie Münchberg for preparation of nanoparticles and assistance with animal handling and Jason Millward (both from the Berlin Ultrahigh Field Facility (B.U.F.F.) at the Max-Delbrueck Center for Molecular Medicine in the Helmholtz Association, Berlin, Germany) for preparation of ex vivo tissue samples.

ORCID

Ludger Starke https://orcid.org/0000-0002-0359-0101
Andreas Pohlmann https://orcid.org/0000-0002-8572-2568
Christian Prinz https://orcid.org/0000-0003-3330-031X
Thoralf Niendorf https://orcid.org/0000-0001-7584-6527
Sonia Waiczies https://orcid.org/0000-0002-9916-9572

REFERENCES

1. Ahrens ET, Flores R, Xu H, Morel PA. In vivo imaging platform for tracking immunotherapeutic cells. *Nat Biotechnol*. 2005; 23:983–987.
2. Ahrens ET, Helfer BM, O'Hanlon CF, Schirda C. Clinical cell therapy imaging using a perfluorocarbon tracer and fluorine-19 MRI. *Magn Reson Med*. 2014;72:1696–1701.
3. Flogel U, Ahrens E. *Fluorine Magnetic Resonance Imaging*. New York, NY: Pan Stanford; 2016.
4. Ruiz-Cabello J, Barnett BP, Bottomley PA, Bulte JW. Fluorine (19F) MRS and MRI in biomedicine. *NMR Biomed*. 2011;24:114–129.
5. Waiczies H, Lepore S, Drechsler S, et al. Visualizing brain inflammation with a shingled-leg radio-frequency head probe for 19F/1H MRI. *Sci Rep*. 2013;3:1280.
6. Waiczies S, Millward JM, Starke L, et al. Enhanced fluorine-19 MRI sensitivity using a cryogenic radiofrequency probe: technical developments and ex vivo demonstration in a mouse model of neuroinflammation. *Sci Rep*. 2017;7:9808.
7. Waiczies S, Rosenberg JT, Kuehne A, et al. Fluorine-19 MRI at 21.1 T: enhanced spin–lattice relaxation of perfluoro-15-crown-5-ether and sensitivity as demonstrated in ex vivo murine neuroinflammation. *MAGMA*. 2019;32:37–49.
8. Mastropietro A, De Bernardi E, Breschi GL, et al. Optimization of rapid acquisition with relaxation enhancement (RARE) pulse sequence parameters for (1)(9)F-MRI studies. *J Magn Reson Imaging*. 2014;40:162–170.
9. Constantinides C, Maguire M, McNeill E, et al. Fast, quantitative, murine cardiac 19F MRI/MRS of PFCE-labeled progenitor stem cells and macrophages at 9.4T. *PLoS ONE*. 2018;13:e0190558.
10. Faber C, Schmid F. Pulse sequence considerations and schemes. In: Flögel U, Ahrens E, eds. *Fluorine Magnetic Resonance Imaging*. New York, NY: Pan Stanford; 2016:1–28.

11. Candes EJ, Romberg J, Tao T. Robust uncertainty principles: exact signal reconstruction from highly incomplete frequency information. *IEEE Trans Inf Theory*. 2006;52:489–509.
12. Donoho DL. Compressed sensing. *IEEE Trans Inf Theory*. 2006;52:1289–1306.
13. Lustig M, Donoho D, Pauly JM. Sparse MRI: the application of compressed sensing for rapid MR imaging. *Magn Reson Med*. 2007;58:1182–1195.
14. Kampf T, Fischer A, Basse-Lüsebrink TC, et al. Application of compressed sensing to in vivo 3D 19F CSI. *J Magn Reson*. 2010;207:262–273.
15. Kampf T, Sturm VJF, Basse-Lusebrink TC, et al. Improved compressed sensing reconstruction for 19F magnetic resonance imaging. *MAGMA*. 2019;32:63–77.
16. Fischer A, Basse-Lüsebrink T, Kampf T, et al. Improved sensitivity in 19F cellular imaging using non-convex compressed sensing. Paper presented at: Proceedings of the 17th Annual Meeting of the ISMRM; 2009; Honolulu, HI. Abstract 3377.
17. Zhong J, Mills PH, Hitchens TK, Ahrens ET. Accelerated fluorine-19 MRI cell tracking using compressed sensing. *Magn Reson Med*. 2013;69:1683–1690.
18. Liang S, Dresselaers T, Louchami K, Zhu C, Liu Y,Himmelreich U. Comparison of different compressed sensing algorithms for low SNR (19) F MRI applications-Imaging of transplanted pancreatic islets and cells labeled with perfluorocarbons. *NMR Biomed*. 2017;30. https://doi.org/10.1002/nbm.3776.
19. Sadykova D, James AP. Quality assessment metrics for edge detection and edge-aware filtering: a tutorial review. Paper presented at: Sixth International Conference on Advances in Computing, Communications and Informatics (ICACCI-2017), Manipal, India, 2017.
20. Yu Z, Wang J, Lu G. Optimized self-adapting contrast enhancement algorithm for wafer contour extraction. *Multimed Tools Appl*. 2019;78:32087–32108.
21. Zhang L, Xing M, Qiu C-W, et al. Resolution enhancement for inversed synthetic aperture radar imaging under low SNR via improved compressive sensing. *IEEE Trans Geosci Remote Sens*. 2010;48:3824–3838.
22. Ji S, Xue Y, Carin L. Bayesian compressive sensing. *IEEE Trans Sig Process*. 2008;56:2346–2356.
23. Morozov VA. On the solution of functional equations by the method of regularization. Paper presented at: Dokl Akad Nauk SSSR; 1966; Moscow, USSR.
24. Kilmer ME, O'Leary DP. Choosing regularization parameters in iterative methods for ill-posed problems. *SIAM J Matrix Anal Appl*. 2001;22:1204–1221.
25. Ahrens ET, Bulte JW. Tracking immune cells in vivo using magnetic resonance imaging. *Nat Rev Immunol*. 2013;13:755–763.
26. Waiczies H, Lepore S, Janitzek N, et al. Perfluorocarbon particle size influences magnetic resonance signal and immunological properties of dendritic cells. *PLoS ONE*. 2011;6:e21981.
27. Flögel U, Ding Z, Hardung H, et al. In vivo monitoring of inflammation after cardiac and cerebral ischemia by fluorine magnetic resonance imaging. *Circulation*. 2008;118:140–148.
28. Jacoby C, Borg N, Heusch P, et al. Visualization of immune cell infiltration in experimental viral myocarditis by (19)F MRI in vivo. *MAGMA*. 2014;27:101–106.
29. Lassmann H. Multiple Sclerosis Pathology. *Cold Spring Harb Perspect Med*. 2018;8:a028936.
30. Qaisar S, Bilal RM, Iqbal W, Naureen M, Lee S. Compressive sensing: from theory to applications, a survey. *J Commun Netw*. 2013;15:443–456.
31. Rudin LI, Osher S, Fatemi E. Nonlinear total variation based noise removal algorithms. *Physica D*. 1992;60:259–268.
32. Jaspan ON, Fleysher R, Lipton ML. Compressed sensing MRI: a review of the clinical literature. *Br J Radiol*. 2015;88:20150487.
33. Goldstein T, O'Donoghue B, Setzer S, Baraniuk R. Fast alternating direction optimization methods. *SIAM J Imaging Sci*. 2014;7:1588–1623.
34. Chen M. On the solution of circulant linear systems. *SIAM J Numer Anal*. 1987;24:668–683.
35. Osher S, Yin W. *Sparse recovery via l1 and L1 optimization*. Los Angeles, CA: California Univ. Los Angeles Dept. of Mathematics; 2014.
36. Dowell M, Jarratt P. A modified regula falsi method for computing the root of an equation. *BIT Numer Math*. 1971;11:168–174.
37. Lepore S, Waiczies H, Hentschel J, et al. Enlargement of cerebral ventricles as an early indicator of encephalomyelitis. *PLoS ONE*. 2013;8:e72841.
38. Waiczies S, Lepore S, Sydow K, et al. Anchoring dipalmitoyl phosphoethanolamine to nanoparticles boosts cellular uptake and fluorine-19 magnetic resonance signal. *Sci Rep*. 2015;5:8427.
39. National Electrical Manufacturers Association. *Determination of signal-to-noise ratio (SNR) in diagnostic magnetic resonance imaging*. NEMA Standards Publication MS 1–2001. Arlington, VA: National Electrical Manufacturers Association; 2001.
40. Zijlstra F, Viergever MA, Seevinck PR. Evaluation of variable density and data-driven k-space undersampling for compressed sensing magnetic resonance imaging. *Invest Radiol*. 2016;51:410–419.
41. Henkelman RM. Measurement of signal intensities in the presence of noise in MR images. *Med Phys*. 1985;12:232–233.
42. Gudbjartsson H, Patz S. The Rician distribution of noisy MRI data. *Magn Reson Med*. 1995;34:910–914.
43. Constantinides CD, Atalar E, McVeigh ER. Signal-to-noise measurements in magnitude images from NMR phased arrays. *Magn Reson Med*. 1997;38:852–857.
44. Becker SR. *Practical compressed sensing: modern data acquisition and signal processing*. Pasadena, CA: California Institute of Technology; 2011.
45. Hu S, Lustig M, Balakrishnan A, et al. 3D compressed sensing for highly accelerated hyperpolarized 13C MRSI with in vivo applications to transgenic mouse models of cancer. *Magn Reson Med*. 2010;63:312–321.
46. Vos SB, Tax CM, Luijten PR, Ourselin S, Leemans A, Froeling M. The importance of correcting for signal drift in diffusion MRI. *Magn Reson Med*. 2017;77:285–299.
47. Bolo NR, Hode Y, Macher JP. Long-term sequestration of fluorinated compounds in tissues after fluvoxamine or fluoxetine treatment: a fluorine magnetic resonance spectroscopy study in vivo. *MAGMA*. 2004;16:268–276.
48. Pan H, Myerson JW, Hu L, et al. Programmable nanoparticle functionalization for in vivo targeting. *FASEB J*. 2013;27:255–264.
49. Keliris A, Mamedov I, Hagberg GE, Logothetis NK, Scheffler K, Engelmann J. A smart 19F and 1H MRI probe with self-immolative linker as a versatile tool for detection of enzymes. *Contrast Media Mol Imaging*. 2012;7:478–483.
50. Bar-Shir A, Yadav NN, Gilad AA, van Zijl PC, McMahon MT, Bulte JW. Single 19F probe for simultaneous detection of multiple metal ions using miCEST MRI. *J Am Chem Soc*. 2015;137:78–81.
51. Ku M-C, Edes I, Bendix I, et al. ERK1 as a therapeutic target for dendritic cell vaccination against high-grade gliomas. *Mol Cancer Ther*. 2016;15:1975–1987.

SUPPORTING INFORMATION

Additional supporting information may be found online in the Supporting Information section.

TABLE S1 Detection performance in the EAE model. Ex vivo and in vivo refer to setups 2 and 3, respectively. Rows 2 and 3 show the reference signal level at which a TPR of 90% is reached. Rows 4 and 5 show the FDR at signal levels just above the background subtraction threshold and rows 6 and 7 the overall FDR

How to cite this article: Starke L, Pohlmann A, Prinz C, Niendorf T, Waiczies S. Performance of compressed sensing for fluorine-19 magnetic resonance imaging at low signal-to-noise ratio conditions. *Magn Reson Med*. 2020;84:592–608. https://doi.org/10.1002/mrm.28135

APPENDIX SIGNAL INTENSITY BIAS IN FOURIER RECONSTRUCTIONS

Following Figure 9C, we assume that the SI rate of occurrence follows an exponential distribution. Thus, the prior distribution over the true signal intensities is (Equation A1):

$$p_0\left(S_t\right)=\varphi\exp\left(-\varphi S_t\right), \tag{A1}$$

with rate parameter φ. We consider a simplified forward model with additive Gaussian noise (Equation A2):

$$p\left(S|S_t\right)=N\left(S;S_t,\sigma\right)=\frac{1}{\sqrt{2\sigma^2}}\exp\left(-\frac{\left(S-S_t\right)^2}{2\sigma^2}\right), \tag{A2}$$

where S denotes the measured signal and σ the noise standard deviation. The posterior distribution follows from the Bayes theorem (Equation A3):

$$\begin{aligned} p\left(S_t|S\right)\propto p\left(S|S_t\right)p_0\left(S_t\right) \quad &|\propto\exp\left(-\frac{\left(S-S_t\right)^2}{2\sigma^2}-\varphi S_t\right)\\ &|\propto\exp\left(-\frac{S^2-2S_t\left(S-\frac{\varphi\sigma^2}{2}\right)}{2\sigma^2}\right)\\ &|\propto N\left(S_t;S-\frac{\varphi\sigma^2}{2},\sigma^2\right). \end{aligned} \tag{A3}$$

Thus, the expected true signal for measured signal S is (Equation A4):

$$<S_t>_{p(S_t|S)}=S-\frac{\varphi\sigma^2}{2}. \tag{A4}$$

10 Publikation 4 Enhanced Fluorine-19 MRI Sensitivity using a Cryogenic Radiofrequency Probe: Technical Developments and Ex Vivo Demonstration in a Mouse Model of Neuroinflammation

www.nature.com/scientificreports

SCIENTIFIC REPORTS

OPEN

Received: 14 March 2017
Accepted: 19 July 2017
Published online: 29 August 2017

Enhanced Fluorine-19 MRI Sensitivity using a Cryogenic Radiofrequency Probe: Technical Developments and *Ex Vivo* Demonstration in a Mouse Model of Neuroinflammation

Sonia Waiczies[1], Jason M. Millward[1], Ludger Starke[1], Paula Ramos Delgado[1], Till Huelnhagen[1], Christian Prinz[1], Daniel Marek[2], Didier Wecker[3], Ralph Wissmann[3], Stefan P. Koch[4], Philipp Boehm-Sturm[4], Helmar Waiczies[5], Thoralf Niendorf[1,5,6] & Andreas Pohlmann[1]

Neuroinflammation can be monitored using fluorine-19 (^{19}F)-containing nanoparticles and ^{19}F MRI. Previously we studied neuroinflammation in experimental autoimmune encephalomyelitis (EAE) using room temperature (RT) ^{19}F radiofrequency (RF) coils and low spatial resolution ^{19}F MRI to overcome constraints in signal-to-noise ratio (SNR). This yielded an approximate localization of inflammatory lesions. Here we used a new ^{19}F transceive cryogenic quadrature RF probe (*^{19}F-CRP*) that provides the SNR necessary to acquire superior spatially-resolved ^{19}F MRI. First we characterized the signal-transmission profile of the *^{19}F-CRP*. The *^{19}F-CRP* was then benchmarked against a RT ^{19}F/^{1}H RF coil. For SNR comparison we used reference compounds including ^{19}F-nanoparticles and *ex vivo* brains from EAE mice administered with ^{19}F-nanoparticles. The transmit/receive profile of the *^{19}F-CRP* diminished with increasing distance from the surface. This was counterbalanced by a substantial SNR gain compared to the RT coil. Intraparenchymal inflammation in the *ex vivo* EAE brains was more sharply defined when using 150 µm isotropic resolution with the *^{19}F-CRP*, and reflected the known distribution of EAE histopathology. At this spatial resolution, most ^{19}F signals were undetectable using the RT coil. The *^{19}F-CRP* is a valuable tool that will allow us to study neuroinflammation with greater detail in future *in vivo* studies.

Central nervous system (CNS) inflammation, as occurs in multiple sclerosis (MS), involves immune cell recruitment from the periphery into the CNS, resulting in tissue destruction and neurodegeneration[1]. During active disease, a massive infiltration of immune cells is predominant, particularly around white matter lesions. T cells find their way into the white matter via a disruption of the blood brain barrier[2]. In MS, T cells may also enter the CNS grey matter such as the cerebral cortex via the meninges[3,4]. Even in the cerebellum, extensive grey matter pathology in secondary progressive MS is linked to inflammation of the subarachnoid space[5]. Studies of the animal model of MS, experimental autoimmune encephalomyelitis (EAE), have helped identify mechanisms of cell migration between the periphery, CNS and lymphatic system during neuroinflammation[6–8]. This is a topic of active interest, with divergent views regarding immune cell entry and exit in the CNS (inside-out versus

[1]Berlin Ultrahigh Field Facility (B.U.F.F.), Max Delbrück Center for Molecular Medicine in the Helmholtz Association, Berlin, Germany. [2]Bruker BioSpin AG, Fällanden, Switzerland. [3]Bruker BioSpin MRI, Ettlingen, Germany. [4]Department of Experimental Neurology, Center for Stroke Research Berlin (CSB), Charité Core Facility 7 T Experimental MRIs, and NeuroCure, Charité University Medicine Berlin, Berlin, Germany. [5]MRI TOOLS GmbH, Berlin, Germany. [6]Experimental and Clinical Research Center, a joint cooperation between the Charité Medical Faculty and the Max Delbrück Center for Molecular Medicine in the Helmholtz Association, Berlin, Germany. Correspondence and requests for materials should be addressed to S.W. (email: sonia@waiczies.de)

outside-in hypotheses) in MS[9,10]. Therefore there is an acute need for more precise and non-invasive methods that support longitudinal studies of inflammatory cell migration during disease progression to resolve some of the discrepancies in the literature.

Previously we studied immune cell infiltration in EAE brains using fluorine-19 (^{19}F)-loaded nanoparticles (NPs) and a room temperature (RT) dual-tuned ^{19}F/^{1}H radio frequency (RF) volume resonator[11]. Intravenously administered NPs are taken up by inflammatory cells during their migration from the systemic circulation into the inflamed organ[11–17]. Although tracking of inflammation following intravenous ^{19}F-NP administration is one application for ^{19}F MRI, several other state-of-the-art applications for ^{19}F imaging exist. These include *in vivo* tracking of cell therapies labeled in culture with ^{19}F-NPs prior to their adoptive transfer[18–20] and intracellular oximetry using ^{19}F-NP emulsions[21] to study changes in pO2 in tumor cells during therapy[22].

One major limitation of ^{19}F MRI is the low signal-to-noise ratio (SNR). The acquisition method is one aspect of ^{19}F MRI that influences SNR. SNR efficiency of the most commonly used acquisition methods — RARE (Rapid Acquisition with Relaxation Enhancement), UTE (Ultra-short Echo Time), and bSSFP (Balanced Steady-State Free Precession) — depends on the T_1 and T_2 values of the particular ^{19}F compound studied[23]. For most T_1 and T_2 combinations, especially those pertaining to intracellular ^{19}F-NPs, bSSFP and 3D RARE sequences have the highest SNR sensitivity. However, while bSSFP often has a higher SNR efficiency, it is not always the method of choice due to the high RF energy deposition associated with longer acquisition times, and pronounced banding artifacts. The SNR and the sensitivity of the radio frequency (RF) probe used are main determinants that dictate the level of spatial resolution. Factors to be kept in mind when designing a probe include the geometry, the filling factor and the homogeneity of the B_1^+ transmit field.

The SNR constraint limited spatial resolution to approximately 600 μm when detailing the dynamics of inflammation during EAE[11]. Given this limited precision, the location of inflammatory cells within the brain was not sharply defined. To overcome the sensitivity constraints in ^{19}F MR and improve detail of inflammatory cell location, we applied the concept of cryogenically-cooling RF coil hardware to improve SNR by reducing thermal noise. Until now this technology has been available only for ^{1}H, ^{13}C and ^{31}P small animal MRI. Here we made use of the first ^{19}F transceive cryogenically-cooled RF probe (*^{19}F-CRP*) to substantially boost SNR beyond that of available RT coils, thus facilitating the acquisition of better spatially-resolved images. In this study we evaluated the advantages and disadvantages of the *^{19}F-CRP* for imaging neuroinflammation.

Methods

Radio frequency coils. The performance of a novel transceive ^{19}F cryogenic quadrature RF surface probe at 9.4T (*^{19}F-CRP*, $f \sim 376$ MHz) was compared to a dual-tunable ^{19}F/^{1}H volume resonator ($\phi_{in} = 18.4$ mm, $l_{total} = 39$ mm), previously developed for imaging mouse brain inflammation[11]. The *^{19}F-CRP* has a similar geometry to the existing Bruker ^{1}H quadrature CryoProbes[24]. The rectangular transceive copper coil elements are overlapping side-by-side on a cylindrical surface ($r \sim 11$ mm, axis parallel to the main magnetic field direction). The outer dimensions (O.D.) of one coil element are: 16×20 mm^2 [arc length ($\phi \times z$)] and the total O.D. are: 27×20 mm^2 [$\phi \times z$]. The *^{19}F-CRP* operates at ~28 K with a dual cooled preamplifier at the base running at ~77 K. Constant cooling is ensured by a closed loop system connected to a remote cryo-cooler. The RF coil is thermally insulated by a vacuum separating it from the surrounding ceramic finger (Fig. 1A). The outer surface of the RF finger is equipped with a temperature sensor and kept at a temperature of choice (35 °C) using a resistive heater. The SNR gain of this CRP relative to a RT coil with similar geometry is expected to be comparable to existing 400 MHz proton CryoProbes[24,25].

Experimental setup. To evaluate the *^{19}F-CRP* performance, three different phantom-setups were prepared (Fig. 1B):

Setup 1 (high concentration ^{19}F): a 10 ml syringe (inner/outer diameter = 17.0 mm/15.5 mm) for the *^{19}F-CRP* and a 5 ml syringe (I.D./O.D. = 13.5/12.0 mm) for the *^{19}F/^{1}H RT-coil*, both containing the same ^{19}F reference compound to study B_1^+ and compare spatial SNR. The reference compound was 33% v/v 2,2,2-Trifluoroethanol (TFE, Sigma-Aldrich, Germany) in water.

Setup 2 (^{19}F nanoparticles): NMR tubes (I.D./O.D. = 4.0/5.0 mm) containing different concentrations of perfluoro-15-crown-5-ether (PFCE) loaded nanoparticles to compare ^{19}F signal sensitivity as a function of the number of ^{19}F atoms. Nanoparticles were prepared by emulsifying 1200 mM PFCE (Fluorochem, UK) with Pluronic F-68 (Sigma-Aldrich, Germany) using a titanium sonotrode (Sonopuls GM70, Bandelin, Germany) as previously described[26]. The PFCE nanoparticle stock was then diluted to 25 mM, 50 mM, 100 mM, 200 mM, 400 mM and 600 mM nanoparticle suspensions. NMR tubes containing different nanoparticle concentrations were placed below the CRP using a spacer of 0.75 mm thickness to mimic the distance of the mouse brain from the CRP surface in *in vivo* applications.

Setup 3 (mouse brain): *Ex vivo* tissues from fixed EAE mice embedded in 15-ml tubes, for comparing ^{19}F signal sensitivity and anatomical detail. All experiments were conducted in accordance with procedures approved by the Animal Welfare Department of the State Office of Health and Social Affairs Berlin (LAGeSo), and conformed to national and international guidelines to minimize discomfort to animals (86/609/EEC). EAE was induced as described previously[11] in SJL/J mice (n = 6, female, 6–8 weeks old). Five days following EAE induction, mice were administered nanoparticles (10μmol PFCE) intravenously each day for 5 d as described previously[11]. EAE mice were transcardially perfused with 20 ml PBS followed by 20 ml 4% paraformaldehyde (PFA) following terminal anesthesia. Mice were cleared from external pelt, extremities, and abdominal tissues. Brain, spinal cord and neck lymphoid organs were preserved *in situ* within the skull and vertebral column. The tissues were transferred into a 15 ml tube filled with 4% PFA and stored at 4 °C.

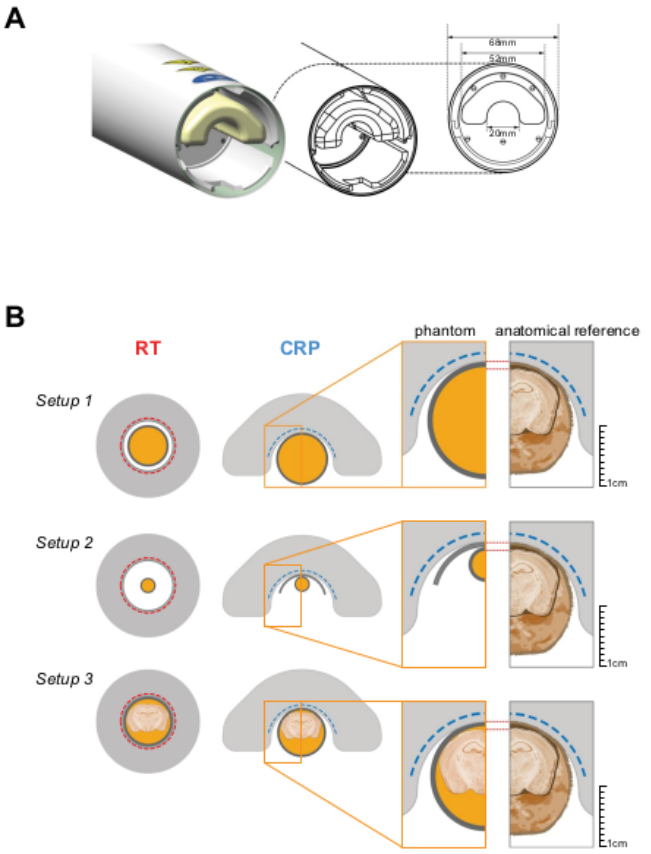

Figure 1. ^{19}F Cryogenic Radiofrequency Probe design and experimental setup. (**A**) Side view of the *^{19}F-CRP* showing its geometry including external protective cylinder and an inner ceramic probe head that encloses the loop coil elements (not shown). The inner diameter dimension for the inner ceramic structure is shown in the cross-sectional view (right). (**B**) Three different experimental setups that were used to assess the *^{19}F-CRP* quality. Shown are Setup 1 for the high concentration ^{19}F phantom (*upper panel*), Setup 2 for the ^{19}F nanoparticle phantoms (*middle panel*) and Setup 3 for the mouse brain phantom (*lower panel*). The dimension of the phantom setups are to scale with the dimensions of both *^{19}F-CRP* and RT coil and an anatomic reference is shown on the right for comparison. The nanoparticles used in this study had the following physical characteristics: Z-average diameter = 164 nm, PdI = 0.06, z-Potential = 0.19 mV.

MRI Methods and Data Analysis. All experiments were carried out on a 9.4 T small animal MR system (BioSpec 94/20, Bruker BioSpin MRI, Ettlingen, Germany) operating at 400 MHz (^{1}H) and 376 MHz (^{19}F).

Transmit Field Characteristics. Using a 15 ml tube containing 33% TFE in water (*Setup 1*), we acquired 2D-FLASH images (TR = 20 s, TE = 4.9 ms, FOV = (20 × 20) mm^2, matrix = 256 × 256, 1 slice of 4 mm thickness, averages = 1, TA = 1 h 25 min) with nominal excitation flip angles $\alpha = 60°$ and $2\alpha = 120°$ and calculated the actual flip angles (FA) using the double-angle method[27,28]:

$$FA = \text{acos}(SI_{2\alpha}/(2SI_{\alpha})) \quad (1)$$

with SI_{α} and $SI_{2\alpha}$ being the signal intensities obtained with α and 2α. FA maps were normalized to a nominal angle of 90° by multiplying by the factor $90°/\alpha$.

SNR assessment in phantoms. To measure the spatial distribution of SNR at increasing distances from the *^{19}F-CRP* surface, a high-concentration ^{19}F phantom (*Setup 1*) and an axial 2D-RARE scan (TR = 10 s, TE = 6.2 ms,

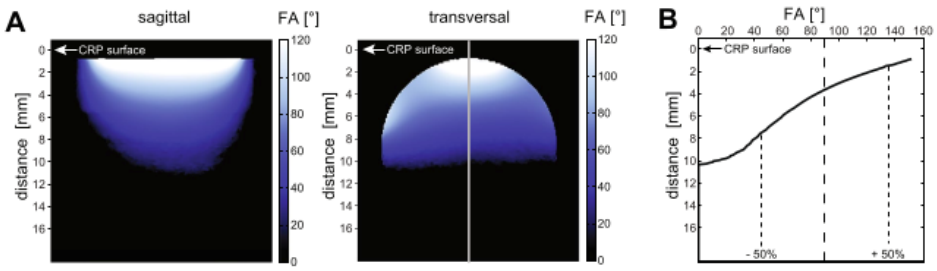

Figure 2. Transmission B_1^+ Field (B_1^+) for the *^{19}F-CRP*. (**A**) Flip angle maps acquired in vertical and transversal orientation using a high concentration ^{19}F phantom (Setup 1). (**B**) Profile plot of the FA along the vertical axis that depicts the change in FA with increasing distance to the CRP surface.

ETL = 256, FOV = (25.6 × 25.6) mm², matrix = 256 × 256, averages = 100, TA = 17 m) was used. To quantify and compare SNR in a way more relevant for brain inflammation, we measured SNR as a function of the number of ^{19}F atoms using phantoms containing different concentrations of ^{19}F nanoparticles (*Setup 2*, Fig. 1B). Measurements involved 2D-RARE scans (TR = 3000 ms, TE = 10.8 ms, ETL = 8, FOV = (10 × 10) mm², matrix = 96 × 96, averages = 1, TA = 36 s) with varying slice thicknesses: 0.4/1.0/1.2/2.0/3.6/4.7/6.0 mm to measure SNR as a function of the number of ^{19}F atoms.

SNR was calculated by dividing signal S_m from magnitude images by background standard deviation σ_m, and corrected to compensate for the non-Gaussian distribution[29]. For single channel RF coils, intensity values of MR images follow a Rician distribution[30,31]. For a two-receiver, quadrature system (*^{19}F-CRP*), they follow a non-central chi distribution[32]. We estimated the true SNR from the S_m and background σ_m using

$$SNR = \frac{S}{\sigma} = \frac{S_m}{\sigma_m} \cdot \frac{f_S(S_m, \sigma_m)}{1/c_\sigma} \quad (2)$$

where c_σ is 0.655 (Rician) and 0.687 (chi), and the correction function f_S is derived from the respective distribution's mean[30,32]. For *Setup* 2, a single SNR value was determined from the mean signal intensity over a central circular region-of-interest covering ~90% of pixels. The number of atoms per image pixel was estimated from nanoparticle concentration and voxel size.

Ex vivo mouse brain ^{19}F and ^{1}H MRI (Setup 3). ^{19}F MR images of the EAE mouse brain were acquired using 3D-RARE: TR = 800 ms, TE = 5.1 ms, ETL=33, FOV=(30 × 20 × 20) mm³, matrix = 195 × 65 × 65 zero-filled to 195 × 130 × 130, averages = 384, TA = 11 h. ^{1}H MR images were acquired using 3D-FLASH (TR = 50 ms, TE = 12.5 ms, FOV = (30 × 20 × 20) mm³, matrix = 384 × 256 × 284 zero-filled to 768 × 512 × 512, averages = 2, TA = 6 h 3 min). ^{19}F MR images from the *^{19}F-CRP* were registered with those from the *^{19}F/^{1}H RT-coil*. Since the *^{19}F-CRP* has no *^{19}F/^{1}H* dual resonant capacity, we registered the CRP ^{19}F images onto the RT ^{19}F images in order for both ^{19}F images (RT and CRP) to be spatially aligned with the RT ^{1}H images. For this, three repetitions of the RT ^{19}F scan were averaged to achieve sufficient ^{19}F signal with the RT-coil and an effective registration. Co-registration was applied using affine diffeomorphic image registration (12 degrees of freedom) by explicit B-spline regularization[33], which is part of the Advanced Normalisation Tool (ANTs)[34]. Registration of the Allen brain atlas[35] to the ^{1}H image was achieved as follows: (1) ^{1}H image and atlas template were segmented in grey matter (GM), white matter (WM) and cerebrospinal fluid (CSF) probability maps with SPMMouse (http://www.spmmouse.org/)[36], (2) two synthetic images were generated with signal intensity in each voxel I(x,y,z) = 1.0 × GM (x y, z) + 2.0 × WM + 4.0 × CSF, i.e. one registered with the ^{1}H image and one registered with the atlas, (3) both synthetic images were warped to the ^{1}H image using nonlinear B-spline registration in ELASTIX (http://elastix.isi.uu.nl/)[37]. Raw ^{1}H MRI files were converted to NIFTI-format and brains segmented with ITK-SNAP version 3.4.0[38]. For 2D representation of ^{19}F/^{1}H MRI we performed overlays of the raw ^{19}F MR data with SNR-based scaling using Matlab. For 3D representation we used ImageJ (National Institutes of Health, USA, http://imagej.nih.gov/ij).

Results

Transmit field characteristics of the *^{19}F-CRP*. Since transceive surface coils do not achieve a spatially uniform excitation like volume resonators[24], we assessed the B_1^+ characteristics of the *^{19}F-CRP* (Fig. 2A) and quantified changes in FA. A profile plot of the FA along the vertical axis (Fig. 2B) reveals a strong FA decrease with increasing distance from the CRP surface. Across a distance of 10.4 mm the measured FA varies between 152° and 0°. From the nominal FA of 90° the actual FA deviates up to 50% within a range of 6.0 mm (1.5–7.5 mm from CRP surface).

SNR assessment in phantoms. To study the SNR performance of the *^{19}F-CRP*, we first used a high ^{19}F concentration (33% TFE solution) (Fig. 3A). The transversal spin-echo ^{19}F MR images demonstrate a homogenous SNR for the RT coil and a spatially varying SNR for the CRP (Fig. 3A). We adjusted the reference pulse

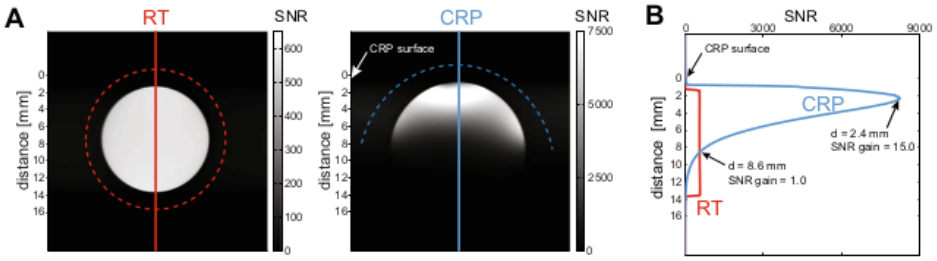

Figure 3. Comparison of SNR between the *^{19}F-CRP* and *^{19}F/^{1}H RT-coil*. (**A**) Cross-sectional spin-echo ^{19}F MR images of a TFE phantom acquired with the RT RF coil (left) and the CRP (right). The CRP showed a spatially varying sensitivity that is typical for transceive surface coils. (**B**) Plots of the SNR profile along the vertical axis at the center of the phantom. For the RT volume resonator (red curve) the SNR was very uniform within the phantom. In contrast, for the CRP the SNR drops rapidly with increasing distance to the RF coil. For this particular reference pulse power, SNR reached its maximum at 2.4 mm from the CRP surface, where it is 15-fold higher than the SNR of the RT coil. Beyond a distance of 8.1 mm the *^{19}F-CRP* did not provide any SNR gain with regard to the *^{19}F/^{1}H RT-coil*.

power in order to avoid substantial signal loss at the dorsal side of the brain. Using this reference pulse power, the SNR reached its peak at a distance of 2.4 mm, where it was ~15-fold higher than the SNR of the RT coil (Fig. 3B). The SNR of both RF coils are approximately equal at a distance of 8.6 mm from the CRP.

We next investigated the detection limits for both coils by measuring ^{19}F nanoparticles, as a biologically relevant preparation. We employed concentrations of PFCE (25 mM–200 mM) yielding a range of 10^{15}–10^{18} ^{19}F atoms per voxel (Fig. 4A). Qualitatively, we reached a detection limit in the order of 10^{15} fluorine atoms using the *^{19}F-CRP*, compared to 10^{16} fluorine atoms with the *^{19}F RT-coil*. Specifically, an SNR of 3.0 was achieved with $(0.1 \times 0.1 \times 0.4)$ mm^3 voxels of a 25 mM PFCE concentration (equating to 5.2×10^{15} fluorine atoms) when using the *^{19}F-CRP*. In contrast an SNR of 2.4 was achieved with $(0.1 \times 0.1 \times 1.2)$ mm^3 voxels of a 100 mM PFCE concentration (equating to 6.2×10^{16} fluorine atoms) when using the *^{19}F- RT-coil*. In both cases the measurement time was 36 s. MR images with an SNR value below 2 were not sharply defined. To estimate SNR provided by the *^{19}F-CRP* compared to the *^{19}F/^{1}H RT-coil*, we used SNR = 2 as a cutoff equating to $\sim 5 \times 10^{16}$ (RT) and $\sim 4 \times 10^{15}$ (CRP) fluorine atoms per voxel. Next we prepared higher concentrations of ^{19}F nanoparticles (200 mM to 1200 mM) to achieve SNR values well above 2, spanning a range of 10^{17}–10^{19} atoms per voxel. From these experiments we calculated an SNR gain of ~16 for the *^{19}F-CRP* when compared to the *^{19}F/^{1}H RT-coil* (Fig. 4B).

High spatially-resolved ^{19}F MRI. An important utilization of the SNR gain is to localize cell infiltrates in the brain with more detail. Previously areas of inflammation were detected using spatial resolutions greater than 600 μm[11]. Here we exploited the superior SNR of the *^{19}F-CRP*, and used an isotropic spatial resolution of 150 μm. *Ex vivo* MR images obtained with the *^{19}F-CRP* from an exemplary EAE mouse (day 10 following EAE induction, score = 1.25) show a more precise distribution of intraparenchymal inflammation. At this spatial resolution, the majority of the ^{19}F signals obtained by the *^{19}F-CRP* were not detected with the RT coil (Fig. 5A–C). In addition we show similar inflammatory patterns in a pre-symptomatic mouse, also sacrificed on day 10 following EAE induction (Supplementary Figure). Within the cerebellum, inflammatory infiltrates were mostly localized within the white matter of the arbor vitae, particularly near deep cerebellar nuclei (Fig. 5B). Clearly delineated inflammatory areas were found in grey matter regions running adjacent to white matter tracts in the cerebellum (Fig. 5A). This is consistent with the expected patterns of inflammation in the EAE model[39,40], also as observed in our own prior studies[11,41,42]. Using the *^{19}F-CRP*, we also observed strong ^{19}F signals in the cerebrum emanating from the striatum and pallidum appearing continuous with ^{19}F signals from the third ventricle (Fig. 5A). Additionally, clear extraparenchymal meningeal inflammation could be seen, consistent with recent reports[43–45]. Especially strong inflammatory signals were observed along the dorsal surface of the brain, including meningeal regions lining fissures between the cerebellar lobules. These inflammatory regions extended ventrally to the prepyramidal fissure, parafloccular sulcus and lateral recess of the fourth ventricle. A dominant ^{19}F signal was observed around the meninges lining the ventral part of the retrosplenial area of the cerebral cortex (Fig. 5B), spreading caudally towards the cerebellum, running in parallel to the superior sagittal sinus, and eventually the retrogleniod vein (Fig. 5C). In these experiments we focused on highly resolved inflammation imaging in the EAE brain, employing long acquisition times in order to compensate for the considerably lower ^{19}F signal sensitivity of the *^{19}F/^{1}H RT-coil*. Since these acquisition times (11 h) are not applicable for *in vivo* studies, we performed further experiments in which we reduced the scan time. Upon reducing the scan time from 11 h to 0.5 h we could still detect ^{19}F signals with the *^{19}F-CRP* (Fig. 6). Despite the clear differences we were nevertheless still able to detect a considerable ^{19}F signal, even with a scan of only 2 h, which is amenable for *in vivo* MRI.

Discussion

In this study we show first ^{19}F MR images obtained with a *^{19}F-CRP* driven in quadrature mode. Compared to the *^{19}F/^{1}H RT-coil* we previously developed[11], we show that the *^{19}F-CRP* facilitates superior *ex vivo* images of brain

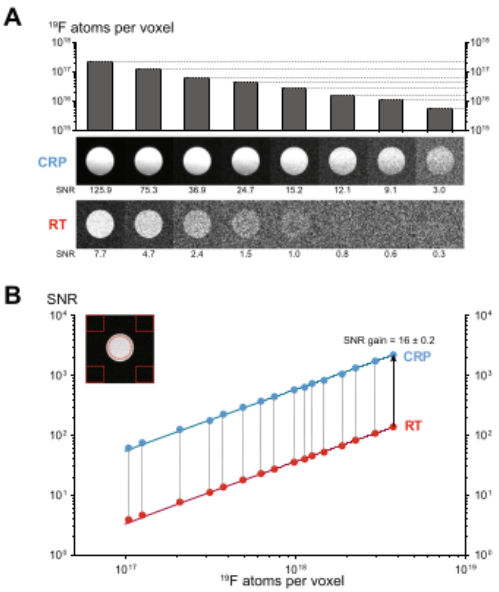

Figure 4. Comparison of ^{19}F signal sensitivity between *^{19}F-CRP* and *^{19}F/^{1}H RT-coil* as a function of the number of ^{19}F atoms. (**A**) Cross-sectional spin-echo ^{19}F MR images of ^{19}F nanoparticle phantoms acquired for both CRP (middle panel) and RT coil (lower panel). Each ^{19}F MR image indicates an MR scan with a defined number of ^{19}F atoms per voxel (upper panel) achieved with different concentrations of PFCE (ranging from 25 mM to 200 mM) and slice thicknesses varying from 0.4 to 2.0 mm. (**B**) Estimation of SNR gain provided by the *^{19}F-CRP* compared to the *^{19}F/^{1}H RT-coil* using high PFCE concentrations (200 mM to 1200 mM) and slice thicknesses varying from 1.0 to 6.0 mm. Shown is a log-log plot of SNR versus ^{19}F atoms per voxel including a linear fit for both CRP ($y = 5e^{-16}x$) and RT coil ($y = 4e^{-17}x$).

inflammation in an animal model of MS. At the current stage of development the *^{19}F-CRP* cannot yet be employed for *in vivo* imaging due to incompatibilities with conventional ^{1}H RT coils, as discussed later. Nevertheless the results are encouraging, and offer proof-of-concept demonstration of the potential for this technology.

After introducing the concept of cryogenically-cooled RF coil hardware to reduce thermal noise and thus increase SNR[46], CRP technologies were developed for small animal MRI, particularly for anatomical ^{1}H MRI of mouse brain[41,47–50]. Introducing a quadrature CRP design, enabled further SNR gains (~2.5) at 400 MHz[24,25] compared to RT coils with similar geometries. The SNR gain prediction for the *^{19}F-CRP* is expected to be equivalent due to the close Larmor frequency (376 MHz at 9.4T).

The potential applications of ^{19}F MR methods to image inflammation have long been recognized[11–17]. For several years, neuroinflammation has been studied using gadolinium-based contrast agents. However, gadolinium-enhancing lesions are diffuse, and lack spatial precision. Improvements have been realized with the use of alternative contrast agents, such iron oxide nanoparticles, although their effects on magnetic susceptibility limit their discrimination from endogenous confounding artifacts. ^{19}F MR methods abrogate this, since ^{19}F signals derive exclusively from exogenously applied ^{19}F nanoparticles. Efforts have been made to boost ^{19}F signal e.g. by promoting ^{19}F nanoparticle cellular uptake[20]. Nevertheless, major challenges of signal sensitivity constraints remain. Improving ^{19}F sensitivity with the *^{19}F-CRP* will be essential to realizing the full potential of ^{19}F MR.

Our motivation to investigate the *^{19}F-CRP* was to increase the sensitivity to detect neuroinflammation. Considering the geometrical differences between both coils, it was imperative to measure SNR at locations below the CRP that correspond to the mouse brain, using phantoms spanning the entire coronal view, as a basis for future *in vivo* studies. We performed SNR measurements for both *^{19}F-CRP* and control *^{19}F/^{1}H RT-coil* using a spin echo sequence (RARE), commonly used for ^{19}F MRI due to its high SNR per unit time compared to spoiled gradient echo sequences.

The sensitivity of the *^{19}F-CRP* is spatially dependent. Given that the CRP is a transceive quadrature surface coil array, both transmit field (B_1^+) and receive sensitivity (B_1^-) diminish with increasing distance from the RF coil – a factor that must be accounted for in quantitative imaging by measuring the actual B_1 and correcting the signal intensities using the signal equation of the employed pulse sequence. This is absolutely essential when signal quantification is necessary in order to ascertain the level of inflammation over the entire region of the brain during EAE. Nevertheless, this characteristic is shared by all transceive surface coils. This adverse effect is counterbalanced by an SNR gain, up to ~15-fold in the practical comparison made within this study. This SNR

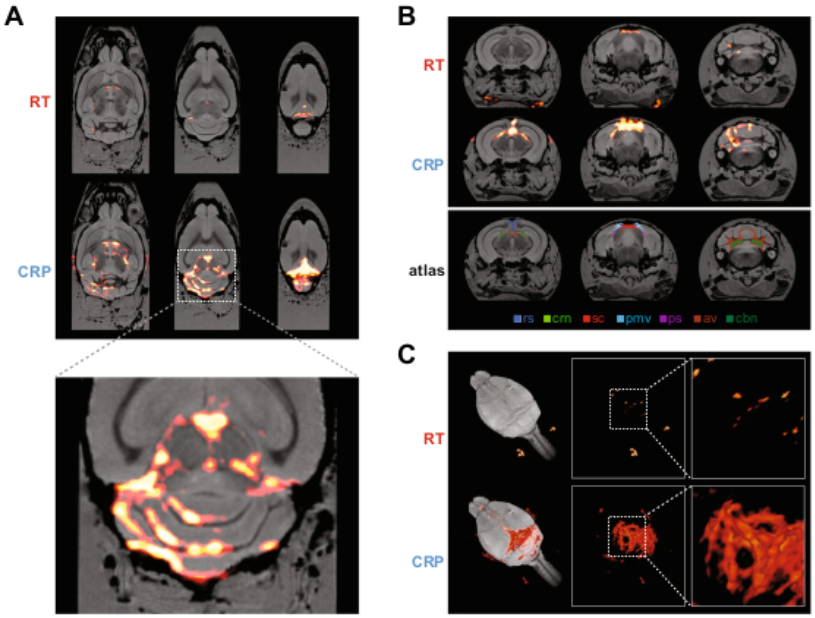

Figure 5. High spatial resolution ^{19}F MR image of an *ex vivo* brain from an EAE mouse showing clinical disease. With both *^{19}F-CRP* and *^{19}F/^{1}H RT-coil*, ^{19}F MR images were acquired using a 3D-RARE sequence. ^{19}F MR images (shown in red) were combined with ^{1}H MR images (shown in grayscale). ^{1}H MR images were acquired using a 3D-FLASH sequence and the *^{19}F/^{1}H RT-coil*. (**A**) Three exemplary slices from horizontal views of combined ^{19}F/^{1}H MR images for both *^{19}F/^{1}H RT-coil* (*upper panel*) and *^{19}F-CRP* (*middle panel*), in the *lower panel* a 300% zoom of the ^{19}F/^{1}H MR images acquired with the CRP. (**B**) Three exemplary slices from coronal views of combined ^{19}F/^{1}H MR images for both RT coil (*upper panel*) and CRP (*middle panel*). Registration of the Allen brain atlas to the ^{1}H image (*lower panel*) shows following labelled brain regions: rs: retrosplenial area; crn: cranial nerves; sc: superior colliculus (sensory related); pmv: posteromedial visual area; ps: postsubiculum; av: arbor vitae; cbn: cerebellar nuclei. (**C**) 3-D rendering of the combined ^{19}F/^{1}H MR images for both *^{19}F/^{1}H RT-coil* (*upper panel*) and *^{19}F-CRP* (*lower panel*).

gain can be attributed to factors including cooling (in the range of 2–3 for ^{1}H[24,25]), differences in RF coil design (birdcage vs. surface coil; quadrature versus linear), RF coil sample loading, and the specific RF pulse power adjustments. Here, pulse power was adjusted in order to avoid substantial signal loss at the dorsal part of the brain, which is observed when using a RARE sequence with excessive RF power. Predicting the sensitivity and detection limits of ^{19}F measurements for specific hardware setups[51] will help facilitate further *^{19}F-CRP* studies with other fluorinated compounds.

An SNR gain of 15 can be exploited in several ways — by reducing scan time by a factor 225 (e.g. from 1 h to ~15 s), or doubling 3D spatial resolution (e.g. from 600 µm to 300 µm) while still gaining SNR (~2.5). In this study we made use of the superior SNR, employing isotropic spatial resolutions of 150 µm to study neuroinflammation. Using the *^{19}F-CRP* at this resolution, we gained more precise information regarding inflammatory cell localization in the brain, compared to our previous study[11]. The ^{19}F MR images with the CRP showed excellent correspondence with the typical pattern of histopathology[39,40]. A robust accumulation of inflammatory lesions, especially in the white matter tracts of the cerebellum, is a hallmark of EAE in SJL mice, which we also observed in our prior studies using high resolution ^{1}H MR[41,42] and low resolution ^{19}F MR[11]. The pathology also extends into the cerebrum, as shown both prior to the occurrence of clinical symptoms (Supplementary Figure) and also during ongoing clinical disease (Figs 5 and 6). The *^{19}F-CRP* MR images also enabled discrimination of extraparenchymal meningeal inflammation, consistent with recent reports highlighting the relevance of inflammatory cell trafficking via the blood meningeal barrier[43,44] and extravasation via leptomeningeal microvessels into the subarachnoid space[45]. This also reflects the situation in MS[3–5]. Recent studies have argued for the presence of a lymphatic circulation in the meninges in association with these vessels, capable of draining immune cells from meningeal spaces[8] and brain parenchyma[7] into deep cervical lymph nodes. Therefore, the capacity to perform non-invasive longitudinal investigations with fidelity ^{19}F MRI to monitor the dynamics and distribution of infiltrating immune cells will be directly relevant for experimental neuroimmunologists.

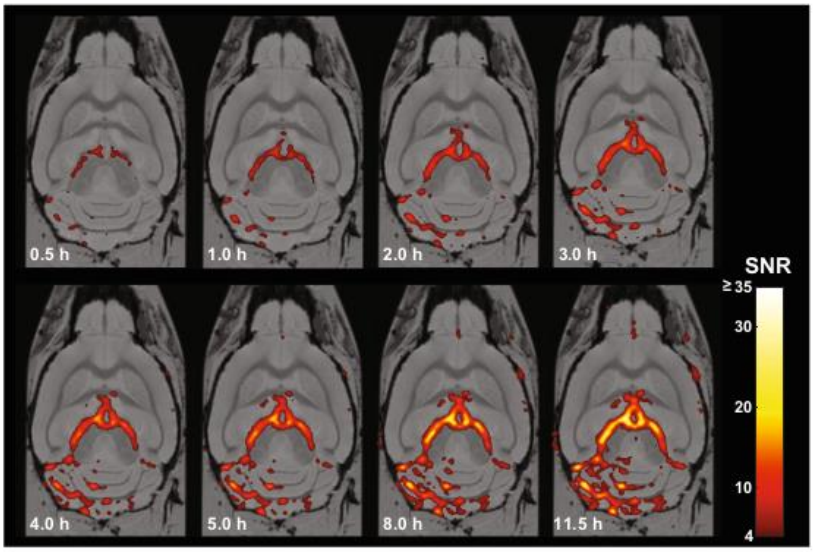

Figure 6. High spatial resolution ^{19}F MRI using acquisition times feasible for *in vivo* imaging. ^{19}F MR images were acquired with the *^{19}F-CRP* using acquisition times between 30 min and 11 h. The ^{19}F images were scaled to units of SNR, thresholded at SNR = 4, and overlayed onto the ^{1}H MR images using a pseudocolor scale.

The gradient in the B_1 field of the *^{19}F-CRP* leads to a gradual decline in ^{19}F MR signal with increasing distance from the probe head. This results in reduced signal in ventral regions. Studies of the EAE model are, in general, more focused on imaging of the CNS, and less so on imaging of the superficial lymph nodes. When imaging of the lymph nodes in the ventral regions is necessary, one could consider measuring the mouse brain in the supine and prone positions, in order to ensure coverage of the dorsal sides comprising the whole brain as well as ventral sides to include the draining lymph nodes. Other possible workarounds include adding an anterior ^{19}F RT RF coil to the mouse bed or combining ^{19}F images from RT and CRP. These approaches could help to overcome this inherent limitation of the *^{19}F-CRP*, while still utilizing its superior SNR. While the spatial dependency poses a constraint for studies investigating the involvement of the draining lymph nodes, the translational applications of the *^{19}F-CRP* are not limited to EAE. The *^{19}F-CRP* will also be useful for studying brain inflammation in animal models of tumour growth (especially those tumours implanted in the cortex or striatum), and studies on the middle cerebral artery occlusion model of stroke. Inflammation in these preclinical models could readily be imaged, since the focus of pathology in these models is located in regions where the *^{19}F-CRP* clearly outperforms the *^{19}F/^{1}H RT-coil*.

In vivo ^{19}F MRI studies require acquisition of anatomical ^{1}H MR images within a reasonable time frame. A dual-tunable RF probe would be most ideal, in order to avoid inaccurate co-registration of both signals[52]. Despite the clear improvement in SNR of the *^{19}F-CRP*, the quadrature design prohibits the presence of a dual resonant MR signal that would be needed for anatomical ^{1}H MRI. Furthermore conventional ^{1}H RF resonators cannot be used in combination with the *^{19}F-CRP* due to coupling between both RF coils. To avoid this, the *^{19}F-CRP* would need to be removed while the *in vivo* ^{1}H images are acquired. This would cause changes in the alignment of the mouse within the scanner during *in vivo* measurements that are serious enough to constitute a major hindrance. Even with the use of reference markers, any slight shift in the position of the markers with respect to the mouse during the procedure will result in an incorrect registration between ^{19}F and ^{1}H images. The current procedure of registering the ^{19}F images of the CRP with those of the RT RF coil is complicated and time consuming, requires sufficient SNR and is an impediment for *in vivo* experiments. A proposed solution to this limitation could be to construct an anterior ^{1}H RT RF coil, specifically designed to be added to the mouse bed while the *^{19}F-CRP* remains installed, in order to provide anatomical guidance. A dual-tunable ^{1}H/^{19}F RT RF coil would also take into account the above approach (implementation of a ^{19}F RF-coil below the mouse head).

This study presents the first demonstration of the performance of a quadrature *^{19}F-CRP* tailored for small rodents, showing superior SNR and ^{19}F MR image quality. The logical extension of this work will be to translate these results into *in vivo* studies, such as those studying pathological changes during neuroinflammatory disease. While the results of the current study are highly encouraging, a challenging road still lies ahead for the application of the *^{19}F-CRP* in *in vivo* studies. Previous studies using ^{19}F MR have been seriously hampered by the low SNR, and compensating for this limitation by using low spatial resolution has generally yielded images with rather poor definition, and therefore limited scientific utility. The current study aims to improve this situation, bringing ^{19}F

MR imaging a step closer to the objective of 'microscopic MRI'. Our results showed a remarkable SNR and detail of neuroinflammation, compared to conventional ^{19}F MRI, heralding a bright potential for the application of ^{19}*F-CRP* for non-invasive MRI *in vivo*.

References

1. Stadelmann, C., Wegner, C. & Bruck, W. Inflammation, demyelination, and degeneration-recent insights from MS pathology. *Biochim. Biophys. Acta* **1812**, 275–282 (2011).
2. Lucchinetti, C. *et al.* Heterogeneity of multiple sclerosis lesions: implications for the pathogenesis of demyelination. *Ann. Neurol.* **47**, 707–717 (2000).
3. Gilmore, C. P. *et al.* Regional variations in the extent and pattern of grey matter demyelination in multiple sclerosis: a comparison between the cerebral cortex, cerebellar cortex, deep grey matter nuclei and the spinal cord. *J. Neurol. Neurosurg. Psychiatry* **80**, 182–187 (2009).
4. Howell, O. W. *et al.* Meningeal inflammation is widespread and linked to cortical pathology in multiple sclerosis. *Brain* **134**, 2755–2771 (2011).
5. Howell, O. W. *et al.* Extensive grey matter pathology in the cerebellum in multiple sclerosis is linked to inflammation in the subarachnoid space. *Neuropathol. Appl. Neurobiol.* **41**, 798–813 (2015).
6. Reboldi, A. *et al.* C-C chemokine receptor 6-regulated entry of TH-17 cells into the CNS through the choroid plexus is required for the initiation of EAE. *Nat. Immunol.* **10**, 514–523 (2009).
7. Aspelund, A. *et al.* A dural lymphatic vascular system that drains brain interstitial fluid and macromolecules. *J. Exp. Med.* **212**, 991 (2015).
8. Louveau, A. *et al.* Structural and functional features of central nervous system lymphatic vessels. *Nature* **523**, 337–341 (2015).
9. Kipnis, J. Multifaceted interactions between adaptive immunity and the central nervous system. *Science* **353**, 766–771 (2016).
10. Engelhardt, B. *et al.* Vascular, glial, and lymphatic immune gateways of the central nervous system. *Acta. Neuropathologica* **132**, 317–338 (2016).
11. Waiczies, H. *et al.* Visualizing brain inflammation with a shingled-leg radio-frequency head probe for 19F/1H MRI. *Sci. Rep.* **3**, 1280 (2013).
12. Flögel, U. *et al.* *In vivo* monitoring of inflammation after cardiac and cerebral ischemia by fluorine magnetic resonance imaging. *Circulation* **118**, 140–148 (2008).
13. Ahrens, E. T., Young, W. B., Xu, H. & Pusateri, L. K. Rapid quantification of inflammation in tissue samples using perfluorocarbon emulsion and fluorine-19 nuclear magnetic resonance. *Biotechniques* **50**, 229–234 (2011).
14. Flogel, U. *et al.* Selective activation of adenosine A2A receptors on immune cells by a CD73-dependent prodrug suppresses joint inflammation in experimental rheumatoid arthritis. *Sci. Transl. Med.* **4**, 146ra108 (2012).
15. Temme, S., Bonner, F., Schrader, J. & Flogel, U. ^{19}F magnetic resonance imaging of endogenous macrophages in inflammation. *Wiley Interdiscip. Rev. Nanomed. Nanobiotechnol.* **4**, 329–343 (2012).
16. Ahrens, E. T. & Zhong, J. In vivo MRI cell tracking using perfluorocarbon probes and fluorine-19 detection. *NMR Biomed.* **26**, 860–871 (2013).
17. Jacoby, C. *et al.* Probing different perfluorocarbons for *in vivo* inflammation imaging by 19F MRI: image reconstruction, biological half-lives and sensitivity. *NMR Biomed.* **27**, 261–271 (2014).
18. Ahrens, E. T., Flores, R., Xu, H. & Morel, P. A. *In vivo* imaging platform for tracking immunotherapeutic cells. *Nat. Biotechnol.* **23**, 983–987 (2005).
19. Ahrens, E. T., Helfer, B. M., O'Hanlon, C. F. & Schirda, C. Clinical cell therapy imaging using a perfluorocarbon tracer and fluorine-19 MRI. *Magn. Reson. Med.* **72**, 1696–701 (2014).
20. Waiczies, S. *et al.* Anchoring dipalmitoyl phosphoethanolamine to nanoparticles boosts cellular uptake and fluorine-19 magnetic resonance signal. *Sci. Rep.* **5**, 8427 (2015).
21. Dardzinski, B. J. & Sotak, C. H. Rapid tissue oxygen tension mapping using ^{19}F inversion-recovery echo-planar imaging of P erfluoro-15-crown-5-ether. *Magnetic resonance in medicine* 32, (88–97 (1994).
22. Kadayakkara, D. K., Janjic, J. M., Pusateri, L. K., Young, W. B. & Ahrens, E. T. *In vivo* observation of intracellular oximetry in perfluorocarbon-labeled glioma cells and chemotherapeutic response in the CNS using fluorine-19 MRI. *Magn. Reson. Med.* **64**, 1252–1259 (2010).
23. Faber, C. & Schmid, F. Pulse Sequence Considerations and Schemes in *Fluorine Magnetic Resonance Imaging* (ed. Flögel, U. and Ahrens, E.) 1–28 (Pan Stanford Publishing (2016).
24. Baltes, C., Radzwill, N., Bosshard, S., Marek, D. & Rudin, M. Micro MRI of the mouse brain using a novel 400 MHz cryogenic quadrature RF probe. *NMR Biomed.* **22**, 834–842 (2009).
25. Junge, S. Cryogenic and Superconducting Coils for MRI in *eMagRes* (ed. Wasylishen, R.) 505–514 (John Wiley & Sons, Ltd (2012).
26. Waiczies, H. *et al.* Perfluorocarbon particle size influences magnetic resonance signal and immunological properties of dendritic cells. *PLoS One* **6**, e21981 (2011).
27. Akoka, S., Franconi, F., Seguin, F. & Le Pape, A. Radiofrequency map of an NMR coil by imaging. *Magn. Reson. Imaging* **11**, 437–441 (1993).
28. Insko, E. K. & Bolinger, L. Mapping of the Radiofrequency Field. *J. Magn. Reson., Series A* **103**, 82–85 (1993).
29. NEMA. Determination of signal-to-noise ratio (SNR) in diagnostic magnetic resonance imaging. *NEMA Standards Publication MS*, 1–2008 (2008).
30. Henkelman, R. M. Measurement of signal intensities in the presence of noise in MR images. *Med. Phys.* **12**, 232–233 (1985).
31. Gudbjartsson, H. & Patz, S. The Rician Distribution of Noisy MRI Data. *Magn. Reson. Med.* **34**, 910–914 (1995).
32. Constantinides, C. D., Atalar, E. & McVeigh, E. R. Signal-to-noise measurements in magnitude images from NMR phased arrays. *Magn. Reson. Med.* **38**, 852–857 (1997).
33. Tustison, N. & Avants, B. Explicit B-spline regularization in diffeomorphic image registration. *Front. Neuroinform.* **7**, doi:10.3389/fninf.2013.00039 (2013).
34. Avants, B. B. *et al.* A reproducible evaluation of ANTs similarity metric performance in brain image registration. *Neuroimage* **54**, 2033–2044 (2011).
35. Lein, E. S. *et al.* Genome-wide atlas of gene expression in the adult mouse brain. *Nature* **445**, 168–176 (2007).
36. Sawiak, S., Wood, N., Williams, G., Morton, A. & Carpenter, T. Use of magnetic resonance imaging for anatomical phenotyping of the R6/2 mouse model of Huntington's disease. *Neurobiol. Dis.* **33**, 12–19 (2009).
37. Shamonin, D. P. *et al.* Fast parallel image registration on CPU and GPU for diagnostic classification of Alzheimer's disease. *Front. Neuroinform.* **7**, 50 (2014).
38. Yushkevich, P. A. *et al.* User-guided 3D active contour segmentation of anatomical structures: Significantly improved efficiency and reliability. *Neuroimage* **31**, 1116–1128 (2006).
39. Gold, R., Linington, C. & Lassmann, H. Understanding pathogenesis and therapy of multiple sclerosis via animal models: 70 years of merits and culprits in experimental autoimmune encephalomyelitis research. *Brain* **129**, 1953–1971 (2006).
40. Brown, D. A. & Sawchenko, P. E. Time course and distribution of inflammatory and neurodegenerative events suggest structural bases for the pathogenesis of experimental autoimmune encephalomyelitis. *J. Comp. Neurol.* **502**, 236–260 (2007).

41. Waiczies, H. *et al*. Identification of Cellular Infiltrates during Early Stages of Brain Inflammation with Magnetic Resonance Microscopy. *PLoS One* **7**, e32796 (2012).
42. Lepore, S. *et al*. Enlargement of cerebral ventricles as an early indicator of encephalomyelitis. *PLoS One* **8**, e72841 (2013).
43. Bartholomaus, I. *et al*. Effector T cell interactions with meningeal vascular structures in nascent autoimmune CNS lesions. *Nature* **462**, 94–98 (2009).
44. Mues, M. *et al*. Real-time *in vivo* analysis of T cell activation in the central nervous system using a genetically encoded calcium indicator. *Nat. Med.* **19**, 778–783 (2013).
45. Schläger, C. *et al*. Effector T-cell trafficking between the leptomeninges and the cerebrospinal fluid. *Nature* **530**, 349–353 (2016).
46. Hoult, D. I. & Richards, R. E. The signal-to-noise ratio of the nuclear magnetic resonance experiment. *J. Magn. Reson. (1969)* **24**, 71–85 (1976).
47. Ratering, D., Baltes, C., Nordmeyer-Massner, J., Marek, D. & Rudin, M. Performance of a 200-MHz cryogenic RF probe designed for MRI and MRS of the murine brain. *Magn. Reson. Med.* **59**, 1440–1447 (2008).
48. Nouls, J. C., Izenson, M. G., Greeley, H. P. & Johnson, G. A. Design of a superconducting volume coil for magnetic resonance microscopy of the mouse brain. *J. Magn. Reson.* **191**, 231–238 (2008).
49. Wagenhaus, B. *et al*. Functional and morphological cardiac magnetic resonance imaging of mice using a cryogenic quadrature radiofrequency coil. *PLoS One* **7**, e42383 (2012).
50. Niendorf, T. *et al*. Advancing Cardiovascular, Neurovascular and Renal Magnetic Resonance Imaging in Small Rodents Using Cryogenic Radiofrequency Coil Technology. . *Front. Pharmacol.* **6**, 255 (2015).
51. Taylor, A. J. *et al*. Probe-Specific Procedure to Estimate Sensitivity and Detection Limits for 19F Magnetic Resonance Imaging. *PLoS One* **11**, e0163704 (2016).
52. Tomanek, B., Volotovskyy, V., Gruwel, M. L. H., McKenzie, E. & King, S. B. Double-frequency birdcage volume coils for 4.7T and 7T. *Concepts Magn. Reson. Part B Magn. Reson. Eng.* **26B**, 16–22 (2005).

Acknowledgements

This study was funded by the Deutsche Forschungsgemeinschaft to S.W. (DFG WA2804) and A.P. (DFG PO1869). The funders had no role in study design, data collection and analysis, decision to publish, or preparation of the manuscript. We thank Stefanie Kox for preparation of nanoparticles, Marco Küng for building and optimizing the RF coil and associated circuitry, and Marco Sacher for contributions to mechanical design.

Author Contributions

S.W., T.N., and A.P. conceived the development of the *19F-C R P* and designed the study S.W., J.M.M, P.R.D., C.P., D.W., R.W. and A.P. carried out the experiments and measurements. S.W., L.S., P.R.D., T.H., S.P.K., P.B.S., H.W. and A.P. performed the analyses. D.M. developed the RF-Probe. S.W., J.M.M., T.N. and A.P. wrote the manuscript with the assistance of all other co-authors.

Additional Information

Competing Interests: The authors declare that they have no competing interests.

Publisher's note: Springer Nature remains neutral with regard to jurisdictional claims in published maps and institutional affiliations.

11 Publikation 5: Fluorine-19 MRI at 21.1 T

Magnetic Resonance Materials in Physics, Biology and Medicine (2019) 32:37–49
https://doi.org/10.1007/s10334-018-0710-z

RESEARCH ARTICLE

Fluorine-19 MRI at 21.1 T: enhanced spin–lattice relaxation of perfluoro-15-crown-5-ether and sensitivity as demonstrated in ex vivo murine neuroinflammation

Sonia Waiczies[1] · Jens T. Rosenberg[2] · Andre Kuehne[3] · Ludger Starke[1] · Paula Ramos Delgado[1] · Jason M. Millward[1] · Christian Prinz[1] · Joao dos Santos Periquito[1] · Andreas Pohlmann[1] · Helmar Waiczies[3] · Thoralf Niendorf[1,3,4]

Received: 4 July 2018 / Revised: 16 October 2018 / Accepted: 18 October 2018 / Published online: 12 November 2018

Abstract

Objective Fluorine MR would benefit greatly from enhancements in signal-to-noise ratio (SNR). This study examines the sensitivity gain of ^{19}F MR that can be practically achieved when moving from 9.4 to 21.1 T.

Materials and methods We studied perfluoro-15-crown-5-ether (PFCE) at both field strengths (B_0), as a pure compound, in the form of nanoparticles (NP) as employed to study inflammation in vivo, as well as in inflamed tissue. Brains, lymph nodes (LNs) and spleens were obtained from mice with experimental autoimmune encephalomyelitis (EAE) that had been administered PFCE NPs. All samples were measured at both B_0 with 2D-RARE and 2D-FLASH using ^{19}F volume radiofrequency resonators together. T_1 and T_2 of PFCE were measured at both B_0 strengths.

Results Compared to 9.4 T, an SNR gain of > 3 was observed for pure PFCE and > 2 for PFCE NPs at 21.1 T using 2D-FLASH. A dependency of ^{19}F T_1 and T_2 relaxation on B_0 was demonstrated. High spatially resolved ^{19}F MRI of EAE brains and LNs at 21.1 T revealed signals not seen at 9.4 T.

Discussion Enhanced SNR and T_1 shortening indicate the potential benefit of in vivo ^{19}F MR at higher B_0 to study inflammatory processes with greater detail.

Keywords Fluorine-19 magnetic resonance imaging · Magnetic fields · Experimental autoimmune encephalomyelitis · Signal-to-noise ratio

Introduction

Fluorine-19 (^{19}F) magnetic resonance (MR) methods have found their application in a wide range of biomedical research areas. One branch of research is the tracking of cells, including inflammatory cells, in vivo with the help of fluorine ^{19}F nanoparticles (NPs) [1–7]. ^{19}F MR methods provide several advantages over methods employing contrast agents such as iron oxide particles that modulate proton relaxation [8, 9]. Iron oxide particles such as ultrasmall iron oxide agents are potentially advantageous with regard to their MR sensitivity, but suffer from drawbacks such as signal quantification and a difficulty to distinguish the contrast which they create in the cells they label from other intrinsic tissue contrasts [8]. Due to the absence of organic ^{19}F in living organisms, the acquired ^{19}F MR images are free from background signal, such that ^{19}F/^{1}H MRI is able to localize labeled cells in vivo with complete signal

Electronic supplementary material The online version of this article (https://doi.org/10.1007/s10334-018-0710-z) contains supplementary material, which is available to authorized users.

✉ Sonia Waiczies
sonia.waiczies@mdc-berlin.de

1 Experimental Ultrahigh Field MRI, Berlin Ultrahigh Field Facility (B.U.F.F.), Max Delbrück Center for Molecular Medicine in the Helmholtz Association, Robert-Roessle-Str. 10, 13125 Berlin, Germany

2 The National High Magnetic Field Laboratory, Florida State University, Tallahassee, FL, USA

3 MRI TOOLS GmbH, Berlin, Germany

4 Experimental and Clinical Research Center, A Joint Cooperation Between the Charité Medical Faculty and the Max Delbrück Center for Molecular Medicine in the Helmholtz Association, Berlin, Germany

selectivity and specificity. ^{19}F MR directly detects the ^{19}F spins in the cells labeled with ^{19}F NPs, meaning that ^{19}F NPs are cell labels, rather than contrast agents. The possibility of quantifying inflammatory cells by ^{19}F MR spectroscopy is another advantage, allowing a quantitative assessment of inflammation and of anti-inflammatory strategies. However, the usefulness of ^{19}F MR in a wide range of biomedical imaging applications is hampered by the low availability of ^{19}F spins in the living organism. This is compounded by the fact that the signal sensitivity of current state-of-the-art MR equipment remains limited, making ^{19}F MR measurements of fluorine compounds present at low concentrations an extremely challenging task.

Therefore, there is a need to improve the sensitivity of the measuring instrument to increase the signal-to-noise ratio (SNR). One way to improve signal sensitivity is to increase the strength of the static magnetic field (B_0) [10], a strategy which has also been actively pursued for clinical application [11]. Intrinsic SNR is expected to grow at least linearly with increasing frequency and B_0 strengths [12–14]. In early seminal studies using solenoid RF coils at frequencies (f) below 1 MHz, the maximum sensitivity was expected to be proportional to the frequency: sensitivity $\propto f^{1.75}$; this proportionality approached linearity when sample losses predominated [12, 13]. At low field strengths, the principle of reciprocity can be used to calculate the receive field (B_1) sensitivity of a single channel RF coil in terms of the transmit field (B_1^+) that can be easily measured [15]. In the high-field domain, the increasing f and the influence of wave propagation need to be considered [10]. The homogeneity of the B_1^+ field is expected to decline with increasing B_0, thereby influencing the overall SNR gain. An experimental study investigating SNR dependency on B_0 in the human brain revealed SNR $\propto B_0^{1.65}$ in the range of 3.0 T to 9.4 T [14]. A recent simulation study also showed that SNR grows super-linearly with frequency, particularly in the deeper regions of the sample; in less deep regions, the SNR versus B_0 trend approached linearity [16]. Ultrahigh field imaging has proven particularly beneficial for X-nuclei imaging such as sodium MR, in which a change in B_0 from 9.4 to 21.1 T resulted in an SNR gain of ~3 compared to a gain of ~2 for ^{1}H MR [17].

Here, we studied the feasibility of ^{19}F MRI at 21.1 T compared to 9.4 T, and the influence of the B_0 change on the SNR and ^{19}F relaxation of the compound fluoro-15-crown-5-ether (PFCE). According to theory and previously published experimental results, we postulated that SNR would increase by a factor of three to four when moving from 9.4 to 21.1 T. We therefore investigated how much of the expected sensitivity gain could be achieved in practical experiments. The rationale behind these experiments was to make use of higher B_0 strengths to study inflammatory cell migration with better resolution and detail. Using ^{19}F MRI and ^{19}F NPs that label immune cells in vivo, we studied inflammation in experimental autoimmune encephalomyelitis (EAE), the animal model of multiple sclerosis [6, 18]. The main driving force for using higher B_0 is to boost sensitivity and therefore resolution of the in vivo ^{19}F MR images.

Materials and methods

Small animal MR scanners

All experiments were carried out on two small animal MR scanners with different magnetic field strengths: a 21.1 T vertical bore MR system operating at 900 MHz (^{1}H) and 844.9 MHz (^{19}F) at the National High Magnetic Field Laboratory (NHMFL) in Tallahassee (Florida, USA) and a 9.4 T horizontal bore MR system (BioSpec 94/20, Bruker BioSpin MRI, Ettlingen) operating at 400 MHz (^{1}H) and 376 MHz (^{19}F) located in Berlin (Germany). The 21.1 T magnet was designed and constructed at the NHMFL [19]. It has a bore size of 105 mm and a 64-mm inner diameter imaging gradients (Resonance Research Inc, Billerica, MA) that provides a peak gradient strength of 6 mT/cm over a 64-mm diameter [20]. The 9.4 T system has a bore of 120 mm and an actively shielded B-GA12 gradient set providing gradient amplitudes of 4 mT/cm. Both MR systems are equipped with a Bruker Avance III console and operated using PV6.1 software (Bruker BioSpin, Ettlingen, Germany).

Radiofrequency (RF) coils and EMF simulations

Experiments were carried out on the 21.1 T using a linear low pass (LP) ^{19}F/^{1}H birdcage RF coil consisting of eight rungs: coil length = 54.5 mm, inner diameter = 33 mm, shield length = 64 mm, shield diameter = 53 mm. For experiments at the 9.4 T MR system, a linear high-pass ^{19}F/^{1}H RF coil of similar dimensions was used (12 rungs, coil length = 50 mm, inner diameter = 35 mm, shield length = 80 mm, shield diameter = 57 mm). To estimate the expected SNR gain, electromagnetic field (EMF) simulations were performed for both RF coils using the finite-element method (FEM) implemented in CST Microwave Studio (CST, Darmstadt, Germany). FEM was chosen over a time-domain solver because the unstructured finite-element meshes can more accurately resolve the current distributions occurring on metal structures with singular edges such as copper strips, thus leading to a more accurate loss estimation. Copper and substrate losses were calculated in the 3D domain by the FEM solver based on their respective conductivity and loss tangent values (copper conductivity σ = 5.8e7 S/m, FR4 tan δ = 0.025). Capacitors were assigned equivalent series resistances according to manufacturer datasheets, and solder losses also modeled as frequency-dependent resistors scaled to the desired frequency based on available literature

data [21]. Both RF coils were loaded with a 15-ml falcon tube phantom filled with tissue equivalent material ($\varepsilon = 78$, $\sigma = 0.79$ S/m for 9.4 T, $\varepsilon = 78$, $\sigma = 0.94$ S/m for 21.1 T). Cable losses and preamplifier noise were approximated by appropriate attenuators inserted between the power source and the RF coil in the simulation; attenuation was set according to the losses at the respective frequency (9.4 T: 0.5 dB preamplifier noise figure, 2 m cable with 0.58 dB/m attenuation; 21.1 T: 1 dB preamp noise figure, 3 m cable with 0.9 dB/m attenuation). The coils were perfectly tuned and matched ($|S_{11}| < -40$ dB) and were fed with a forward power of 1 kW, which is dissipated in the system according to the noise power contribution of the different noise sources (Table 1). The average receive field (B_1^-) magnitude was calculated in a $5 \times 5 \times 5$ mm cube in the isocenter of the coil. The relative estimated SNR between both systems was then calculated as follows:

$$\frac{\mathrm{SNR}_{21.1\mathrm{T}}}{\mathrm{SNR}_{9.4\mathrm{T}}} = \left(\frac{f_{0|21.1\mathrm{T}}}{f_{0|9.4\mathrm{T}}}\right)^2 \cdot \left(\frac{B_{1|21.1\mathrm{T}}^-}{B_{1|9.4\mathrm{T}}^-}\right), \quad (1)$$

where B_1^- is the average receive field strength of each RF coil in $\mu T/\sqrt{kW}$ [15].

Animal experiments

All experiments were conducted in accordance with the procedures approved by the Animal Welfare Department of the State Office of Health and Social Affairs Berlin (LAGeSo), and conformed to national and international guidelines to minimize discomfort to animals (86/609/EEC). Experimental autoimmune encephalomyelitis (EAE) was actively induced in SJL/J mice as previously described [18]. Female SJL/J mice (Janvier SAS, Le Genest-St-Isle, France) were immunized subcutaneously with 250 µg $PLP_{139-151}$ purity > 95% (Pepceuticals Ltd., UK) together with Complete Freund's Adjuvant and heat-killed *Mycobacterium tuberculosis* (H37Ra, Difco). On each day following immunization, mice were weighed and scored as follows: 0, no disease; 1, tail weakness and righting reflex weakness; 2, paraparesis; 3, paraplegia; 4, paraplegia with forelimb weakness or paralysis; 5, moribund or dead animal. Five days following EAE induction, mice were administered NPs containing 5 µmol of the ^{19}F compound fluoro-15-crown-5-ether (PFCE) [18]. NPs were prepared by emulsifying 1200 mM PFCE (Fluorochem, UK) with Pluronic F-68 (Sigma-Aldrich, Germany) using a titanium sonotrode (Sonopuls GM70, Bandelin, Germany), as previously described [22]. NPs were administered daily to EAE mice from day 5 to day 10 after immunization. On day 10, the mice were transcardially perfused with 20 ml PBS followed by 20 ml 4% paraformaldehyde (PFA) following terminal anesthesia, after which the tissue was prepared for ex vivo MRI [18].

Table 1 Contribution of each noise source to the total noise power

Noise Source	B_0 (T)	Noise power contribution (%)
Preamplifier	9.4	11.0
	21.1	20.6
Connection cables	9.4	20.9
	21.1	36.8
Capacitors	9.4	24.8
	21.1	1.1
Copper and housing	9.4	7.8
	21.1	4.3
Sample	9.4	35.5
	21.1	37.1

A forward power of 1 kW used for simulating the B_1^- field was dissipated in the system according to the different contributions of these sources to the total noise power. The 9.4 T coil is just minimally sample noise dominated (35.5% sample losses vs. 32.6% intrinsic coil losses), whereas at 21.1 T sample noise almost completely dominates (37.1% vs 5.4%)

Sample preparation

In this study, we focused on PFCE since this ^{19}F compound is commonly used to image inflammation and to track cells in vivo. We prepared (1) PFCE phantoms containing only pure PFCE (*Setup 1*), (2) NPs containing different concentrations of PFCE (*Setup 2*), (3) inflamed tissue infiltrated by inflammatory cells labeled with PFCE NPs (*Setup 3*). The same phantoms were used at both 9.4 T and 21.1 T B_0 strengths.

For studying PFCE in pure form, we submerged an NMR tube containing pure PFCE in a 15-ml tube filled with water containing 4.5 g/L NaCl (this NaCl concentration provides the best electrodynamic loading conditions for a 15-ml tube for the RF coils used). For studying PFCE in nanoparticle form, four NMR tubes containing different PFCE concentrations (60 mM, 120 mM, 600 mM, 1200 mM PFCE) were submerged in a 50-ml tube containing 4.5 g/L NaCl. For studying PFCE in inflamed tissue, we prepared EAE mice that had been transcardially perfused with PBS and 4% PFA (see above). To examine PFCE in the inflamed central nervous system (CNS), as well as associated lymphatic tissue, the mice were cleared of the external pelt, extremities, and thoracic and abdominal tissues. Brain and spinal cord (CNS) were kept in situ within the skull and vertebral column, keeping head and neck draining lymph nodes (LNs) in the preparation. Other lymphoid tissue such as spleen was also harvested and stored separately in 2-ml tubes containing 4% PFA. All fixed tissue was stored at 4 °C. CNS/LNs

preparations were transferred and secured within 15-ml tubes filled with 4% PFA. Spleens were inserted and secured within NMR tubes to maintain the longitudinal alignment of the tissue along the z-axis (B_0 field) for both horizontal (9.4 T) and vertical (21.1 T) bores. The NMR tubes holding the spleens were then transferred to 15-ml tubes filled with 4.5 g/L NaCl. All 15-ml tubes (containing pure compound, CNS/LNs tissue or spleens) were positioned within a 50-ml tube.

MR measurements

To determine SNR differences in ^{19}F measurements between the two magnetic field strengths, we made use of two of the above phantom setups (*Setup 1* and *Setup 2*). For the ^{19}F phantom with pure PFCE (*Setup 1*) we employed a 2D-FLASH technique with variable repetitions times (TRs) and flip angles (FAs): TR = 14–4000 ms, TE = 4.2 ms, FA = 5°–90°, dummy scans = 80, exc. pulse = sinc10H (3000 Hz), FOV = [32 × 32] mm^2, matrix = 256 × 256, averages (NA) = 6, TA (acquisition time) = 0.5–30 min (according to TR). To quantify and compare SNR in a way more relevant for brain inflammation, we measured SNR as a function of the number of ^{19}F atoms using phantoms containing different concentrations of ^{19}F nanoparticles and different slice thickness (*Setup 2*). We acquired axial ^{19}F MR images using 2D-RARE: TR = 4000 ms, TE = 9.1 ms, ETL (echo train length, rare factor) = 4, FOV = [30 × 30] mm^2, matrix = 128 × 126, slices = 1–10 mm, NA = 1, TA = 17 min.

Parametric mapping was performed on axial slices of *Setup 1* and *Setup 2*, as well as coronal slices of *Setup 3* (EAE spleen tissue) to determine T_1 and T_2 of PFCE. A RARE sequence with variable repetition times (RARE-VTR) was used for T_1-mapping. A multi-spin echo (MSE) technique was employed for T_2-mapping. For *Setup 1* (pure PFCE) we used the following parameters for RARE-VTR: 14 TRs = 29–5000 ms, TE = 5.6 ms, ETL = 4, FOV = [20 × 20] mm^2, matrix = 144 × 144, slice thickness = 5 mm, NA = 2, TA = 17 min; for MSE: TR = 30 s, 40 × TEs = 160–6400 ms, FOV = [20 × 20] mm^2, matrix = 96 × 96, slice thickness = 10 mm, NA = 4, TA = 3 h 12 min. For *Setup 2* (PFCE nanoparticles) we used the following parameters for RARE-VTR: 15 TRs = 24–8000 ms, TE = 4.6 ms, ETL = 4, FOV = [30 × 30] mm^2, matrix = 96 × 96, slice thickness = 10 mm, NA = 36, TA = 5 h 42 m; for MSE: TR = 4000 ms, 150 TEs = 7–1050 ms, FOV = [30 × 30] mm^2, matrix = 96 × 96, slice thickness = 10 mm, NA = 64, TA = 6 h 49 min. For *Setup 3* (spleens from EAE mice administered with nanoparticles) we acquired different repetitions of the same coronal spleen slice using RARE-VTR: 9 TRs = 50–12000 ms, TE = 6.9 ms, ETL = 4, FOV = [20 × 30] mm^2, matrix = 44 × 64, slice thickness = 3.6 mm, NA = 128, TA = 15 h 50 min.

For visualizing inflammation in the EAE mouse CNS and associated lymph nodes, we acquired ^{1}H MR images using 3D-FLASH: TR = 150 ms, TE = 7.5 ms, FOV = 30 × 20 × 20 mm, matrix = 600 × 400 × 400, NA = 2, TA = 3 h 20 min and ^{19}F MR images at different spatial resolutions using 3D-RARE: TR = 800 ms, TE = 4.9 ms, FOV = 30 × 20 × 20 mm, NA = 256, *high-resolution*: matrix = 195 × 130 × 130, ETL = 33, TA = 7 h 30 min; *medium-resolution*: matrix = 135 × 90 × 90, ETL = 23, TA = 5 h 14 min; *low-resolution*: matrix = 90 × 60 × 60, ETL = 15, TA = 3 h 24 min.

Data analysis

SNR was calculated using MATLAB® (R2018a, The Mathworks, Natick, USA) by dividing the signal from magnitude images (S_m) by the standard deviation of the background (σ_m). For both *Setup 1* and *Setup* 2, a single SNR value was determined from the mean signal intensity over one central circular regions of interest covering ~ 90% of visible sample and the standard deviation of the noise of four region of interests positioned at the corners of the image. SNR was corrected to compensate for the non-Gaussian distribution [23]. For both single channel RF coils used, the intensity values of the MR images are expected to follow a Rician distribution [24, 25]. We estimated the true SNR from the S_m and background σ_m using:

$$\mathrm{SNR} = \frac{S}{\sigma} = \frac{S_m}{\sigma_m} \cdot \frac{f_S(S_m, \sigma_m)}{1/c_\sigma}, \tag{2}$$

where c_σ is 0.655 (for Rician distribution) and the correction function f_S is derived from the mean of the respective distribution [24, 26]. The noise-induced signal bias of the conventional Fourier reconstructed images was corrected [24]. All image reconstructions were thresholded to 3.5σ to distinguish between background and signal voxels. The number of ^{19}F atoms per image pixel was estimated from the PFCE concentration and the voxel size, and plotted against the SNR. Two-factor ANOVA was used to compare SNR (dependent variable) at various numbers of fluorine atoms between the two field strengths (independent variables). GraphPad Prism v.5.01 (GraphPad Software, Inc. La Jolla, CA, USA) was used for the analysis. SNR efficiency ($\mathrm{SNR}_{\mathrm{eff}}$) for 2D-FLASH data was calculated as follows [27]:

$$\mathrm{SNR}_{\mathrm{eff}} = \frac{\mathrm{SNR}}{\sqrt{\mathrm{NA} \times \mathrm{TR}}}. \tag{3}$$

Calculations of PFCE T_1 and T_2 relaxation times were performed on MSE and RARE-VTR scans using parametric mapping developed in MATLAB® in-house. T_1 and T_2 were determined by fitting the following relation [28] to the obtained data points using least-squares optimization:

$$S_{(\mathrm{TR})} = S_0 \cdot \left(1 - \exp\left(\frac{-\mathrm{TR}}{T_1}\right)\right), \tag{4}$$

$$S_{(\mathrm{TE})} = S_0 \cdot \exp\left(\frac{-\mathrm{TE}}{T_2}\right), \tag{5}$$

where $S_{(\mathrm{TR})}$ and $S_{(\mathrm{TE})}$ are the signal intensity at a specific repetition time and specific echo time, respectively, S_0 is the maximum signal and TR and TE are a specific repetition time and specific echo time, respectively. Depending on the experiments, relaxation times were calculated either as pixel-based data points or averaged data within specific regions of interest, corrected for the non-Gaussian noise distribution in MR magnitude images [24].

Calculations of T_1 relaxation time for PFCE were also performed on 2D-FLASH acquisitions with different TRs and FAs (α). T_1 was calculated from the Ernst equation [29]:

$$S_{(\mathrm{TR},\alpha)} = S_{0,\alpha} \cdot \sin \cdot \frac{1 - \exp(^{-\mathrm{TR}}/_{T_1})}{1 - \cos\exp(^{-\mathrm{TR}}/_{T_1})}, \tag{6}$$

where $S_{(\mathrm{TR},\alpha)}$ is signal intensity at a specific repetition time and flip angle (α) and $S_{(0,\alpha)}$ is the maximum signal intensity at a specific α.

For a 3D representation of ^{19}F ^{1}H MR image overlays of *Setup 3* (EAE mouse brain and associated lymph nodes), ^{1}H MR data were first converted to NIFTI-format in *ImageJ* (National Institutes of Health, USA, http://imagej.nih.gov/ij and ^{1}H MR images of inflamed regions (CNS) and draining lymph nodes were segmented using *ITK snap* (version 3.4) [30].

Results

Estimation of noise contribution and SNR gain from 9.4 to 21.1 T

Prior to performing the practical experiments, we estimated the SNR gain to be expected at 21.1 T from simulations. We first studied the noise contributions for both the 9.4 T and 21.1 T MR systems. The intrinsic noise contribution of the RF coil (capacitors, copper and housing) compared to the total noise power (Table 1) showed that the 9.4 T coil was only slightly more sample noise dominated (35.5% sample vs. 32.6% intrinsic coil losses). The intrinsic noise contribution of the 21.1 T coil is lower: in contrast to the 9.4 T coil, the sample noise dominates over the coil noise contribution (37.1% sample vs. 5.4% intrinsic coil losses). At 21.1 T, the noise contributed by the total cable length (between preamplifier and coil) as well as preamplifier noise appeared to be higher, almost double that of the 9.4 T system. For birdcage coils, as used in this study, the transmit field (B_1^+) is expected to be approximately equal to the receive field (B_1^-). From the simulations we calculated an average B_1^- field strength of 288 µT at 9.4 T and 153 µT at 21.1 T, for a forward power of 1 kW. Using the principle of reciprocity [15], and ignoring all flip angle, sequence and relaxation-dependent effects, the expected SNR ratio was calculated as 2.68 using Eq. (1). This ratio represents a baseline estimation of the expected SNR gain, based on the information available for the specific hardware of each system. Additionally, one can estimate the SNR gain between the two systems by considering the relationship of the individual reference powers required for calibrating a 90° flip angle. The reference power required at 9.4 T and 21.1 T was 0.257 W and 0.338 W, respectively. This translates to a field magnitude of 12.3 $\mu T/\sqrt{kW}$ at 9.4 T and 9.3 $\mu T/\sqrt{kW}$ at 21.1 T. The ratio between the two field magnitudes (0.76) can be used as a scaling factor in Eq. (1) to calculate SNR gain from the quadratically increasing MR signal strength. This yields an estimated SNR gain of ~3.8, when reference power is factored into the Eq. (1).

Experimental SNR difference between 9.4 T and 21.1 T

To determine the actual SNR gain we acquired axial ^{19}F MR scans of a nanoparticle phantom (*Setup 2*) containing four different concentrations of PFCE (Fig. 1a). We used a 2D-RARE sequence with variable slice thicknesses (1–10 mm, in steps of 0.5 mm). This together with the four different PFCE concentrations resulted in a total of 76 experiments to estimate SNR as a function of the number of ^{19}F atoms per voxel for both B_0 strengths. Figure 1a illustrates 20 of these SNR experiments (only 5 slice thicknesses are shown). Results of all SNR experiments were then plotted against the number of ^{19}F atoms per voxel for both B_0 strengths (Fig. 1b). There was a significant difference in the SNR for all 76 experiments between the two B_0 strengths observed at varying numbers of fluorine atoms ($p < 0.0001$, two-factor ANOVA). A mean SNR gain of 2.1 was estimated. For these experiments, we used a long TR in the 2D-RARE method to measure SNR differences between B_0 strengths.

In the next experiments, we studied the dependency of the actual SNR gain on the TR and flip angle (α) at both B_0 strengths. Axial ^{19}F MR scans of the pure PFCE compound (*Setup 1*) were acquired using a wide range of TRs (14–4000 ms) and α (5°–90°). SNR changes over the relaxation period were studied and the T_1 relaxation values for both B_0 strengths determined (Fig. 2). A 2-D fit of the measured data points resulted in $T_{1|9.4\mathrm{T}} = 788$ ms (Fig. 2a) and $T_{1|2\,1.1\mathrm{T}} = 409$ ms (Fig. 2b). The choice of TR has a

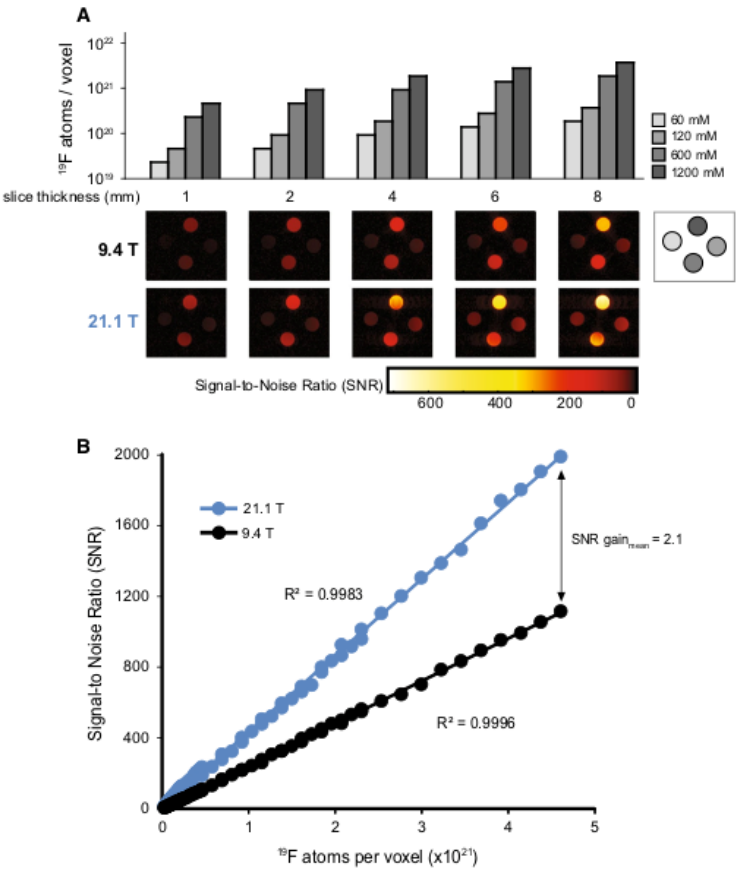

Fig. 1 Comparison of SNR between 21.1 and 9.4 T B_0 strengths in PFCE nanoparticles using a 2D-RARE sequence. **a** SNR was calculated from axial images of four NMR tubes (60 mM, 120 mM, 600 mM, 1200 mM) with varying slice thicknesses (shown are MR images of 1, 2, 4, 6 and 8 mm slice thickness). SNR was calculated by dividing signal from magnitude images by the background standard deviation, and corrected to compensate for the non-Gaussian Rician distribution. **b** Plot of SNR versus ^{19}F atoms per voxel. A linear fit was determined for both 21.1 T ($y=4e{-}19x$, $R^2=0.9983$) and 9.4 T ($y=2e{-}19x$, $R^2=0.9996$). A significant difference was determined between 9.4 and 21.1 T, $p<0.0001$, two-factor ANOVA

direct impact on the total acquisition time. A shorter TR permits more averages to be acquired in the same time period. To take this into consideration we estimated the SNR achievable in a fixed amount of time [27] (SNR efficiency = SNR/$\sqrt{t}$) from the data obtained at 9.4 T (Fig. 2c) and 21.1 T (Fig. 2d). For all scans with TR shorter than 4 s, we calculated how many averages would be possible within the fixed acquisition time, and then added the corresponding SNR improvement, based on the theoretical relationship SNR ~ $\sqrt{NA}$. As expected, SNR/$\sqrt{t}$ favors very short TRs for both B_0 strengths. The maximal SNR/$\sqrt{t}$ for 9.4 T was calculated to be 96/$\sqrt{min}$ at TR = 20 ms and $\alpha=13°$, while the maximal SNR/$\sqrt{t}$ for 21.1 T was calculated to be 701/$\sqrt{min}$ at TR = 20 ms and $\alpha=18°$. At the optimal condition for 9.4 T, i.e., TR = 20 ms and $\alpha=13°$, the SNR/$\sqrt{t}$ for 21.1 T was calculated to be 668/$\sqrt{min}$. The SNR/$\sqrt{t}$ ratio (between 21.1 T and 9.4 T) at these conditions is therefore 6.95, while the SNR/$\sqrt{t}$ ratio when comparing the best possible conditions for 21.1 T with the best possible conditions for 9.4 T is estimated to be 7.29. The SNR/$\sqrt{t}$ ratio will vary between the two B_0 strengths, according to the specific α and TR chosen for the particular experimental setup. Within a sensible range of α (1°–90°) and TR (15–4000 ms), the minimum SNR/$\sqrt{t}$ ratio would be 5.5 (at TR = 4000 ms, $\alpha=1°$) and the maximum would be 10.0 (at TR = 15 ms, $\alpha=90°$). However, these results illustrate the SNR/$\sqrt{t}$ ratio due to changes in both B_0 and T_1. To distinguish between both influencing factors, we modeled the SNR/$\sqrt{t}$ at 21.1 T for the T_1 observed at 9.4 T ($T_{1|21.1T}=T_{1|9.4T}=788$ ms). With this we could determine the B_0 effect on SNR efficiency independent of T_1 effects (Fig. 3): the maximal SNR/$\sqrt{t}$ for 21.1 T was calculated to be 505/$\sqrt{min}$ at TR = 20 ms and $\alpha=13°$, in comparison to the 96/$\sqrt{min}$ at the same TR and

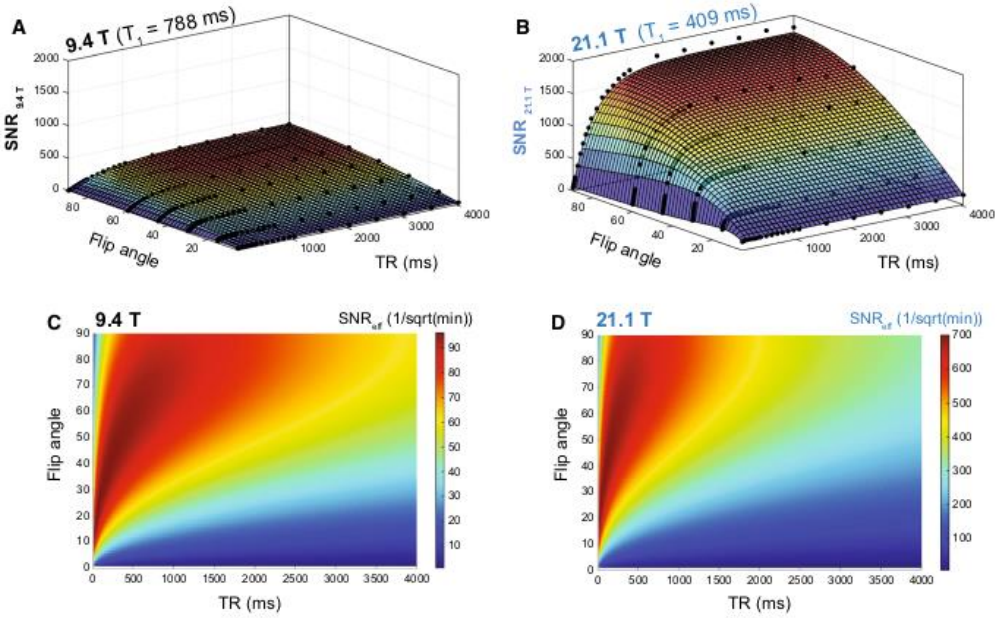

Fig. 2 Comparison of SNR between 21.1 T and 9.4 T B_0 strengths for pure PFCE using a 2D-FLASH sequence. SNR measurements at various repetition times (TR = 14–4000 ms) and flip angles ($\alpha = 5°–90°$) for both 9.4 T (**a**) and 21.1 T (**b**) B_0 strengths. 2-D fitting of these data points resulted in $T_{19.4T} = 778$ ms and $T_{1121.1T} = 409$ ms. SNR efficiency (SNR/$\sqrt{t}$) defined as the SNR achievable in a fixed amount of time was estimated for data obtained at 9.4 T (**c**) and 21.1 T (**d**)

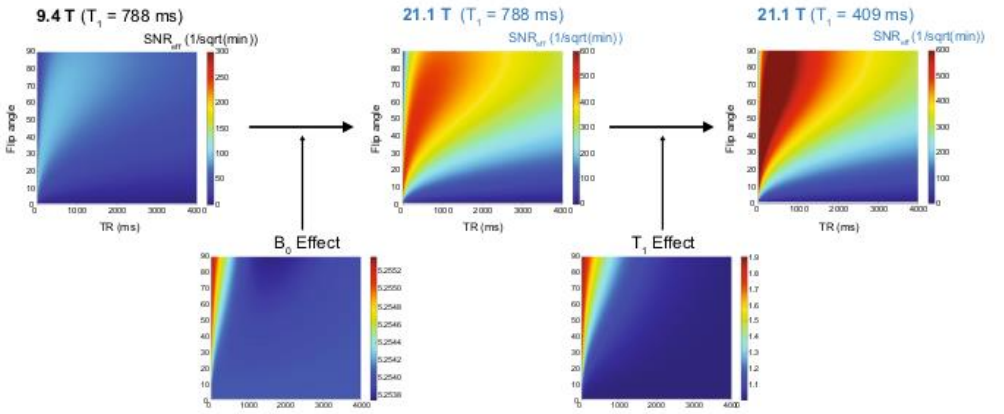

Fig. 3 SNR efficiency changes between 21.1 T and 9.4 T B_0 strengths for PFCE as a result of B_0 and T_1 effects. The B_0 factor on SNR efficiency at 21.1 T was calculated to be 5.25 after modeling SNR/$\sqrt{t}$ to keep T_1 between both magnetic fields constant ($T_{1121.1T} = T_{19.4T} = 788$ ms). The T_1 factor on SNR efficiency at 21.1 T was calculated to be 1.3

α for 9.4 T. This translates into an SNR/$\sqrt{t}$ ratio of 5.25 in comparison to 6.95 (when T_1 relaxation effects at 21.1 T were considered, $T_{1|21.1T}$ = 409 ms). In consequence, the T_1 shortening at 21.1 T results in an additional increase in SNR efficiency by a factor of 1.3 (Fig. 3).

We recently reported on the sensitivity gain achieved when comparing a cryogenically cooled ^{19}F RF probe (^{19}F CRP) with a room temperature ^{19}F RF coil of similar size [18]. Here, we attempted to compare the sensitivity gain achieved when moving from 9.4 T to 21.1 T with that achieved by using the ^{19}F CRP (Fig. 4). Although the two volume resonators used in the B_0 comparison were designed for the mouse body, the two RF coils used to determine SNR gains with the ^{19}F CRP were designed for the mouse head (Fig. 4, left panels). For all four RF coil configurations, we studied the SNR of the same phantom (pure PFCE, Setup 1) employing the parameters TR = 18.4 ms and $\alpha = 15°$, which are close to the conditions calculated to give the best SNR/$\sqrt{t}$ for the same sequence. The ^{19}F CRP is a transceive surface RF coil and does not achieve a spatially uniform excitation [18]. When studying the B_1 characteristics of this coil, a strong FA decrease is observed with increasing distance from the ^{19}F CRP surface [18]. In the previous experiments, we used one NMR tube with PFCE in the middle of the phantom. For the RT versus CRP comparison, we used two NMR tubes with PFCE to study the SNR gain at regions distal and proximal to the ^{19}F CRP surface. While the factor in the SNR change for the B_0 comparison was 6.59, the factor in SNR change from RT to ^{19}F CRP was 7.49 when measuring proximal to the ^{19}F CRP surface (upper ROI) and 0.93 when measuring distal to the ^{19}F CRP (lower ROI) (Fig. 4).

Relaxation times of PFCE at 9.4 T and 21.1 T

From the previous experiments, it was evident that T_1 relaxation was influenced by B_0. We next studied the impact of increasing B_0 to 21.1 T on both the T_1 and T_2 relaxation for PFCE nanoparticles. Similar to other nuclei, the transverse spin–spin (T_2) relaxation was decreased when moving from 9.4 T to 21.1 T (Fig. 5a). The PFCE concentration did not influence changes in the T_2 values of the nanoparticles at either B_0 strengths (Table 2). The longitudinal spin–lattice (T_1) relaxation time of PFCE nanoparticles was substantially shorter at 21.1 T, approximately 50% compared to 9.4 T (Fig. 5b). T_1

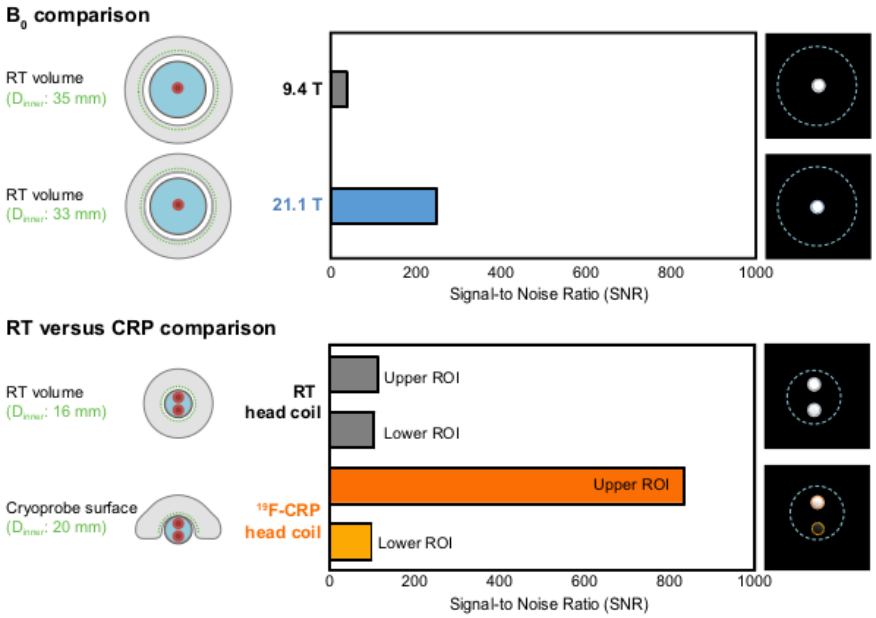

Fig. 4 ^{19}F MR sensitivity gain differences between the B_0 comparison from 9.4 to 21.1 T and a RT versus ^{19}F CRP comparison. Upper panel: B_0 comparison between 9.4 and 21.1 T using room temperature (RT) ^{19}F mouse body volume resonators with a diameter of 33–35 mm. Lower panel: RT versus CRP comparison using a RT ^{19}F mouse head coil and a ^{19}F CRP

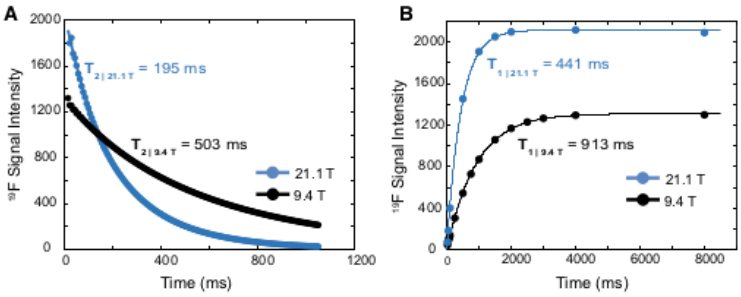

Fig. 5 ^{19}F relaxation times for PFCE nanoparticles measured at 21.1 T and 9.4 T. **a** T_2 relaxation of PFCE nanoparticles at 21.1 T was shorter than T_2 relaxation at 9.4 T ($T_{2|21.1T}$ = 195 ms $T_{2|9.4T}$ = 503 ms). **b** T_1 relaxation of PFCE nanoparticles at 21.1 T was shorter than T_1 relaxation at 9.4 T ($T_{1|21.1T}$ = 441 ms; $T_{1|9.4T}$ = 913 ms)

Table 2 No influence of PFCE concentration on T_1 and T_2 in ^{19}F nanoparticles

PFCE concentration	1200 mM	600 mM	120 mM	60 mM
$T_{2|9.4\,T}$ (ms)	500	350	580	535
$T_{1|9.4\,T}$ (ms)	910	920	925	950
$T_{2|21.1\,T}$ (ms)	195	105	185	230
$T_{1|21.1\,T}$ (ms)	440	445	495	460

PFCE concentration in the ^{19}F nanoparticles did not influence T_1 and T_2 values. Both T_1 and T_2 values for PFCE nanoparticles were influenced by B_0 strength, but neither value was influenced by changes in the ^{19}F content at either B_0 strength

Table 3 T_1 shortening at 21.1 T is consistent in all PFCE samples studied

Sample	B_0 (T)	T_1 (ms)
Pure PFCE	9.4	855
	21.1	435
PFCE nanoparticles (1200 mM)	9.4	915
	21.1	440
Ex vivo EAE spleen	9.4	1005
	21.1	400

Decrease in T_1 at 21.1 T is observed consistently for PFCE in all forms tested, as pure compound, in nanoparticle form or in ex vivo tissue from EAE mice that had been administered with PFCE nanoparticles

values were also not influenced by the PFCE concentration in the nanoparticles (Table 2). Shortening of the T_1 at higher B_0 strengths is not common for ^{1}H, where T_1 values are typically known to increase with increasing B_0 [31, 32]. The shortening of T_1 for PFCE at 21.1 T was consistent for different forms of the ^{19}F compound (Table 3). The 50% decrease in T_1 was observed in the pure compound (Fig. 2a), PFCE nanoparticles (Fig. 5b) and in ex vivo tissue from EAE mice administered PFCE nanoparticles (Fig. 6).

High spatially resolved ^{19}F MR imaging of EAE inflammation

To utilize the SNR gain observed in the above experiments to maximum advantage within the context of neuroinflammation, we investigated the feasibility of ^{19}F MR imaging at 21.1 T to detect brain inflammation in EAE at high spatial resolutions (Fig. 7). We observed a high level of detail of immune cell distribution in the inflamed brain and accompanying draining lymph nodes. Employing a resolution of 150 µm^3 at 21.1 T, ^{19}F MR signals were observed especially localized to the brain parenchyma (Fig. 7a). At this spatial resolution, these ^{19}F signals were not observed at 9.4 T when using a smaller room temperature coil [18]. When using the same RF coils employed in the present study to compare ^{19}F MR images in EAE mice, we observed even larger differences between 9.4 T and 21.1 T; even at low and medium spatial resolutions (222 µm^3 and 333 µm^3) most ^{19}F MR signals detected at 21.1 T were no longer identified at 9.4 T (Supplementary Figure). Given the highly homogeneous field provided by the RF coil used at 21.1 T, we could equally observe very prominent ^{19}F MR signals within the draining lymph nodes in the ventral region of the EAE mouse head.

Discussion

In this study, we demonstrate the feasibility and increased sensitivity of ^{19}F MR methods at 21.1 T for detecting inflammation with high spatial definition in the brain and adjacent lymphatic system in the animal model of multiple sclerosis. The potential applications of ^{19}F MR methods to image inflammation have long been recognized [1–5, 7], even in autoimmune encephalomyelitis [6, 33, 34]. ^{19}F MR methods

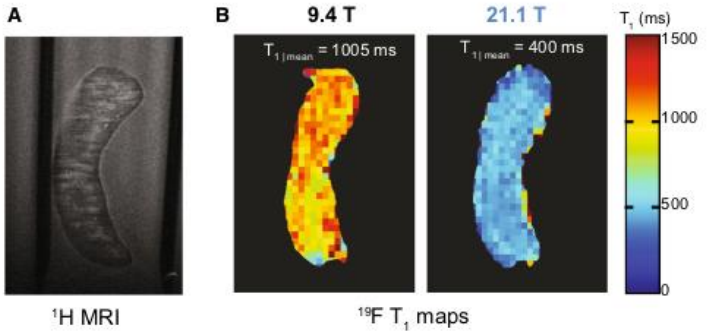

Fig. 6 ^{19}F relaxation times for PFCE in ex vivo EAE spleen measured at 21.1 T and 9.4 T. Spleens were harvested from EAE mice that had been administered PFCE nanoparticles for 5 days during imitation of disease. **a** ^{1}H MR scan of the ex vivo EAE spleen positioned in an NMR tube using 3D-FLASH: TR = 1500 ms, TE = 6.5 ms, FOV = [20 × 30 × 3.6] mm^3, matrix = 400 × 600 × 72, NA = 1, TA = 23 m. **b** T_1 maps were generated on one coronal slice of the spleen using RARE-VTR: 9 × TRs = 50–12,000 ms, TE = 6.9 ms, ETL = 4, FOV = [20 × 30] mm^2, matrix = 44 × 64, slice thickness = 3.6 mm, NA = 128, TA = 15 h 50 m. The averaged intensities over the coronal slice for all image series were fitted to the T_1 and T_2 equations

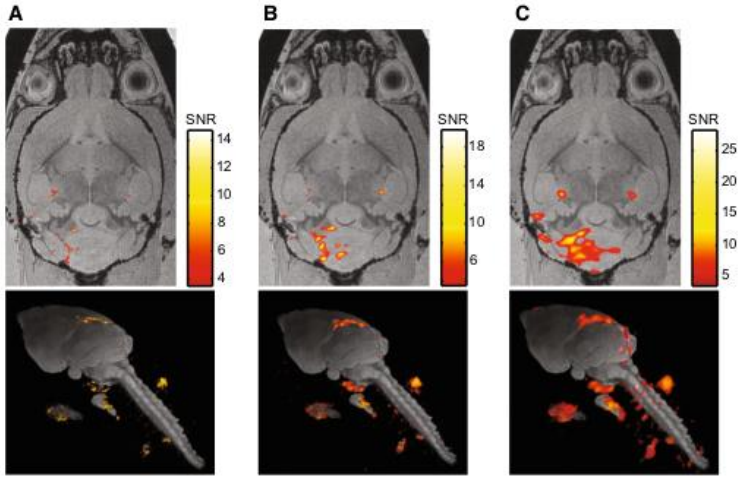

Fig. 7 ^{19}F MR image of an ex vivo EAE mouse acquired at 21.1 T and at different spatial resolutions. ^{19}F MR images were acquired using a 3D-RARE sequence acquired at three different spatial resolutions: **a** high: matrix = 195 × 130 × 130, resolution = 153 µm^3, **b** medium: matrix = 135 × 90 × 90, resolution = 222 µm^3, **c** low: matrix = 90 × 60 × 60, resolution = 333 µm^3. ^{19}F MR images (shown in red) were scaled to units of SNR (pseudocolor scale), thresholded at SNR = 4, and overlayed onto the FLASH ^{1}H anatomical MR images (shown in grayscale). For all three spatial resolutions both horizontal (upper panel) and 3D-render (lower panel) views of the EAE mouse brain and accompanying draining lymph nodes are shown

are conceptually appealing due to the superiority of ^{19}F nuclei over other MR-sensitive nuclei with regard to signal selectivity and specificity. However, they are constrained by sensitivity due to their typically low availability in vivo. Therefore, numerous efforts have been made to boost ^{19}F signal, e.g., by optimizing the efficiency of the acquisition methods according to the T_1 and T_2 values of the specific ^{19}F compounds [27], increasing the number of available ^{19}F nuclei by promoting ^{19}F nanoparticle cellular uptake [35] or by improving the sensitivity of the RF hardware by

introducing cryogenically cooled RF probes [18]. Nevertheless, major challenges in signal sensitivity constraints remain. Improving ^{19}F sensitivity using a combination of all currently available strategies, as well as developing new solutions, will be essential to realize the full potential of ^{19}F MR.

Here, we studied the potential of increasing B_0 for improving ^{19}F MR signal sensitivity. Prior to the practical experiments, we estimated the expected SNR gain to be 2.7, when moving from 9.4 to 21.1 T, taking into account the noise contributions for both MR systems and using the principle of reciprocity [15]. When we introduced the relationship of the reference power for both MR systems into Eq. (1), we estimated an SNR gain of ~ 3.8. In our practical experiments, we realized an SNR gain of 2.1 when employing a 2D-RARE technique on different concentrations of nanoparticles. In 2D-FLASH measurements, the ratio in SNR efficiency (SNR/$\sqrt{t}$ ratio) was estimated to be 7.29, when comparing the best possible conditions (optimal TR and α) at 21.1 T with those at 9.4 T and when including T_1 relaxation effects. Differences between the actual SNR gains determined experimentally and those expected from theory and simulations are conceivable, due to minor inaccuracies in the assumptions made for the EMF simulations. Factors such as sample noise, RF coil geometries, receive chain losses and preamplifier noise figure may add to the confounding influences that alter the actual SNR gain. In contrast to human imaging, the measurement noise in small animal imaging is dominated by the measurement hardware and not by the sample [36]. Thus in small animal MR scanners, differences in coil geometries and detector electronics can have a larger impact on the variations from expected sensitivity gains. Our estimations showed that in contrast to the 9.4 T RF coil, the intrinsic noise contribution of the 21.1 T RF coil was much lower than the sample noise contribution. However, the noise contributed by the relative long cables needed for the probe body (~ 2 m) with the 21.1 T and preamplifier was estimated to be higher, indeed almost double those at the 9.4 T system. Therefore, the highest potential for increased SNR gains (potentially up to ~ 40%) at 21.1 T could be achieved by using the shortest cables possible (e.g., by placing the preamplifier as close to the coil as possible) or using preamplifiers with a lower noise figure.

Another factor that must be considered when investigating B_0-influenced SNR changes is the potential changes in relaxation. Both spin–lattice (T_1) and spin–spin (T_2) relaxation times are expected to change with increasing B_0 fields. The SNR gain of 3.8 derived from the simulations does not take changes in relaxation time into account. When T_1 relaxation effects were removed from the experimental data, we calculated an SNR/$\sqrt{t}$ ratio of 5.25 (instead of 7). It is only in the fully relaxed regime that the SNR gain is expected to be influenced primarily by B_0 and not influenced by T_1-weighting. Water shows a highly significant increase in T_1 relaxation and decrease in T_2 relaxation in different regions of the rat brain with increasing B_0 in the range from 4.0 to 11.7 T [31]. Knowledge of T_1 relaxation is particularly crucial for MR spectroscopy and quantification of specific compounds. Brain metabolites show a similar, but less pronounced trend as water with respect to proton relaxation. Conversely, macromolecules display a strong dependency of T_1 on B_0, but T_2 is field independent [31]. Proton T_1 relaxation of brain metabolites does not increase substantially beyond 9.4 T (up to 14 T) and any changes likely have minimal impact on sensitivity [37]. Particularly for ^{19}F MR methods, where sensitivity is a crucial factor, it is critical to understand the mechanisms of T_1 relaxation. Interestingly, T_1 relaxation for ^{19}F compounds appears to be inversely related to B_0 strength. The decline in T_2 at higher B_0 could hamper the expected increase in ^{19}F MR signal at 21.1 T and warrants further consideration. The decline in T_1 with increasing B_0 is consistent with previous studies [38, 39]. Thus far, a decrease in ^{19}F T_1 for ^{19}F compounds has been attributed to an influence from dipole–dipole interactions and chemical shift anisotropy [38].

A decrease in T_1 for ^{19}F compounds with increasing B_0 has substantial ramifications, since this suggests the opportunity to increase SNR per unit time at higher magnetic field strengths by introducing more averaging. The T_1 shortening at 21.1 T observed in this study could provide one mechanism for the ratio in SNR efficiency (7.29) estimated from the 2D-FLASH experiments using optimal TRs and α specific to each B_0 strength. The observations made here at 21.1 T are especially meaningful for studies that are hampered by the low availability of ^{19}F spins and thus have a pressing need for sensitivity gains. An SNR gain could be exploited in several ways: e.g.. for a gain of 7.29, either the scan time could be reduced by a factor of 53 (e.g., from 60 to ~ 1.1 min) to obtain the original SNR or higher spatial resolution could be employed to achieve better image definition. In this study we made use of the SNR gain to acquire isotropic spatial resolutions of 150 μm^3 to study neuroinflammation (^{19}F MR signals) more precisely. At this resolution, we aimed to gain more precise information regarding inflammatory cell localization in the brain, compared to our previous studies [6]. The level of detail achieved at 21.1 T was similar to that of the ^{19}F MR images we recently obtained with a ^{19}F cryogenic RF probe (CRP) where we reported on a maximal SNR gain of 15 and were able to study intraparenchymal inflammation at a high isotropic resolution of 150 µm [18]. In the present study, we made the best feasible comparison of the sensitivity gains achievable between ^{19}F CRP and a B_0 increase to 21.1 T, given the current hardware limitations. Although different RF coil sizes and geometries were used to make this comparison, we measured

the same sample (pure PFCE) and used the same sequence parameters. Employing the 2D-FLASH technique used in the present study, we observed an SNR gain of 6.59 at 21.1 T when compared to 9.4 T, and an SNR gain of 7.49 with the CRP when compared to a room temperature coil of similar size. As discussed previously [18], the SNR gains achieved with the ^{19}F CRP can be attributed to several factors in addition to cooling: differences in RF coil design (birdcage vs. surface coil; quadrature versus linear), RF coil sample loading, and the specific RF pulse power adjustments all play important roles [18]. Even though the SNR gain achieved by moving from 9.4 T to 21.1 T is slightly lower than that realized at 9.4 T with a ^{19}F CRP, the SNR gain at 21.1 T is consistent throughout the entire field of view due to the homogeneity of the RF volume coils used. This is in striking contrast to the CRP, which has an inherent limitation due to the declining gradient in the B_1 field with increasing distance from the surface due to the transceive surface coil design [18]. Therefore in contrast to the ^{19}F CRP, ^{19}F signals in ventral regions of the head were prominently detected with a resolution of 150 µm at 21.1 T. Given the difficulty of detecting ^{19}F signals in these distal structures, most studies of the EAE model tend to focus exclusively on imaging of the brain. The advantages gained from using volume resonators at 21.1 T will allow a more comprehensive and detailed study of immune cell dynamics within the draining lymph nodes. On the other hand, studies focusing on the brain could be enhanced by using a CRP at this field strength. A fusion of both SNR boosting strategies has the potential for realizing even greater levels of detail when studying experimental brain pathologies.

Acknowledgements Part of this work was performed at the US National High Magnetic Field Laboratory (NHMFL), which is supported by the State of Florida and the National Science Foundation Cooperative Agreement No. DMR-1157490 and DMR-1644779. The study was funded by the Visiting Scientist Program of the NHMFL (227000-110, Project 12643 and by a research grant from the Deutsche Forschungsgemeinschaft to SW and AP (DFG WA2804, DFG PO1869). We thank Dr. Peter Schmieder, NMR expert at the Leibniz-Forschungsinstitut für Molekulare Pharmakologie (FMP), for helpful discussions on ^{19}F relaxation.

Author contributions S. Waiczies: study conception and design, acquisition of data, analysis and interpretation of data, drafting of manuscript; J.T. Rosenberg: study conception and design, acquisition of data; A. Kuehne: analysis and interpretation of data, drafting of manuscript; L. Starke: analysis and interpretation of data; P. Ramos Delgado: analysis and interpretation of data, critical revision; J.M. Millward: drafting of manuscript, critical revision; C. Prinz: analysis and interpretation of data; J. dos Santos Periquito: analysis and interpretation of data; A. Pohlmann: analysis and interpretation of data, critical revision; H. Waiczies: study conception and design, acquisition of data, analysis and interpretation of data; T. Niendorf: study conception and design, critical revision.

Funding The study was partly funded by the Visiting Scientist Program of the NHMFL (227000-110, Project 12643) and part of this work was performed at the US National High Magnetic Field Laboratory (NHMFL), which is supported by the State of Florida and the National Science Foundation Cooperative Agreement No. DMR-1157490 and DMR-1644779. This study was also partly funded by the Deutsche Forschungsgemeinschaft to S.W. (DFG WA2804) and A.P. (DFG PO1869). Thoralf Niendorf was funded (in part) by the European Research Council, ERC (ThermalMR, EU project 743077).

Compliance with ethical standards

Conflict of interest Thoralf Niendorf is founder and CEO of MRI.TOOLS GmbH, Berlin, Germany. All other authors declare no conflict of interest. Andre Kuehne and Helmar Waiczies are employees of MRI.TOOLS GmbH, Berlin, Germany.

Ethical approval All animal experiments were conducted in accordance with procedures approved by the Animal Welfare Department of the State Office of Health and Social Affairs Berlin (LAGeSo), and conformed to national and international guidelines to minimize discomfort to animals (86/609/EEC).

References

1. Flögel U, Ding Z, Hardung H, Jander S, Reichmann G, Jacoby C, Schubert R, Schrader J (2008) In vivo monitoring of inflammation after cardiac and cerebral ischemia by fluorine magnetic resonance imaging. Circulation 118(2):140–148
2. Ahrens ET, Young WB, Xu H, Pusateri LK (2011) Rapid quantification of inflammation in tissue samples using perfluorocarbon emulsion and fluorine-19 nuclear magnetic resonance. Biotechniques 50(4):229–234
3. Flogel U, Burghoff S, van Lent PL, Temme S, Galbarz L, Ding Z, El-Tayeb A, Huels S, Bonner F, Borg N, Jacoby C, Muller CE, van den Berg WB, Schrader J (2012) Selective activation of adenosine A2A receptors on immune cells by a CD73-dependent prodrug suppresses joint inflammation in experimental rheumatoid arthritis. Sci Transl Med 4(146):146ra108
4. Temme S, Bonner F, Schrader J, Flogel U (2012) 19F magnetic resonance imaging of endogenous macrophages in inflammation. Wiley interdisciplinary reviews. Nanomed Nanobiotechnol 4(3):329–343
5. Ahrens ET, Zhong J (2013) In vivo MRI cell tracking using perfluorocarbon probes and fluorine-19 detection. NMR Biomed 26(7):860–871
6. Waiczies H, Lepore S, Drechsler S, Qadri F, Purfurst B, Sydow K, Dathe M, Kuhne A, Lindel T, Hoffmann W, Pohlmann A, Niendorf T, Waiczies S (2013) Visualizing brain inflammation with a shingled-leg radio-frequency head probe for 19F/1H MRI. Sci Rep 3:1280
7. Jacoby C, Temme S, Mayenfels F, Benoit N, Krafft MP, Schubert R, Schrader J, Flogel U (2014) Probing different perfluorocarbons for in vivo inflammation imaging by 19F MRI: image

reconstruction, biological half-lives and sensitivity. NMR Biomed 27(3):261–271
8. Grenier N, Merville P, Combe C (2016) Radiologic imaging of the renal parenchyma structure and function. Nat Rev Nephrol 12(6):348–359
9. Hueper K, Gutberlet M, Bräsen JH, Jang M-S, Thorenz A, Chen R, Hertel B, Barrmeyer A, Schmidbauer M, Meier M, von Vietinghoff S, Khalifa A, Hartung D, Haller H, Wacker F, Rong S, Gueler F (2016) Multiparametric functional MRI: non-invasive imaging of inflammation and edema formation after kidney transplantation in mice. PLoS One 11(9):e0162705
10. Ladd ME (2018) The quest for higher sensitivity in MRI through higher magnetic fields. Zeitschrift für Medizinische Physik 28(1):1–3
11. Niendorf T, Barth M, Kober F, Trattnig S (2016) From ultrahigh to extreme field magnetic resonance: where physics, biology and medicine meet. Magn Reson Mater Phys Biol Med 29(3):309–311
12. Hoult DI, Richards RE (1976) The signal-to-noise ratio of the nuclear magnetic resonance experiment. JMagn Reson (1969) 24(1):71–85
13. Hoult DI, Lauterbur PC (1979) Sensitivity of the zeugmatographic experiment involving human samples. J Magn Reson 34(2):425–433
14. Pohmann R, Speck O, Scheffler K (2016) Signal-to-noise ratio and MR tissue parameters in human brain imaging at 3, 7, and 9.4 tesla using current receive coil arrays. Magn Reson Med 75(2):801–809
15. Hoult DI (2000) The principle of reciprocity in signal strength calculations—a mathematical guide. Concepts Magn Reson 12(4):173–187
16. Guérin B, Villena JF, Polimeridis AG, Adalsteinsson E, Daniel L, White JK, Wald LL (2017) The ultimate signal-to-noise ratio in realistic body models. Magn Reson Med 78(5):1969–1980
17. Schepkin VD, Brey WW, Gor'kov PL, Grant SC (2010) Initial in vivo rodent sodium and proton MR imaging at 21.1 T. Magn Reson Imaging 28(3):400–407
18. Waiczies S, Millward JM, Starke L, Delgado PR, Huelnhagen T, Prinz C, Marek D, Wecker D, Wissmann R, Koch SP, Boehm-Sturm P, Waiczies H, Niendorf T, Pohlmann A (2017) Enhanced fluorine-19 MRI sensitivity using a cryogenic radiofrequency probe: technical developments and ex vivo demonstration in a mouse model of neuroinflammation. Sci Rep 7(1):9808
19. Fu R, Brey WW, Shetty K, Gorkov P, Saha S, Long JR, Grant SC, Chekmenev EY, Hu J, Gan Z, Sharma M, Zhang F, Logan TM, Brüschweller R, Edison A, Blue A, Dixon IR, Markiewicz WD, Cross TA (2005) Ultra-wide bore 900 MHz high-resolution NMR at the national high magnetic field laboratory. J Magn Reson 177(1):1–8
20. Abad N, Rosenberg JT, Roussel T, Grice DC, Harrington MG, Grant SC (2018) Metabolic assessment of a migraine model using relaxation-enhanced 1 H spectroscopy at ultrahigh field. Magn Reson Med 79(3):1266–1275
21. Ananda K, Edelstein WA, Bottomley PA (2009) Noise figure limits for circular loop MR coils. Magnetic Resonance in Medicine 61(5):1201–1209
22. Waiczies H, Lepore S, Janitzek N, Hagen U, Seifert F, Ittermann B, Purfurst B, Pezzutto A, Paul F, Niendorf T, Waiczies S (2011) Perfluorocarbon particle size influences magnetic resonance signal and immunological properties of dendritic cells. PLoS One 6(7):e21981
23. NEMA (2008) Determination of signal-to-noise ratio (SNR) in diagnostic magnetic resonance imaging. National Electrical Manufacturers Association Standards Publication MS:1-2008
24. Henkelman RM (1985) Measurement of signal intensities in the presence of noise in MR images. Med Phys 12(2):232–233
25. Gudbjartsson H, Patz S (1995) The Rician Distribution of Noisy MRI Data. Magn Reson Med 34(6):910–914
26. Constantinides CD, Atalar E, McVeigh ER (1997) Signal-to-noise measurements in magnitude images from NMR phased arrays. Magn Reson Med 38(5):852–857
27. Faber C, Schmid F (2016) Chapter 1 pulse sequence considerations and schemes. In: Fluorine magnetic resonance imaging. Pan Stanford Publishing, pp 1–28
28. Haacke EM (1999) Magnetic resonance imaging physical principles and sequence design, vol xxvii. Wiley, Hoboken, p 914
29. Ernst RR, Anderson WA (1966) Application of Fourier transform spectroscopy to magnetic resonance. Rev Sci Instrum 37(1):93–102
30. Yushkevich PA, Piven J, Hazlett HC, Smith RG, Ho S, Gee JC, Gerig G (2006) User-guided 3D active contour segmentation of anatomical structures: Significantly improved efficiency and reliability. NeuroImage 31(3):1116–1128
31. de Graaf RA, Brown PB, McIntyre S, Nixon TW, Behar KL, Rothman DL (2006) High magnetic field water and metabolite proton T_1 and T_2 relaxation in rat brain in vivo. Magn Reson Med 56(2):386–394
32. Rooney WD, Johnson G, Li X, Cohen ER, Kim S-G, Ugurbil K, Springer CS (2007) Magnetic field and tissue dependencies of human brain longitudinal 1H2O relaxation in vivo. Magn Reson Med 57(2):308–318
33. Nöth U, Morrissey SP, Deichmann R, Jung S, Adolf H, Haase A, Lutz J (1997) Perfluoro-15-crown-5-ether labelled macrophages in adoptive transfer experimental allergic encephalomyelitis. Artif Cells Blood Substitutes Biotechnol 25(3):243–254
34. Zhong J, Narsinh K, Morel PA, Xu H, Ahrens ET (2015) In vivo quantification of inflammation in experimental autoimmune encephalomyelitis rats using fluorine-19 magnetic resonance imaging reveals immune cell recruitment outside the nervous system. PLoS ONE 10(10):e0140238
35. Waiczies S, Lepore S, Sydow K, Drechsler S, Ku MC, Martin C, Lorenz D, Schutz I, Reimann HM, Purfurst B, Dieringer MA, Waiczies H, Dathe M, Pohlmann A, Niendorf T (2015) Anchoring dipalmitoyl phosphoethanolamine to nanoparticles boosts cellular uptake and fluorine-19 magnetic resonance signal. Sci Rep 5:8427
36. Niendorf T, Pohlmann A, Reimann HM, Waiczies H, Peper E, Huelnhagen T, Seeliger E, Schreiber A, Kettritz R, Strobel K, Ku MC, Waiczies S (2015) Advancing cardiovascular, neurovascular, and renal magnetic resonance imaging in small rodents using cryogenic radiofrequency coil technology. Front Pharmacol 6:255
37. Cristina C, Vladimír M, Lijing X, Rolf G (2009) Comparison of T_1 relaxation times of the neurochemical profile in rat brain at 9.4 and 14.1 tesla. Magn Reson Med 62(4):862–867
38. Kadayakkara DK, Damodaran K, Hitchens TK, Bulte JW, Ahrens ET (2014) 19)F spin-lattice relaxation of perfluoropolyethers: dependence on temperature and magnetic field strength (7.0–14.1 T. J Magn Reson 242:18–22
39. Duong TQ, Iadecola C, Kim S-G (2001) Effect of hyperoxia, hypercapnia, and hypoxia on cerebral interstitial oxygen tension and cerebral blood flow. Magn Reson Med 45(1):61–70

12 Lebenslauf

Mein Lebenslauf wird aus datenschutzrechtlichen Gründen in der elektronischen Version meiner Arbeit nicht veröffentlicht.

13 Publikationsliste

13.1 Publikationen in Fachzeitschriften

Prinz, C., Starke, L., Millward, J. M., Fillmer, A., Delgado, P. R., Waiczies, H., Pohlmann, A., Rothe, M., Nazaré, M., Paul, F., Niendorf, T., & Waiczies, S. (2021). *In vivo* detection of teriflunomide-derived fluorine signal during neuroinflammation using fluorine MR spectroscopy. *Theranostics*, *11*(6), 2490–2504. https://doi.org/10.7150/thno.47130

Millward, J. M., Ramos Delgado, P., Smorodchenko, A., Boehmert, L., Periquito, J., Reimann, H. M., **Prinz, C.**, Els, A., Scheel, M., Bellmann-Strobl, J., Waiczies, H., Wuerfel, J., Infante-Duarte, C., Chien, C., Kuchling, J., Pohlmann, A., Zipp, F., Paul, F., Niendorf, T., & Waiczies, S. (2020). Transient enlargement of brain ventricles during relapsing-remitting multiple sclerosis and experimental autoimmune encephalomyelitis. *JCI insight*, *5*(21), e140040. https://doi.org/10.1172/jci.insight.140040

Eigentler, T. W., Winter, L., Han, H., Oberacker, E., Kuehne, A., Waiczies, H., Schmitter, S., Boehmert, L., **Prinz, C.**, Trefna, H. D., & Niendorf, T. (2020). Wideband Self-Grounded Bow-Tie Antenna for Thermal MR. *NMR in biomedicine*, *33*(5), e4274. https://doi.org/10.1002/nbm.4274

Starke, L., Pohlmann, A., **Prinz, C.**, Niendorf, T., & Waiczies, S. (2020). Performance of compressed sensing for fluorine-19 magnetic resonance imaging at low signal-to-noise ratio conditions. *Magnetic resonance in medicine*, *84*(2), 592–608. https://doi.org/10.1002/mrm.28135

Prinz, C., Delgado, P. R., Eigentler, T. W., Starke, L., Niendorf, T., & Waiczies, S. (2019). Toward ^{19}F magnetic resonance thermometry: spin-lattice and spin-spin-relaxation times and temperature dependence of fluorinated drugs at 9.4 T. *Magma (New York, N.Y.)*, *32*(1), 51–61. https://doi.org/10.1007/s10334-018-0722-8

Waiczies, S., Rosenberg, J. T., Kuehne, A., Starke, L., Delgado, P. R., Millward, J. M., **Prinz, C.**, Dos Santos Periquito, J., Pohlmann, A., Waiczies, H., & Niendorf, T. (2019). Fluorine-19 MRI at 21.1 T: enhanced spin-lattice relaxation of perfluoro-15-crown-5-ether and sensitivity as demonstrated in ex vivo murine neuroinflammation. *Magma (New York, N.Y.)*, *32*(1), 37–49. https://doi.org/10.1007/s10334-018-0710-z

Waiczies, S., Millward, J. M., Starke, L., Delgado, P. R., Huelnhagen, T., **Prinz, C.**, Marek, D., Wecker, D., Wissmann, R., Koch, S. P., Boehm-Sturm, P., Waiczies, H., Niendorf, T., & Pohlmann, A. (2017). Enhanced Fluorine-19 MRI Sensitivity using a Cryogenic Radiofrequency Probe: Technical Developments and Ex Vivo Demonstration in a Mouse

Model of Neuroinflammation. *Scientific reports*, *7*(1), 9808. https://doi.org/10.1038/s41598-017-09622-2

13.2 Buchkapitel

Millward, J. M., Periquito, J. S., Delgado, P. R., **Prinz, C.**, Niendorf, T., & Waiczies, S. (2021). Preparation of Ex Vivo Rodent Phantoms for Developing, Testing, and Training MR Imaging of the Kidney and Other Organs. *Methods in molecular biology (Clifton, N.J.)*, *2216*, 75–85. https://doi.org/10.1007/978-1-0716-0978-1_5

Waiczies, S., **Prinz, C.**, Starke, L., Millward, J. M., Delgado, P. R., Rosenberg, J., Nazaré, M., Waiczies, H., Pohlmann, A., & Niendorf, T. (2021). Functional Imaging Using Fluorine (^{19}F) MR Methods: Basic Concepts. *Methods in molecular biology (Clifton, N.J.)*, *2216*, 279–299. https://doi.org/10.1007/978-1-0716-0978-1_17

14 Danksagungen

Mein besonderer Dank gilt meiner Mentorin Sonia Waiczies für die rückhaltlose, fachliche und menschliche Unterstützung bei meiner Forschungsarbeit und diesem Promotionsvorhaben.

Ebenso danke ich meinem Doktorvater Thoralf Niendorf für den wertvollen fachlichen Input bei meiner Arbeit, sowie die Unterstützung bei Chancen und Herausforderungen.

Ich danke meinen Co-Autoren und Kollegen für die beispiellos vorzügliche Zusammenarbeit innerhalb der Forschungsgruppe und Unterstützung bei der Planung, Durchführung, Analyse und wissenschaftlichen Darstellung von Experimenten und dem erfolgreichen Abschluss unserer Forschungsprojekte.

Auch gilt mein Dank meinen Kooperationspartnern am Leibniz-Institut für molekulare Pharmakologie der Charité, der Physikalisch Technischen Bundesanstalt und MRI.TOOLS GmbH, Berlin für die wertvollen Beiträge zu unserer gemeinsamen Arbeit.

Ich danke meiner Ehefrau Sabrina, die mich in den zurückliegenden Jahren immer ermutigt und bestärkt und immer an mich geglaubt hat.